NORTHWESTERN UNIVERSITY

Improving Thermoelectric Performance Through Defect Engineering with an Emphasis on the Mesoscale

A DISSERTATION

SUBMITTED TO THE GRADUATE SCHOOL

IN PARTIAL FULFILLMENT OF THE REQUIREMENTS

for the degree

DOCTOR OF PHILOSOPHY

Field of Materials Science and Engineering

By

Jann Albert Grovogui

EVANSTON, ILLINOIS

December 2020

Abstract

Improving Thermoelectric Performance through Defect Engineering with an Emphasis on the Mesoscale

Jann Albert Grovogui

Thermoelectric materials are of particular interest in a variety of fields because of their ability to directly convert heat to electricity (and vice versa), however, they struggle to gain widespread adoption because of their low efficiency. A common strategy in the field of thermoelectricity is to introduce material defects into thermoelectrics from the atomic to the millimeter scale to increase the energy conversion efficiency. This dissertation discusses how the incorporation of electron microscopy, particularly at the mesoscale, was used to study structural defects to formulate processing-structure-property relationships and to develop design principles necessary for the fabrication of high performance bulk chalcogenide thermoelectric materials. Electron Backscattered Diffraction (EBSD) and Energy Dispersive Spectroscopy (EDS) were used in parallel to reveal compositional changes that occur during Spark Plasma Sintering in $NaPb_mSbTe_{m+2}$, and subsequent studies of the Se and S analogues helped uncover a grain boundary screening effect that can be used to optimize any material that has a low dielectric constant. Melt-Centrifugation of Bismuth Antimony Telluride (BST) proved the benefits of including microstructural defects across multiple length scales, while Induction Hot Pressing and thermal annealing of BST illustrated that similar microstructures could be introduced in a more controlled fashion. Furthermore, sample swelling during annealing implicated creep as a critical mechanism for property enhancement. Lastly, a fundamental study of extrinsic doping in PbSe emphasized the

effect that dopants and microstructure have on the thermal stability of thermoelectric materials and revealed a variety of microstructural-dopant relationships that can be manipulated by controlling specific processing procedures.

Acknowledgements

This dissertation isn't just my work or accomplishment, but it is the product of the love, support, and sacrifice of all of my friends, family, teachers, mentors, and countless others that have invested in me throughout my life. It is said in West Africa that "it takes a village to raise a child", and without my village, I would not be where I am today. I consider myself lucky to have such a large circle of support, but unfortunately that means that I almost certainly won't be able to thank everyone by name. So, at the outset of this acknowledgement, I would just like to formally thank everyone in my village who has been a part of my life and gotten me to this point.

The first person that I would like to thank by name is my advisor, Professor Vinayak Dravid. I could not imagine what my graduate school experience would have been like had I not been in your group. From my first meeting with you, I could sense that you genuinely cared about your students as people, and that feeling proved to be very true. During my time here you have ensured that I was able to grow both as a scientist and as a person by supporting me in the pursuit of my various passions. From making sure that I could leave on Friday afternoons to go to Junior Science Club, to encouraging me to apply for internships, you have been supportive of me forging my own path. You also have worked hard to create an inclusive group environment where I have made some of my best friends and colleagues. Graduate school can be mentally and emotionally tough, but with the network of support between the VPD Group and NU*ANCE*, I never doubted for a second that I would make it through, and I even had a lot of fun along the way.

I would also like to thank Professor Mercouri Kanatzidis, Professor Jeff Snyder, and Professor Chris Wolverton for being a part of my qualifying and defense committees. Professor

Kanatzidis, working closely with your group over the last 5 years has been a great experience. Your chemical intuition is remarkable, and you always know how to ask the tough questions. Working with your group has definitely pushed me to be extremely thorough in my microscopy, and I am very proud to have been a part of the work that we have done together. Professor Snyder, even though I was never officially part of your group, I have always felt that you have treated me almost as if I were one of your own students. Thank you for taking me under your wing and inviting me to all your group's different events (ranging from your group meetings to the International Thermoelectric Workshop/Birthday Party) and for opening my eyes to the depths of solid-state physics. Although my graduate work only scratched the surface of what you do, I am inspired to continue further down that road as I continue my scientific career. And to Professor Wolverton, thank you for kindness and approachability, in addition to providing your expertise on computational materials science. I would also like to say that although your course took me the furthest outside of my comfort zone, it ended up being one of my favorite graduate classes. Working with your group also helped my understanding of computational materials science and I think that this understanding will become increasingly more valuable as time goes on. In fact, my familiarity with computational techniques gave me the confidence to pivot during the first months of the Covid-19 Pandemic and allowed me to successfully finish my internship remotely. Thank you all again for taking the extra time to serve on my committee, for inspiring me, and for pushing me during my time as a PhD student.

Next, I would like to give a shout out to my collaborators. The first three I would like to thank are those with whom I worked with on the projects discussed in this dissertation. To Dr. Tyler Slade, I appreciated working so closely with you throughout our graduate school careers.

Thank you for the meticulous work that you did synthesizing all these lead chalcogenides and measuring transport data. Your attention to detail was key to a lot of our success. Dr. Ian Witting, your work ethic is inspiring, and I will forever be in shock by the sheer amount of BST samples that you synthesized, measured, and catalogued. I am thankful to have had the opportunity to work with you and to learn from you, and I am proud of what we were able to accomplish together. Dr. Shiqiang Hao, thank you for your patience and for sharing some of your wisdom with me. I appreciate you working with me on the PbSe doping project and for performing all the DFT that went into this dissertation. In addition, I would like to thank my many other collaborators who have either worked with me directly on other projects or were a part of the thermoelectric collaboration at Northwestern. They include, but are not limited to: Dr. Xiaomi Zhang, Songting Cai, Dr. Riley Hanus, Dr. James Hodges, Dr. Sumanta Sarkar, Dr. Zhong-Zhen Luo, Dr. Eric Isaacs, Dr. Hongyao Xie, Dr. Koushik Pal, Dr. Yi Xia, Dr. Xia Hua, and Shashwat Anand.

I would also like to thank all the NU*ANCE* staff and post-docs who helped me along the way as I learned about microscopy and materials characterization. I would like to thank Dr. Jinsong Wu, Dr. Kai He, Dr. Yaobin Xu, Dr. Hee Joon Jung, Dr. Sungkyu Kim, Dr. Roberto dos Reis, Dr. Kun He, Dr. Xiaobing Hu, and Dr. Paul Smeets for providing me with S/TEM training, advice, and help over the years. I also appreciate all of Dr. Poya Yasaei and Dr. Qing Tu's help with AFM and other thin film microscopy and measurement techniques. I would also like to thank Dr. Ben Myers, Karl Hagglund, and Tirzah Abbott for helping me with all my SEM questions and making the EPIC facility a fun (but also safe and productive) work environment. I enjoyed working for you all (and Chad Goeser) as a lab assistant. You were the best bosses I could have asked for and great friends as well…. even if Chad was forced to "fire" me during the shutdown. A special thank

you also needs to goe to Amy Morgan Rose. Simply put, you are the real MVP, thanks for making our group run so smoothly and for just being an awesome person.

This next section is dedicated to all the other friends I've made along the way who have helped me grow and succeed. The VPD group is full of some of the most intelligent, thoughtful, caring, and fun people. As happy as I am to graduate, I will definitely miss my time with everyone, and leaving the group is extremely bittersweet. I would especially like to acknowledge my Cook Hall officemates: Dr. Fernando Castro, Dr. Xiaomi Zhang, Cesar Villa, Dr. Poya Yasaei, and Stephanie Ribet. I'm doing my best here not to write a book, so I just want to say that my grad school experience was defined by the friendships and experiences that I shared with those of you in the office. I also would like to thank some of the friends I made in my cohort. Allessandra DiCorato, Jennifer DiStefano, Dr. David Delgado, Dr. Megan Hill, Dr. Akshay Murthy, and Thaddeus Reese, we've come a long way from doing problem sets together and I would like to thank you for your friendship and for keeping me sane throughout this whole process. Physical health is also critically important to graduate school success, so I would like to thank everyone who I played Intramural Sports with as well. Outside of my department I feel lucky to have met many other students across Northwestern who have enriched my time here. They are all rockstars. Among them are: Yves Nazon II, Izaiah Wallace, Dr. Marc Warrior, Schnaude Dorizan, Sarah Peko-Spicer, Dr. Alexandra Garr-Schultz, Dr. Lawrence Crosby, Ellesse Bess, Mecca Islam, Camille Calvin, Alisa White, Michael Threatt, Dara Gaines, and Will Corcoran. I'd also like to thank Penny Warren for her tireless work at Northwestern and for creating an environment within the Black Graduate Student Association that allowed me to meet most of the people I just named. Additionally, while we already knew each other, it was really nice to have my Pitt EXCEL family

nearby, so a huge thank you also goes to Alex Horn, Bon Ikwuagwu, Nina Maxey, and Kiara Lee. I also had the privilege to meet both friends and mentors while I was a graduate intern at the Johnson Space Center, so a big thank you goes to Dr. David Delafuente for giving me the opportunity to work with the Battery Safety Group, as well as to Jacob Darst and Amul Surelia for welcoming me in and showing me the ropes. I would also like to thank Cheryl Lawrence for hosting me during my stay in Houston and Vivaan Patel for being an excellent roommate (and for helping me get my job). I couldn't be more thankful for how well the three of us got along, and I can't imagine going through the Covid shutdown in Houston with anyone else. This section would not be complete without an enormous thank you to my wonderful girlfriend Courtney Bernat. I don't know why you've stuck around so long, but I'm sure glad you did. You're smart, funny, and beautiful, and my friends like you more than they like me. I really hit the jackpot! But additionally, you have been a really amazing support system for me, and your family (shout out to them as well) has given me a home away from home, which has made the last 3 years far better than I could've ever hoped for. Thank you for all you do, and I can't wait for our move to LA.

I think it is also important to note, that there was an incredibly long line of people who helped me even get to graduate school in the first place. I would like to send a huge thank you to my Pitt EXCEL advisors Dr. Alaine Allen, Dr. Yvette Moore, and Dr. Simeon Saunders who pushed me to become the best version of myself. As well as the rest of my Pitt EXCEL family and friends. Among them I would like to especially thank Dr. Ohi Dibua and Christopher Cameron who showed me what it took to prepare myself for graduate school. In addition, I would like to acknowledge Professor Karl H. Lewis for being a trailblazer for Black and minority students in STEM by founding the precursor to Pitt EXCEL (Pitt IMPACT) in 1969, and for personally being

a mentor to me up until his passing in 2019. Thanks also goes to SaLisa Berrien and Steven Jones for giving me the chance to meet Dr. Lewis and for giving me the opportunity to become the second Karl H. Lewis Scholar at The University of Pittsburgh. I would also like to thank my undergraduate research advisors Professor Mark Kimber and Professor Jung-Kun Lee, as well as those who mentored me during my summer internships (Professor Reuben Collins, Dr. Chito Kendrick, Professor Charles (Chuck) Stone IV, and Dr. Meltem Urgun-Demirtas) for investing in me at such an early stage of my engineering career. Another huge thank you goes to Assistant Dean Bruce Lindvall for seeing promise in me and recruiting me to come to Northwestern. Thanks also goes to the teachers and coaches I had throughout my primary and secondary education. I would like to thank my high school wrestling coaches, Coach Phil Simmonds and Coach Andy Posil in particular, for pushing me to excel academically. I also would like to thank Coach Simmonds for taking me on a tour of the CP Crane coal-fired power plant and kickstarting my passion for sustainable energy. I am fortunate to say I have had my share of great teachers, but I want to thank three in particular for actively changing my academic trajectory. So, I would like to give special thanks to Ms. Beverly White, Mr. Kevin Dalsimer, and Mr. Matthew Jochmans.

Finally, I would like to thank my family for their love and support. I love you all and I am truly lucky to have all of you in my life and to have such a strong foundation. Obviously, I need to specifically acknowledge my parents for raising me and giving me the chances and opportunities to succeed. But I also want to thank you for teaching me important life lessons: to think critically, to treat people fairly and with compassion, and to be curious about the world. You are both incredible people and I can only hope to do half as much good for the world as either of you already have. Although I have come far, I hope that this degree is just the beginning of that journey.

Dedication

To My “Village”

Table of Contents

List of Figures

List of Tables

Chapter 1. An Introduction to Studying Defects in Thermoelectric Materials

This chapter introduces the fundamental concepts governing thermoelectric energy conversion and discusses some of the main motivations driving research in this field, as well as the current limitations and challenges associated with thermoelectric research. Specifically, the relationship between processing, microstructure, and material properties will be explained and used as motivation for the work discussed in this dissertation. Scanning/Transmission Electron Microscopy (S/TEM) techniques are particularly useful in the study of the structure and composition of the microstructures introduced into thermoelectric materials, because of the variety of signals produced by electron-sample interactions. As a key technology in the study of thermoelectrics, this chapter also discusses conventional nano- and microscale imaging, diffraction, and chemical analysis techniques. A unique focus of this dissertation is the emphasis on the importance of the mesoscale (1 μm - 1 mm) in governing thermoelectric performance, and the dependence of bulk processing procedures on mesoscale microstructure. As a result of this work's focus on the mesoscale, Electron Backscattered Diffraction (EBSD) will be introduced as an instrumental technique that will be highly utilized for developing a deeper understanding of processing-structure-property relationships in bulk thermoelectric materials.

1.1. Thermoelectric Materials: Fundamentals, Recent Advances, and the Role of Bulk Processing

1.1.1. The Thermoelectric Effect and Its Applications

The Seebeck Effect is a phenomenon that allows thermoelectric generators to directly convert heat into electricity.[1] Its namesake is the Estonian-German physicist Thomas Johann

Seebeck who is credited with first documenting that a temperature gradient across two dissimilar metals (connected in a closed loop) is capable of deflecting a magnetic needle, in what he called thermomagentism, in 1820.[2] Our modern understanding of the Seebeck effect is that a voltage develops in a material that has a temperature gradient across it. This potential gradient is formed by majority charge carriers diffusing from the hot end to the cold end and the resultant voltage is called the Seebeck voltage. The Seebeck voltage is proportional to the temperature gradient, and the constant relating these two potentials is a material property known as the Seebeck coefficient.[1,3] A related effect is the Peltier effect in which a temperature gradient can be created by passing current through a junction between two different materials.[1,3]

Thermoelectric devices can take advantage of either the Peltier or Seebeck effect, enabling them to be utilized for generating electrical power from heat sources or for electronic cooling. Thermoelectric modules are also appealing because they are solid-state devices (i.e. they have no moving parts), leading to quiet, vibration-free operation as well as long device lifetimes.[3]

1.1.2. Thermoelectric Devices and the Figure of Merit

Semiconductors have intrinsically large Seebeck coefficients, which is one reason that they are often selected as ideal thermoelectric candidates.[4] In addition, semiconductors can be degenerately doped to obtain either negative or positive majority charge carriers (n-type and p-type respectively). These n- and p-type materials can be used to create a thermoelectric device by connecting n- and p-type legs electrically in series and thermally in parallel along the direction of the temperature gradient. This arrangement is shown in **Figure 1.1a**. On the hot side of the modules, majority carriers will diffuse more quickly than in the cold side, resulting in a net flow

of majority carriers from the hot side to the cold side. If the device is attached to an electrical circuit, then unidirectional current flow can be established.[1,5]

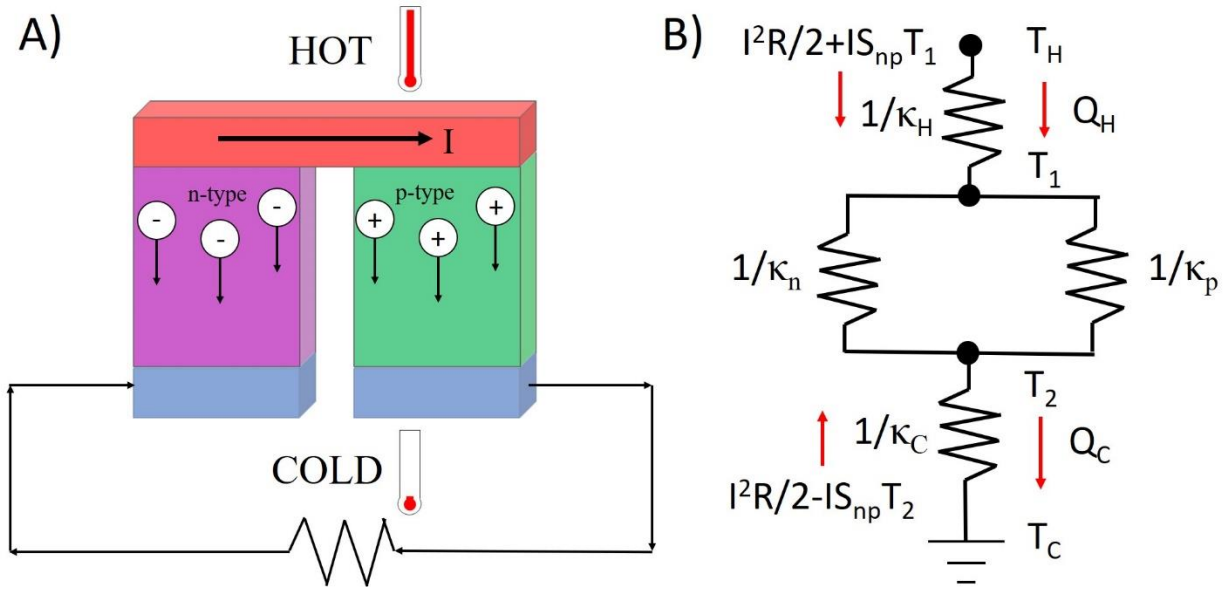

Figure 1.1. A) p- and n-type legs joined thermally in parallel and electrically in series to form a thermoelectric device. B) The simplified equivalent thermal circuit for the thermoelectric device which includes temperatures at the top and bottom of the heat exchangers (T_H and T_C), temperatures at the hot and cold side of the thermoelectric legs (T_1 and T_2), thermal conductivities of the heat exchangers (κ_H and κ_C), thermal conductivities of the leg components (κ_n and κ_p), and terms for Joule Heating and the Peltier Heating/Cooling at each junction($I^2R/2$ and $IS_{np}T$).

The energy conversion efficiency of a thermoelectric generator is derived by setting up a thermal circuit and by analyzing the device physics with a few basic generalizations. The thermal circuit representing a thermoelectric device (excluding heat transfer between the thermoelectric leg components or heat losses due to convection or radiation) is shown in Figure 1.1b.[6] The generalizations are: 1) the n- and p- type legs have equivalent thermal and electrical properties

(with the exception that their Seebeck Coefficients are equal and opposite), 2) the legs have the same length and cross sectional area, and 3) the thermal and electrical contact resistances are negligible.[6] Using these assumptions, the equations for efficiency can be solved (yielding one equation for maximum efficiency and one equation for maximum power) and are given as follows:

$$\eta_{Max\ Power} = \left(\frac{ZT_1}{ZT_{avg}+ZT_1+4}\right)\left(\frac{T_1-T_2}{T_1}\right) = \left(\frac{ZT_1}{ZT_{avg}+ZT_1+4}\right)\eta_{carnot} \qquad (1.1)$$

$$\eta_{Max\ Efficiency} = \left(\frac{\sqrt{1+ZT_{avg}}-1}{\sqrt{1+ZT_{avg}}+\frac{T_2}{T_1}}\right)\left(\frac{T_1-T_2}{T_1}\right) \qquad (1.2)$$

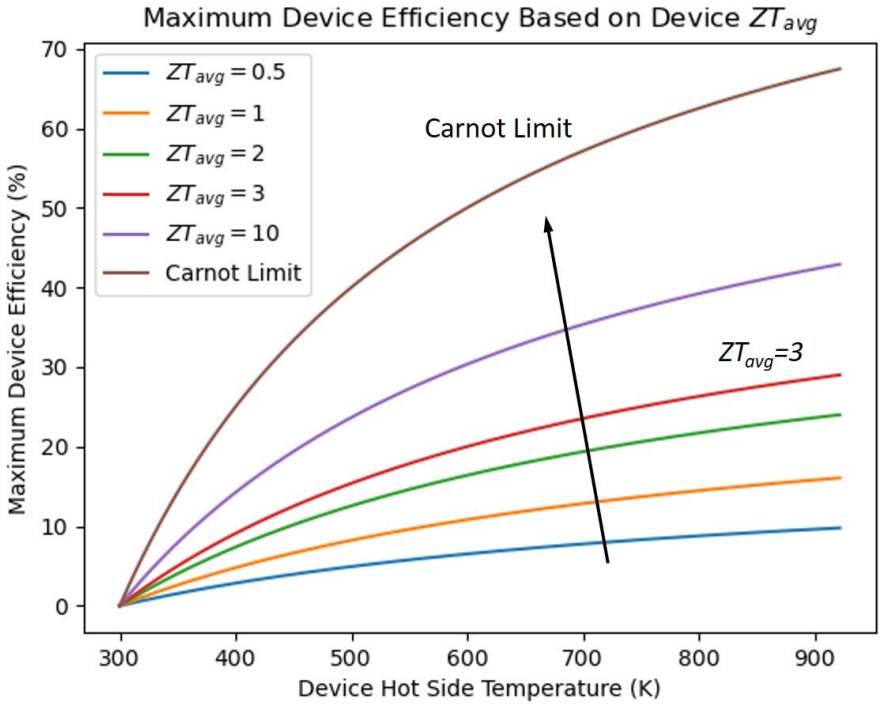

Figure 1.2. A graph of the increase in maximum device efficiency as the device ZT_{avg} increases, with the cold side device leg temperature set to T_2=300 K. A current goal in the field of thermoelectricity is to achieve devices with $ZT_{avg} \geq 3$ for thermoelectrics to become economically feasible for a wider variety of applications.

In both the operational conditions of maximum efficiency and maximum power, efficiency is related to the Carnot efficiency multiplied by a complex coefficient. Because these coefficients cannot exceed a value of 1, these equations indicate that the efficiency for thermoelectric devices cannot surpass the Carnot Limit.[6,7] Both coefficients also possess a term, *ZT*, which is referred to as the device figure of merit. By increasing this factor, the overall device efficiency will increase. The device *ZT* depends on factors such as the properties of the heat exchangers, as well as the material properties of the p- and n-type legs. However, if the heat exchangers were perfect (i.e. $T_1 = T_H$ and $T_2 = T_C$), and if the material properties were matched in both legs (excluding Seebeck coefficients which must be equal and opposite), and the material properties across the temperature gradient were assumed to be temperature independent, then the device *ZT* would only depend on the material properties of the thermoelectric legs. This special case of *ZT*, is known as the material figure of merit and is denoted as *zT*. [5,6,8]

The material figure of merit is:

$$zT = \frac{\sigma S^2}{\kappa} T \tag{1.3}$$

where $\sigma \left[\frac{S}{cm}\right]$ is electrical conductivity, S is the Seebeck coefficient $\left[\frac{\mu V}{K}\right]$, and κ $\left[\frac{W}{m\,K}\right]$ is the total thermal conductivity. Unfortunately, in a real device, the material properties are temperature dependent and there are device heat losses at the heat exchangers. Therefore, the device figure of merit (*ZT*) is often much lower than the material figure of merit (*zT*). For example, the material *zT* for commercial bismuth telluride is 1.1 while the device *ZT* is 0.7.[5] None the less, it is clear that by increasing in the material figure of merit, the overall device efficiency can be increased as well. Consequently, in the field of thermoelectrics, one of the main strategies to increasing device

efficiency is to increase zT by increasing the power factor (σS^2) while decreasing the thermal conductivity (κ).

1.1.3. Competing Mechanisms Governing Thermoelectric Material Properties

One theoretical framework for the advancement of thermoelectric performance is the Phonon Glass Electron Crystal (PGEC) construct. In PGEC, the goal is to develop materials that are simultaneously poor thermal conductors (like an amorphous glass), yet efficient electrical conductors (like a crystal).[4,9,10] If solid state materials could be designed in this manner zT could be improved drastically. However, the challenge with discovering and designing new thermoelectric materials is that electrical and thermal properties are often concomitant, and therefore rise and fall simultaneously. This means that unless electronic and thermal properties can be decoupled, there will be little improvement in the overall zT. Before attempting to decouple material properties, it is first important to understand the origins and interdependencies of the Seebeck coefficient, electrical conductivity, and thermal conductivity.

As mentioned earlier, the Seebeck coefficient is a material property relating the temperature gradient across a material to the induced voltage across said gradient.[5,11,12] The magnitude of the Seebeck coefficient is a result of the asymmetry in the transport function (which depends on the electronic density of states), as well as the change in the fermi distribution function with respect to energy.[11] In metals, the states above and below the fermi energy level are similar in magnitude and therefore there is little asymmetry leading to small overall Seebeck coefficients. However, in semiconductors, because of the large difference in available states between the conduction and valence bands, the Seebeck coefficient can be at least one order of magnitude larger than for those in metals.[13] In fact, semiconductors replaced metals as the material class of

interest for thermoelectrics, in part, because of their higher Seebeck coefficients.[11] However, semiconductors are not nearly as conductive as metals, so in order to improve electrical conductivity semiconductors are usually doped to become degenerate. Degenerate doping unfortunately makes the asymmetry in the Density of States less extreme and lowers the Seebeck coefficient. However, because of the high intrinsic Seebeck coefficients prior to doping, the overall power factor in degenerately doped semiconductors is still favorable. Using the single parabolic band model (with the assumption of energy independent scattering), the relationship between the Seebeck coefficient and the carrier concentration is revealed by the equation:

$$S = \frac{8\pi^2 k_B^2 m^* T}{3eh^2}\left(\frac{\pi}{3n}\right)^{2/3} \tag{1.4}$$

where k_B is the Boltzmann constant, h is Planck's constant, T is absolute temperature, m^* is effective mass, e is the elementary charge, and n is carrier concentration. This equation not only shows that the Seebeck coefficient is related to carrier concentration via the relation $n^{-2/3}$, but also reveals a linear dependence on effective mass.[5]

In addition to the Seebeck coefficient, to increase the power factor, the electrical conductivity needs to be increased as well. Represented using the Drude formula, electrical conductivity is expressed as:

$$\sigma = \frac{ne^2\tau}{m^*} \tag{1.5}$$

This equation reveals that electrical conductivity is proportional to carrier concentration (n) and inversely proportional to effective mass (m^*).[5,12] The effective mass can be envisioned as describing the way in which external forces interact with electrons in a material. The electrons will be accelerated by an external electric or magnetic field relative to the material lattice as if the electron's mass were its effective mass, rather than the true mass of an electron.[14] This means that electrons with larger effective masses, have a lower mobilities leading to lower electrical conductivity. Likewise, electrons with small effective masses are more mobile and result in larger electrical conductivites.[5]

Thermal conductivity is a linear combination of electrical thermal conductivity and lattice thermal conductivity.[5] Electrical thermal conductivity is caused by the transfer of heat from charge carriers, and can be calculated using the Wiedemann-Frantz law. This law states that the electrical component of thermal conductivity can be calculated by multiplying the electrical conductivity of a material by a constant, the Lorentz number multiplied by absolute temperature. The Lorentz number is approximately $2.4 \times 10^{-8} J^2 K^{-2} C^{-2}$, but it should be noted that it can change with carrier concentration.[5,15] The electronic component of the total thermal conductivity is difficult to manipulate, and therefore, when optimizing total thermal conductivity, most effort focuses on reducing the lattice thermal conductivity. This term can be reduced through several methods which include increasing size of the primitive unit cell, and introducing phonon scattering sites.[5,16–18] Phonons are lattice vibrations and can be scattered by defects on the same order of magnitude as their wavelengths which can range from 1 nm to 10 μm.[5,16] These defects therefore vary in size and dimensionality from atomic scale 0D defects such as vacancies and substitutional point

defects, to nano- and microscale defects such as 1D dislocations and 2D grain boundaries, to 3D nano- and microscale second phase precipitates.[17–19]

As can be seen by investigating the origins of materials properties above, increasing thermoelectric device performance by maximizing the material figure of merit (zT) is difficult because of the coupling of material properties and their shared interdependencies. Many of these material properties are dependent on similar variables (such as effective mass and carrier concentration) resulting in competing mechanisms, which leads to a peaks in zT.[5,16] The grand challenge of the field of thermoelectricity is to decouple these properties, which is performed by utilizing a variety of techniques and strategies that will be described in the following section.

1.1.4. Decoupling Thermoelectric Material Properties

1.1.4.1 Introducing Doping, Alloying, and Band Alignment to Increase Power Factor

Improving the power factor of conventional thermoelectric materials generally involves introducing impurities to dope materials and for the purpose of band engineering. As mentioned earlier, doping is a method of introducing impurities to increase the carrier concentration of semiconductors.[4] However, impurities can also be added with the intention of engineering a material's band structure to increase band degeneracy and altering the density of states.[19,20] Band degeneracy is achieved by alloying thermoelectric materials. The convergence of electronic bands can provide more conduction pathways for charge carriers, as well as change the structure of the bands.[21] In the case of PbTe, the heavier Σ band and lighter L band converge within a few k_BT through cation substitution.[20,21] Specifically, Sr^{2+} and Mg^{2+} can be substituted in place of Pb^{2+}, and because of their more ionic character, have valence bands comprised mostly of Te p-states. This

moves the PbTe-SrTe L band down lower to the Σ band, which has more p-state character.[21] Because the Σ band is wider, it has a higher effective mass and the convergence of these bands allows for the higher effective mass electrons to contribute to conduction. Although this lowers the mobility, it does increase the Seebeck Coefficient, raising the overall power factor of the alloy compared to pure PbTe.

This example leads to the idea that the density of states can be altered to provide enhancement to the power factor. Peaks in density of states can be introduced through resonant doping or with the introduction of microstructures.[19,22] In the case of PbTe, the change in effective mass occurred because of band convergence, yet in the case of resonant states and nanostructuring, the effective mass can be altered by inducing a spike in the density of states. This spike allows for a high Seebeck coefficient at particular levels of doping that allow for enhanced thermoelectric performance.[19,22]

Another strategy in thermoelectric band engineering (for materials which contain nanoscale, second-phase precipitates) is to align the bands between the matrix and the precipitate. In PbTe-SrTe system, the valence band of the SrTe phase is aligned with that of the PbTe phase. This maintains the carrier mobility by preventing holes from being scattered as they move through the material, thus ultimately maintaining a high power factor, despite the presence of multiple phases in the material.[23]

1.1.4.2. Introducing Defects to Decrease Lattice Thermal Conductivity

Along with increasing the power factor, microstructure can be utilized to decrease the thermal conductivity. Phonons and electrons are scattered by defect sites that are similar in size to their mean free paths, or the average distance they can travel before being scattered. Since,

electrons have a mean free paths of different lengths, *zT* can be improved by introducing defects that are the correct size to scatter phonons, yet will not inhibit electron mobility.[16,24] Due to the large range of phonon mean free path, there are several length scales of defects that can act as scattering sites for phonons.[16] Therefore, introducing defects on length scales ranging from the atomic to microscale can maximize the increase in phonon scattering.

The ability of defects to scatter phonons is dependent on the frequency of phonons present in a thermoelectric system. For example the Debye-Callaway model shows that grain boundaries have a larger effect on low frequency phonon modes, while point defects scatter high frequency modes.[25,26] This is intuitive based on the size difference of these defects, but the phonon mode distribution is highly temperature dependent, and therefore multiple defects may be needed in a single material in order to reduce its thermal conductivity over a large temperature range. According to the Debye-Callaway model, the contributions of different defects to lattice thermal conductivity are incorporated through their contribution to the frequency dependent relaxation time coefficient. Through Mathiessen's rule, the inverse of the total relaxation time (τ_{tot}) is obtained through a summation of the reciprocal of each individual defect's relaxation time (point defects, grain boundaries, dislocation cores, dislocation strain, etc.):

$$\tau_{tot}(\omega)^{-1} = \tau_{Umklapp}(\omega)^{-1} + \tau_{PD}(\omega)^{-1} + \tau_{GB}(\omega)^{-1} + \tau_{DC}(\omega)^{-1} + \tau_{DS}(\omega)^{-1} + \cdots \quad (1.6)$$

$$\kappa_{lat} = \frac{1}{3}\int_0^{\omega_{max}} C_s(\omega)\, v_s^2 \tau_{tot}(\omega) d\omega \quad (1.7)$$

where C_s is the thermal capacity, and v_s is the speed of sound.[17,25] To obtain optimal performance from thermoelectric materials, composition and structure must be intentionally designed to enhance the power factor while reducing total thermal conductivity. As the field of thermoelectricity continually pushes the limits of zT enhancement, it will only become increasingly important to control materials synthesis and processing to obtain the microstructures that will allow thermoelectrics to achieve their peak performance.

1.1.5. Processing Bulk Thermoelectric Materials

If thermoelectrics are to become more widely used, not only will materials have to become more efficient, but manufacturing will have to keep up with demand. This means that high-yield manufacturing techniques will be necessary to keep up with demand, and it is for this reason that bulk thermoelectric material manufacturing methods are often utilized.[27] As such, studying bulk thermoelectric synthesis and post-synthetic processes and their relationship to microstructure and thermoelectric performance are vitally important. Many bulk materials, and specifically materials discussed in this dissertation, are processed in two general steps. First the chemistry of the material is established by growing ingots, followed by a heat treatment that is established to obtain the desired microstructure. Once the ingots have been heat treated, they are usually quite brittle and thus are crushed into a powder and then re-sintered into a solid pellet to give added mechanical robustness.[27–31]

1.1.5.1. Bulk Material Synthesis

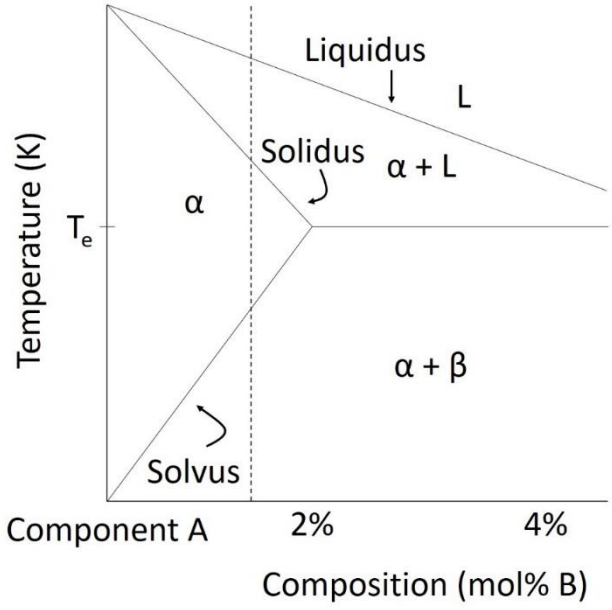

Figure 1.3. A schematic of an example Temperature-Composition phase diagram of a two-component system. The Solvus, Solidus, Liquidus and Eutectic Temperature (denoted by T_e) lines separate the regions in which different combinations of phases (α, β, and L). The dotted line denotes a fixed composition in which equilibrium heating or cooling would result in a phase change in the sample. These diagrams only show the thermodynamically stable phases at each temperature, so it is possible to obtain high temperature phases at lower temperatures by using quenching (or non-equilibrium cooling) to kinetically trap high temperature phases.

Processing thermoelectric materials usually starts with the synthesis of the material, which involved adding the correct combination of constituent elements and compounds to ensure that the chemistry of the material is correct. It is usually important for both property and microstructural control to understand the phase diagram of the material being synthesized.[27,32] Figure 1.3 is a schematic of a simplified temperature-composition phase diagram of a two-component material

systems. By studying the phase diagrams of real chalcogenides,[32,33] scientists can design thermoelectrics that exist within the targeted phase regimes to obtain the desired microstructure (if composition and thermal treatments are implemented properly). Synthetic steps usually involve raising constituent materials to their melting temperature and mixing the liquid components in a single-phase region to obtain a homogenous solution. The liquid mix is then rapidly quenched to prevent atomic diffusion, essentially trapping the high temperature phase at room temperature. Finally, if a two-phase material is desired, the phase diagram can be used to ensure the annealing temperature is within the two-phase region (below the solvus) to allow for precipitation and growth of a second phase. If a second phase is not desired, and the composition is appropriate, the sample can be heated into the single-phase region (usually above the solvus but below the solidus temperature to avoid re-melting) for additional homogenization.

1.1.5.2. Post Synthetic Processes

Once the chemistry and precipitate structure have been established, the resultant material is an ingot that is usually quite brittle and not very mechanically robust.[28] In addition to poor mechanical properties, ingots usually have large crystals and if there is any crystallographic anisotropy this could result in undesired directionality of thermal, electrical, and mechanical properties in the material. One way to combat the brittleness and potential anisotropy of material properties is to crush the ingot into a powder and then sinter the powder into a pellet. Because the grain size of the ingots is comparably large, the new grain sizes are governed by the size of the powder. An example of this drastic change in grain size was documented in the $NaPb_mSbTe_{m+2}$ (SALT) which will be discussed at length in the proceeding chapter.[28] The sintered material has

more strength and more preferable thermal properties due to the increased presence of grain boundaries as grain sizes are reduced drastically.[34]

Two common methods of sintering that will be discussed are Rapid Hot Pressing (RHP) and Spark Plasma Sintering (SPS). Both processes are preferred over conventional hot pressing because, although all three of these methods provide powder densification, SPS and RHP perform this process under much shorter time conditions. The short time required for the fusing and consolidation of powder particles is beneficial because it lessens the overall exposure to high temperatures in which undesired grain growth may occur or alterations in the microstructure which have already been induced by heat treating the constituent powder.[35] Because the grain size in controlled by the size of the powder, ingots are crushed (either by hand crushing or ball milling) and then sieved through a mesh with a fixed hole size. This will allow for the selection of powder particles of a specific size for sintering and therefore fix the final grain size.

SPS functions by running a current (on the order of kiloamps and under a few volts of potential) through the die and the powder being pressed to increase its temperature while pressing at high pressure.[36] RHP on the other hand uses RF induction heating to heat the die surround the powder while the press applies pressure.[35] In both cases there are many parameters to control (heating and cooling rates, maximum temperature, pressing time, pressing temperature, etc.), and it is also important to understand how material microstructure is altered during these steps, since sintering typically occurs after the annealing heat treatment of the ingot.

1.1.5.3. Importance of Studying Processing

Processing thermoelectric materials is vital for ensuring both cost effective and efficient manufacturing, as well as ensuring that thermoelectrics function at the highest possible level by intentionally introducing the appropriate microstructure into these materials. This dissertation focuses on the study of multiple processing techniques, as well as introduces additional design principles that should be considered when manufacturing thermoelectric materials. To study the relationship between processing and microstructure, materials characterization techniques are needed that are capable of studying a variety of material defects across length scales ranging from the atomic to the mesoscale.

1.2. Studying the Structure and Composition of Defects Across Multiple Length Scales

1.2.1. Nanoscale Analysis of Thermoelectric Materials

All-scale hierarchical architecturing has proven to be a valuable strategy in the enhancement of thermoelectric performance. As such, the use of electron microscopes has developed as one of the leading tools to study nanoscale defects. The advantages of electron microscopy derive from the fact that an electron beam is used to probe specimens of interest. Because electrons have mass and are charged particles, they have a strong interaction with matter.[37] This strong interaction results in both a variety of signals that are created due to electron-specimen interaction, and enables these signals to be highly localized, allowing small volumes to be individually probed. The signals from localized areas can then be detected by a variety of different detectors and under a variety of different conditions to perform a multitude of imaging, chemical analysis, and diffraction techniques. The combination of these modes of operation allows electron

microscopy to unveil a variety of information about defect structure and composition and enables scientists to advance the study of structure-property relationships in materials. This section describes some of the fundamental Transmission Electron Microscopy (TEM), Scanning Transmission Electron Microscopy (STEM), and Scanning Electron Microscopy (SEM) techniques that are used to obtain information that is imperative for drawing connections between processing, microstructure, and properties in thermoelectric materials.

1.2.1.1. Imaging with Transmission Electron Microscopy (TEM)

To explain how to identify and interpret structural defects in TEM, image construction must first be understood. In TEM imaging, the image construction mechanism requires parallel illumination of the sample by the electron beam, which creates coherency in the electrons. Because atomic spacing is similar in magnitude to the wavelength of electrons, the coherency of electrons prior to entering the specimen enables constructive and destructive interference of coherently scattered electrons passing through the sample as they scatter off of different sets of crystallographic planes.[38] The resultant interference patterns manifest as spots in reciprocal space in the back focal plane of the microscope as seen in Figure 1.4a. These diffracted spots each correspond to electrons that have been scattered by certain crystallographic planes, with the center bright spot corresponding to electrons that transmitted through the sample without scattering.[38] Using the Objective Aperture (OA), different beams can be selected to construct the final image, and the image plane will only contain electrons that originate from diffracted beams that were not filtered out in the back focal plane by the OA.[39] Figure 1.4b shows a ray diagram of the electron microscope optics, and in particular the location of the back focal plane, the OA, and the location of the final image on the screen when the TEM is in imaging mode.

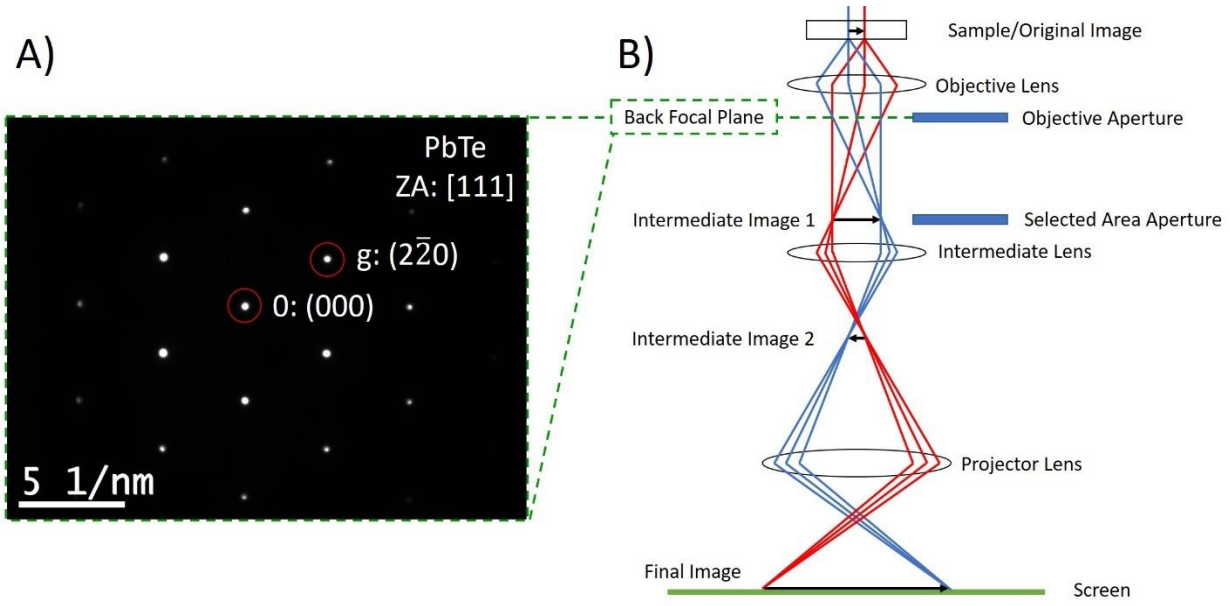

Figure 1.4. A) A diffraction pattern of the [111] Zone Axis of a PbTe sample is the reciprocal space representation of the specimen. B) A ray diagram of the optics of a TEM below the sample in imaging mode. In this mode, the diffraction pattern is in the back focal plane and the objective lens aperture can be used to select diffracted beams to be used in the desired imaging mode.

Several types of imaging modes may be used in TEM which take advantage of different types of contrast mechanisms. Bright Field (BF) TEM, is useful for qualitatively identifying a variety of structural defects because it takes advantage of diffraction contrast, which results in a variation in intensity due to orientation. By selecting only the central transmitted beam (0) for imaging, electrons that are scattered by any crystallographic planes are excluded from image formation.[39] This means that the average grain intensity will be related to the orientation of the grain, but this imaging mode will also have the effect of creating variations in intensity due to the changing of crystallographic orientation. This means that structural defects, such as dislocations, which distort the lattice in the vicinity of the dislocation core due to their strain fields will create

contrast gradients that can be observed using diffraction contrast techniques. By selecting a specific diffracted beams (for example, g in Figure 1.4a), dark-field (DF) images are produced in which only electrons diffracted by specific crystallographic planes make up the image.[39] This can be useful for highlighting features or planes of interest as well as specific phases which may have different diffracted spots than other phases present in the material.

When more than one beam contributes to image construction, the result is a phase contrast image. The two or more beams interfere with one another in the image plane as the electrons in different beams have different phases. As the OA increases in size, it allows more beams to contribute to the image. Unfortunately, these types of images are very sensitive to many sample and microscope conditions, and the complexity of these types of images means that they are difficult to interpret. For example, fringes that result from the interference between different diffracted beams are notoriously hard to interpret and are often mistakenly identified as atoms. However, if microscope conditions can be controlled, HRTEM allows microscopists to achieve incredibly high resolution without the additional enhancement of an aberration corrector.[39] Additionally, HRTEM images can be used in conjunction with image simulation software to unveil the true atomic structure of the sample revealing the intricacies of structures such as grain boundaries, phase interfaces, and dislocations which are all important to understand for the enhancement of thermoelectric materials.

In summary, TEM uses a coherent beam of electrons that transmits through the sample to construct images that take advantage of phase and diffraction contrast. This technique requires an understanding of the mechanisms at play to properly interpret images but can be greatly aided by

accompanying image simulation. TEM techniques provide the most utility in the study of thermoelectrics and other materials when crystallography or crystal orientation may be major factors in the features of interest in a sample and high resolution is required to obtain accurate information.

1.2.1.2. Imaging with Scanning Transmission Electron Microscopy (STEM)

STEM image construction is fundamentally different from image construction in conventional TEM and therefore can take advantage of slightly different contrast mechanisms. This imaging technique uses a converged, incoherent beam which is rastered across the sample, resulting in image construction that is performed on a pixel by pixel basis.[40,41] The detectors used are annular (circular or donut shaped detectors) so that only certain electrons that the user defines are collected. This enables only electrons scattered through a particular solid angle to be collected, which is important for controlling contrast mechanisms.[42] For each pixel in a pre-selected area of interest, the annular detectors collect all electrons that scatter between specified solid angles. It is the integrated intensity of all electrons in the specified solid angle range that are used as the scalar pixel intensity at that point.[41] This process is performed for all pixels to create an image and an example of this process can be seen in **Figure 1.5b** and 1.5c.

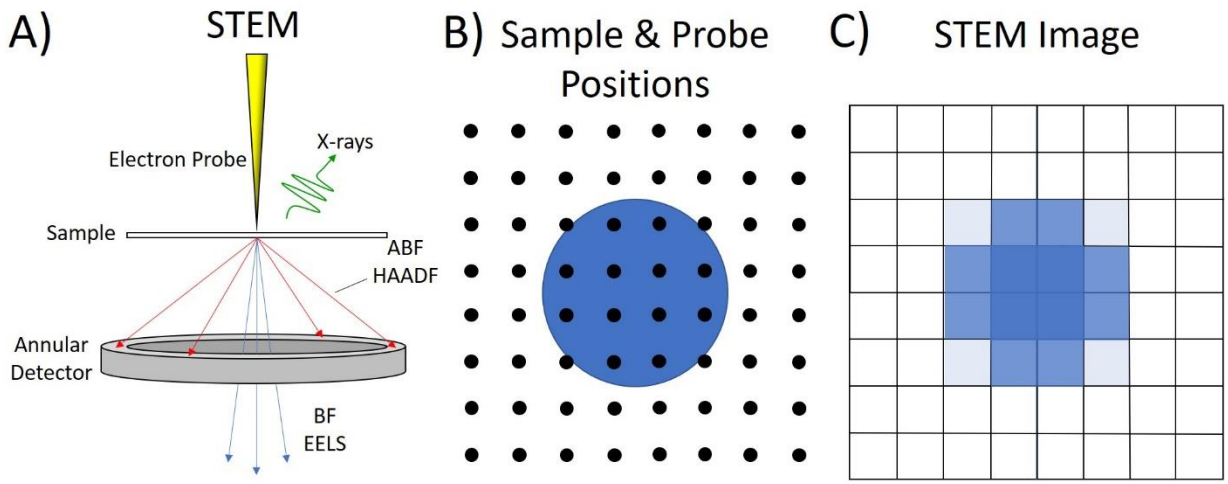

Figure 1.5. A) A schematic of the setup of a Scanning Transmission Electron Microscope illustrating the different types of electron sample interaction and signals that can be collected for analysis. B) A circular or spherical particle in the sample plane, as viewed from above. The black dots represent areas at which the probe will stop to collect signal. C) The reconstructed STEM image of the sample in B) with pixel intensity corresponding to the integrated intensity of signal collected at each scan position.

In many studies, but in this dissertation in particular, STEM High Angle Annular Dark Field (HAADF) is a popular technique. STEM-HAADF collects incoherently and elastically scattered electrons which are scattered to high angles due to interacting with atomic nuclei. This mechanism is known as Rutherford scattering.[41,42] This results in a strong intensity dependence (in STEM-HAADF) on the atomic number of the elements present in the sample. This differs from TEM-DF in which intensity is dependent on the crystallographic planes that diffract incident electrons. Therefore, STEM-HAADF is not only a useful imaging technique, but it also reveals qualitative information about the relative atomic mass of the elements present in a sample, which

is especially useful in the case of multiphase systems, or systems in which there is elemental segregation. A variety of other STEM imaging techniques exist such as Bright Field (BF), Annular Bright Field (ABF), and Annular Dark Field (ADF). These techniques incorporate various contributions of mass contrast and diffraction contrast and can be used (in some cases in unison) to collect complementing images with varying qualitative information about sample composition and structure. In addition, the advent of aberration correction technology enabled aberration corrected STEM (ac-STEM) to achieve image resolutions below an angstrom allowing for the imaging of individual atoms in modes like HAADF and ABF which allow various levels of mass contrast.[40]

1.2.1.3. Chemical Analysis using Analytical Microscopy

STEM is also preferable to TEM for analytical techniques, such as Energy Dispersive Xray Spectroscopy (EDS) and Electron Energy Loss Spectrometry (EELS), because of the high control the user has over the electron probe. Because of the high maneuverability of the probe in STEM, analytical STEM techniques are not only capable of collecting average spectra over a large area (as can be done with TEM-EDS), but they can also collect spectra at specific locations with resolution approaching the size of the electron probe, perform accurate line scans over features of interest, and produce EDS maps in which spectra can be extracted.

In this dissertation, the main analytical technique used is EDS. The mechanism that allows EDS to detect sample composition starts when energized electrons from the beam interact with electrons in the sample. During electron-specimen interaction, some incident electrons undergo inelastic scattering, transferring energy to electrons in the sample. The electrons in the sample then

become briefly excited, and upon relaxation back to their ground state, they will lose energy in the form of a photon with a wavelength in the x-ray spectrum. Every atom has its own characteristic wavelengths, and so by documenting the type and intensity of x-rays that reach the detector, the composition of the sample can be calculated.[41] This technique only works for elements heavier than Na because elements lighter than Na do not have enough orbitals for excitation and de-excitation to occur. This technique also has an energy resolution of approximate 0.1 keV and a sensitivity of about 1000 ppm.[41,43]

Analytical techniques such as EDS compliment the imaging capabilities of electron microscopes by allowing scientists the ability to understand chemical composition in conjunction with information collected via imaging. This can help with bridging the gap in understanding between structure-composition-property relationships in materials such as the composition of second phase nanoprecipitates in thermoelectric materials.

1.2.1.4. Crystallographic Analysis using Electron Diffraction

HRTEM and ac-STEM are both imaging techniques that are capable of revealing the atomic structure of samples (especially when used in conjunction with multi-slice electron microscopy image simulation). However, both of these imaging techniques are limited in a sense because they only provide a 2D projections of the sample.[37,44] Electron diffraction can help recover some of the information lost in the imaging process because it provides information about how electrons interact with the 3D lattice.

At high voltage, the wavelength of an electron becomes small enough that it can interact with a sample's atomic crystal structure.[37] The reciprocal space representation of the sample provides the pattern that is the manifestation of the constructive and destructive interference

patterns that area a result of this interaction. Therefore, by changing the electron optics to ensure that the reciprocal space representation of the sample coincides with the detector (rather than the real space image), diffraction patterns can be collected using an electron microscope. By indexing these diffraction patterns, additional information about a material's crystallography (phase, lattice parameters, orientation, etc.) can be extracted, much of which would not be measurable using imaging techniques alone. One of the most common techniques performed in TEM is Selected Area Electron Diffraction (SAED), which is shown in Figure 1.4a and **Figure 1.6a**. This technique uses the Selected-Area Aperture (SA) in imaging mode to ensure that only the electrons that contribute to a certain part of the image are involved in creating the diffraction pattern. This allows researchers to identify anomalies in crystal structure in precise locations. SAED is by no means the only diffraction technique, and different techniques focus on extracting different types of information about a crystal lattice. For example, another common technique (shown in Figure 1.6b) is Convergent Beam Electron Diffraction (CBED), which can reveal 3D information about crystal symmetry (and even strain) through an analysis of Higher Order Laue Zone (HOLZ) lines.[38]

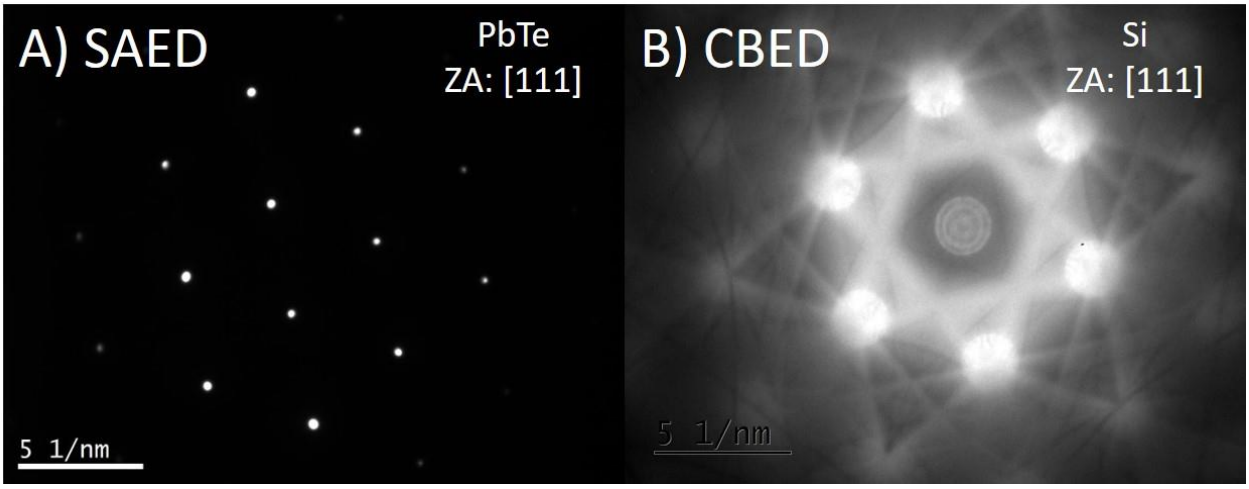

Figure 1.6. A) A Selected Area Electron Diffraction (SAED) Pattern taken with a parallel beam. The precise spot patterns may be used to index crystals and obtain information such as lattice parameters. B) A Convergent Beam Electron Diffraction (CBED) Pattern formed using a converged beam results in incoherent effects, such as spots growing into disks, and the formation of Kikuchi and Higher Order Laue Zone (HOLZ) Lines which can yield 3D crystallographic and higher order symmetry information.

Diffraction is a useful tool for studying materials defects in thermoelectrics for several reasons. Crystallographic and structural information becomes especially pertinent when examining complex structural defects, such as grain boundaries, which require 5 macroscopic Degrees of Freedom (DOF) to be identified in order to be defined, three of which come from the misorientation of the grains on either side of the boundary.[45] Additionally in TEM particularly, some imaging modes require the sample to be oriented so that the incident beam points down a crystallographic axis. This allows for precise diffraction of the incident beam across multiple crystallographic planes and enables the selection of specific beams for BF, DF, two-beam conditions, HREM, etc.[39] Without the flexibility of electron optics to change operational modes,

the precision of these techniques would be much reduced and the ability to study 3D crystallography in addition to 2D imaging and chemical analysis would be unachievable.

1.2.2. Mesoscale Characterization of Thermoelectric Materials

1.2.2.1. Large-Area Sampling in the Electron Microscope

A multitude of works have focused on using high resolution transmission electron microscopy techniques to observe and identify structural defects in thermoelectric materials. A large motivation for this in the study of chalcogenide thermoelectrics (as well as other thermoelectric systems) is that a large portion of the phonons in these materials can be scattered by features at the nanoscale.[16] As a result, a surge in research focusing on second phase nanoprecipitates and dislocations, have dominated the field of thermoelectrics.[15,17,23,26,46] This is in part due to the ideal size of these defects, but also because of the unique ability of high-resolution electron microscopy to probe localized nanoscale features such as precipitate size and composition, boundary coherency and strain, dislocation Burger's vectors, etc. However, one of the limiting factors of high-resolution electron microscopy techniques is that they have a limited field of view and therefore are not able to show the pervasiveness of these defects throughout the sample in a meaningful way.[37] In other words, defects can be identified, but, in many instances it is difficult measure the true defect density to relate property changes to defects densities. Additionally, some features are too large to be observed with techniques that are only capable of documenting a small field of view. One fix to the problem of the limited field of view associated with TEMs is to utilize scanning electron microscopy (SEM) techniques. SEMs have lower magnification, but their advantage comes from their much larger field-of-view. This gives SEM techniques the ability to

measure larger scale features (up to millimeters in size), as well as obtain data that provides more concrete evidence of defect densities.

1.2.2.2. Crystallographic Mapping: An Introduction to Electron Backscattered Diffraction

Electron Backscattered Diffraction (EBSD) is an SEM technique that is based on electron diffraction. As stated previously, many earlier works on thermoelectric materials focused on the micron and nanoscale, but the introduction of SEM-EBSD allows the study of the mesoscale (between 1 micron and 1 mm). Additionally, the diffraction information specifically provided by EBSD allows the study of features such as grain size, grain boundary orientation, twin boundary ratio, and texturing, all of which are important for formulating a more concrete understanding of structure property relationships in thermoelectric materials. Furthermore, with the added ability to measure the mesoscale, the importance of processing control will become more evident as will be shown in the following chapters. This dissertation will illustrate the utility of EBSD and encourage the future use of this technique in the study of thermoelectric materials. However, before the results of EBSD are discussed, it is important to fully understand the mechanisms, experimental setup, and data processing that are required to obtain accurate results from this technique.

Unlike conventional backscattered electron imaging in which a detector is placed directly above a flat sample, EBSD requires a sample to be mounted at an approximately 70° tilt with a side mounted detector present in the microscope chamber. Backscattered electrons are primary electrons from the beam that travel deep into the sample before experiencing an elastic scattering event.[47] This results in many backscattered electrons being unable to escape the sample and reach the detector for imaging or analysis. The sample tilt helps increase the number of elastically and

incoherently scattered electrons (those required to produce backscattered electron diffraction patterns or EBSPs) to escape the sample, while also ensuring that these escaped electrons are scattered predominantly in the forward direction.[48]

Before data collection begins, the relevant phases need to be known so that a crystal file can be created. These crystal files assist the software in identifying which Kikuchi patterns belong to specific phases and crystal orientations.[49] In addition to selecting the correct phases that will be present in the sample, the microscope parameters also need to be set to obtain the best quality maps. The microscope parameters that are usually important are the probe current, and probe size (controlled by the objective aperture size and spot size), accelerating voltage, step size, dwell time, and chamber pressure. Often these parameters have trade-offs, so it is important to understand the correct combinations of parameters to improve the quality of the pattern being collected. One of the most important parameters is the accelerating voltage. As voltage increases, patterns become sharper because each electron that hits the phosphorous detector screen has more energy and therefore more intensity is produced.[50] The important trade off here is that as voltage increases, so does the interaction volume, which can potentially lower the overall spatial resolution, as signal can originate from electron sample interactions within this volume, not just at the point at which the electron probe meets the sample surface.[51]

There are a variety of parameters that influence the size of the interaction volume, another of which is probe size. The probe is not an infinitely sharp point at the surface but has a finite size which is determined by the probe size selection. As the probe size gets larger so does the interaction volume, but more signal also is introduced into the sample which improves the signal to noise ratio of the EBSPs. The signal to noise ratio is also improved by the selection of larger condenser

apertures. A similar trade off occurs with condenser aperture size as with probe size. Larger apertures allow much more current to be introduced to the sample, yet this will usually coincide with a larger probe size.

Step size is arguable the largest influencing factor of spatial resolution in EBSD, but its contribution to overall spatial resolution depends on the step size selected. If you are scanning a large area with large features, to achieve reasonable scan times, the step size will usually be larger, and the resolution will be mostly dependent on the step size selected. If you are scanning over small areas, the step size can become much smaller than the interaction volume and it is at this point the influence of the interaction volume becomes more important for determining spatial resolution.

The last consideration during EBSD setup is how to reduce charging that may occur during data collection. Metal samples usually do not experience charging effects, such as drifting, in SEMs, however, because most thermoelectrics are semiconductors, it is important to ensure that charging causes minimal effects to retain scan integrity. During EBSD, there are longer dwell times at each step than would occur during typical image capture. This is because there need to be long enough integration times for EBSD patterns to be captured that have enough signal to noise so that the Kikuchi lines can be indexed. Therefore, to combat charging, samples should be mounted to ensure they are grounded (with copper tape) but may also require the user to operate the SEM in variable pressure mode. This assists with the dissipation of charge because as neutral

gas species interact with the beam in the chamber, they become ionized. The negative charge on the surface can then be dissipated by positively charged gas ions that contact the sample surface.[52]

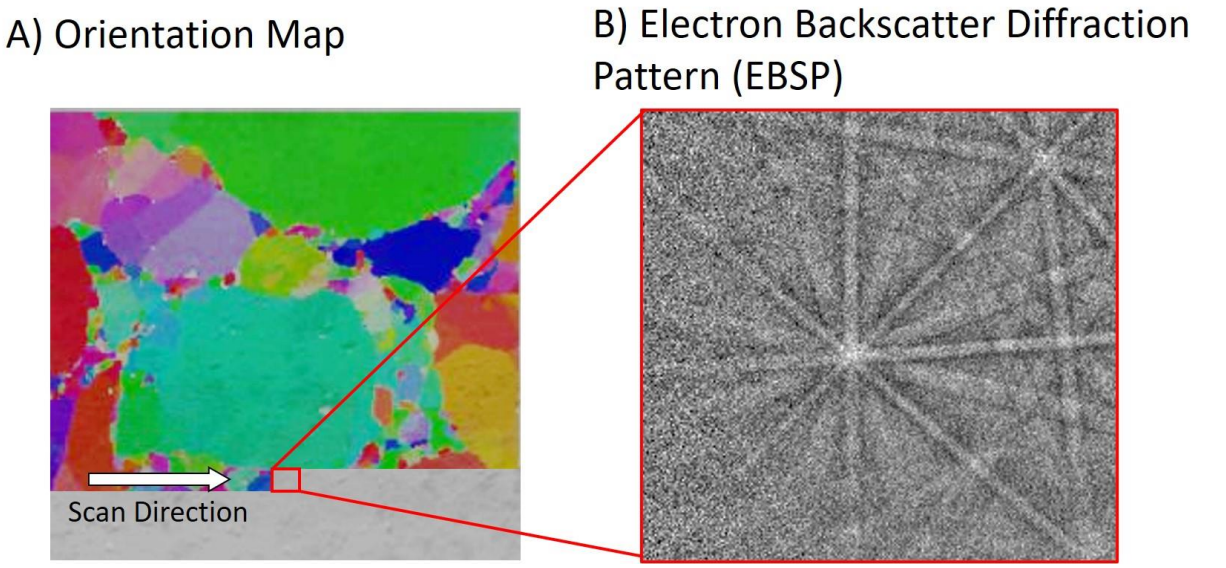

Figure 1.7. A) An EBSD map being created (over a secondary electron image), revealing grain orientation information. B) A sample EBSP that would be collected at each scan position and used to reconstruct EBSD maps pixel-by-pixel.

Once the microscope parameters have been set and the appropriate crystal files have been selected, the user selects an area of interest. As shown in Figure 1.7, an EBSP is collected at each scan position and automatically indexed. Once a pattern is indexed at each point, the data can be saved and processed to extract a variety of information. The most common images constructed using this technique are orientation maps which reveal the grain structure of a material by color coding each pixel according to the orientation of the crystal. An image created in this fashion will then reveal the grain structure because pixels within the same grain will be the same color, resulting in a multicolor grain map. EBSD data can also be used to quantitatively measure grain size

averages, as well as grain boundary orientation distributions, twin boundary ratios, and pole figures can even be extracted to measure texturing (or orientation alignment) of grains within the area of interest.

1.2.2.2. Importance of Sample Preparation and Post-Processing for Interpretation of EBSD

As illustrated in the previous section, to properly interpret EBSD data it is imperative to first obtain the best quality EBSPs. EBSP pattern quality can be enhanced by altering microscope conditions; however, the microscope conditions are ultimately rendered irrelevant if a high quality of polishing is not achieved prior to sample characterization.

Electron Backscattered Diffraction (EBSD) is sensitive to surface quality and therefore samples with minimal scratches and surface deformation are required to obtain useful and interpretable signal. Unfortunately, surface deformation from grinding steps can extend several microns below the surface for ductile materials, and increases with larger grit size.[53] To ensure the elimination of the deformation layer from prior cutting and grinding steps, I developed a set of sample preparation steps that retuned excellent EBSPs in thermoelectric materials (which are often times much softer and more prone to scratching and deformation than metallic samples). First, samples were cold mounted into fast-curing epoxy, which is often an excellent way to provide material stability from fracture and excessive deformation when grinding and polishing. Next, samples were manually ground using 600, 800, and 1200 grit SiC grinding paper (decreasing grit size) for 10 minutes each on a grinding wheel. A polishing pad with 1 μm and 0.1 μm diamond slurry were then used to polish samples on the grinding wheel for 30 min and 45 min respectively. Finally, the mounted samples were placed into a vibratory polisher with 0.1 μm diamond slurry for 3 hours at 150 V and 62.7 Hz. An added benefit of this rigorous sample preparation was that

samples prepared for EBSD in this way could then also be used for SEM-EDS analysis with no additional sample preparation as the surfaces were already flat and defect free.

Finally, it is important to note that EBSD should not be treated as a turn-key technique and that careful post-processing analysis must be performed in order to obtain the most accurate results. Depending on if the user wants to obtain data regarding grain size, grain boundary population, or the types of grain boundaries, different post-processing steps may be desirable or should be avoided due to the risk of unintentionally manipulating data. One example of this would be grain cleaning. Should a researcher be interested in grain size or phase distribution alone, filling in unindexed pixels from an image that is mostly indexed correctly should not alter data too severely (although it should be a step that is indicated in published works). However, if measuring grain boundary populations, as will be discussed in Chapter 4, cleaning unindexed pixels has the possibility to change values such as twin boundary ratios. Therefore, it is extremely pertinent that researchers are careful of when they are and when they are not post-processing data, that they document how this may be altering their results. Furthermore, for reproducibility and transparency it is imperative that they record and share how they are processing their EBSD data upon publication of their results.

1.3. Scope of the Dissertation

Thermoelectric devices are attractive for their potential to be incorporated into a variety of applications. Thermoelectric efficiency has limited the use of these devices to niche applications, however with recent advances in microstructural enhancement in the 1990's, the possibility of wider adoption of thermoelectrics has become feasible. Electron microscopy has become a key tool in studying the microstructures due to its ability to probe small volumes of material at high

resolution, and for its ability to produce and interpret a wide variety of signals, enabling the study of defect structure and chemistry from the atomic to the mesoscale.

Specifically, this dissertation will:

1) Investigate bulk synthetic processes, such as Spark Plasma Sintering, Melt-Centrifugation, and Induction Hot Pressing, to document the types of hierarchical defects introduced by these processing steps. Additionally, this dissertation will explore defect structure-property relationships and microstructural design principles required to advance the performance of bulk thermoelectric materials.

2) Emphasize the relevance of the mesoscale for its ability to provide insight into the populations of defects at other length-scales. Furthermore, this dissertation will show how mesoscale defects alter thermoelectric efficiency and thermal stability, and how specific modifications to bulk processing steps can be intentionally modified to obtain optimized material microstructure.

3) Discuss the intricacies of collecting and processing Electron Backscattered Diffraction data for analyzing mesoscale defects.

To cover these topics, this dissertation is organized as follows. **Chapter 1** serves as an introduction to both the field of thermoelectrics and the field of electron microscopy. This chapter sets the motivation for studying defects across multiple length-scales, and describes how various signals arising from electron-sample interaction are analyzed in order to perform imaging, chemical analysis, and electron diffraction to probe local structural and compositional defects in

solid materials. EBSD is also introduced along with a discussion of the tradeoffs between high resolution and high-volume sampling techniques. In **Chapter 2**, the study solid solution $NaPb_mSbQ_{m+2}$ (Q=Te,Se,S) compounds is aided by the incorporation of mesoscale compositional and structural analysis using EBSD. The documentation of grain size and composition brings to light the effects of SPS on compositional homogeneity of bulk thermoelectrics, as well as enables the development of a new design parameter in ionic thermoelectric materials. **Chapter 3** introduces Melt-Centrifugation as a kinetic processing technique, capable of producing porous Bismuth Antimony Telluride (BST) that out-perform its fully-dense counter parts. Nanoscale analysis combined with thermal modelling suggest that this synthesis technique incorporates a variety of micro- and nanostructures into the material that contribute to a large decrease in lattice thermal conductivity. **Chapter 4** discusses the attempt to reproduce the microstructure present in melt-centrifuged BST using a less kinetic processing method, Induction Hot Pressing, followed by a thermal treatment. EBSD is combined with traditional micro and nanoscale analysis in addition to thermal modeling and experimental data, to illustrate that the pore formation mechanism (creep) is critical to introducing defects into porous BST that lead to its thermoelectric performance enhancement over dense BST. **Chapter 5** explores the effects of extrinsic doping on the microstructure and thermal stability of PbSe by incorporating Density Functional Theory to provide insight on the point defects introduced into PbSe by intrinsic doping. SEM-EDS and EBSD reveal how these point defects manifest in altered mesoscale microstructure. Chapter 5 also shows how, with an improved understanding of dopant-microstructure relationships, intentional modification of powder processing and SPS conditions can help scientists achieve the desired

microstructure in their thermoelectric materials. **Chapter 6** is a summary of the work covered in the dissertation and provides suggestions of future work.

Chapter 2. Microstructural Control of Spark Plasma Sintered Lead Chalcogenides

The purpose of this chapter is to demonstrate how mesoscale characterization was used to form processing-structure-property relationships as well as establish new design criterion for improved thermoelectric performance in chalcogenide compounds $NaPb_mSbTe_{m+2}$ (SALT) and $NaPb_mSbSe_{m+2}$ (SALSe). Two main projects are highlighted in this chapter. In the first project, TEM imaging and electron diffraction were used to investigate the nanoscale of these samples and it was found (contrary to intuition and previous reports of analogous materials) that there are no nanoprecipitates present in these compounds, despite their high average zT (zT_{avg}). Mesoscale characterization using SEM imaging, EDS, and EBSD revealed the large-scale elemental segregation of Sb in the SALT ingots. These techniques helped further illustrate that the change of SALT thermoelectrics from p-type to n-type during SPS is due to the diffusion and homogenization of Sb into the parent phase. Once intentional compositional control could be achieved during synthesis, both SALT and SALSe compounds were fabricated that were capable of achieving high zT_{avg}. Upon closer investigation of the transport properties of these two compounds, a low temperature suppression of electrical conductivity in $NaPb_mSbQ_{m+2}$ compounds was observed when the chalcogen species (Q) was S or Se, but not when the chalcogen was Te. The second project highlighted in this chapter uses mesoscale electron microscopy characterization techniques, such as EBSD, to highlight that this effect is grain size dependent. Ultimately it was determined that this effect is due to grain boundary screening of charge carriers, the magnitude of which is directly related to the permeability and diaelectric constants of the material. This discovery adds a new design consideration into the microstructural optimization of thermoelectric materials. Portions of this chapter were previously published and are reprinted (adapted) with

2.1. Studying the Nanoscale in Thermoelectric Materials

2.1.1. Contributions of Nanoprecipitates to Thermoelectric Performance

The following work focuses on PbQ(Q=Te, Se, S)-based thermoelectric systems which were originally expected to show some amount of nanostructuring. However, the absence of nanoprecipitates, in combination with an increased focus on microscale and mesoscale features, enabled the identification of novel mechanisms related to materials processing that aided in the design of higher performing lead chalcogenide thermoelectrics. However, before discussing the novel mechanisms found in these solid solution thermoelectric systems, it is important to discuss why property enhancement is typically attributed to nanoprecipitates in similar material systems, and how nanoprecipitates can be ruled out as contributing factors in these PbQ-based thermoelectrics. Specifically, this section will discuss (1) how it is thought that nanoprecipitates contribute to thermoelectric enhancement, (2) why one might expect to see nanostructures in these specific thermoelectric systems, and (3) how to identify and study nanoprecipitates (or the lack thereof).

As stated in Chapter 1, the objective of microstructural design in thermoelectric materials is to increase phonon scattering while minimizing charge carrier scattering. Unfortunately,

thermoelectric materials do not function optimally in every temperature regime, due to the temperature dependence of their electronic and thermal properties, and therefore, not all microstructures will be as effective in improving efficiency in every thermoelectric system. One of the most commonly studied thermoelectric materials is PbTe with peak *zT* typically documented at intermediate temperatures (~800 K – 900 K).[28] PbTe is a favorable material because of its intrinsically low lattice thermal conductivity of approximately 2 W/mK, and because of its ideal electronic band structure which has closely situated valence bands that are capable of achieving a high density of states with degenerate doping.[54,55] Nanostructuring is specifically predicted to improve PbTe performance because a majority of the thermal conductivity (up to 80%) is derived from phonons with mean free paths under 100 nm.[16,56] This means that nanoscale features are of the correct size to impede phonon propagation.

Second phase nanoprecipitates are a particularly attractive feature at the nanoscale, because they are complex and have the ability to contribute multiple types of defects (some of which can be further controlled) such as dislocations and strain fields at interfaces (depending on the level of coherency),[23,57,58] as well as compositional variation. Interfaces are intriguing both structurally and chemically in two-phase materials. For example, it has been shown through atom probe tomography that dopants, such as Na, have a tendency to segregate to boundary interfaces.[16] Furthermore the crystallography of the matrix and precipitate phases are important because the crystal structure and lattice parameter mismatch can result in a variety of interfaces (coherent, semi-coherent, or incoherent), some of which may have strain or strain relieving mechanisms.[23,58] In the PbTe-SrTe material system, coherent boundaries constrain the precipitate phase to fit the lattice parameter of the parent phase when the precipitates occur below a particular size (2-5 nm

precipitate size). However, once precipitates get larger, they develop dislocations at the interface to relieve the strain needed to keep the lattice parameters equal.[23] Coherency is predicted to be beneficial because strain at the interface will increase phonon scattering, while the coherent lattice will allow for minimal charge carrier scattering.[57]

Thermoelectric enhancement can be performed by manipulating more than just the size of the precipitates. In fact, the composition of the second phase precipitates can also be altered to enhance charge transport. By ensuring the band structure of the precipitates matches that of the matrix, charge carriers will remain mobile throughout the entire two-phase system. It is not necessary for both the conduction and valence bands to match between the matrix and the precipitate, only the bands which conduct primary charge carriers need to be similar energies. For example, SrTe and PbTe have closely aligned valence bands, which allows high hole mobility in this system. In fact, this strategy has been used to show how precipitate composition can be selected to retain electronic charge carrier mobility in PbSe systems as well.[17]

Controlling the microstructure of thermoelectrics has proven to be quite successful. Since the idea of nano- and microscale manipulation of thermoelectric materials was introduced in the 1990's, recorded figures of merit began to surpass 1, which had been a previous ceiling for most thermoelectric materials.[59] With the incorporation of nanoscale defects and second phases, materials that had been known for decades, such as PbTe, began to show drastic improvements.[59,60] This led to the development of high performance alloys such as $AgPb_mSbTe_{m+2}$ (LAST),[61–63] $AgPb_mSn_nSbTe_{m+n+2}$ (LASTT),[64] PbTe-PbS,[15] and PbTe-SrTe,[17,65] which have all shown evidence of nanoprecipitation while achieving *zT*s above 1, and in some cases as high as 2.5.[59,65]

2.1.2. Preparing Samples for Accurate Identification of Nanostructures

Due to the variety of parameters that can be manipulated to create optimal nanoprecipitates, different electron microscopy tools are utilized to study how second phases interact with their parent phase. As discussed in Chapter 1, electron microscopes can perform imaging, diffraction, and analytical techniques, all of which can be used to investigate nanoprecipitate structure and composition. Yet before S/TEM analysis can occur, it is critically important that researchers understand how to properly prepare microscopy samples so that image interpretation and other analyses are as unambiguous as possible.[66]

Because transmission electron microscopy techniques require electrons to transmit through the material of interest, these samples must be incredibly thin (less than 100 nm for imaging and less than 50 nm for analytical techniques like EELS).[37] Because of the thin sample, electrons cannot scatter and spread throughout a large volume like they do in SEM, and therefore the interaction volume in TEM approaches the size of the electron probe. This allows incredibly high spatial resolutions, especially in aberration corrected STEM, where the size of the probe can be reduced to less than an angstrom.[40] This means that TEM is the ideal technique for studying nanoscale precipitates, with high spatial resolution imaging and analytical precision. Unfortunately, because the samples need to be very thin, the sample preparation (especially for bulk materials) is complex, and researchers need to be careful not to induce artifacts that could be misinterpreted as intrinsic defects.

One of the most common ways to prepare TEM samples by using a Focused Ion Beam (FIB) which uses Ga^+ ions to cut and thin specimens for vertical lift-out. Specimens are usually a

few microns in size, but because FIB is performed in an SEM, cross-sectional samples can be taken from extremely precise areas such as grain boundaries or other areas of interest. The downside to FIB sample preparation is that Ga^+ ions have a strong tendency to become implanted in samples.[67,68] Many thermoelectric materials such as PbTe and $Bi_{0.5}Sb_{1.5}Te_3$ are sensitive to implantation, resulting in large amounts of sample damage. This can manifest in Ga showing up in analytical measurements of composition, but can also result in amorphization, and point defects like vacancy and interstitial formation that is not intrinsic to the samples of interest.[67,68]

Ar^+ ion milling is preferred to FIB for sensitive samples because of the reduced tendency of Ar^+ to implant into samples.[67,68] The sample preparation required for bulk TEM specimens using argon ion milling is quite different from the preparation that would be needed for FIB specimen preparation. This is because Ar^+ ion milling does not take place in an SEM (meaning one cannot precisely target a small area of interest), and because of Ar^+ ion milling is much more gentile. This leads to the need for additional steps to be included in sample preparation prior to using the Ar^+ ion mill. The general concept behind this type of sample preparation is that it is desirable to form a hole in the middle of the sample during the ion milling step using the ion guns that are angled above and below the surface (see **Figure 2.1**). When the guns form the hole, the resultant cross section at the edge of the hole will be a wedge shape, with a thickness of zero at the hole and gradually increasing thickness moving away from the hole. That means there should be a region bordering the hole that is less than 100 nm and suitable for analysis. To obtain samples that are appropriately thin prior to milling, samples are attached to a TEM grid, ground and polished on a grinding wheel until they are approximately 50 μm thin, and then dimpled so that they have a

circular crater in the middle (the bottom of which should only have a few microns of thickness prior to milling).

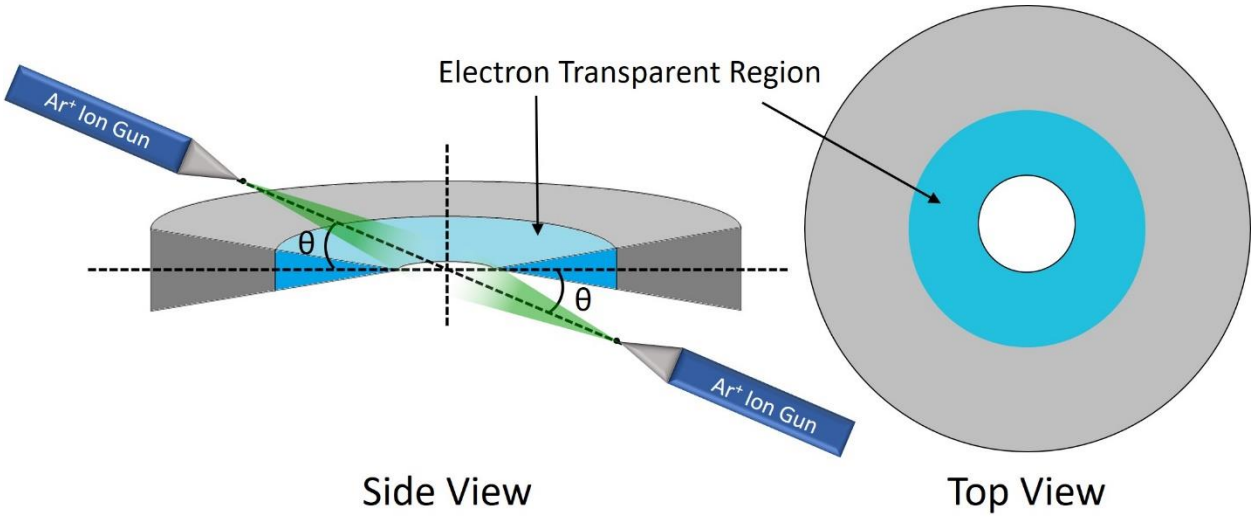

Figure 2.1. Top and Side views of a TEM sample prepared via Argon ion milling to achieve a region of electron transparency.

Although the Ar^+ ions are less invasive than Ga^+ it is still important that the proper steps are taken during milling to reduce damage. This includes ensuring samples are at cryogenic temperatures throughout the milling process (by using a cryogenic stage) which helps reduce the localized heating from milling to accumulate and cause changes to the sample. Additionally after milling at higher kV, there should be a gradual reduction in both the incidence angle and voltage, to ensure that the final polishing process removes surface damage from prior steps, while keeping the addition of new damage to a minimum. Specifically in lead chalcogenides this is important because some defects from the ion milling process form ordered vacancy clusters which can be mistaken as intrinsic defects.[66]

2.2. Controlling Phase Segregation in Spark Plasma Sintered $NaPb_mSbTe_{m+2}$ (SALT)

2.2.1. Spark Plasma Sintering for Mechanical Property Enhancement

As mentioned in the section above, the LAST system is a proven high performance, nanostructured thermoelectric material, however, prior to this study, little information was available on the Na analogue to this system, despite Na being a common dopant in PbQ-based thermoelectrics. The Na analogue is attractive to researchers though because the compound is essentially a mixture of two rocksalt phases, PbTe and $NaSbTe_2$, similar to the phases PbTe and $AgSbTe_2$ that exist in LAST (which manifests as a two phase system with nanoprecipitation). The reason that the $NaPb_mSbTe_{m+2}$ (SALT) material system was not well studied prior to our investigation is because the compounds that are rich in $NaSbTe_2$ (or in other words those with low m) are very brittle and therefore difficult to fabricate into samples that can be measured for electrical and thermal transport. Since the incorporation of solidification and strengthening techniques such as Spark Plasma Sintering (SPS) have become more widely available, it has become possible to fabricate brittle ceramics (such as low m SALT) with more mechanical robustness. This has enabled an in-depth analysis of m=1 to m=20 SALT thermoelectrics, a range of composition that had not previously been explored in this material system. Once the samples could be synthesized, transport measurements and electron microscopy were carried out on the materials to help form an understanding of the relationship between the new processing procedure, material microstructure, and thermoelectric properties.

2.2.2. Processing of SALT Samples

The goal for processing SALT samples was to consistently produce a range of compositions so that thermoelectric properties and microstructure could be recorded across a spectrum of solid solution and phase segregated samples to identify where the ideal composition for thermoelectric performance may exist. Polycrystalline ingots with nominal compositions of $Na_{1+x}Pb_{m-x}Sb_{1-y}Te_{m+2}$ (m = 0.25−20, x =0−0.15, y = 0−0.25) were synthesized by weighing stoichiometric quantities of each element into 13 mm diameter carbon coated fused silica tubes, which were then flame-sealed at ~2×10^{-3} Torr. The tubes were heated in a box furnace to 1273 K over 14 hrs and held at this temperature for 6 hrs. During this time, the tubes were periodically shaken to ensure good mixing and homogeneity in the melt. After 6 hrs, the tubes were quenched in ice water, and the polycrystalline ingots were removed and ground into powders in an N2-filled glovebox. The powders were sieved (53 μm), loaded into 12.7 mm graphite dies, and sintered by SPS (SPS-211LX, Fuji Electronic Industrial Co. Ltd.) at 823 K and 40 MPa for 10 min into pellets, which were then resealed in 18 mm diameter tubes at ~2×10^{-3} Torr and annealed at 673 K for 24 hrs to achieve improved thermal stability. The pellets were last cut and polished into $3 \times 3 \times 10$ mm^3 bars and $6 \times 6 \times 2$ mm^3 squares for thermoelectric characterization. The cuts were made such that transport measurements were done perpendicular to the pressing direction in the SPS, although minimal differences were observed between measurement directions.

As will be described in the next section, there was also a need to study the thermoelectric properties and microstructure of polycrystalline ingots (i.e. the samples that had not undergone SPS). However, water quenching from the melt resulted in samples too brittle to be cut and polished as described above. To help avoid embrittlement, the tubes were instead heated to 1273

K in a rocking furnace where they were held for 2 hrs. Afterward, the rocking furnace was turned on to provide continuous mixing for an additional 2 hrs. The furnace was then fixed in an upright position and cooled to 820 K over 44 hrs and finally turned off to allow the tubes to naturally cool to room temperature. Significantly lower electrical conductivities were observed when the rocking furnace was not utilized, indicating the importance of homogeneity in the melt in the case of the ingots. Using this technique, the resulting polycrystalline ingots were considerably less brittle than those prepared from quenching; however, great care was still needed in subsequent handling. Lastly, the ingots were carefully cut and polished into $3 \times 3 \times 10$ mm^3 bars and $6 \times 6 \times 2$ mm^3 squares for property measurements, as described above.

2.2.3. Spark Plasma Sintering

2.2.3.1. Change in Transport Properties due to SPS

Preliminary ingots and SPS samples of $NaPb_mSbTe_{m+2}$ with compositions m = 1, 6, 10, 18 were prepared so that they would span most of the compositional space between PbTe and $NaSbTe_2$ to gain a general understanding of the trends in electrical and thermal properties across this phase space. The thermoelectric property data for the SPSed $NaPb_mSbTe_{m+2}$ samples are shown in **Figure 2.2a−c**. For these samples, the total thermal conductivities decrease with decreasing m (i.e., greater $NaSbTe_2$ fraction), and are low in the range of 1.4−0.4 $W \cdot m^{-1} \cdot K^{-1}$ over 300−900 K. The electrical conductivities are also low, under 100 $S \cdot cm^{-1}$ and increase with temperature while the Seebeck coefficients are negative with large values of −300 to −900 $\mu V \cdot K^{-1}$ at 300 K that decrease with temperature. Collectively, these electronic properties are indicative of nearly intrinsic n-type semiconductors with low charge carrier concentrations. Unfortunately,

degenerate carrier concentrations in the range 10^{19}–10^{20} cm^{-3} are desired to optimize the power factor ($\sigma \cdot S^2$),[5] and therefore the essentially intrinsic semiconductor behavior of the SPS $NaPb_mSbTe_{m+2}$ samples results in poor *zT*s (below 0.10) for all compositions.

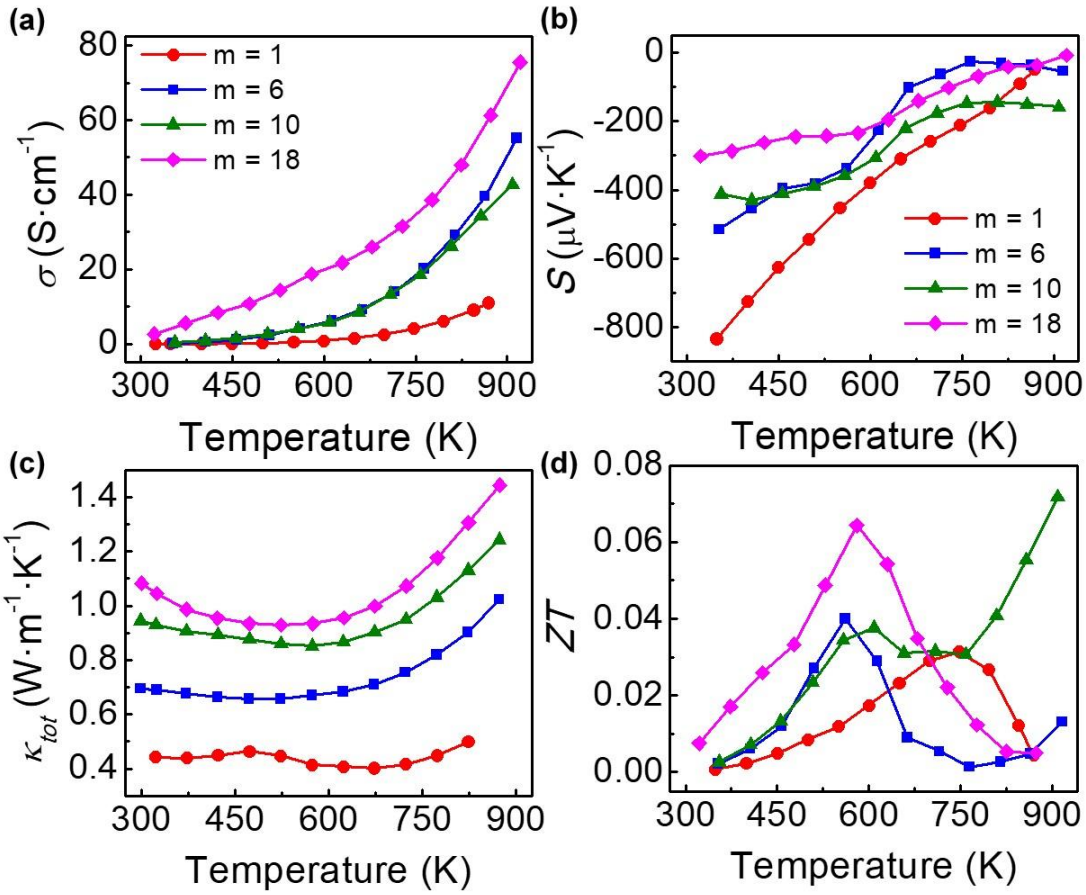

Figure 2.2. A-C) Thermoelectric property data (electrical conductivity, Seebeck coefficient, and lattice thermal conductivity respectively) for SPSed $NaPb_mSbTe_{m+2}$ for compositions of m=1, 6, 10, 18 and D) the resultant *zT* for these compositions.

The negative Seebeck coefficients of the SPS samples indicate n-type charge transport, which contrasts with prior experimental studies in which polycrystalline ingots were p-type. One previous study on as-cast ingots of $NaPb_mSbTe_{m+2}$ reported degenerate p-type conduction for the

compositions m = 19−20,[69] and preliminary measurements on ingot samples performed internally by past collaborators prior to this work, revealed that m=6−10 samples also show degenerate p-type conduction. To further investigate the discrepancy between literature and past experimental values of ingot samples, with the current SPS samples, polycrystalline ingots of $NaPb_mSbTe_{m+2}$ were synthesized and directly measured using the synthesis methods described above. By excluding the post-synthetic, powder processing steps and measuring thermoelectric properties directly from samples cut from the ingots, the thermoelectric properties of SALT compounds can be measured without the inclusion of SPS as a processing step.

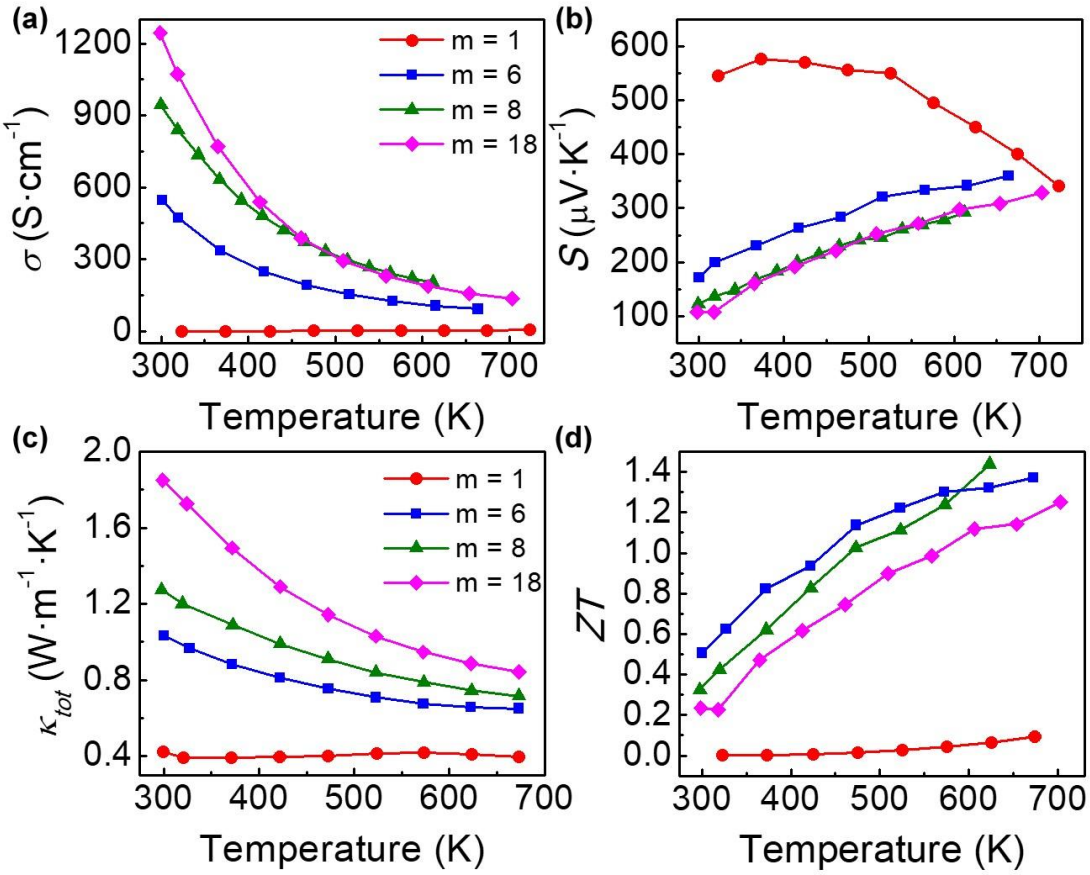

Figure 2.3. A-C) Thermoelectric property data (electrical conductivity, Seebeck coefficient, and lattice thermal conductivity respectively) for as-cast $NaPb_mSbTe_{m+2}$ ingots for compositions of m=1, 6, 8, 18 and D) the resultant *zT* for these compositions.

Figure 2.3d−f shows the thermoelectric data for the as-cast ingots when m = 1, 6, 8, 18. For samples with m=6−18, the electrical conductivities are considerably higher than those of the respective SPS samples and monotonically decrease with temperature from 600−1200 $S \cdot cm^{-1}$ at 300 K to ~100 $S \cdot cm^{-1}$ at 700 K. The Seebeck coefficients are positive and increase with temperature from ~100 to 300 $\mu V \cdot K^{-1}$ over the interval 300−700 K. These charge transport properties show that $NaPb_mSbTe_{m+2}$ (m=6−18) ingots behave as degenerate p-type semiconductors

with hole concentrations that appear to decrease as one progresses toward the $NaSbTe_2$ rich side of the system, reaching behavior characteristic of nearly intrinsic semiconductors by m = 1. Because of the increased κ_{elec}, the thermal conductivities of the ingots are higher than in the corresponding SPS samples and decrease from ∼1−1.8 $W \cdot m^{-1} \cdot K^{-1}$ at 300 K to 0.9−0.7 $W \cdot m^{-1} \cdot K^{-1}$ at 700 K when m=6−18. The higher carrier concentrations lead to better performance compared to the SPS samples, with *zT*s reaching a maximum of 1.2−1.4 at 650 K when m=6−18. These results reveal that ingots of $NaPb_mSbTe_{m+2}$ exhibit reasonably high thermoelectric performance across a much wider range of the $NaSbTe_2$−PbTe compositional spectrum than previously explored.

While the $NaPb_mSbTe_{m+2}$ ingots indeed show promising *zT*s when m is greater than or equal to 6, their poor mechanical toughness limits the practicality of further optimization. Therefore, understanding the significant differences in the electrical properties of the as-cast ingots and SPS samples warrants further investigation to enable the fabrication of high performing and mechanically robust SPS samples. Typically, SPS is considered to be fast on the time scale of solid-state transformations, occurring in 30 min or less with no changes expected in the material. However, in the case of $NaPb_mSbTe_{m+2}$, Spark Plasma Sintering appears cause a transition from degenerate p-type semiconductors with high *zT*s (as seen in the ingots) to almost intrinsically semiconducting n-type materials with poor thermoelectric properties (as seen in the SPS samples). An explanation of this phenomenon is crucial to understanding the fundamental chemistry of the system and to enhance the thermoelectric properties of the SPS samples. Furthermore, because SPS is widely used in the field of thermoelectrics to consolidate powders into high-density samples, understanding the chemical changes that occur during SPS processing of common

thermoelectric materials, such as PbTe-based compounds, is of value to the thermoelectric community at large.

2.2.3.2. Bulk Analysis using X-ray Diffraction.

Like electrons, x-rays can interact with the crystal lattice and reveal crystallographic information of a bulk material. However, due to the fact that electrons are scattered by matter much more strongly than x-rays, x-ray diffraction techniques generally give information related to the bulk material rather than a localized area of the sample.[37] To gain more insight into the behavior of the $NaPb_mSbTe_{m+2}$ compound as a function of composition (identifying phases changes, changes in lattice parameters, etc.) and to understand the impact of SPS on the physical properties, powder samples were prepared with compositions m = 0.25−20 spanning the full compositional range of the $NaSbTe_2$−PbTe solid solution. **Figure 2.4a** shows the laboratory powder X-ray diffraction (PXRD) patterns for the SPSed samples. The experimental diffraction patterns correspond closely to the projected $NaSbTe_2$ (m = 0) pattern, and show that each member (m) of $NaPb_mSbTe_{m+2}$ has the expected $Fm\bar{3}m$ structure and that no secondary phases were detectable using this technique. As shown in Figure 2.4b, the lattice parameters for the ingots decrease linearly with decreasing PbTe fraction, closely following the trend predicted by Vegard's law and supporting the notion that $NaSbTe_2$ and PbTe form a solid solution across all compositions. Interestingly, however, for all compositions the lattice parameters of the SPS samples are smaller than those of their respective ingots and deviate significantly from the trend predicted by Vegard's

law. This unusual result is particularly pronounced at intermediate ratios of $(PbTe)_{1-x}$–$(NaSbTe_2)_x$. (x = 0.5 or equivalently m = 1).

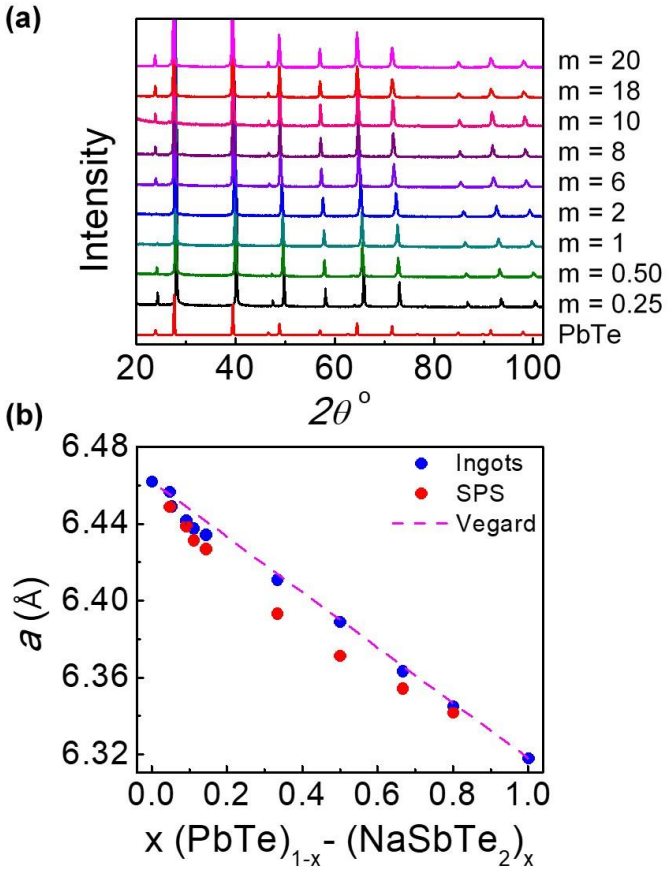

Figure 2.4. A) Experimental PXRD pattern for SPSed $NaPb_mSbTe_{m+2}$ samples for m = 0.25–20 along with the simulated spectrum for PbTe in red. B) Refined lattice parameters for as-cast ingots and SPSed $NaPb_mSbTe_{m+2}$ samples. The dashed line is the theoretical change in lattice parameter as predicted by Vegard's law for a solid solution of $NaSbTe_2$ and PbTe.

To further probe the structural differences of the two sample forms, high resolution synchrotron powder diffraction was performed at APS−11BM at the Argonne National Laboratory. Close-up views of several high-angle reflections are shown in **Figures 2.5a** and 2.5b

for ingot and SPS samples, respectively. In the case of the SPS samples, Figures 2.5b reveals sharp diffraction peaks corresponding to the expected rock-salt structure and is in excellent agreement with the laboratory diffraction data indicating that the SPS samples remain phase-pure even to m = 1 (50:50 PbTe:$NaSbTe_2$). Interestingly, however, the diffraction patterns for the ingots (Figure 2.5a) show significant peak broadening when compared with the corresponding SPS data, an effect that becomes more pronounced at lower values of m. The broader peaks for the ingots suggests that they are not phase-pure, and instead contain a second cubic phase with very similar lattice parameters to that of the primary $NaPb_mSbTe_{m+2}$ such that the synchrotron diffraction cannot fully resolve the individual phases. These results suggest that despite following Vegard's law, $NaSbTe_2$−PbTe ingots do not form a perfect solid solution. It is predicted that the phase separation in the as-cast ingots is the origin of the surprising behavior described above and has major consequences for the electrical properties, resulting in the large discrepancies between the ingots and SPS samples.

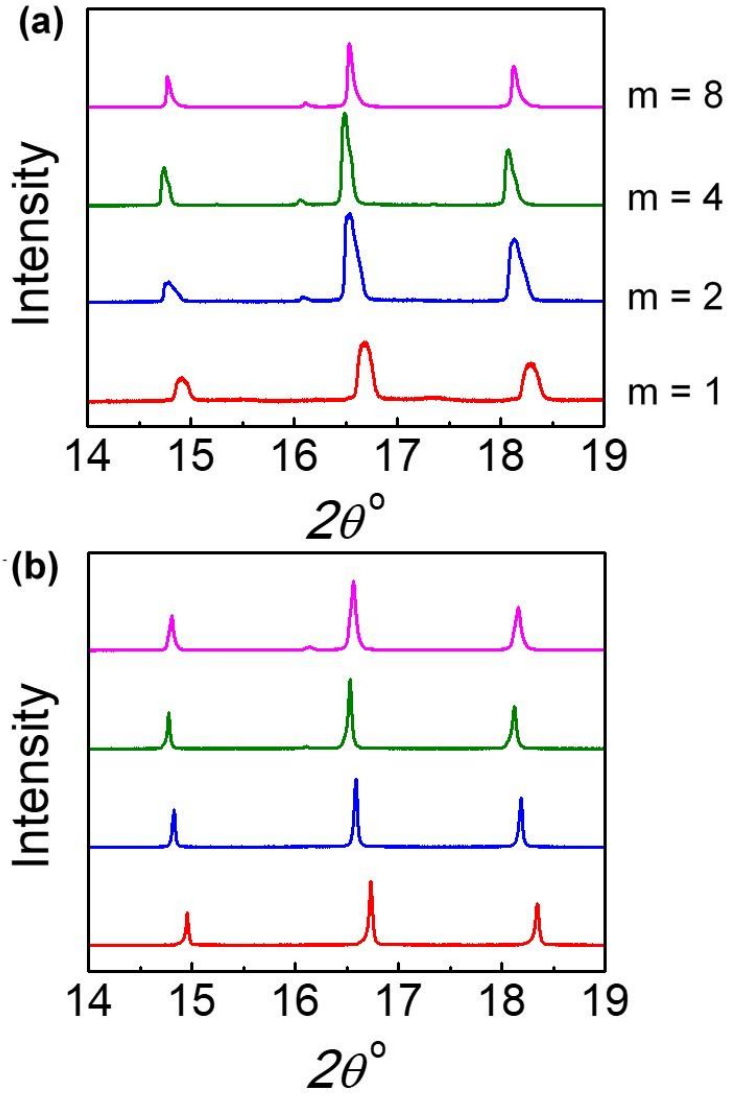

Figure 2.5. Close up views of the synchrotron diffraction peaks for A) as-cast ingots and B) SPSed samples of $NaPb_mSbTe_{m+2}$ (m = 1, 2, 4, 8) which shows significantly broader peaks in the case of the ingots.

2.2.3.3. Mesoscale Analysis using Scanning Electron Microscopy

To more thoroughly investigate the phase separation indicated by XRD, scanning electron microscopy (SEM) and energy dispersive spectroscopy (EDS) were used to analyze both the ingot and SPS samples. **Figure 2.6a** shows a representative SEM image of the m = 1 ingot whose powder

diffraction data is displayed in Figure 2.5a. The EDS elemental maps obtained over this region reveal severe inhomogeneity with Pb-rich regions and Na/Sb-rich regions. While Te appears to also be segregated, point scans shown in **Figure 2.7** and **Table 2.1** show a uniform distribution of Te while retaining the Pb/Na/Sb separation, indicating that the similarity between Te and Sb elemental maps is an artifact of the mapping software and stems from the nearly overlapping Lα peaks for these two elements. These results are in good agreement with the synchrotron X-ray diffraction data, revealing clear phase separation in the ingots and suggesting that the detected second phase is rich in Na and Sb. The electron backscatter diffraction (EBSD) orientation maps show that the phase separation is not confined to the grain boundaries but is pervasive throughout the whole sample. As shown in Figure 2.5a, the two phases are not fully resolved by the synchrotron powder diffraction, suggesting that both phases are cubic materials with similar lattice parameters. These factors indicate that the as-cast ingots phase separate upon cooling into different $NaPb_mSbTe_{m+2}$ members with slightly different compositions (m), one of which is rich in Na and Sb and the other rich in Pb.

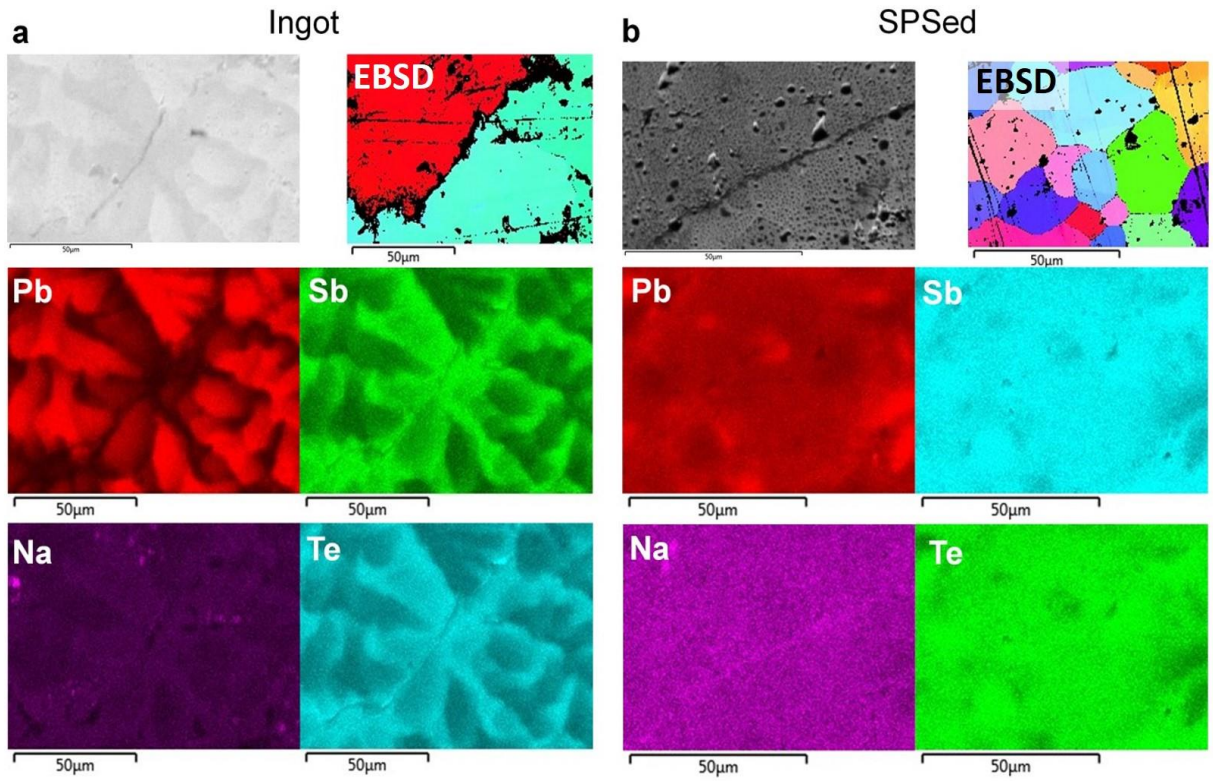

Figure 2.6. SEM images and EBSD orientation maps with accompanying EDS elemental maps for Pb, Sb, Na and Te in a $NaPbSbTe_3$ as-cast ingot A) and SPSed sample B). Upper left and right images for each are the electron images and electron backscatter diffraction (EBSD) images, respectively. The EDS images show that there is clear chemical segregation in the ingot sample (Na/Sb-rich and Pb-rich phases) and that Spark Plasma Sintering results in a more homogenous sample. The diffusion of Na and Sb into the matrix phase accounts for the recorded property changes after SPS. Additionally, EBSD in the ingot sample reveals that chemical segregation is not relegated to the grain boundary, but pervasive throughout the grains. Likewise, in the SPS sample, there is no dependence of elemental distribution on grain boundary location.

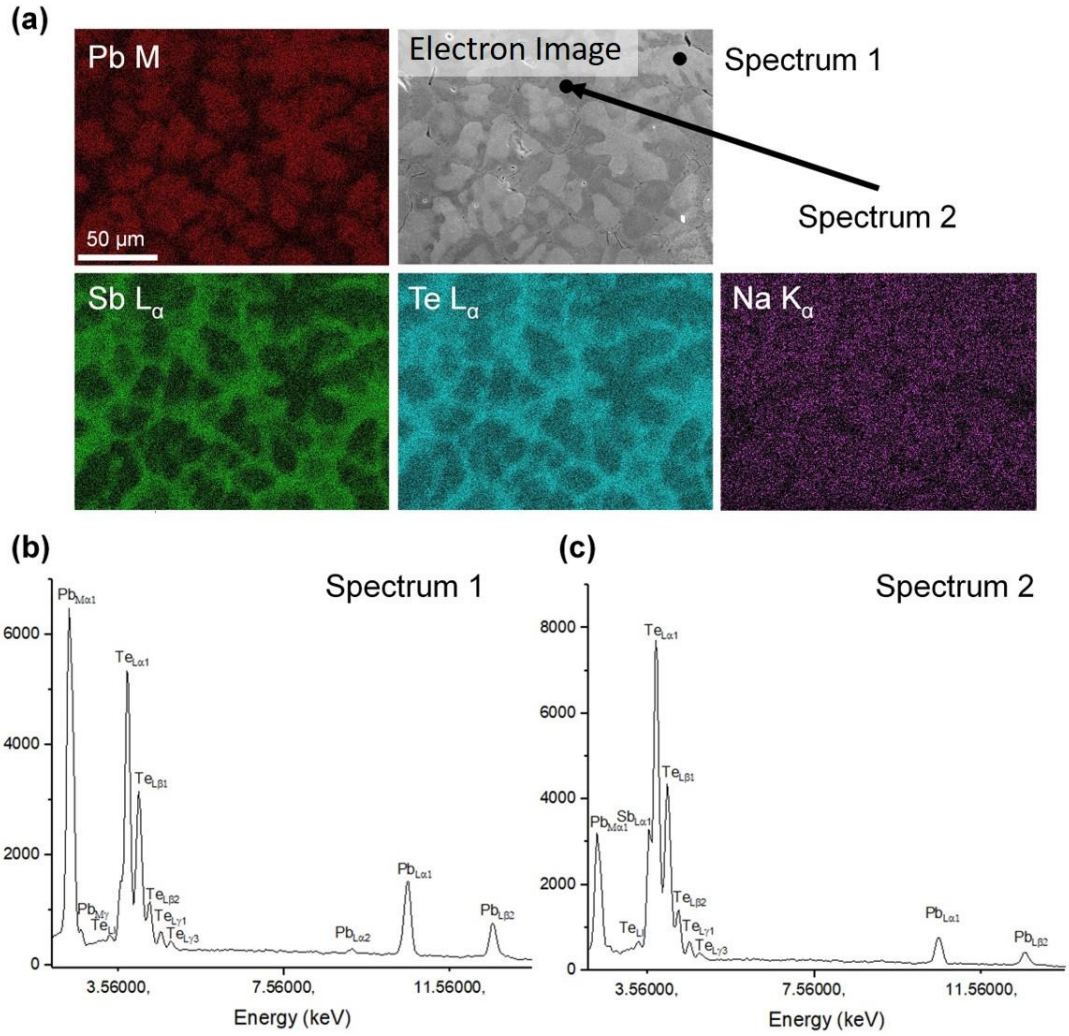

Figure 2.7. A) EDS elemental maps of Pb, Sb, Te, and Na in a $NaPbSbTe_3$ as-cast ingot showing severe elemental inhomogeneity consistent with the results shown in Figure 2.6. B) and C) are the spectra for the EDS point scans of region 1 and 2, showing Pb-rich and Sb-rich regions, respectively.

Table 2.1. Qualitative atomic percentages from the EDS point spectra 1 and 2 taken on $NaPbSbTe_3$ shown in Figure 2.7. The point spectra show that the Te is uniformly distributed while the Pb and Na/Sb are segregated, confirming the phase segregation in the ingots and suggesting that the similarity of Sb and Te elemental maps is due to the nearly overlapping L_α EDS peaks.

Spectrum 1		Spectrum 2	
Element	**Atomic (%)**	**Element**	**Atomic (%)**
Na	10.09	Na	18.81
Sb	9.77	Sb	19.01
Pb	31.30	Pb	12.75
Te	48.84	Te	49.35

Figure 2.6b shows the elemental maps of the m = 1 SPS sample. These maps are strikingly different than those for the as-cast ingot, revealing a significantly more uniform and homogeneous elemental distribution. While there still appears to be minor inhomogeneity in the SPS sample, the elemental segregation is clearly reduced compared to the ingot, and this minor inhomogeneity vanishes for higher m compositions. Therefore, based on both the EDS results and synchrotron diffraction data, it is concluded that the SPS samples are effectively phase-pure solid solutions. In addition, the TEM images and electron diffraction patterns shown in **Figure 2.8** reveal that there is no additional phase segregation in SPSed samples on the nanoscale. Without the utilization of microscale analytical and diffraction techniques (EDS and EBSD respectively), the second phase would not have been able to be identified due to the combination of the limited field of view of TEM and the length scale of the phase segregation.

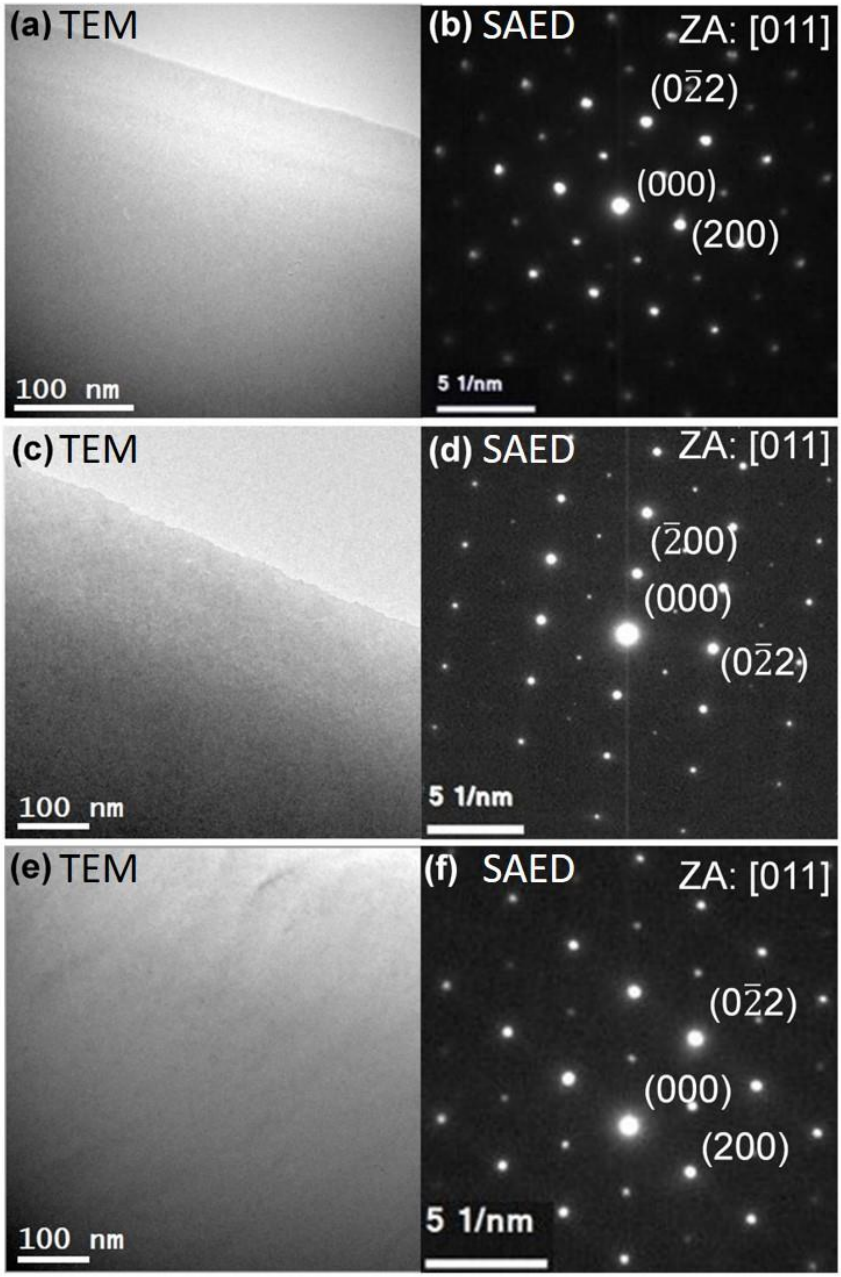

Figure 2.8. TEM images of SPSed A) $NaPbSbTe_3$ (m=1), C) $Na_{1.10}Pb_{9.90}Sb_{0.85}Te_{12}$ (m=10), and E) $Na_{1.15}Pb_{19.85}Sb_{0.85}Te_{22}$ (m=20). B), D), and F) show selected area electron diffraction patterns (SAED) for each respective sample. All images reveal a single phase and homogenous microstructure with no evidence of nanostructures.

2.2.3.4. Implications of Compositional Control During Spark Plasma Sintering

Together, the diffraction and microscopy data suggest an explanation for the unusual electrical properties. The $NaPb_mSbTe_{m+2}$ ingots are not perfect solid solutions but instead phase separate into two $NaPb_mSbTe_{m+2}$ members (different m), a primary phase rich in Pb and a secondary phase rich in Na and Sb. On the basis of both the width of the ingots' synchrotron diffraction peaks and the relative change in lattice parameters between ingots and SPS samples, the degree of phase separation is clearly most severe in ingots with intermediate ratios of $NaSbTe_2$ and PbTe (m near 1). It should be noted that the composition of the second phase will change for different values of m due to the different overall stoichiometries; however, the secondary phase will be rich in Na and Sb for all compositions. In the SPS samples, both the synchrotron diffraction data and SEM demonstrate that the materials are single phase.

On the basis of these observations, it is hypothesized that the secondary Na/ Sb-rich phase dissolves into the primary matrix during SPS, forming a solid solution. Because Na^+ and Sb^{3+} have smaller ionic radii than Pb^{2+}, the dissolution of the Na/Sb-rich secondary phase into the primary matrix also explains the origin of the shrinking lattice parameters after SPS. Most importantly, we believe the phase separation leaves the primary phase with a significant fraction of cation vacancies, which would be expected to yield strong p-type charge transport in line with the measured electrical properties for the ingots. Lastly, dissolution of the secondary phase into the primary matrix would leave the final material very close to the stoichiometric composition of $NaPb_mSbTe_{m+2}$. In PbTe, Na is typically an acceptor and Sb a donor; therefore, a perfectly stoichiometric $NaPb_mSbTe_{m+2}$ compound would be completely charge compensated. The measured electronic properties, displayed in Figure 2.2a and 2.2b, strongly support almost full

charge compensation, with temperature-dependent electrical conductivities and Seebeck coefficients characteristic of nearly intrinsic semiconductors for the SPS samples.

Having uncovered the origin of the unusual change in electronic properties between ingot and SPS samples, the more mechanically robust SPS samples are now able to be optimized compositionally to achieve peak thermoelectric performance. Ideally, p-type charge transport is desirable for $NaPb_mSbTe_{m+2}$ because of the favorable valence band structure of PbTe-based materials.[20] Accordingly, the strategy to tune the stoichiometry of the cations to achieve more holes was to substitute additional Na for Pb while introducing Sb vacancies into the matrix, yielding $Na_{1+x}Pb_{m-x}Sb_{1-y}Te_{m+2}$. A summary of the best performing $Na_{1+x}Pb_{m-x}Sb_{0.85}Te_{m+2}$ compositions for each value of m is shown in **Figure 2.9** and it can be seen that by for m=20, x=0.15, y=0.15 a maximum *zT* of 1.6 was achieved for mechanically robust p-type SPS samples. This is a significant improvement over the *zT* of 0.1 of the original p-type SPS samples, and the origin of the anomalous property changes would not have been identified without an in-depth study of the influence of SPS on microstructure. These results show that significant chemical changes are possible during SPS of PbTe based materials, contrary to conventional wisdom. Furthermore, this suggest that attention should be directed toward the investigation of microstructural evolution during SPS (with the inclusion of microscale analysis) if optimal performance is to be achieved in any thermoelectric materials experiencing similar property variations during the SPS process.

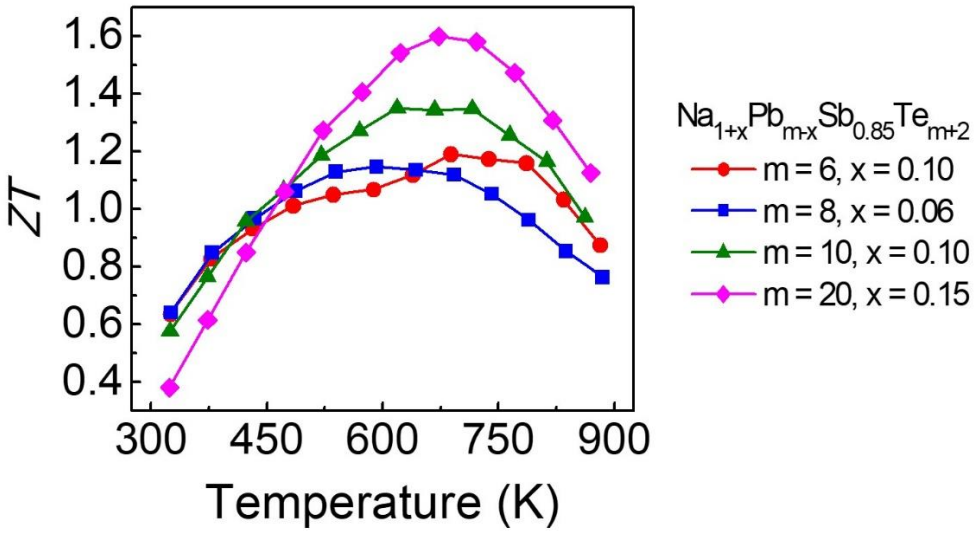

Figure 2.9. *zT* of top performing samples from each m series (m = 6, 8, 10, 20) of optimized SPSed $Na_{1+x}Pb_{m-x}Sb_{0.85}Te_{m+2}$ with x = 0–0.15.

2.2.4. Explaining the Origins of Solid Solution Thermoelectric Enhancement in $NaPb_mSbTe_{m+2}$

As mentioned previously, to more thoroughly explore the low lattice thermal conductivities of $Na_{1+x}Pb_{m-x}Sb_{1-y}Te_{m+2}$, transmission electron microscopy (TEM) was conducted on these samples. Representative TEM images and diffraction patterns were obtained for SPS samples of composition $Na_{1.10}Pb_{9.90}Sb_{0.85}Te_{12}$, $Na_{1.15}Pb_{19.85}Sb_{0.85}Te_{22}$, and $NaPb_mSbTe_{m+2}$ (m =1−10) which are shown in Figure 2.8. None of these images or diffraction patterns show evidence of phase separation or nanostructuring, even down to m = 1 (50% $NaSbTe_2$). Instead, all samples investigated exhibit a homogeneous nanostructure. These results are consistent with the SEM and synchrotron X-ray diffraction data discussed earlier and confirm the single-phase nature of $NaPb_mSbTe_{m+2}$ after SPS.

Initially this result is surprising considering that the analogous compound, $AgPb_mSbTe_{m+2}$ (LAST), achieves low thermal conductivity while exhibiting nanoprecipitation. Yet, despite the lack of nanostructures, the high degree of structural complexity present in the $NaPb_mSbTe_{m+2}$ system should intuitively provide a variety of phonon scattering mechanisms. For example, the heavy alloying of both Na^+ and Sb^{3+} ions onto the Pb^{2+} site should provide very strong point defect scattering, which should cause a reduction of lattice thermal conductivity at elevated temperatures. Furthermore, cation vacancies were recently shown to strongly contribute to phonon scattering in the structurally analogous $AgSn_mSbTe_{m+2}$ compounds,[70] indicating that the Sb vacancies introduced here in $Na_{1+x}Pb_{m-x}Sb_{1-y}Te_{m+2}$ may play a similar role. Mesoscale grain boundaries resulting from SPS have also been shown to effectively scatter phonons, particularly at low temperatures, and therefore also likely contribute to the low thermal conductivities.[16,71] Lastly, the end member of the system, $NaSbTe_2$, is known to possess highly anharmonic acoustic phonon modes that give rise to extremely low thermal conductivity.[72] Similar effects may play a role in reducing the κ_{lat} in $NaPb_mSbTe_{m+2}$ as more $NaSbTe_2$ is incorporated into the system (lower m). Therefore, despite the lack of observed nanostructures, the very low lattice thermal conductivities found in $Na_{1+x}Pb_{m-x}Sb_{1-y}Te_{m+2}$ can be rationalized by known mechanisms such as point defect scattering, mesostructuring, and lattice anharmonicity.

Although it is confirmed that SPS $NaPb_mSbTe_{m+2}$ materials are not nanostructured, and do not need nanostructures to achieve low thermal conductivity, it is still intriguing that the closely related Ag analogues $AgPb_mSbTe_{m+2}$[63] and $AgPb_mSbSe_{m+2}$[73] are reported to be nanostructured while $NaPb_mSbTe_{m+2}$ is not. It should be noted here that the Ag analogues that were studied were as-cast ingots, while the final $NaPb_mSbTe_{m+2}$ samples were spark plasma sintered. In the Ag

systems, it has been suggested that Coulombic interactions between the negatively charged Ag ions (relative to the primarily Pb^{2+} sublattice) and positively charged Sb ions drives the nucleation of the Ag- and Sb-rich nanoscale precipitates found in these systems.[74,75] Considering the similarities between $AgPb_mSbTe_{m+2}$ and $NaPb_mSbTe_{m+2}$, one would expect similar driving forces for the formation of Na^- and Sb-rich precipitates in SPS $NaPb_mSbTe_{m+2}$. To explore this, we used DFT to calculate the mixing energies of $Pb(NaSb)_{0.5}Te_2$ ($NaPb_2SbTe_4$, m =2), $Pb(AgSb)_{0.5}Te_2$ ($AgPb_2SbTe_4$), and $Pb(AgSb)_{0.5}Se_2$ ($AgPb_2SbSe_4$) solid solutions, with PBEsol exchange-correlation functional.[74] The solid solutions were simulated using special quasi-random structures (SQS).[76] The mixing energies were calculated with respect to PbTe and $NaSbTe_2$ (L11) for $Pb(NaSb)_{0.5}Te_2$, PbTe and $NaAgTe_2$ (D4) for $Pb(AgSb)_{0.5}Te_2$, and PbSe and $NaAgSe_2$ (L11) for $Pb(AgSb)_{0.5}Se_2$. L11 and D4 are ordered rocksalt-based structures found with the lowest energy for $NaSbTe_2$ and $AgSbSe_2$, and for $AgSbTe_2$, respectively.[75] The data is shown in Table 2.2, and reveals that the mixing energy of $NaPb_2SbTe_4$ is considerably smaller than that of both $AgPb_2SbTe_4$, indicating that the driving force for phase separation is much smaller in the Na compound. This result agrees with the experimental finding that SPS $NaPb_mSbTe_{m+2}$ forms a solid solution while $AgPb_mSbTe_{m+2}$ and $AgPb_mSbSe_{m+2}$ phase separate.

2.2.5. Summary of the Study of $NaPb_mSbTe_{m+2}$

There are three main takeaways from the study of $NaPb_mSbTe_{m+2}$ that were applied to future projects in this thesis. 1) Thermoelectric enhancement is possible in solid solutions. Although this has been known, this material system proved that nanostructures are not always necessary to improve thermoelectric performance. In fact, as will be shown in future work, the ability to eliminate second phases (whether through compositional control or processing) improves

the ability of researchers to perform more fundamental studies on transport phenomena. 2) Processing Control, such as the control of SPS, can vastly affect material microstructure and properties. Understanding processing can help scientists make informed decisions concerning material design that will ultimately help in the optimization of thermoelectric materials. 3) Analysis of the microscale can be useful in the study of mesoscale (1 μm-1 mm) microstructural features. The added ability of EBSD to provide diffraction information in the SEM also enables the storage and processing of data for expanded analysis capabilities.

2.3. Manipulating Grain Boundary Screening for Improved Charge Carrier Transport

2.3.1. $NaPb_mSbSe_{m+2}$ (SALSe): An Analogue to the SALT System

PbSe has a slightly lower figure of merit than PbTe but remains an attractive alternative to because of the lower cost of Se, lower intrinsic lattice thermal conductivity,[77] superior mechanical properties, and because of its supposedly higher maximum operating temperature.[78] Therefore, following the success of the Te based system, alloys of PbSe with $NaSbSe_2$ (represented here as $NaPb_mSbSe_{m+2}$ or equivalently $NaSbSe_2$ + mPbSe) were synthesized. Like with the SALT system, this PbSe based analogue is a family of compounds that can be envisioned as solid solutions between $NaSbSe_2$ and PbSe, in which the three cations are randomly distributed across the Pb sites in the $Fm\bar{3}m$ crystal structure.

Na and Sb individually have limited solubility (under 2%) in lead chalcogenides,[79,80] although joint integration of both Na^+ and Sb^{3+} in equal quantities mimics the Pb^{2+} and allows for dramatically higher solubility. In fact, previous work on $NaSbTe_2$–PbTe demonstrated that with proper processing, single phase samples can be prepared with even up to 50% $NaSbTe_2$.[28] Such

high solubility allows access to a broad compositional space over which to study and optimize the thermoelectric properties. To explore the solubility of $NaSbSe_2$ in PbSe, a range of $NaPb_mSbSe_{m+2}$ compounds was synthesized with m =2–30 (or equivalently ≈3–33% $NaSbSe_2$).

The investigation revealed that alloying $NaSbSe_2$ into PbSe has two beneficial effects on the thermoelectric properties: 1) reduction of the energy separation between L- and Σ-valence bands raises the density of states effective mass and boosts the power factors; 2) strong point-defect phonon scattering yields exceptionally low thermal conductivity without nanostructuring (similar to $NaPb_mSbTe_{m+2}$). As a result, properly doped $NaPb_mSbSe_{m+2}$ achieved maximum zT of 1.4 near 900 K and critically, a record estimated zT_{avg} for p-type PbSe of 0.64 over 400–873 K, a significant improvement on existing tellurium free p-type PbSe-based thermoelectrics.

As stated previously, one of the benefits of studying solid solution systems is that novel transport properties can be studied without the influence of second phases. One of the interesting discoveries that was made while measuring this solid solution compound, was that even when possessing degenerate carrier densities over 10^{20} cm^{-3}, the heavily doped samples of $NaPb_mSbSe_{m+2}$ compounds exhibit intrinsic semiconducting behavior with thermally activated electrical conductivity below 500 K. The initial hypothesis was that the electrical transport under 500 K is the result of charge carrier scattering by the grain boundaries analogous to the behavior recently observed in Mg_3Sb_2 thermoelectrics.[81–83] This phenomena was of interest because if this effect could be understood (and eliminated) it could present a future path toward the improvement the low temperature thermoelectric performance of $NaPb_mSbSe_{m+2}$.

2.3.2. Anomalous Low Temperature Electrical Conductivity in Ionic Compounds

2.3.2.1. Grain Size Control and Mesoscale Analysis

$NaPb_mSbSe_{m+2}$ has atypical electrical transport behavior consisting of semiconducting electrical conductivity below 500 K, despite being degenerately doped to charge carrier densities over 10^{20} cm^{-3}.[29] The initial hypothesis was that this behavior was derived from grain boundary (GB) charge carrier scattering. Because other models such as ionized impurity scattering can in principle give a similar temperature dependence (and have been invoked to explain comparable transport properties in Mg_3Sb_2.),[81,84] it was important to obtain conclusive experimental evidence regarding the source of the unusual charge transport properties measured in $NaPb_mSbSe_{m+2}$. To test if the thermally activated scattering is rooted at the GBs, large grained samples of $NaPbmSbSe_{m+2}$ (that by default possessed fewer GBs) were prepared and their electrical properties were compared with the data from previously reported small grained SPS processed materials.[29]

The primary results are outlined in **Figure 2.10**, which shows a comparison of the grain structures and electrical properties of two differently doped samples of $Na_{1+x}Pb_{10-x}SbSe_{12}$ (nominally ~9% $NaSbSe_2$ in PbSe, with additional Na dopant fractions of x = 0.03, 0.15) prepared by slowly cooling the ingots and through rapid quenching and subsequent SPS processing. These compositions were chosen to compare the electrical properties of both lightly and heavily doped samples in small- and large-grained forms. Electron backscatter diffraction (EBSD) was used to analyze the grain morphologies of the different samples. Figure 2.10a and b show characteristic EBSD images, demonstrating that while the SPS processed material contains relatively small grains on the order of ~50 μm or less in size, the slow cooled ingot has much larger grains on the

order of 1 mm. This implies that there is a dramatically lower density of GBs in the slow cooled ingot. As anticipated from the GB scattering model, the lower GB density has direct consequences on the electrical conductivity. Most importantly, for both sample pairs (x = 0.03 and 0.15), Figure 2.10c shows that the semiconducting charge transport observed in the SPS processed samples vanishes in the slow cooled ingots, and the expected metallic behavior is recovered. Furthermore, Figure 2.10d demonstrates that the Seebeck coefficients of each pair are nearly identical over the full temperature window, indicating the charge carrier densities are approximately equal between ingot and SPS processed samples. Moreover, because the Seebeck coefficients and PXRD data indicate that each pair of compounds has nominally identical doping and chemical composition, impurity scattering in each should be comparable. As such, the results presented in Figure 2.10 unambiguously link the thermally activated charge transport to the GBs, providing strong evidence in favor of the GB carrier scattering model.

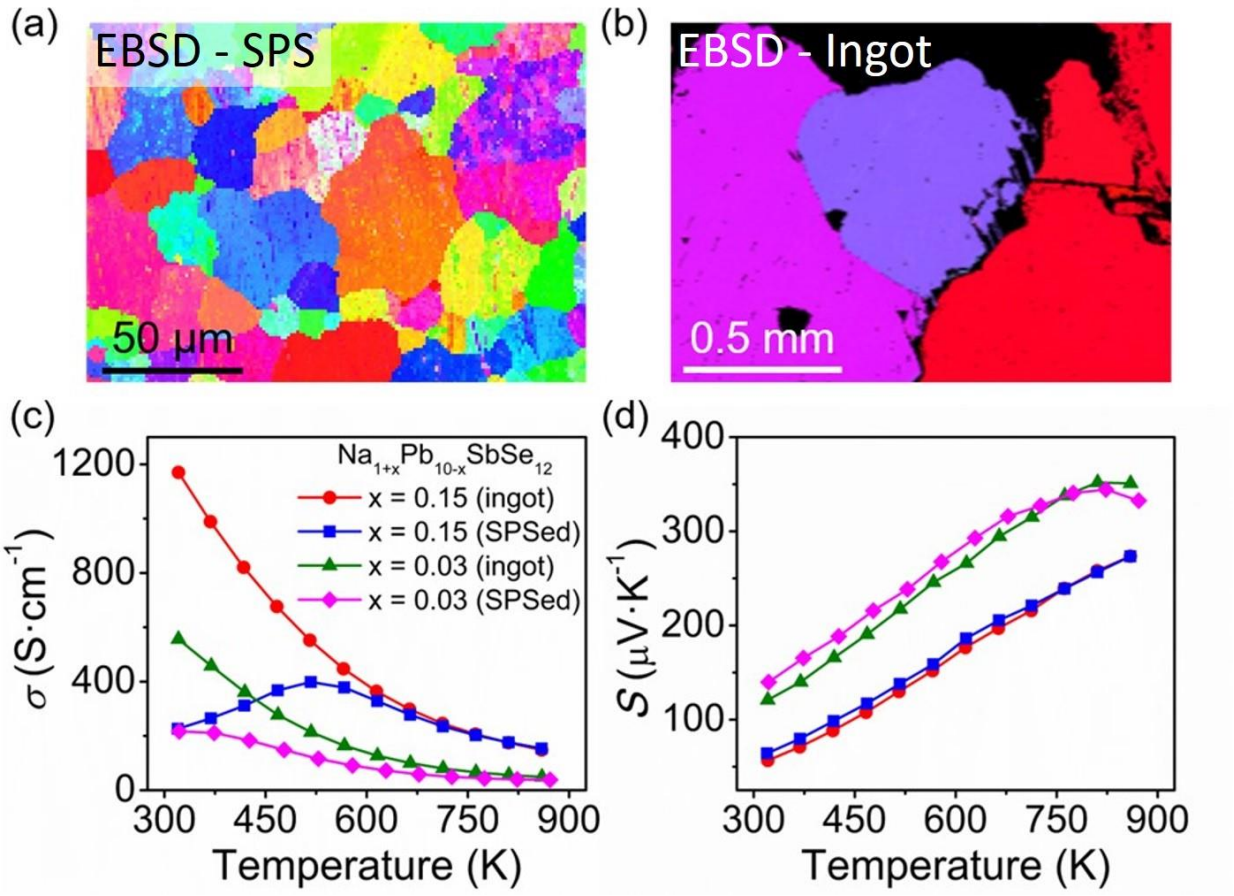

Figure 2.10. Electron backscatter diffraction (EBSD) images showing the grain structure of $Na_{1.15}Pb_{9.85}SbSe_{12}$ samples prepared by A) water quenching followed by powdering and SPS sintering and B) slow cooling of ingots. Comparison of the C) electrical conductivities and D) Seebeck coefficients for large grained (slow cooled ingots), and small grained (SPS processed) Na-doped $Na_{1+x}Pb_{10-x}SbSe_{12}$.

To further strengthen the case for GB scattering, samples with different densities of GBs were prepared by passing sample powders through sieves with different mesh sizes prior to SPS sintering. In principle, samples passed through smaller mesh sieves should have on average smaller grains and therefore a greater density of boundaries. Here, meshes of 53, 70, and 150 μm were

utilized, as well as one sample that was not sieved. The thermoelectric data for the resulting samples is shown in **Figure 2.11** and again demonstrates a direct link between GBs and low temperature carrier scattering. As the mesh (and presumably the grain) size is decreased, the electrical conductivity is increasingly suppressed under 500 K, while the values all approximately converge past 500 K. The Seebeck coefficients of these samples are likewise extremely similar, indicating comparable carrier concentrations. The combination of electrical data and EBSD of the slow-cooled ingots and samples prepared with varying GB density provide substantial experimental support that the low temperature carrier scattering found in $NaPb_mSbSe_{m+2}$ originates from the GBs.

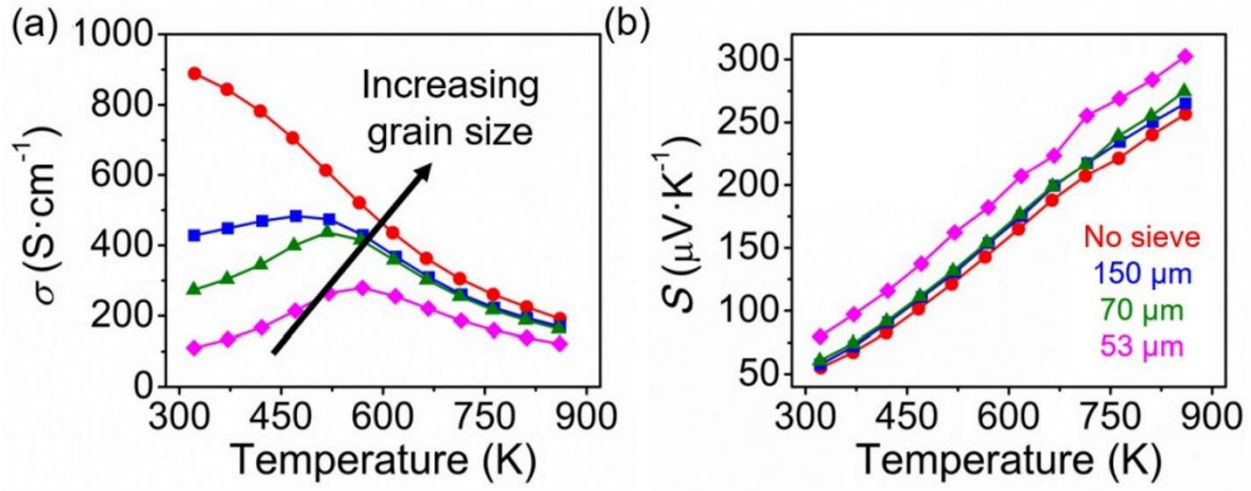

Figure 2.11. A) Electrical conductivities and B) Seebeck coefficients of $Na_{1.10}Pb_{9.90}Sb_{0.90}Se_{12}$ samples prepared by passing powdered ingots through different mesh sieves to achieve various grain sizes.

2.3.2.2. Nanoscale Analysis of Grain Boundary Composition

After having directly linked the low temperature charge carrier scattering in $NaPb_mSbSe_{m+2}$ to the GBs, it was surprising that the chemically similar telluride analogues ($NaPb_mSbTe_{m+2}$) do not show GB charge carrier scattering and instead exhibit degenerate semiconducting electrical

behavior.[28,69] Because lead chalcogenide thermoelectrics do not typically feature GB scattering, the apparent uniqueness of the $NaPb_mSbSe_{m+2}$ family warrants an explanation. One hypothesis was that the GBs in $NaPb_mSbSe_{m+2}$ act as sinks for phase or dopant separation, thereby leading to thin resistive barriers along the boundaries that impede the flow of charge carriers. Indeed, small quantities of SnO_2 are known to form along the GBs and dramatically restrict charge transport in polycrystalline SnSe.[85,86] To investigate if similar phase segregation is occurring in our materials, STEM and TEM were performed on several samples of SPS-processed $NaPb_mSbSe_{m+2}$ and $NaPb_mSbTe_{m+2}$ to elucidate any structural and chemical differences along the grain boundaries.

Several representative HRTEM and HAADF-STEM images of a sample with nominal composition $Na_{1.15}Pb_{9.85}SbSe_{12}$ are presented in **Figure 2.12**. Both the HRTEM and HAADF-STEM images in Figure 2.12a and 2.12b reveal a clean boundary free of obvious signs of phase segregation. In addition, EDS elemental maps (shown in Figure 2.12c-f) of the GB regions lack evidence for any significant phase or impurity segregation along the boundary, supporting the interpretation of Figure 2.12a and 2.12b. Taken together, the microscopy data suggests the GBs in $NaPb_mSbSe_{m+2}$ to be reasonably free of any secondary phase segregation within the limits of STEM-EDS analysis. Likewise, $NaPb_mSbTe_{m+2}$ compounds were also characterized to compare GBs in these materials to GBs in the selenides. HRTEM and HAADF-STEM images of a GB in a telluride sample with nominal composition $Na_{1.10}Pb_{9.90}Sb_{0.85}Te_{12}$ are presented in Figure 2.12g and 2.12h. Again, both the high and low magnification STEM images and EDS maps indicate clean GBs without observable phase segregation. Therefore, this electron microscopy analysis indicates there is negligible secondary phase segregation at the GBs in either $NaPb_mSbSe_{m+2}$ or $NaPb_mSbTe_{m+2}$. Other techniques, such as atom probe tomography (APT), indicate that some Na

often segregates to the GBs in heavily sodium-doped lead chalcogenides,[16,23,87–89] yet this does not typically lead to thermally activated conduction in these materials. Because these two samples exhibit nearly identical microstructure and phase homogeneity, a different explanation is needed to account for the presence of strong GB scattering in $NaPb_mSbSe_{m+2}$ that does not occur in the Te analogue.

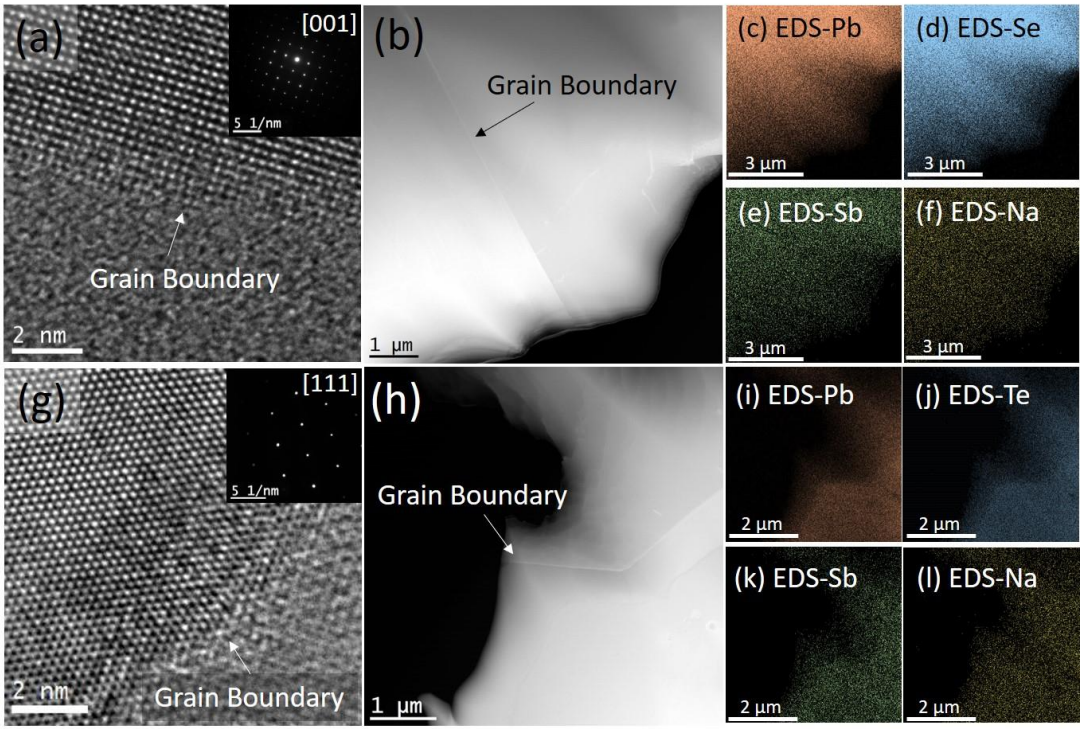

Figure 2.12. A) A characteristic high resolution TEM image of a grain boundary in a m = 10 selenide sample with nominal composition $Na_{1.15}Pb_{9.85}SbSe_{12}$. The image shows a clean boundary with no evidence for phase segregation. The inset displays a selected area electron diffraction pattern showing only the expected rocksalt spots. B) A HAADF-STEM image of another GB in the same sample also showing a clean boundary. C-F) EDS chemical maps of the area in B). G-L) are the corresponding images and maps for telluride samples with nominal composition $Na_{1.10}Pb_{9.90}Sb_{0.85}Te_{12}$.

2.3.2.3. Grain Boundary Screening Effect

Many polycrystalline semiconductors are known to intrinsically host energy barriers localized at the grain boundaries that manifest in thermally activated charge carrier mobility.[90–92] Such a situation is well summarized by Seto, who argues the energy barriers form because the atoms at the GB are more likely to have incomplete atomic bonding, or in other words that the GB region is rich with under coordinated atoms and dangling bonds compared to the bulk. The GB defects can act as trap states that immobilize charge carriers.[93] After trapping electrons or holes, the GBs become electrically charged, creating potential barriers physically analogous to a double Schottky barrier centered on the boundary. The barriers then strongly impede the flow of charge carriers through the material. Analysis of such a theoretical situation shows that in one dimension, the barrier height at the GBs takes the following form:[93]

$$E_b = \frac{e^2 Q_t^2}{8N\varepsilon} \tag{2.1}$$

where e is the electron charge, Q_t is the density of trapping states at the GB, N is the concentration of dopant atoms, and ε is the static dielectric permittivity. This equation is derived under the assumption that the doping density is greater than the concentration of GB trap states, which seems reasonable considering that the bulk electrical conductivities and Seebeck coefficients indicate degenerate carrier concentrations. While Equation (2.1) was derived for a single dimension, it provides the necessary intuition to understand the GB scattering in these bulk lead chalcogenide materials. Within the grains, the charge transport is dominated by phonon (deformation potential) scattering; however, the carriers are impeded by the energy barriers at the GBs, and here the

conduction is modeled as thermionic emission over the boundary to give electrical conductivity as follows:[93]

$$\sigma_{GB} = e^2 Ln \left(\frac{1}{2\pi m^* k_B T}\right)^{1/2} \exp\left(\frac{-E_b}{k_B T}\right) \quad (2.2)$$

If two samples have comparably sized grains, Equations (2.1) and (2.2) show that the height of the GB potential barriers are proportional to the square of the density of GB trapping states and inversely proportional to the doping level and the dielectric constant. Considering that lead chalcogenides have been extensively studied across a wide range of carrier concentration and with numerous dopants, yet do not normally exhibit strong GB scattering, it is proposed that $NaPb_mSbSe_{m+2}$ is more susceptible to GB scattering because of its relatively low dielectric constant compared to that of pure PbSe. This is intuitive, as smaller values of *e* indicate weaker screening of the charge carriers from any electric fields. Moreover, the lower dielectric constant of $NaPb_mSbSe_{m+2}$ can be rationalized with simple chemical principles. Namely, the dielectric constant (and strength of charge carrier screening) is expected to be smaller (weaker) in more ionic and less polarizable crystals than in highly covalent and polarizable compounds. With this in mind, alloying the significantly more ionic $NaSbSe_2$ into PbSe is expected to yield a less polarizable crystal with weaker carrier screening and lower *e* than pure PbSe. Furthermore, the argument also explains the lack of GB scattering in the otherwise similar $NaPb_mSbTe_{m+2}$ materials. Because PbTe has a much larger dielectric constant than PbSe, respectively 414 vs. 210 at 300 K,[94,95] it is reasonable to expect the charge carrier screening in $NaPb_mSbTe_{m+2}$ to be considerably stronger than in $NaPb_mSbSe_{m+2}$, leading to weaker GB scattering in the tellurides, as was observed.

To support the qualitative picture outlined above, density functional theory (DFT) was used to calculate the relative static dielectric constants of each lead chalcogenide and $NaSbQ_2$ compound, and the results are presented in Table 2.2. While the calculated values for the pure lead chalcogenides are somewhat higher than the experimental numbers,[94–96] these results are in general agreement with other DFT calculated dielectric constants for these materials. Crucially, the calculated dielectric constants trend as anticipated, with three to five times higher values for the pure lead chalcogenides, which are all greater than 328, compared to their respective $NaSbQ_2$ analogues that are all under 113. Moreover, the calculated values of *e* decrease moving down the periodic table from PbTe (501) to PbS (328), as anticipated by the polarizability of each compound. Somewhat surprisingly, $NaSbTe_2$ has the smallest calculated dielectric constant of the $NaSbQ_2$ materials; however, because the values of *e* are all much larger for the pure lead chalcogenides, we do not anticipate this finding to alter the analysis.

Table 2.2. DFT calculated relative isotropic dielectric constants for each PbQ and $NaSbQ_2$ (Q = S, Se, Te), as well as Mg_3Sb_2, TiCoSb, and Mg_2Si. Calculations were performed at 0 K.

Compounds	Calculated ε
PbTe	501
PbSe	338
PbS	328
$NaSbTe_2$	58
$NaSbSe_2$	71.8
$NaSbS_2$	113
Mg_3Sb_2	32
TiCoSb	32
Mg_2Si	23

Considering the above calculations and discussion, direct experimental evidence is needed to link the GB scattering to the charge carrier screening in $NaPb_mSbSe_{m+2}$. $NaPb_{20}SbSe_{22}$ (m = 20, ~4% $NaSbSe_2$) and $NaPb_6SbSe_8$ (m =6, ~14% $NaSbSe_2$) samples were prepared and the electrical transport properties were compared with the data from the previously reported $NaPb_{10}SbSe_{12}$ (m = 10, ~9% $NaSbSe_2$) materials.[29] In order to make a meaningful comparison between samples, it is imperative for the materials to have similarly sized grains. Therefore synthesis, grinding, sieving, and sintering procedures for each compound were made to be identical. The measured electrical data for all m = 20 and m = 6 samples of $NaPb_mSbSe_{m+2}$ is shown in **Figure 2.13**. Inspection of the data clearly shows the temperature dependence of the electrical conductivities the m = 20 samples are much closer to the expected metallic behavior than in the m = 6 samples, which feature strongly suppressed and thermally activated electrical conductivity below ~525 K. These results provide qualitative evidence in support of the carrier screening hypothesis.

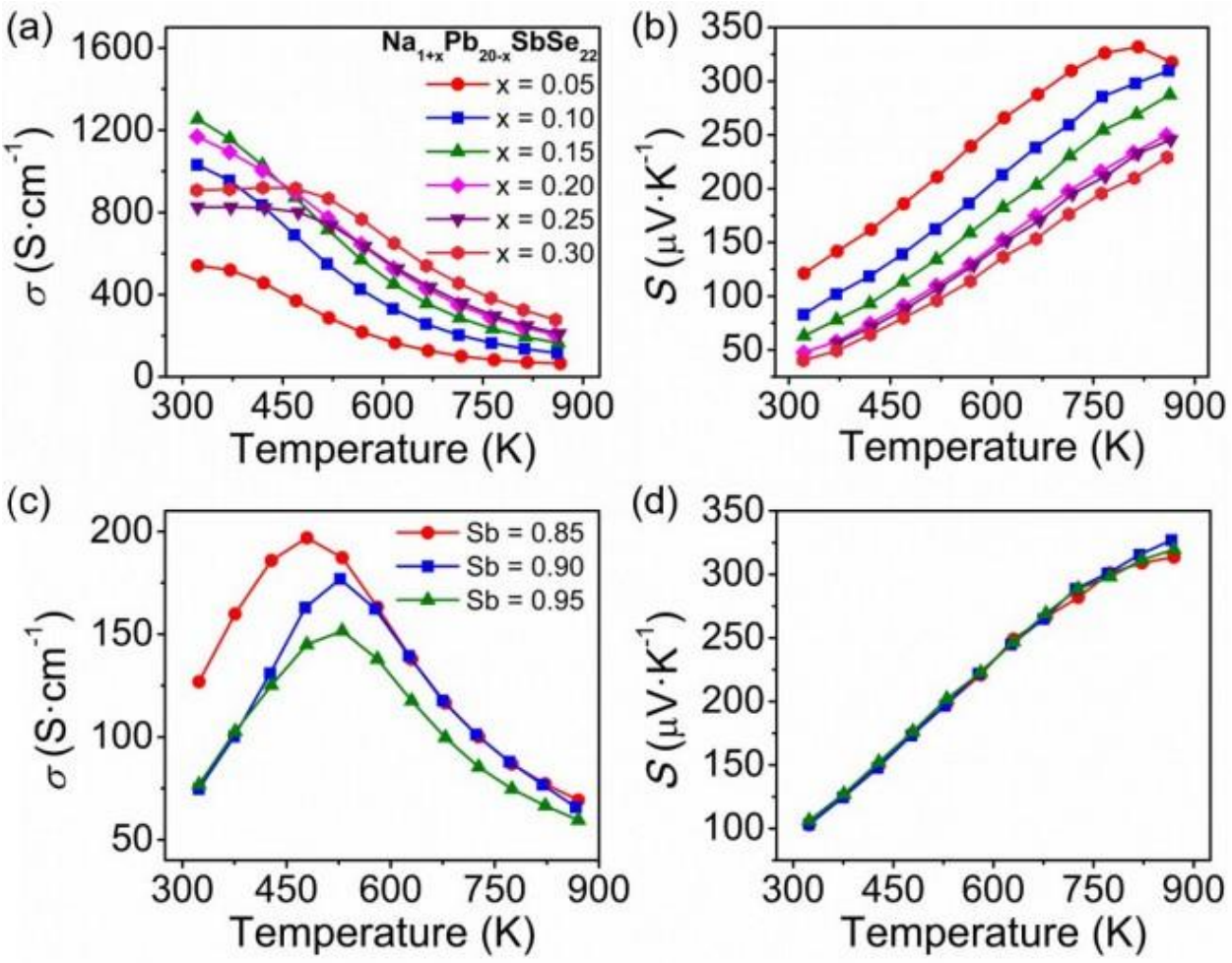

Figure 2.13. Comparison of the electrical properties for p-type $Na_{1+x}Pb_{20-x}SbSe_{22}$ (m=20) and $Na_{1.10}Pb_{5.90}Sb_xSe_8$ (m=6) compounds. A) Electrical conductivities and B) Seebeck coefficients for the m = 20 compounds. C) Electrical conductivities and D) Seebeck coefficients for the m = 6 compounds. The m = 6 compounds have qualitatively stronger GB scattering resulting in a greater degree of suppression of σ under ~ 525 K.

2.3.3. Summary of Grain Boundary Screening Study

Through the comparison of transport properties of PbQ-based solid solution thermoelectrics, an anomalous low temperature electrical conductivity effect was observed. The original suspected mechanism, ionized impurity scattering, was ruled out once grain size was proven to alter the magnitude of the conductivity repression. This was done by using EBSD to document grain size in ingot and SPS samples. Once grain boundaries were determined to be the cause of the electrical conductivity suppression, elemental segregation was ruled out based on STEM-EDS and HRTEM performed at the grain boundaries to show a homogenous phase in both $NaPb_mSbTe_{m+2}$ and $NaPb_mSbSe_{m+2}$ samples. Once chemical variation at the boundary could be ruled out, the exact mechanism was found to be a result of grain boundary screening due to the ionic nature of the specific phase and could be decreased through decreasing the quantity of ionic compounds (with smaller dielectric constants) in the solid solution or by increasing grain size. Without the ability of nano- to mesoscale analysis to rule out the competing hypotheses, the exact mechanism that leads to low temperature electrical conductivity repression could not have been isolated. Now that this mechanism has been proven, a new design principle has been introduced that enables scientists to optimize grain size depending on the ionicity and dielectric constants of their thermoelectrics. In this way future thermoelectrics can be designed to both maximize phonon scattering while minimizing low temperature charge carrier scattering.

2.4. Summary and Conclusions

In summary, past studies of lead chalcogenides have attempted to improve thermoelectric performance via hierarchical architecturing. This had been successfully achieved through the incorporation of nanoprecipitates in a multitude of compounds. In these experiments the

compositional space of $NaPb_mSbQ_{m+2}$ (Q=Te, Se, S) was explored. These compounds are structural and chemical analogues to the $AgPb_mSbTe_{m+2}$ (LAST) system which is a known high performing nanostructured lead chalcogenide thermoelectric. In the course of these investigations, conventional S/TEM microscopy techniques were used to confirm that the $NaPb_mSbQ_{m+2}$ compounds were in fact solid solutions, proving that point defects are still relevant defects that can enhance thermoelectric efficiency in PbQ based compounds and other intermediate temperature thermoelectrics.

Furthermore, the introduction of microscale electron microscopy techniques such as SEM imaging, EDS, and EBSD helped develop an understanding of key processing and design principles that can be more generally applied to other thermoelectric systems. Joint EDS-EBSD scans enabled the documentation of elemental homogenization during SPS. This was a significant finding because SPS was previously thought to be purely a solidification method that had no effects on material chemistry or transport properties. However, it was shown that diffusion of Sb into the matrix during SPS, results in n-type behavior. This discovery lead to a more informed synthesis in which composition was altered to obtain high performing SPS p-type SALT thermoelectric materials that were also mechanically robust.

Lastly, nano to mesoscale analysis confirmed the effects of grain size on low temperature electrical conductivity in ionic materials with low diaelectric constants. This helped unveil a new design principle that had formerly been overlooked by the thermoelectric community. Conventional wisdom had been that decreasing grain size is always beneficial because it provides more scattering of phonons, however it was shown here that in materials with low diaelectric

constants large amounts of grain boundaries will result in low temperature suppression in electrical conductivity, lowering overall zT_{avg}. The mechanism of grain boundary screening can now be leveraged by future scientists to design thermoelectrics with grain sizes optimized to scatter phonons while providing minimum grain boundary screening to charge carriers.

Chapter 3. Kinetic Synthesis and Property Enhancement in BST via Melt-Centrifugation

This chapter explores how recent efforts in microstructural engineering have led to the introduction of kinetic synthetic processes meant to introduce defects into low-temperature chalcogenide based thermoelectrics. This work focuses on a process known as melt-centrifugation that is used to expel excess eutectic liquid Te from $Bi_{0.5}Sb_{1.5}Te_{3+x}$ to yield stoichiometric $Bi_{0.5}Sb_{1.5}Te_3$ (BST) with a porous network of platelet shaped grains. The microstructures created using this synthesis technique impede phonon transport by introducing scattering centers across multiple length scales through a combination of porosity, pore surfaces/junctions, and grain boundary and lattice dislocations. These collectively result in a ~50 % reduction of lattice thermal conductivity (κ_l) compared to the zone melted ingot, while the charge carriers remain relatively mobile across the liquid-fused grains. This chapter lays the groundwork for Chapter 4 by outlining the specific advantages and challenges associated with developing processing methods to introduce dislocations, pores, and other nano/microstructures into thermoelectric materials, as well as the challenges of attributing property changes to specific observable defects. Portions of this chapter were previously published in *Adv. Mater.* 2018, **30**, 1802016, and are reproduced (adapted) with permission from © 2018 WILEY-VCH Verlag GmbH & Co. KGaA, Weinheim.

3.1. Microstructural Engineering of Bismuth Antimony Telluride

3.1.1. Bismuth Antimony Telluride: A Promising Room Temperature Thermoelectric

In the 1950's, it was hypothesized that semiconductors with high atomic weights would make promising legs for thermoelectric coolers, because of their combination of intrinsically high Seebeck coefficients and low lattice thermal conductivities. Bi_2Te_3 was soon discovered to be a promising thermoelectric material.[97] Since then, alloys of Bi_2Te_3 and Sb_2Te_3 (a structural

analogues) have gained prominence as high performing thermoelectrics near room temperature (< 500 K).[18] Specifically, the highest performing p-type compound is the intermetallic compound $Bi_{0.5}Sb_{1.5}Te_3$ (referred to here as BST) which consistently achieves peak zT of 1.1 around 300 K.[46] Currently BST is one of the dominant commercially produced thermoelectrics, because of both its high performance, and because of its high zT at low temperature, which makes it desirable for low temperature applications like refrigeration, and wearable electronics.[98] Although BST has been one of the few high efficiency, low temperature thermoelectrics, there was little improvement in its zT for decades following its discovery.[46,98] However recent advancements in processing and materials characterization have allowed the introduction of controlled microstructures into BST and other thermoelectrics, enabling increases in zT that had previously been unachievable.[98]

3.1.2. Reducing Thermal Conductivity in Bismuth Antimony Telluride

Recently, dislocation strain scattering has been found to be effective in scattering a broad range of phonons and reducing κ_l.[26,46,99,100] For example, Kim *et al.* achieved an extremely high zT of 1.86 in $Bi_{0.5}Sb_{1.5}Te_3$ by introducing dense dislocations at the grain boundaries using liquid phase sintering, whose zT is ~80 % higher than that of the conventional zone melted ingot.[46] In addition, introducing pores into the microstructure has also been applied to dramatically reduce the thermal conductivity.[101,102] In the context of porous thermoelectric materials two observations should be mentioned. The absence of a conduction medium in the pores will proportionally decrease the thermal conductivity and the electrical conductivity leading to no net gain in zT. However, pore-interface scattering of phonons may additionally reduce the thermal conductivity since phonons have larger mean free path than charge carriers. As a porous structure arising from a poor sintering process typically results in poor thermoelectric performance, the electrical conductivity is severely

reduced and is not adequately compensated by the reduction of thermal conductivity. Therefore, introducing a hierarchical microstructure with good electrical connections may be expected to enhance the *zT* of a porous matrix.

3.1.3. Melt-Centrifugation: A Synthesis Method to Introduce Microstructuring

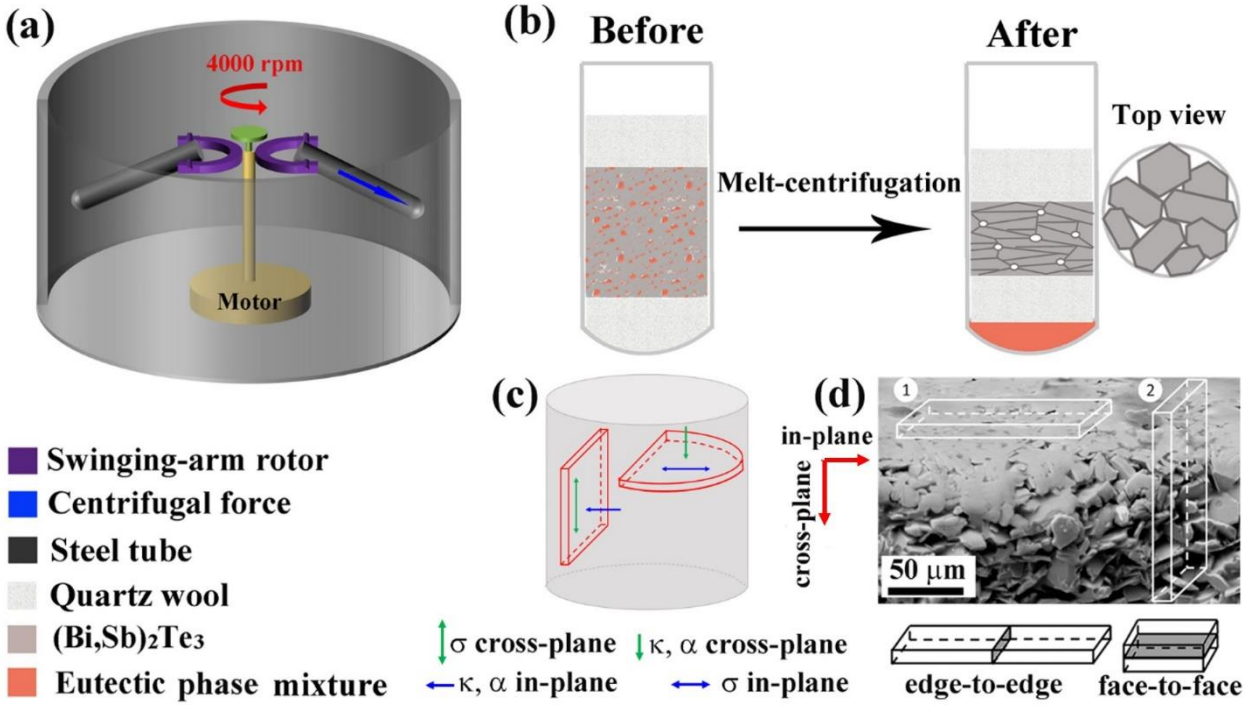

Figure 3.1. A) Schematic illustration of centrifugation. B) Sample condition in the silica ampoule before and after melt-centrifugation. Microstructure of the sample becomes anisotropic and porous after melt-centrifugation. C) Schematic illustration of the measurement direction of thermoelectric transport properties. D) SEM image of a cross section of a melt-centrifuged sample, with a description of the platelets' edge-to-edge and face-to-face contact (grey planes) in the in-plane and cross-plane directions, respectively.

This chapter reports on a melt-centrifugation technique to achieve a liquid-fused p-type $(Bi,Sb)_2Te_3$ alloy with microscale dislocation arrays and large porosity. Melt-centrifugation engineers the microstructure via separating the liquid eutectic phase mixture from the solid

$(Bi,Sb)_2Te_3$ phase under strong centrifugal force. By rotating around a fixed axis, a strong force perpendicular to the spin axis is applied to the sample, as schematically shown in **Figure 3.1a**. Before centrifugation, the sample consists of a mixture of two phases: $(Bi,Sb)_2Te_3$ and Te. At 500 ºC, the Te-rich eutectic (melting point: ~425 ºC) melts and dissolves some of the $(Bi,Sb)_2Te_3$. During centrifugation, the randomly distributed liquid eutectic is forced out of the bulk sample to the bottom of the silica ampoule, leaving behind nearly pure $(Bi,Sb)_2Te_3$ with a low density (**Table 3.1**), as schematically shown in Figure 3.1b. Note that the pores originate from the centrifugation process rather than being the result of insufficient sintering which may occur during hot pressing. In addition, the pre-centrifugation heating process occurs at 500 ºC for 30 min, which only melts the Te, but also plays a role in annealing the samples, improving the overall crystallinity. Hence although porous, the samples show large grain domains and a layered structure, as seen in Figure 3.1d.

Table 3.1. Density of the samples before and after centrifugation.

Samples	Geometric density (g/cm^3)	Relative density (%)
$Bi_{0.5}Sb_{1.5}Te_{4.31}$ (before)	5.96	91.88
$Bi_{0.5}Sb_{1.5}Te_3$ (after)	5.02	73.72
$Bi_{0.3}Sb_{1.7}Te_{4.28}$ (before)	5.88	91.37
$Bi_{0.3}Sb_{1.7}Te_3$ (after)	4.85	72.54

Due to the BST crystal structure and strong centrifugal force, anisotropy is observed in all samples. The orientation factor calculated from the XRD results of the bulk sample is about 0.16.

In-plane and cross-plane directions are defined with respect to the direction of centrifugation, as schematically illustrated in Figure 3.1c and 3.1d. The crystal structure of $(Bi,Sb)_2Te_3$ manifests in the disc shaped grains which orient under the influence of both heating process and the centrifugal force in the presence of liquid eutectic. Figure 3.1d shows that the in-plane direction has edge-to-edge contact between the platelets, while cross-plane has face-to-face contact. The face-to-face contact has more surface area for interaction, and therefore results in the observation of more grain boundary area at which dislocations form due to grain misorientation.

Melt-centrifugation was introduced as a method to introduce a variety of microstructures into low temperature bulk BST. Based on prior research in the field, the idea behind this kinetic synthesis method is that once excess Te is rejected from the material, it will leave behind hierarchically structured BST with pores, interfaces, and dislocations that will increase phonon scattering. Melt-centrifugation is an effective method for introducing microstructures into BST using this kinetic synthesis process, and the work in this chapter will be followed up in Chapter 4 by an attempt to reproduce the inclusion of defects into BST using a more controlled synthesis method. Despite the drawbacks to kinetic synthesis, the methodologies that are used to study melt-centrifugation, will prove to be instrumental in improving the understanding of how processing and microstructure contribute to improved thermoelectric performance in chalcogenide-based thermoelectric systems.

3.2 Techniques and Methodologies for Studying Microstructured Thermoelectric Materials

3.2.1. The Thermoelectric Quality Factor: Comparing Materials with Different Carrier Concentrations

Prior to this point, thermoelectric efficiency has been described solely by the dimensionless figure of merit defined as zT. Because the thermoelectric performance has a complex dependence upon the Fermi level, it can be difficult to accurately determine or compare the impact of materials engineering efforts on zT if a material is not optimally doped. To evaluate thermoelectric performance more fundamentally, the material quality factor B may be used.

$$B = \left(\frac{8\pi k_B^{3.5}(2m_e)^{1.5}}{3eh^3}\right)\left(\frac{m^*}{m_e}\right)^{1.5} T^{2.5}\frac{\mu_0}{\kappa_l} \propto T^{2.5}\left(\frac{\mu_w}{\kappa_l}\right) \tag{3.1}$$

where k_B is the Boltzmann constant, e is elementary charge, h is Planck's constant, m^* and m_e are the density of states (DOS) effective and electron rest masses, respectively, μ_0 is the mobility at nondegenerate limit, and $\mu_w = (m^*/m_e)^{1.5}\mu_0$ is the weighted mobility.[103–105] In some cases, phonon scattering centers that are introduced into a material, may also scatter charge carriers and therefore the evaluation of B should be used to determine if there is a net gain in potential thermoelectric performance.[106] This quality factor is independent of doping for carriers in a single band and can therefore be used to compare samples that are not optimally doped to compare their potentials for maximum zT when they are doped optimally.[107,108]

3.2.2. Effective Medium Theory: Comparing Samples with Different Densities

To describe the effects of having a mixture of two materials (in this case the experimental material and air), effective medium theory (EMT) is used to analyze the electrical and thermal conductivity of porous materials.[109] Generalized EMT developed by Bruggeman and Landauer,

and described by Stroud[110–112] was used to explain the low field Hall effect by Cohen.[113] For a porous material, the general form should be $\sigma_p = \sigma_d f_\sigma(\varepsilon)$, where f is an EMT function of the porosity ε, σ_p and σ_d presents the conductivity of porous and dense materials respectively. Similarly, for thermal conductivity, $\kappa_p = \kappa_d f_\kappa(\varepsilon)$. The EMT function f depends weakly on the shape of the pores, to first order $f_\sigma(\varepsilon) = f_\kappa(\varepsilon) = (1–3\varepsilon/2)$ and the Hall mobility and carrier concentration decrease by $(1–3\varepsilon/4)$ where ε is porosity volume fraction.[114] Since the same pores effect both the thermal and electrical conductivity, zT may not be expected to vary significantly with porosity.[115]

This methodology is important because it allows for the comparison of material properties of fully dense and porous materials. Naturally, a decrease in thermal conductivity is expected in the porous BST samples, because of a lack of conduction medium. However, in order to prove that the reduction is due to factors beyond the absence of conduction medium, there needs to be an established method to account for the expected decrease in thermal conductivity due to the decrease in density. Once EMT is used to account for this difference, any remaining differences in thermal conductivity can be concluded to be a result of the microstructuring induced by melt-centrifugation. The same comparison is necessary for accounting for differences in electrical conductivity.

3.2.3. The Debye-Callaway Model for Lattice Thermal Conductivity

A systematic thermal model is required to separate the different contributions to the reduction in κ_l. Reductions in thermal conductivity can stem from various phonon scattering mechanisms and/or the lack of thermal conduction through empty space created by pores. These two effects are treated separately. The first cause of reduction, or the absence of thermal conduction within the pores, is described classically by the EMT, as described above, leading to a reduction in lattice

thermal conductivity described by $\kappa_{l,d} = \kappa_{l,p}/f_\kappa(\varepsilon)$. Using EMT, the lattice thermal conductivity for the corresponding, fully-dense material, $\kappa_{l,d}$, can be obtained, resulting in the corrected thermal conductivity values of the dense material constructing the $(Bi,Sb)_2Te_3$ network.

The second cause of lattice thermal conductivity reduction, phonon scattering due to various phonon scattering mechanisms, is described with a Debye-Callaway model used to calculate the reduction of thermal conductivity for a fully dense equivalent material, or $\kappa_{l,d}$:[116]

$$\kappa_{l,\mathrm{d}} = \frac{k_\mathrm{B}}{2\pi^2 v}\left(\frac{k_\mathrm{B}T}{\hbar}\right)^3 \int_0^{\theta_\mathrm{D}/T} \tau(x)\frac{e^x x^4}{\left(e^x-1\right)^2}\mathrm{d}x \tag{3.2}$$

where the total phonon relaxation time is determined via Matthiassen's rule $\tau(x)^{-1} = \sum_i \tau_i(x)^{-1}$. First, the effect of phonon-phonon scattering ($\tau_{\text{p-p}}$) and phonon-point defect scattering (τ_{PD}) were accounted for by fitting the model to the in-plane κ_l (lowest thermal conductivity direction) of a zone melted crystal[117] with the following expressions:

$$\tau_{\text{p-p}}^{-1} = Ax^2T^3 \tag{3.3}$$

$$\tau_{\text{PD}}^{-1} = \frac{k_B^4 V_{PUC}}{4\pi\hbar^4 v^3}\Gamma x^4 T^4 \ , \ \Gamma = \sum_i f_i\left(\frac{M_i-\overline{M}}{\overline{M}}\right)^2 \tag{3.4}$$

The term τ_{PD} was determined by considering only mass difference which is known to work well for the Bi_2Te_3-Sb_2Te_3 system.[118,119] The phonon-phonon scattering strength coefficient *A* was fit to the experimental data of the in-plane κ_l of fully dense, large grained $Bi_{0.5}Sb_{1.5}Te_3$[117] where $\tau^{-1}=\tau_{\text{p-p}}^{-1}+\tau_{\text{PD}}^{-1}$ and was fixed for the rest of the model.

Next, the effect of pore interfaces on the thermal conductivity was estimated. The presence of pore interfaces limits the mean free path of phonons within the dense matrix to the average

distance between the pores (L) and thus introduces a Casmir-like phonon-interface scattering term:[120]

$$\tau_{\mathrm{I}}^{-1} = \frac{\nu}{L} \tag{3.5}$$

where L is determined via porosity and average pore size. It was determined through the study of the mesoscale structure that L=4 μm, which is much larger than the phonon mean free path due to phonon-phonon and phonon-point defect scattering, and as a result these calculations indicate that pore interfaces produce minor reductions in $\kappa_{l,d}$. The contribution of interfaces can be seen in **Figure 3.2a** in pink. This demonstrates that the reduction of thermal conductivity cannot be explained by the porosity alone and requires additional scattering mechanisms such as grain boundary scattering which can also be modeled as grain boundary dislocation strain scattering.[26]

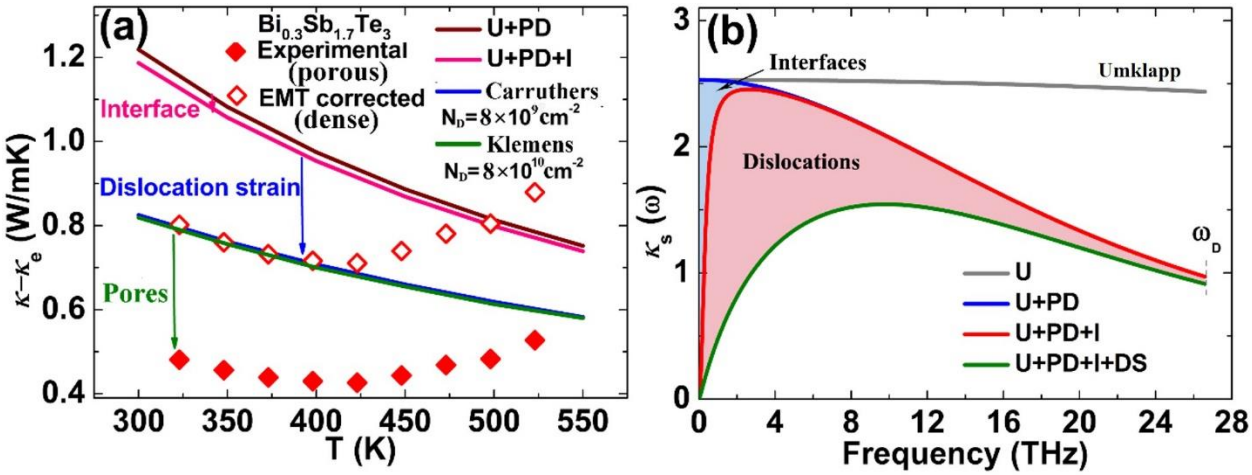

Figure 3.2. A) In-plane lattice thermal conductivity of the centrifuged $Bi_{0.3}Sb_{1.7}Te_3$. Empty symbols presents $\kappa_{l,d}$ which are corrected from experimental results $\kappa_{l,p}$ (filled symbols) by EMT. Experimental results can be explained by the absence of thermal conduction medium (pores) and by using reasonable values for Umklapp (U), point defect (PD), porous interface (I) and dislocation strain (DS) into account. B) Frequency dependent lattice thermal conductivity of the dense $Bi_{0.3}Sb_{1.7}Te_3$. Interfaces target low frequency phonons while dislocations impact a broad range of phonons.

We include the effect of phonon-dislocation strain scattering through the expression:

$$\tau_{\mathrm{DS}}^{-1} = CN_{\mathrm{D}}B_{\mathrm{D}}{}^{2}\gamma^{2}x\frac{k_{\mathrm{B}}}{\hbar}T \tag{3.6}$$

where N_D is the dislocation density, B_D is the Burgers vector, and γ is the Gruneissen parameter of the alloy. This calculation is dependent on two material parameters N_D and B_D which can be found using TEM. However, although these defects can be identified, the true density of dislocations (not just the density within the areas of interest, but the true density throughout the material) is difficult to accurately measure using small field-of-view techniques (like TEM) alone. Furthermore, thermal models such as those being used in this investigation, often assume homogeneity of

features such as grain boundary composition or an even distribution of dislocations throughout a sample, which is not often the case. Therefore, it is important for thorough analysis to be performed on samples to ensure that these assumptions about grain boundary composition, dislocation density, etc. are justifiable and accurate for the material system being investigated.

3.2.4. Using Electron Microscopy to Obtain Parameters for Thermal Modeling

3.2.4.1. Studying Grain Boundaries with Transmission Electron Microscopy

At a broad level, it is known that grain boundaries scatter low frequency (large mean free path) phonons.[5,16,34] The true complexity of boundary transport is still relatively unexplored in bulk thermoelectric materials, although it has been shown that structure and orientation, as well as composition (impurity atoms), can alter the transmission of phonons passing through the grain boundaries.[121] It is often energetically favorable for solutes to segregate to grain boundaries because of the presence of dangling bonds and structural imperfections, such as dislocations. Furthermore, this means that materials can develop chemical segregation at boundary sites.[122,123] Changes in grain boundary orientations can also lead to differences in the size and spacing of vacancies, altering the likelihood of certain chemicals to segregate at boundaries with different structural orientation.[92] As a result, not only are imaging and diffraction important for the study of grain boundaries, but so are analytical techniques, such as Energy Dispersive Spectroscopy (EDS) and Electron Energy Loss Spectroscopy (EELS), which are capable of determining local chemical composition.

3.2.4.2. Studying Dislocations with Transmission Electron Microscopy

Dislocations contribute to thermal conductivity via scattering from dislocation cores and from the strain fields that result from lattice distortions surrounding the defect. Dislocation cores can be imaged using TEM, but the contrast provided by dislocations is often due to the diffracted beams as they interact with curved areas of the lattice around the dislocation defect.[37] An important feature of dislocations is their Burgers vector (B_D), as this helps us understand how the lattice planes are distorting. In addition, as seen in Equation (3.6), the Burgers vector is a required feature for determining the contribution of dislocation strain to phonon relaxation time (and subsequently lattice thermal conductivity).[124]

To determine the Burgers vector using electron microscopy it is helpful to know if dislocations are either edge, screw, or of mixed character. If the dislocation is purely screw in character, the Burgers vector can be determined through two-beam tilting experiments. Two-beam tilting experiments involve tilting the sample so that the reciprocal space diffraction pattern primarily consists of two bright spots (the transmitted beam and a diffracted beam) with all other diffracted spots remaining very dim. In this condition, phase contrast in imaging mode is influenced almost exclusively by electrons in the transmitted beam and the selected diffracted beam. Because of constructive and destructive interference effects, some dislocations will lose much of their contrast when specific diffracted beams are selected in a two-beam condition. This is known as the invisibility criterion and indicates that the dislocation line is parallel to the g vector selected in the two-beam condition. If dislocations have edge character this procedure is complicated, but nonetheless diffraction and tilting experiments can be used to take advantage of contrast mechanisms to identify the Burgers vectors of dislocations.

The dislocation density (N_D) is also an important material parameter to document in order to obtain an accurate thermal model. Dislocation density can be documented in an area of interest using a TEM by using the line intercept method. The line intercept method calculates dislocation density using the formula:[125]

$$N_D = \frac{P}{L_{Tot} \times t} \tag{3.7}$$

In this equation, the dislocation density (N_D) is calculated by drawing random lines of known length throughout an area of interest in the image of interest. Then the number of intersection points (P) between the drawn lines and dislocations should be counted and divided by the total line length (L_{Tot}, calibrated to the scale of the image) and the thickness of the sample (t). The resulting dislocation density should have units of cm^{-2} or m^{-2}. The limitations of this method are that any given selected area may have a dislocation density that is not representative of the sample. Additionally, lines may be drawn in orientations that are not truly random (examples of which can be shown in **Figure 3.3**). Both factors may result in misleading dislocation density measurements. For example, a line drawn perpendicular to an array of dislocations would provide a high density compared to a line drawn parallel to the array. It is also important to obtain an accurate thickness which can be obtained by performing a variety of techniques which include but are not limited to: thickness fringe analysis in a two-beam condition, convergent beam electron diffraction, or electron energy loss spectroscopy mean free path analysis.[125] In summary it can be seen that electron microscopy is a useful tool for obtaining material parameters critical to improving the accuracy of thermal models, however one should also be aware of the inaccuracies that could occur in order to obtain the most representative results.

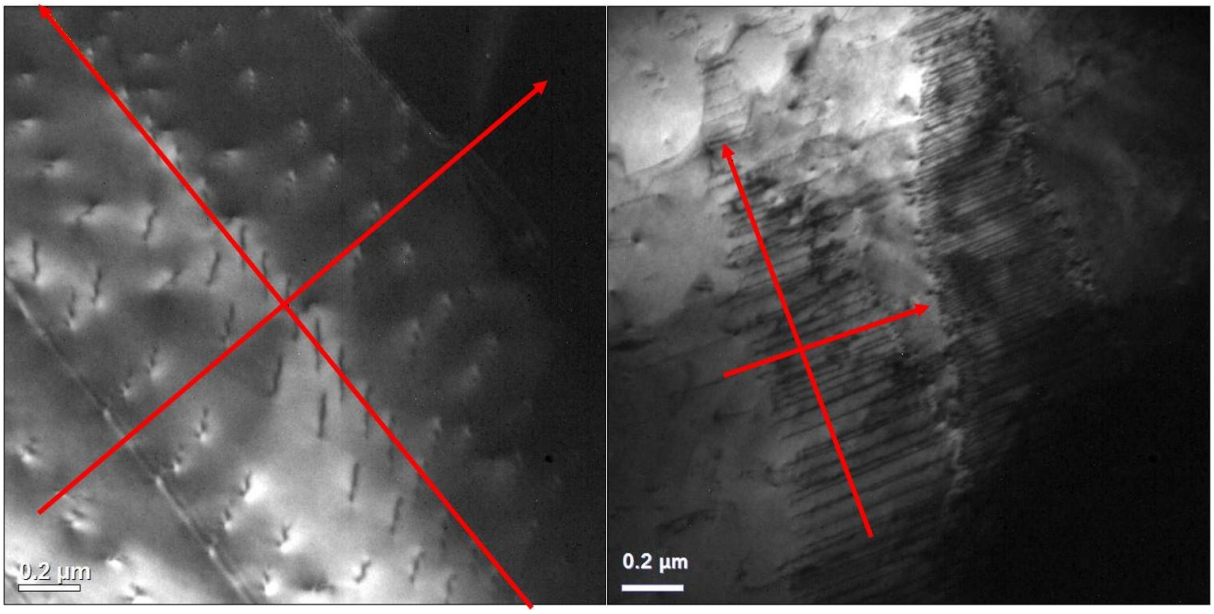

Figure 3.3. Two BF-TEM images of dislocation arrays in BST with lines drawn parallel and perpendicular to the dislocation arrays. Using the Line Intercept Method, these two lines will calculate vastly different dislocation densities (N_D) based on the directionality of the dislocation arrays.

3.2.5. Experimental Setup for the Study of Melt-Centrifuged BST

3.2.5.1. Sample preparation

Bi, Sb and Te (Alfa Aesar, >99.999%) chunks were weighed according to stoichiometries of $Bi_{0.5}Sb_{1.5}Te_{4.31}$ and $Bi_{0.3}Sb_{1.7}Te_{4.28}$ and subjected to high energy ball milling for 1 hr. The ball milled powders were then hot pressed rapidly (RHP)[35] at 673 K for 1 hr with an axial pressure of ~45 MPa under argon atmosphere. Pressing was performed in a 12.7 mm diameter graphite die and produced a pellet ~15 mm tall. No liquid came out during hot pressing. Next, the sintered pellet was sealed under vacuum in a silica ampoule with quartz wool on top of and beneath the sample. The ampoule was placed in a vertical furnace and heated to 773 K for 30 min. This

temperature is higher than the melting point of Te, but lower than that of $(Bi,Sb)_2Te_3$. Next the ampoule was quickly (in ~3s) transferred from the furnace and centrifuged at 4000 rpm for 105 s.

3.2.5.2. Experimental Procedures and Instrumentation

Phase purity was evaluated by X-ray diffraction (XRD, STOE STADI MP, Cu-$K_{\alpha1}$, scan step of 0.015°). The microstructure was investigated by field emission scanning electron microscopy (FESEM, Hitachi SU8030 and FEI Quanta 650 ESEM) and transmission electron microscopy (TEM, Hitachi, H-8100 and JEOL JEM-ARM300CF). Hall coefficients (R_H) and resistivity (ρ) were measured simultaneously using van der Pauw and four-probe methods under a 2 T magnetic field.[126] Hall carrier concentration (n_H) and mobility (μ_H) were calculated by $n_H=1/(eR_H)$ and $\mu_H=R_H/\rho$. Seebeck coefficients were measured under vacuum using a home-built instrument.[127] The thermal conductivity (κ) was calculated by $\kappa = D\times C_p\times d$, in which d is the geometrical density, C_p is the Dulong-Petit specific heat (0.186 J/gK for $Bi_{0.5}Sb_{1.5}Te_3$ and 0.191 J/gK for $Bi_{0.3}Sb_{1.7}Te_3$), and D is the thermal diffusivity measured by the laser flash method (Netzsch LFA 457, Germany). The κ_e was calculated using the Wiedeman–Franz law ($\kappa_e=LT/\rho$),[116] where the Lorenz factor (L) is estimated using the effective mass model.[128] The minimum thermal conductivity is calculated from Cahill limit[129] using the measured speed of sound. Transport properties were measured in both directions parallel (cross-plane) and perpendicular (in-plane) to the direction of centrifugal force/HP pressure.

3.3. Relating Microstructure to Thermal Transport Properties

3.3.1. Using EMT to Calculate the Contribution of Porosity to Electronic Properties

The electronic band structure related transport properties are analyzed by the effective mass model. The electrical properties (of EMT corrected to full density) are comparable to high performance dense $Bi_xSb_{2-x}Te_3$ alloys fabricated by different methods, including Te-excess melt-spun (Te-MS),[46] melt-spun (MS),[117] hot press (HP),[130] hot deformation (HD),[130,131] and zone melting (ZM).[117] The band structure appears to be unchanged with the modified microstructure. As shown in the Pisarenko plot (Seebeck coefficient versus carrier concentration)[132] of **Figure 3.4a**, the $Bi_{0.5}Sb_{1.5}Te_3$ samples can be well fitted by a DOS effective mass of ~1.1m_e. The $Bi_{0.3}Sb_{1.7}Te_3$ samples have a slightly lower value, which is consistent with the band convergence occurring for $Bi_xSb_{2-x}Te_3$ at x=0.5.[133] Note that the slightly lower m* of the centrifuged samples compared with Te-MS[46] and MS[117] samples could be caused by the lower density since porosity decreases the carrier concentration but hardly changes the Seebeck coefficient. By corrected to

fully dense materials, as shown by the orange star symbols, the m^* is similar to the Te-MS[46] and MS[117] samples.

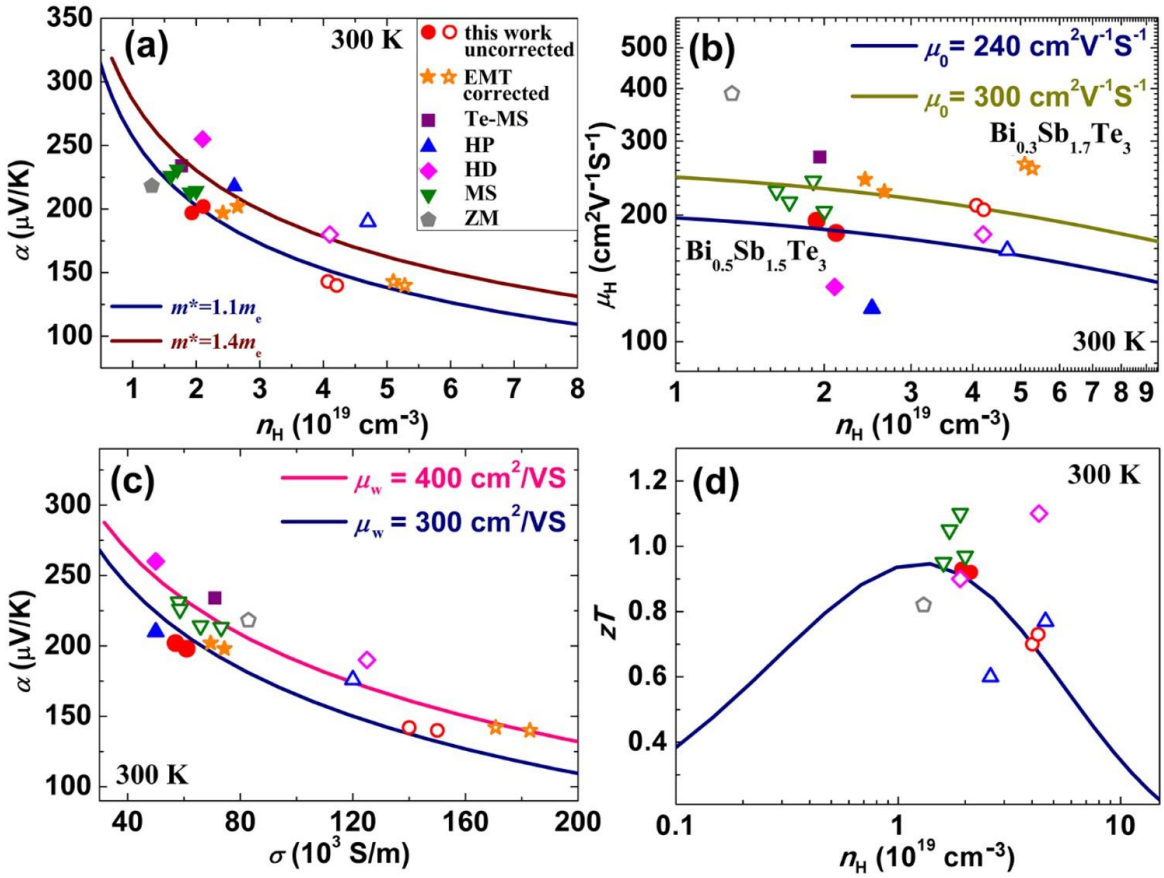

Figure 3.4. A) Hall carrier concentration dependence of Seebeck coefficient (Pisarenko plot) at 300 K. B) Hall carrier concentration dependence of Hall mobility at 300 K. C) Conductivity dependence of Seebeck coefficient (Jonker plot). D) *zT* values as a function of Hall carrier concentration predicted by μ_w of 300 cm^2/VS and κ_l of 0.5 W/mK at 300 K. Filled and empty symbols represent the data of $Bi_{0.5}Sb_{1.5}Te_3$ and $Bi_{0.3}Sb_{1.7}Te_3$, respectively. Here experimental results and EMT corrected values are shown by the red circle and orange star symbols respectively

The Hall carrier mobility of the connected matrix is hardly affected by the porosity. Using typical porosity of the centrifuged material of ε ~0.27, $\mu_{H,d}$ of the present $Bi_{0.5}Sb_{1.5}Te_3$ alloy would be $\mu_{H,d}=\mu_{H,p}/(1-3\varepsilon/4)=\mu_{H,p}/0.79=250$ $cm^2V^{-1}S^{-1}$, which is comparable to the dense melt-spun

alloys.[117] The competitive intrinsic mobility of the framework originates from the highly-fused nature of the matrix. As shown in Figure 3.4b, the porous centrifuged $Bi_{0.5}Sb_{1.5}Te_3$ samples and the dense melt-spun[117] materials show μ_0 values of ~240 cm^2/VS and 240-300 cm^2/VS, respectively. Since μ_0 of the framework corrected by EMT is equally and even slightly higher compared to that of fully dense melt-spun materials, lower μ_0 of the porous samples is only due to the absence of conduction matrix. Higher mobilities of $Bi_{0.3}Sb_{1.7}Te_3$ samples than $Bi_{0.5}Sb_{1.5}Te_3$ samples are due to the lower m^*. This is also the case for weighted mobility as shown in Figure 3.4c. Overall, the preserved high Hall mobilities of the centrifuged samples demonstrate a good connection of the matrix for electronic transport.

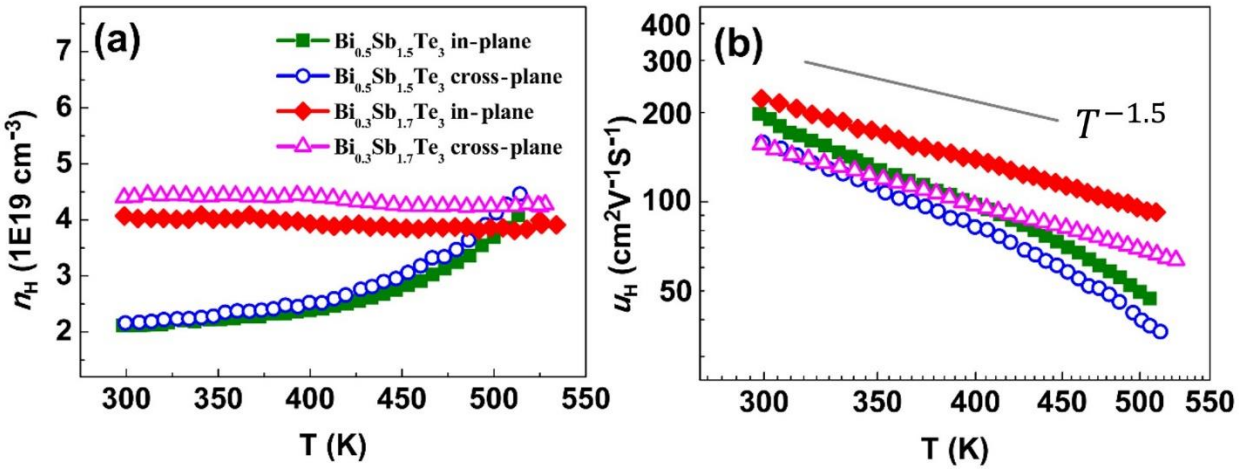

Figure 3.5. Temperature dependence of (a) Hall carrier concentration and (b) Hall mobility in both in-plane and cross-plane directions.

Based on an effective mass model and acoustic phonon scattering, which is demonstrated by the $T^{-1.5}$ dependence of Hall mobility shown in **Figure 3.5b**, the peak zT at 300 K lies at the carrier concentration of ~2×10^{19} cm^{-3}. As shown in Figure 3.4d, the majority of the experimental data lies on the expected curve, and the zT values of porous centrifuged samples are very similar to those

of the fully dense materials possessing almost optimum doping levels. The melt-spun samples[117] show higher *zT* values as the mobility is higher, while the discrepancy of hot-pressed and hot-deformed samples[130,131] could be due to the different effective masses. The melt-centrifuged $Bi_{0.5}Sb_{1.5}Te_3$ attains higher *zT* values than the zone melted and hot pressed samples. This is in parallel with higher *B* value obtained ($B = 0.48$) for this sample compared to the zone melted ($B = 0.32$) and the hot-pressed ($B = 0.25$) samples.

3.3.2 The Contribution of Structural Defects to the Reduction in Lattice Thermal Conductivity

Microstructure observation were further conducted by TEM. **Figure 3.6** show two different types of dislocations: lattice dislocations with little to no ordering within the grains and highly ordered arrays of grain boundary (GB) dislocations. Lattice dislocations and GB dislocation arrays are observed in the in-plane direction (Figure 3.6a and b), but they are less often observed due to the edge-to-edge contact; while they are commonly observed in the cross-plane direction (Figure 3.6c-f) due to face-to-face contact. It is worth noting that amorphous/glassy phases are not observed at the grain boundaries, indicating the necessity of the dislocations and dislocation arrays in order to compensate the grain misorientation. Here the grain misfit comes from the face-to-face stack of anisotropic $(Bi,Sb)_2Te_3$ platelets that can be rotated in relation to one another, which is facilitated by the uniaxial centrifugal force and liquid extrusion during melt-centrifugation. Hot pressed samples without centrifugation show few dislocations. Dislocations introduce strain fields in their vicinity can interfere with the propagation of phonons and thus decrease the thermal conductivity.

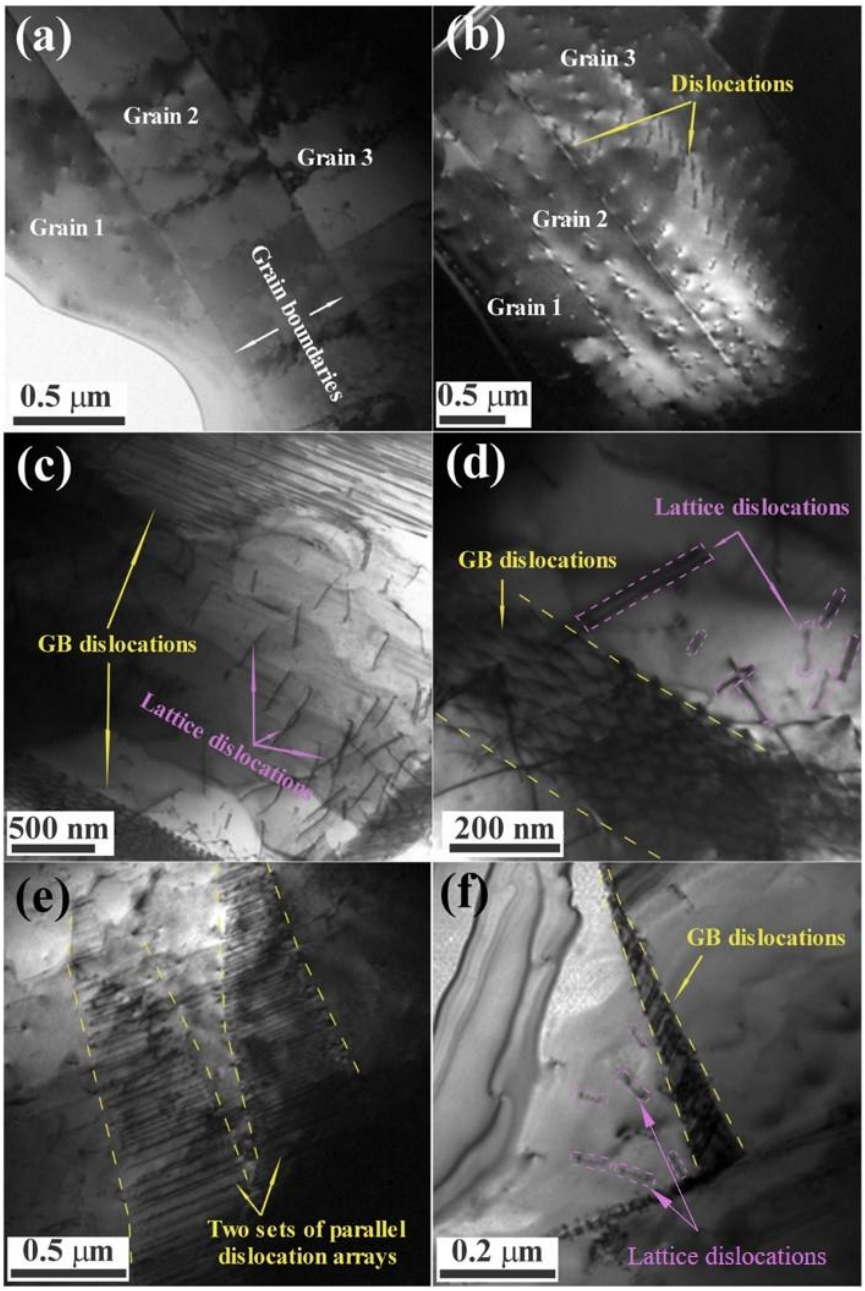

Figure 3.6. A) Bright Field and B) Dark Field of in-plane direction that displays dislocation arrays originating from grain boundaries. C) Weak beam image illustrating randomly oriented lattice dislocations surrounded by ordered arrays of grain boundary dislocations. D) A higher magnification of one of the ordered dislocation arrays from image C). E) Bright field of two sets of parallel dislocation arrays. F) Ordered grain boundary dislocations alongside lattice disordered within the grain.

The TEM study presented above found the maximum dislocation density of melt-centrifuged samples to be on the order of 10^9 to 10^{10} cm^{-2}. Mion *et al.* showed that dislocation densities above 10^7 cm^{-2} have a significant effect on the κ_l of GaN,[134] and thus we conclude that the dislocation density observed here is of an appropriate order of magnitude to further lower the overall thermal conductivity. Considering the orders of magnitude uncertainty in the dislocation density, Burgers vector, and even the constant C (Klemens[46,135] vs Carruthers[136]) it is possible to explain the experimental thermal conductivity with a range of parameters; with one set of physically reasonable parameters given in **Table 3.2**. It should be noted that a 2 nm Burgers vector is quite large, but Burgers vectors of 1.048 nm have been reported in the structural analogue Bi_2Te_3.[137] The blue lines in Figure 3.2a give an order of magnitude estimation for the influence of phonon-dislocation scattering on $\kappa_{l,d}$.

Table 3.2. Parameters for lattice thermal conductivity modeling.

Variables	Notes	Values	Methods
v	In-plane average speed of sound	2147 m/s	Ref. [138]
A	Prefactor of Umklapp scattering time	300000	Fitted
γ_{pure}	Grüneisen constant	2.3	Ref. [46]
L	Average distance between pores	4 μm	Experimental
V	Average volume per atom	3.13×10^{-29} m^3	Ref. [46]
V_{PUC}	Volume of the primitive unit cell	$5\times V$	
N_D	Dislocation density	5×10^{10} cm^{-2}	Fitted
		($Bi_{0.5}Sb_{1.5}Te_3$)	
		8×10^{10} cm^{-2}	
		($Bi_{0.3}Sb_{1.7}Te_3$)	
B_D	Burgers vector	2 nm	
r	Poisson's ratio	0.24	Ref. [46]
v_L	Longitudinal sound speed	2884 m/s	Ref. [138]
v_T	Transverse sound speed	1780 m/s	Ref. [138]
c_0	Concentration of Bi_2Te_3 in $Bi_{0.5}Sb_{1.5}Te_3$/	0.25/0.15	Calculated
	$Bi_{0.3}Sb_{1.7}Te_3$		
K	Bulk modulus	44.8 GPa	Ref. [46]
T_a	HP sintering temperature	673 K	Experimental
V_{Sb2Te3}	Average volume per atom of Sb_2Te_3	3.13×10^{-29} m^3	Ref. [46]
V_{Bi2Te3}	Average volume per atom of Bi_2Te_3	3.40×10^{-29} m^3	Ref. [46]
M_{Sb2Te3}	Average mass per atom of Sb_2Te_3	2.07×10^{-25} kg	Ref. [46]
M_{Bi2Te3}	Average mass per atom of Bi_2Te_3	2.79×10^{-25} kg	Ref. [46]
γ_1	$Bi_{0.5}Sb_{1.5}Te_3$	1.2	Calculated
	$Bi_{0.3}Sb_{1.7}Te_3$	0.7	

By combining EMT and the Debye-Callaway thermal model, it can be shown that the pore structure (the pores and their interfaces) results in as much as ~50 % total reduction of thermal conductivity. The additional reduction is due to additional phonon scattering, and a case has been made that this is potentially a result of dislocation strain fields which were introduced during the melt-centrifugation process. The phonon-pore interface scattering targets low frequency phonons, since the average distance between the pores are large. Dislocation strain scatters mid-frequency range which haven't been affected by pore interfaces or point defects, as shown in Figure 3.2b. The large decrease of thermal conductivity from engineering porosity and microstructure, along with good electrical performance, can improve the thermoelectric performance.

3.3.3. Thermoelectric Device Efficiency

In- and cross-plane temperature dependent transport properties are shown in **Figure 3.7a-d**. High zT value around 1.2 is achieved in the cross-plane of centrifuged $Bi_{0.5}Sb_{1.5}Te_3$ at 373, and the zT_{max} is shown to be shifted to higher temperatures by adjusting the Bi/Sb ratio from 0.5/1.5 to 0.3/1.7 due to higher carrier concentration, resulting in a zT_{max} of 1 at 448 K for $Bi_{0.3}Sb_{1.7}Te_3$ (Figure 3.4e). From a device standpoint, the ability to produce high zT values at different temperature ranges using one material is beneficial for segmented design,[139] for which two compositions ($Bi_{0.5}Sb_{1.5}Te_3$ and $Bi_{0.3}Sb_{1.7}Te_3$) have been made with low and high carrier concentrations, respectively. As depicted in Figure 3.7f, by utilizing $Bi_{0.5}Sb_{1.5}Te_3$ between 323-400 K and $Bi_{0.3}Sb_{1.7}Te_3$ for 400-523 K in a segmented module, the calculated cross-plane device ZT can be as high as 1.05 over the entire temperature range.[8] The corresponding calculated theoretical maximum efficiency could reach up to 9 % when the hot and cold side temperature at 523 K and 300 K, respectively. The present simulated p-type $(Bi,Sb)_2Te_3$ segmented leg with a

high device *ZT* at the wide temperature range is attractive for high performance module application in mid-temperature waste heat recovery.

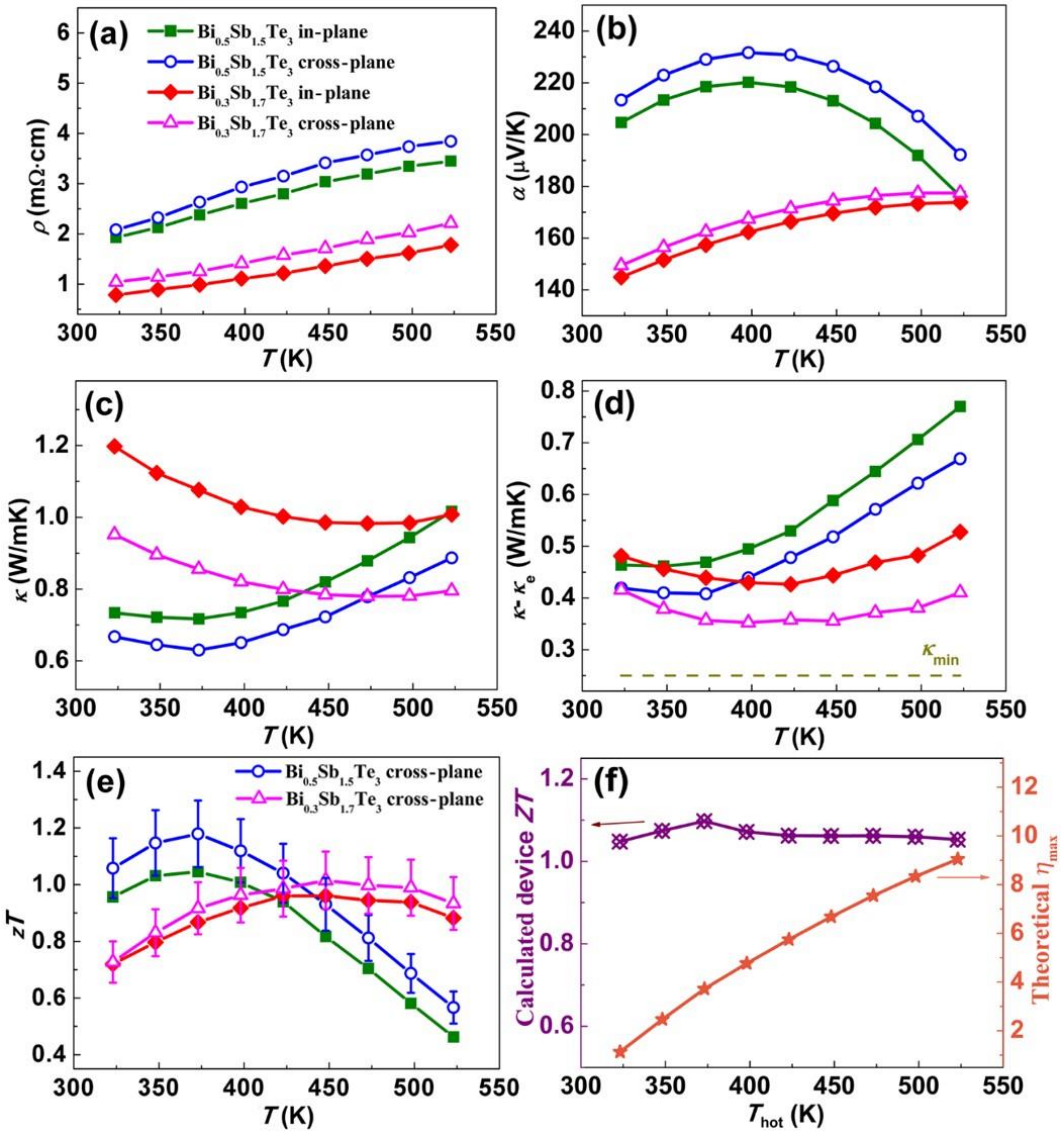

Figure 3.7. Temperature dependence of A) resistivity, B) Seebeck coefficient, C) total and D) lattice thermal conductivity, (e) *zT* values in both in-plane and cross-plane directions. All data in A)-E) are measured values without the correction of EMT. F) Calculated device *ZT* and calculated theoretical maximum efficiency of segmented $Bi_{0.5}Sb_{1.5}Te_3$ and $Bi_{0.3}Sb_{1.7}Te_3$ in cross-plane direction, with a cold side temperature fixed at 300 K.

3.4. Summary and Conclusions

By engineering the overall microstructure of $(Bi,Sb)_2Te_3$ via melt-centrifugation, low κ_l and high zT values are achieved despite large material porosity. The melt-centrifugation process removes the liquid eutectic, resulting in an electrically conductive well-fused grain framework with requisite microscale dislocation arrays and distributed porosity. It was shown how reduction in the κ_l due to the absence of conducting material does not increase zT, as this will reduce the electrical conductivity by the same amount from effective medium considerations. Although, the reduction in electrical conductivity is attributed to the absence of conduction medium, while the reduction in thermal conductivity cannot be fully explained by classical EMT considerations alone. Through Debye-Callaway and EMT modeling, it was determined that the reduction of κ_l stems from both the lack of thermal conduction medium at the pore sites and the scattering of phonons at pore surfaces/interfaces and grain boundaries through the dislocation strain fields. In addition, electron microscopy, primarily through nano and microscale TEM techniques, proved to be a key tool to link the thermal model with the actual material parameters present in the material such as pore and dislocation density. However, it was shown that there were some limitations (and potential inaccuracies) that can occur because of using nanoscale characterization tools to obtain material parameters such as dislocation densities. This emphasizes the need for additional tools to help measure the overall density or distribution of defects within bulk samples more accurately. In total, melt-centrifugation proved to be useful in introducing a variety of microstructures into BST. Despite this experiment's success in validating the importance of specific structures, such as dislocations, the kinetic nature of melt-centrifugation leads to the need to establish a synthesis

techniques that may be able to create a similar microstructure with improved control and repeatability.

Chapter 4. Equilibrium Synthesis of Bismuth Antimony Telluride via Induction Hot Pressing and Thermal Annealing

Chapter 3 was an exploration of how melt-centrifugation was able to improve zT by introducing a variety of defects into $Bi_{0.5}Sb_{1.5}Te_{3+x}$ (BST). Unfortunately, melt-centrifugation is highly kinetic and therefore it is desirable to establish an equilibrium processing technique to create porous BST samples with similar microstructural features and thermoelectric performance as melt-centrifuged materials. This chapter investigates the improvement in performance of induction hot pressed BST (with excess Te) in conjunction with increasing porosity, which typically results in either no net gain or even a decrease in overall thermoelectric energy conversion efficiency due to the lack of conduction medium. It was found that porosity can be controlled based on the time and temperature used to anneal samples, and by introducing a variety of electron microscopy techniques the root causes of property enhancement were identified in the porous BST samples. Characterization was performed by using conventional Scanning/Transmission Electron Microscopy (S/TEM) techniques such as Scanning Transmission Electron Microscopy-High Angle Annular Dark Field (STEM-HAADF) and Energy Dispersive Spectroscopy (STEM-EDS), Transmission Electron Microscopy-Bright Field (TEM-BF), and Select Area Electron Diffraction (SAED) to identify nanoscale and microscale defects in both as-pressed and thermally annealed BST samples. These techniques, although useful for identifying defects, suffer from small fields-of-view. Therefore, this chapter emphasizes how EBSD was incorporated to document the prevalence of defects by providing statistically significant measurements of defect populations, obtaining measurements such as the average grain size, the degree of texturing, and the twin

boundary ratio. Portions of this chapter were previously published in *J. Materiomics.* 2020, **6**(3), 532-544 and are reproduced (adapted) with permission from Copyright © 2020 Elsevier.

4.1 Recent Advances in Processing and Performance in Bismuth Antimony Telluride Alloys

4.1.1. Innovations in Processing of Bismuth Antimony Telluride

4.1.1.1. Benefits of Grain Boundaries and Dislocations in Reducing Lattice Thermal Conductivity

In the previous chapter, it was shown how a variety of defects across varying length scales contributed to a decrease in lattice thermal conductivity. However, because BST is a low temperature thermoelectric, historically, two defects have been of particular interest to scientists attempting to decreasing the lattice thermal conductivity (κ_l): grain boundaries and dislocations. The reason for this is that at low temperatures, a larger percentage of phonons traversing through a material will consist of low frequency phonons. As the Debye-Callaway Model illustrated in Chapter 3, different structural defects provide different contributions to the total relaxation time (τ_{tot}) which is linearly related to the lattice thermal conductivity:

$$\tau_{tot}(\omega)^{-1} = \tau_{Umklapp}(\omega)^{-1} + \tau_{PD}(\omega)^{-1} + \tau_{GB}(\omega)^{-1} + \tau_{DC}(\omega)^{-1} + \tau_{DS}(\omega)^{-1} + \cdots \quad (4.1)$$

$$\kappa_l = \frac{1}{3}\int_0^{\omega_{max}} C_s(\omega)\, v(\omega)^2 \tau_{tot}(\omega) d\omega \quad (4.2)$$

By taking note of the frequency dependence of each structural defect, it can be seen how different defects scatter specific phonons more effectively than others. For example, the contribution to the relaxation time from boundaries is a frequency independent term. However, because the spectral heat capacity ($C_s(\omega)$) approaches a ω^2 dependence at high temperatures, the contributions of boundaries to the lattice thermal conductivity are approximated as having a ω^2 dependence.[25,26]

$$\tau_B = \frac{d}{v_g} \tag{4.3}$$

$$C_{S,High\ Temp}(\omega) = \frac{3k_B\omega^2}{2\pi^2 v_g v_p^2} \tag{4.4}$$

This means that the smallest contributions to κ_{lat} will come from lower frequency phonons, making grain boundaries more effective at scattering phonons in low temperature regimes. Therefore, when working with room temperature thermoelectric systems, like BST, grain boundaries will be beneficial defects to incorporate to suppress lattice thermal conductivity.

Similarly, dislocation cores and strain both contribute to the relaxation time of phonons. Dislocation cores have a relaxation time that is proportional to ω^{-3}, while dislocation strain fields have a relaxation time that is proportional to ω^{-1}. As a result, when accounting for the ω^2 dependence of the spectral heat capacity, contributions to the lattice thermal conductivity will then have ω^{-1} and ω frequency dependencies due to the inclusion of dislocation cores and dislocation strain fields respectively.[26] Because grain boundaries and point defects provide ω^2 and ω^{-2} dependencies to the lattice thermal conductivity (respectively), it can be seen that dislocations are important for scattering phonons at the intermediate frequency regime.[25,26] Therefore, it is understood that including dislocations into BST can help improve performance by scattering intermediate length phonons.

Because the Debye-Callaway model indicates that boundaries and dislocations are the most effective defects at scattering phonons in the low temperature regime (the temperature regime of maximum thermoelectric efficiency for BST), these defects are often targeted for inclusion in BST because of their potential to further improve overall *zT*. The decrease in spectral thermal

conductivity due to the scattering of low and intermediate wavelength phonons by interfaces and dislocations can be seen in Figure 3.2b. These defects are included into thermoelectric materials by modifying synthetic processes in a controlled manner so that the specific final microstructure can be achieved. Chapter 3 illustrated how one technique, melt-centrifugation, was used to modify the microstructure. Furthermore, it provided experimental confirmation that the lattice thermal conductivity was decreased drastically in melt-centrifuged samples which included dislocations and boundaries in addition to an increased porosity.

4.1.1.2. Developing Reproducible Processing Methods for Te-Rich $Bi_{0.5}Sb_{1.5}Te_3$

One of the most intriguing improvements of *p*-type $Bi_{0.5}Sb_{1.5}Te_3$ performance was reported by Kim *et al.* using liquid phase sintering of melt spun $Bi_{0.5}Sb_{1.5}Te_3$ incorporating molten Te-rich eutectic as the sintering aid (Te-MS).[46] Using this technique, a peak *zT* of 1.8 was reported along with an unprecedented thermoelectric cooling performance presumably due to the remarkably low lattice thermal conductivity of 0.35 W m^{-1} K^{-1} while still maintaining a very high electrical mobility. This excellent combination of thermal and electrical transport was attributed to dense dislocation arrays formed at grain boundaries during liquid phase sintering which effectively scattered phonons but not charge carriers.[26]

Efforts to reproduce these results have so far yielded mixed results. Zhang *et al.* produced BST by liquid phase sintering using solution derived nanoparticles and reported *zT* values of ~1.6, seemingly confirming the original Te-MS results.[140] The claim of reproduction should be evaluated with caution, as the samples were all less than 90% of the theoretical density. An attempt at direct reproduction by Deng *et al.* only realized a peak *zT* of 1.2 with a lattice thermal conductivity of

0.65 W m^{-1} K^{-1}.[141] They reported a correlation between *zT* and the amount of liquid Te initially present during sintering. This also correlated with the degree of alignment of the anisotropic grains of BST, and Te was hypothesized to act as a lubricant allowing translation of grains. Kim *et al.* reported a *zT* of 1.4 using liquid phase sintering of BST.[142] They too found that the liquid phase enhanced preferential alignment during pressing.

Although the successfully processed BST samples described above are not fully dense, the introduction of pores is not expected to be able to produce a material having a larger *zT* than the host matrix.[115] Instead, introducing pores into a solid matrix increases the path length that heat and charge must traverse which results in a decrease in both electrical and thermal conductivity. In a classical (length scales greater than the mean free path of electrons and phonons), isotropic solid matrix with non-conducting pores, the change in the two conductivities due to porosity should be identical, resulting in no change in *zT*.[143] In reality, pores allow some heat transfer via radiation between surfaces and gas phase convection. Therefore, the electrical conductivity should decrease slightly more than thermal conductivity resulting in an overall loss of *zT* with porosity. A more complicated treatment which considered scattering of electrons and phonons by pores in SiGe also found that porosity should be detrimental to *zT* due to the more severe loss of charge carrier mobility.[144] Despite the expectation of performance reduction due to porosity, porous bismuth telluride alloys have, at times, demonstrated enhanced *zT* over their fully dense counterparts.[145–150] A common explanation given for the improvement in these reports is that scattering was enhanced due to pore distribution being on the same length scale as the mean free path of heat carrying phonons but much greater than that of electrons. First principles calculations predict that most of the heat in bismuth telluride is carried by phonons with mean free paths under 10 nm,

while that of electrons is 100 nm.[151,152] Nevertheless, *zT* improvement with porosity has been observed by Pan *et al.* in BST samples having grains and pores with sizes over 1 μm.[148] This hints at the fact that there may be other factors at play during pore formation that contribute to a decrease in lattice thermal conductivity.

The inconsistency in the ability of various groups to reproduce the Te-MS results suggests that either the mechanism of *zT* improvement is not well characterized, or that the critical aspects of fabrication are not well described. Liquid phase sintering induces rapid changes in the microstructure due to the solubility of the solid BST phase within the liquid.[153] Hot pressing times as short as three minutes are reported[46], which is of the same order as the amount of time required to heat the pressing die and significantly less than the time required to cool it. Beyond the typically reported processing values of pressing temperature, pressure, and time, variables such as heating rate, time of pressure application and release, cooling rate, etc. could play a crucial role in determining the final microstructure of the produced BST samples. While much of the excess Te phase is expelled during the liquid phase sintering process, certainly some remains and its location and its effects on transport are unclear.

4.1.2. Equilibrium Hot Pressing: Synthesis and Transport Measurements

4.1.2.1. Synthesis of Te-Rich $Bi_{0.5}Sb_{1.5}Te_3$

The aim in this report is to explore some of these outstanding questions regarding the role of dislocations, and pores, as well as the role and location of excess Te in BST. This chapter presents a reproducible method of fabricating BST with slight excess Te (+3.8 wt. %) having porosities up to ~25%. This sample production method differs from past studies in that the initial

sintering occurs below the eutectic temperature and over a longer period of time. This greatly reduces the initial sample-to-sample variation and allows for better processing control. Furthermore, since Te is not expelled during processing, the amount of excess Te in the sample is known and consistent. Thermoelectric transport is measured in these porous samples parallel to the pressing direction, finding an enhancement in *B* as high as 45% (parallel to the pressing direction) between as-pressed, fully dense BST and a sample having ~20% porosity. To gain insight into this performance enhancement, microstructural changes that occur during the fabrication of porous samples and their relationship to transport are investigated.

Elemental Bi, Sb, and Te (99.999% 5N Plus) and Pb (Alfa Aesar 99.999%) were sealed in fused quartz ampules evacuated to $5*10^{-5}$ Torr. Lead at a concentration of 0.1 at% was added as an acceptor dopant to ensure extrinsic behavior for clear evaluation of the lattice thermal conductivity. Elements were heated to 800°C to melt and react and subsequently water quenched. Resulting ingots were annealed for 24 hours at 500°C and allowed to furnace cool to aid homogenization. Annealed ingots were powdered using high energy ball milling in stainless steel cannisters sealed in an argon environment. Powders were stored in an argon atmosphere until pressing. Pellets were made by inductive hot pressing[35] 10 g of powder in a ½" graphite die at 400°C under a pressure of 45 MPa for 30 minutes. This pressing temperature is below the melting point of the Te-rich eutectic at 425°C meaning these samples are not liquid phase sintered and the excess Te remains present. Pressure was applied once the die had reached 300°C. During cooling, the pressure was relieved through slow decay by thermal contraction of the sample and press. The density of the pellets before pressing and after swelling was determined using the Archimedes method by measuring the mass in air and in pure ethanol. The Archimedes method can provide

accurate density measurements for irregularly shaped samples but is susceptible to errors if liquid infiltrates the solid during measurement. During the swelling anneal, the outer surface of the pellet became smooth and shiny and thus no liquid entered the pellet during Archimedes measurement. The accuracy of the measurement was verified by geometric measurement of the density. The densities of all as pressed samples exceed 99% of the theoretical values, 6.82 g cm^{-3} for $Bi_{0.5}Sb_{1.5}Te_{3.2}$ and 6.84 g cm^{-3} for $Bi_{0.5}Sb_{1.5}Te_3$. Annealing at temperatures between 250-350°C were used to induce swelling and the porosity of the pellets was found to increase reproducibly with annealing temperature and time. To create porous samples, the as-pressed pellets were sealed atop graphite foil and a small amount of glass wool within an evacuated fused quartz tube of large enough diameter so as not to impede expansion. Pellet annealing was performed in a vertical tube furnace by heating at 100°C h^{-1} to the target temperature and holding for the specified time followed by furnace cooling. Samples were cut from each pellet perpendicular and parallel to the pressing direction for measurements and ground to a thickness of ~1 mm using 600 grit SiC paper.

4.1.2.2. Measuring Thermoelectric Material Properties

Seebeck measurements were performed under vacuum using a home-built uniaxial 4-point system.[127] The Seebeck coefficient was evaluated using the linear slope of the voltage versus temperature difference data collected with a maximum temperature difference of ±12°C. The Hall coefficient and electrical conductivity were measured under vacuum in a home built system using the van der Pauw method and a magnetic field strength of 2T.[126] Thermal diffusivity was measured using a Netzch LFA 457 with continuous argon purge. Thermal conductivity was calculated as the product of heat capacity, thermal diffusivity, and density. The temperature dependent heat capacity reported by Shtern *et al.* for BST was used.[154] Density was measured by the Archimedes method

in pure ethanol. The density was verified geometrically to ensure any fluid infiltration into the sample did not cause overestimation during Archimedes measurement. Both density values agreed to within 2% for all samples.

4.1.2.3. Deviations of Material Properties from Effective Medium Theory

Presented in **Figure 4.1** are the data for representative samples showing the variation of thermoelectric transport values with temperature, measured both parallel and perpendicular to the original pressing axis of the pellet. Tellurium excess suppresses the hole concentration in BST, shifting the influence of bipolar effects towards lower temperatures.[155] In all samples, the carrier concentration was intentionally biased above an optimal level for 300 K *zT* by extrinsic doping with Pb. This was done to allow for more accurate determination of lattice thermal conductivity and weighted mobility at 300 K, as bipolar effects should be small. The amount of Pb added to each ingot was small and some sample-to-sample variation in carrier concentration occurred. This is evident in the Seebeck curves of Figure 4.1a. The 90.5% dense sample had a slightly lower Hall hole concentration when corrected for porosity ($1.78*10^{19}$ cm^{-3}) than the other samples in this figure ($2.25*10^{19}$ and $2.24*10^{19}$ cm^{-3} for the 99.4 and 81.0% dense samples, respectively) resulting in its larger Seebeck at 300 K and lower peak Seebeck temperature. All samples behave as degenerate semiconductors near room temperature as evidenced by the increasing Seebeck coefficient, linearly increasing resistivity, and decreasing thermal conductivity (Figure 4.1a-c). The peak *zT* of these samples occurs slightly above 350 K (Figure 4.1d) and decreases with further increasing temperature due to the onset of bipolar thermal conductivity.

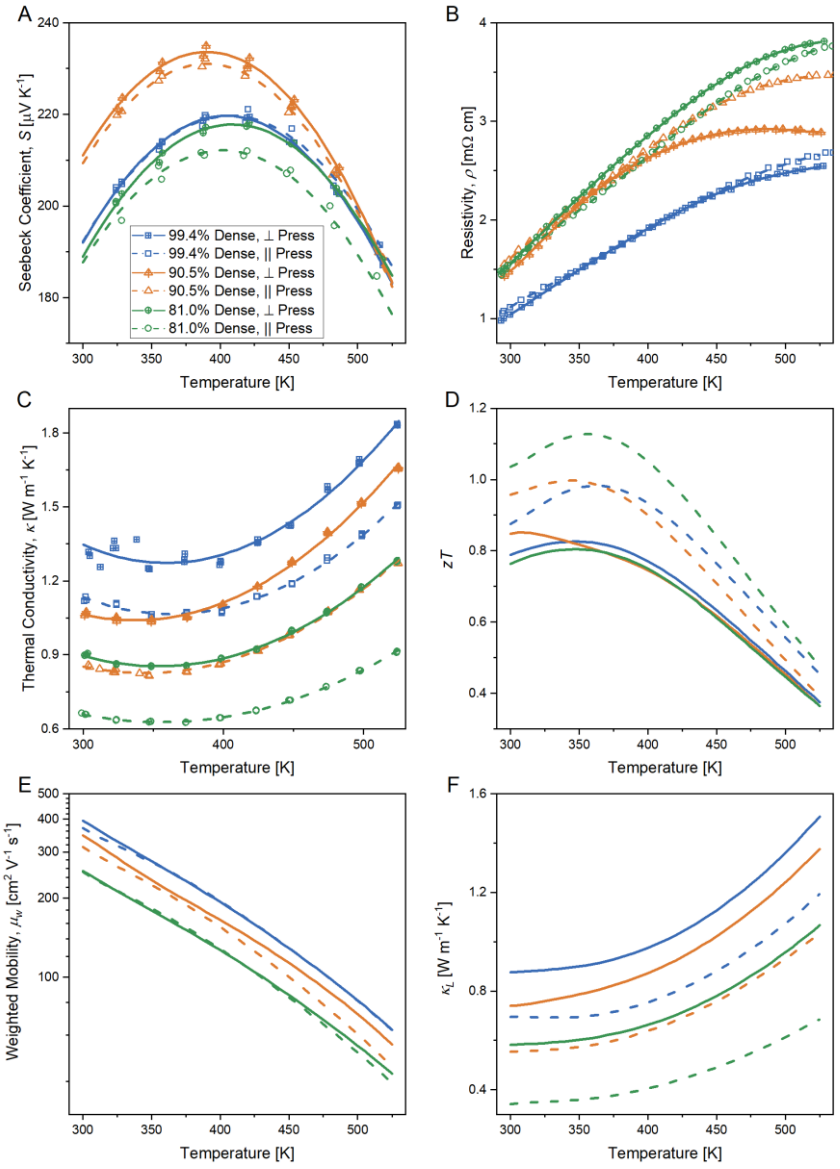

Figure 4.1. The variation of thermoelectric transport properties with temperature of select samples. Variations in Seebeck coefficient A) are attributable to carrier concentration differences. The increasing electrical resistivity B) and decreasing thermal conductivity C) near 300 K shows the material behaving like a degenerately doped semiconductor without bipolar contributions. The observed increase in *zT* D) is due to the swelling of the sample. This increase occurs because while the weighted mobility E) decreases with porosity, the lattice thermal conductivity F) decreases comparatively more.

Using an effective mass model[156], the weighted mobility, μ_w, and lattice thermal conductivity, κ_l, can be utilized for the comparison of samples which may have different carrier concentrations. The electrochemical potential, η, is evaluated from the Seebeck coefficient, *S*. The weighted mobility can be evaluated using this chemical potential and the measurement of electrical conductivity, σ. The Lorenz number can also be evaluated using η.

$$S = \frac{k_B}{e}\left(\frac{2F_1}{F_0} - \eta\right) \tag{4.5}$$

$$\sigma = \frac{8\pi e}{3}\left(\frac{2m_e k_B T}{h^2}\right)^{3/2} \mu_w F_0 \tag{4.6}$$

$$L = \frac{k_B^2}{e^2}\frac{3F_0F_2 - 4F_1^2}{F_0^2} \tag{4.7}$$

Where F_j indicates a Fermi integral of order j.

$$F_j(\eta) = \int_0^\infty \frac{\varepsilon^j \mathrm{d}\varepsilon}{1+\exp[\varepsilon-\eta]} \tag{4.8}$$

The weighted mobility and lattice thermal conductivity variation with temperature are shown in Figure 4.1e and 4.1f. The effect of porosity is clear. In both measurement directions, both the weighted mobility and lattice thermal conductivity decrease with increasing porosity over the entire temperature range. The impact of porosity on lattice thermal conductivity appears stronger in the direction parallel to the pressing axis and this is the primary cause of the observed *zT* enhancement for the 81% dense sample.

Shown in **Figure 4.2a** and 4.2b are weighted mobility and lattice thermal conductivity evaluated at 300 K for all samples. While there is some noise in the results, the decreasing trends

with porosity are evident. The decrease of these two parameters counter each other in their impact on *zT*. As discussed in Chapter 3, the thermoelectric quality factor, *B*, correlates with *zT* and can be used to determine if the increase in porosity is beneficial without requiring carrier concentration optimization. The *B* values for the samples in this study are shown in Figure 4.2c.

$$B = \left(\frac{k_B}{e}\right)^2 \frac{8\pi e(2m_e k_B)^{3/2}}{h^3} \frac{\mu_w T^{5/2}}{\kappa_L} = 4.33 \cdot 10^{-10} \frac{\mu_w T^{5/2}}{\kappa_L} \tag{4.9}$$

The improvement in *B* with increased porosity arises due to the swelling process and not the anneal itself. Three nominally $Bi_{0.5}Sb_{1.5}Te_3$ (no excess Te) pellets were annealed at 300°C for 24 hours. These pellets were >98.7% of the theoretical density after annealing, and they all showed a decrease in quality factor relative to the unannealed pellet. This loss in performance seems primarily attributable to a decrease in weighted mobility, falling from 384/429 $cm^2V^{-1}s^{-1}$ (as measured parallel/normal to the pressing direction) to 307/324 $cm^2V^{-1}s^{-1}$. Annealing in the presence of excess Te where swelling does not occur also fails to significantly improve *zT*. Annealing zone melted BST ingots containing excess Te at 350°C for 48 hours was shown not produce any change in *zT*.[157]

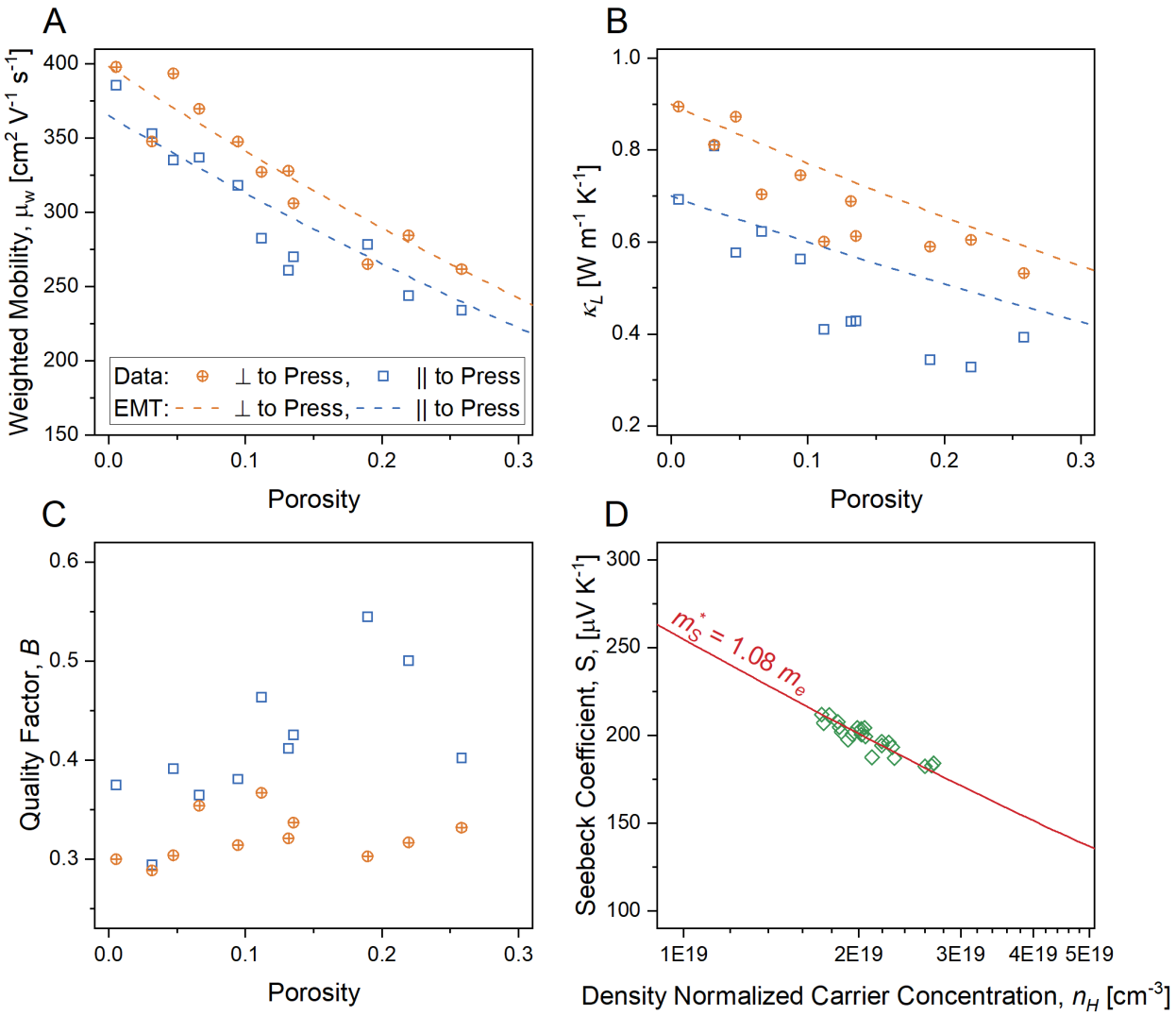

Figure 4.2. Effective mass modeling of transport at 300K allows for trends to be analyzed independent of doping levels. The weighted mobility A) and lattice thermal conductivity B) both decrease as expected with increasing porosity. The weighted mobility trends (dashed lines) are very close to those predicted by the Maxwell-Garnett effective medium theory (EMT), but the lattice thermal conductivity decreases much more than would be expected. This leads to an increase in the quality factor, *B*, C) which is particularly large in the direction parallel to pressing. When the Hall carrier concentration is normalized by the fractional density, the Pisarenko plot D) finds they are all well fit by a Seebeck mass of 1.08 m_e suggesting no change in electronic structure or scattering mechanism with porosity.

The porous samples produced for this report are multiphase (BST, Te-rich phase, and pores) and thus complicates modeling. In BST with added dopant, the primary doping native defects are single acceptor Bi_{Te} and Sb_{Te} anti-sites.[158–161] In Te-rich BST, the concentrations of these defects are reduced along with the hole concentration. Excess Te has been used to tune the carrier concentrations in BST to optimum values.[133] The presence of excess Te ensures that the BST composition remains on the Te-rich side of its phase width. Predictable native point defects allow for the carrier concentration to be accurately controlled by extrinsic doping. Beyond these carrier concentration effects, the presence of a small amount of excess Te is not expected to be detrimental to transport. It should be *p*-type and any circulating currents which could occur due to its presence should be negligible.[162] The Te-rich phase is excluded from the following analysis based on its small expected impact on transport and its constant presence in both the as-pressed and annealed phases (as will be discussed later).

One of the simplest effective medium theories (EMT) is the Maxwell-Garnett model which assumes a dilute dispersion of spherical second phase particles in a conducting matrix.[163] It should be noted that some of the assumptions behind the Maxwell-Garnett model are not valid in this system: pores are not spherical and dilute and transport is not isotropic in the matrix. Therefore, coincidental fitting by the EMT model unfortunately cannot be excluded, but it is still useful none-the-less to understand the property trends that this theory predicts.[143] This model can be used to predict both the electrical and thermal conductivity variation with porosity. If the pore phase is assumed to be non-conducting, the effective conductivities of the porous material can be predicted by

$$\sigma_{eff} = \sigma_{matrix} \frac{2-2\varphi}{2+\varphi} \tag{4.10}$$

$$\kappa_{eff} = \kappa_{matrix} \frac{2-2\varphi}{2+\varphi} \tag{4.11}$$

As the electrical and thermal conductivities of the BST phase far exceed those of the pores, the Seebeck coefficient should not vary with porosity.[164,165] The ratio of effective conductivities is the same as their fully dense counterparts, thus the EMT model would predict porosity to have no effect on overall *zT*. Figure 4.2c shows increasing *B* with porosity illustrating that this is not the case in these experimental samples. In Figures 4.2a and 4.2b are an attempt to provide some insight into the origins of the deviation of the experimental material's behavior from ideal EMT behavior by plotting experimental data alongside the Maxwell-Garnett EMT model (represented by the dashed lines). This model makes a reasonable estimate of variation in weighted mobility with porosity, but it overestimates the lattice thermal conductivity. Because the pores should provide no net effect, the low lattice thermal conductivity of the porous material suggests that the lattice thermal conductivity of the BST matrix phase is being changed (κ_{matrix} decreasing) during the swelling process and this change is responsible for the increase in *zT*. The weighted mobility matching the expectation along with all samples being fit with the expected Seebeck mass of 1.08 m_e in a Pisarenko plot (Figure 4.2d) indicates that the electronic structure and carrier scattering of the BST matrix may be unchanged during swelling.[133] To document whether the microstructure of the material is changing during swelling, electron microscopy was employed across multiple length-scales to document the material structure and composition at different stages of the annealing process.

4.2. Methods to Investigate Microstructure using Electron Microscopy

4.2.1. Nano and Microscale Characterization Methods

Scanning/Transmission Electron Microscopy (S/TEM) techniques were described in Chapters 2 and 3 as they relate to studying nanoprecipitates in lead chalcogenides, and qualitatively identifying dislocations and pores in BST. This chapter will show how Scanning Electron Microscopy (SEM), in particular Electron Backscattered Diffraction (EBSD), can be used in conjunction with high resolution electron microscopy techniques to reveal information about materials that cannot be obtained with high resolution electron microscopy techniques alone. In addition to large field-of-view SEM techniques, TEM-BF was used for the identification of structural defects, while STEM-HAADF and STEM-EDS were used for qualitative and semi-quantitative chemical analysis at the nano and microscale.

4.2.2. Mesoscale Characterization Methods

4.2.2.1. EBSD: Large-Scale Crystallographic Data Collection

Scanning Electron Microscopes (SEMs) complement high resolution studies of materials performed on S/TEMs. Although SEMs and S/TEMs can provide similar types of analysis (due to the same types of electron-sample interactions), SEMs analyze bulk samples on a much larger length scale. Due to the large interaction volumes of electrons within the bulk samples and differences in magnification, resolution, and field-of-view, some techniques do vary between the two types of instruments. A particularly useful SEM technique used in this study was Electron Backscattered Diffraction. This technique uses diffracted backscattered electrons to collect electron backscattered diffraction patterns (EBSPs) at each point in a scan, and then construct maps

based on the electron diffraction information gained through scanning. One of the most common types of EBSD maps is the inverse pole figure orientation map. These maps are able to highlight different grains by assigning a color to a specific crystallographic orientation. These maps are useful in SEM because the wide field-of-view allows the collection of large maps from the micron to the millimeter scale (in what we denote as the mesoscale), while also providing a spatial resolution just under 100 nm (this value was specific to the instrument used in this investigation: a FEI Quanta 650 ESEM). This enables the identification of many grains and as well as allows scientists to gather statistically significant datasets concerning bulk material trends such as the average grain size of a sample. These types of measurements can be observed, but not statistically verified in TEM unless the grain size is on the nanometer scale which is not true for many thermoelectric materials.

However, EBSD is not used for grain size analysis alone. Because patterns and data can be stored, other useful mesoscale measurements include phase distributions, grain boundary angle distributions, and texture analysis. Again, these types of measurements are able to be performed using EBSD because of the SEM's unique combination of resolution and field-of-view. However, it should be noted that EBSD is a very sensitive technique to polishing and surface quality. Scratches and surface deformation can result in errors in pixel indexing and this can change the results of these mesoscale measurements. If maps are being used to observe qualitative material parameters, this may not be a significant issue, but in some cases, especially when extracting quantifiable data, it is important to understand what data is being collected, and how pattern quality and pixel indexing can affect the final results of mesoscale measurements.

4.2.2.2. Proper Post-Processing of EBSD

To illustrate the importance of proper data processing, the steps to calculate the percentage of twin boundaries in a sample is discussed below. This measurement was chosen to demonstrate the importance of correctly post-processing data because of the dramatic effect that post-processing has on twin boundary ratio results, and because of the relevance of twin boundaries in understanding thermoelectric performance (as will be revealed later in this chapter). For this specific study, data from EBSD was processed using Tango, a subset of the CHANNEL 5 software suit from Oxford Instruments. Using this software package, 60° tilt boundaries about the [0001] crystallographic axis were highlighted, as this is the structure of the only twin boundary in the BST crystal system (space group 166). The twin boundary percentage is calculated by dividing the length of twin boundary lines highlighted, by the total length of grain boundaries detected in EBSD. Unfortunately, this calculated ratio can change for a given map as a result of cleaning (i.e. filling in unindexed pixels), which leads to uncertainty to what the true twin boundary percentage is. Because twin boundaries are very prevalent in this system, it was important to create a methodology to systematically clean data, in order to yield the most accurate measurement of this value.

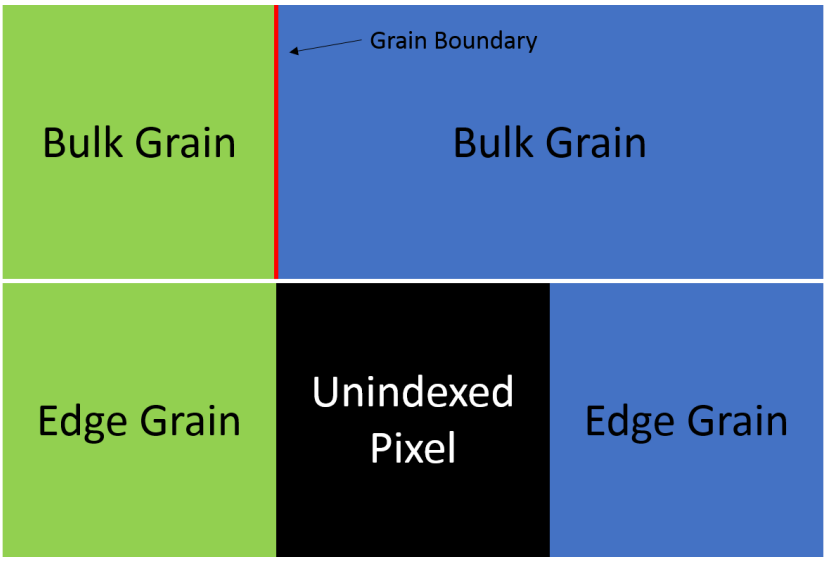

Figure 4.3. Two 2D pixel arrays illustrating how the software determines the presence of grain boundaries. (Top) Three pixels that are indexed as bulk grains with a grain boundary in between them. (Bottom) The absence of a middle pixel results in no grain boundary being detected and the formerly bulk grains being labeled as edge grains.

Boundaries are interpreted by the software as the interface between two adjacent pixels that have different orientations. However, if an unindexed pixel lies in between two pixels belonging to two separate grains, the two indexed pixels are considered edge grains, as if they lay on the edge of a pore or cavity (see **Figure 4.3**). If the EBSD scan is unable to index pixels that lie on grain boundaries, even if those boundaries are obvious to the human eye, the grains involved will be considered edge grains and no grain boundary will be identified by the software. This problem is amplified by the fact that pixels in the vicinity of twin boundaries are indexed at high rates, whereas pixels in the vicinity of arbitrary high angle boundaries are indexed far less often. This leads to a decrease in the calculated total grain boundary length, which is mostly due to a lack of high angle grain boundaries being recorded. The lack of documented high angle boundaries

coupled with twin boundaries being identified at much higher frequencies, yields artificially inflated twin boundary ratios of upwards of 42%.

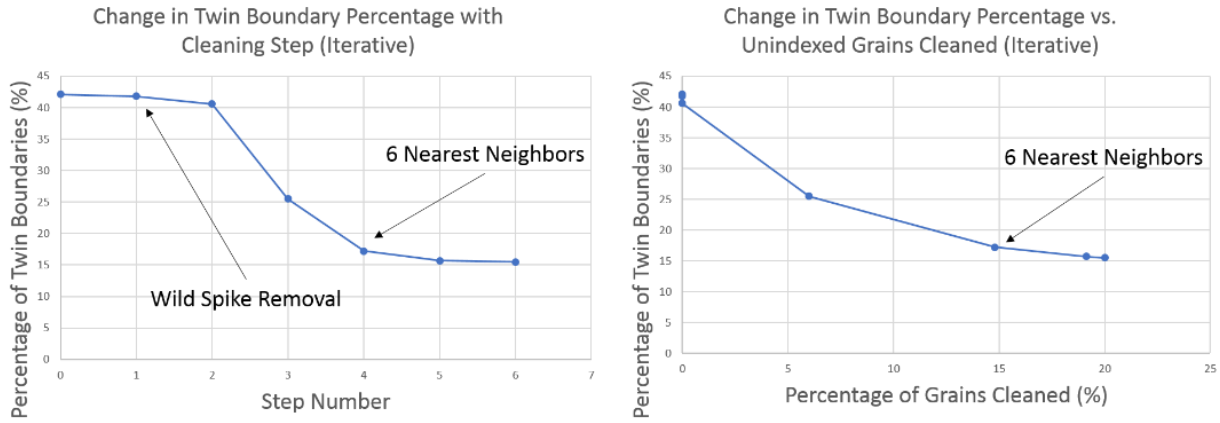

Figure 4.4. Plots illustrating the twin boundary percentage approaching a lower limit as all of the unindexed pixels are filled in. A cleaning regiment is selected for each EBSD map in which the lower limit is approached sufficiently, while filling in as few pixels as possible. This will prevent us from artificially filling in true voids and only fill in the areas that are truly unindexed grain boundaries.

The solution to this problem is to clean the EBSD data by filling in unindexed pixels. The Tango program from Oxford Instrument's CHANNEL 5 software suite can be used for this step as well. It is not as critical which grain the unindexed pixels are assigned to, because as long as the unindexed pixel is filled, a unit length of grain boundary will be recorded, turning edge grains into neighboring grains. This will increase the total boundary length (by increasing primarily the length of high angle grain boundaries) and yield more accurate twin boundary ratios. As tempting as it may be to fill in all unindexed pixels, the trick is to fill in the pixels that are unindexed along known grain boundaries, without filling in areas that are known voids. In other words, one should be careful not to inadvertently "make up" data. Therefore, to prevent this type of "over-cleaning" a series of cleaning experiments was performed on a sample dataset in which the change in the

twin boundary ratio was plotted as a function of the percentage of pixels cleaned and as a function of the number of iterative cleaning steps (see **Figure 4.4**).

The first cleaning step was to clean up wild spikes, or isolated mis-indexed pixels. This was followed by identifying unindexed pixels whose 8 nearest neighbors (NN) were the same orientation. These pixels were then given the orientation of their 8 neighbors, and the process was performed iteratively until no more grains could be indexed in this fashion. Then pixels that had 7 NN indexed were cleaned iteratively, then 6 NN, etc. until all pixels were filled. As can be seen there is a clear drop in the grain boundary ratio and then a leveling off as grain boundaries are cleaned indicating that a true value is approached as all pixels in the map are filled. However, we also see that the percentage of pixels that were filled in increased as less stringent filling parameters were used, indicating that the pixels filled in this way had less probability of being real data. This was evident by the fact that known voids in the sample were filled by the software. By comparing these graphs, there is a point where the twin boundary percentage has sufficiently approached its true limit, yet not all the unindexed pixels have been filled in. This is the point selected for this specific dataset to stop cleaning so as not to make up false data. Using the same dataset, maps extracted from raw and optimally cleaned data are shown in **Figure 4.5**. In Figure 4.5b, grain boundaries that were unindexed have been filled (they are no longer black unindexed pixels) yet large voids remain unfilled. This visually represents that unindexed pixels have been filled (allowing a more accurate count of total grain boundary length and twin boundary ratios to be achieved), while keeping the data as true to reality as possible. With proper post-processing techniques set in place, EBSD results can be interpreted accurately to reveal valuable insights about material microstructure on the micro- and mesoscale.

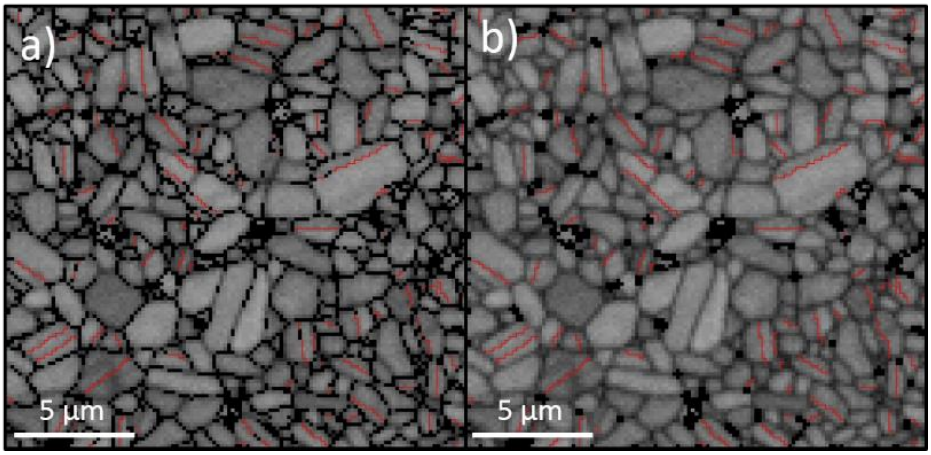

Figure 4.5. EBSD band contrast maps with twin boundaries highlighted in red. A) Raw map corresponding to the uncleaned dataset in Figure 4.4, and B) the same map with pixel cleaning (taken from data labeled 6 Nearest Neighbors in Figure 4.4). Black areas are unindexed pixels, so the change in the boundaries from black in A) to grey (or red) in B) indicates that those boundaries will now be counted in the total grain boundary area.

4.2.3. Sample Preparation and Instrumentation Setup

4.2.3.1. Preparing Samples for SEM and TEM Analysis

As-pressed and annealed BST samples were prepared for Scanning Electron Microscopy (SEM), specifically Electron Backscatter Diffraction (EBSD) analysis, by cold mounting them to prevent cracking and excessive surface deformation that could occur while grinding and polishing. Any deformation remaining from sample cutting was removed by manually grinding using 600, 800, and 1200 grit SiC grinding paper on a grinding wheel for 10 min each.[53] Samples were polished on a polishing pad with 1 µm and 0.1 µm diamond slurry for 30 and 45 min respectively. Final polishing was performed in a vibratory polisher using 0.1 µm diamond slurry for 3 hours at 150 V and 62.7 Hz.

EBSD was performed at 30 kV on a FEI Quanta 650 ESEM using an Oxford Instruments Nordlys II detector. To mitigate charging effects, EBSD was performed at 0.5 Torr in low vacuum mode. EBSD maps of a 200 x 200 μm^2 area were collected using a step size of 0.115 - 0.150 µm. Data from EBSD was processed using the CHANNEL 5 software suite from Oxford Instruments.

TEM samples were cut from the EBSD samples using a wire saw. Molybdenum grids were attached using M-Bond to the EBSD polished surface, and the sample thinned to ~50 µm using 600 and 800 grit SiC paper. The samples were then dimpled and ion milled at 4 kV with a top gun angle of 6° and a lower gun angle of -4° until a hole was formed, followed by milling at 2.8 kV at 4° and -2° for 1 hour, 1 kV at 4° and -2° for 1 hour, and 0.3 kV at 4° and -2° for 30 min. Bright Field Transmission Electron Microscopy (BF-TEM) was performed on a JEOL ARM300F GrandARM TEM at 300 kV, and Scanning Transmission Electron Microscopy-High Angle Annular Dark Field (STEM-HAADF) and Energy Dispersive Spectroscopy (STEM-EDS) were performed on a JEOL JEM-2100F TEM in STEM mode at 200 kV.

4.2.3.2 Post-Processing EBSD for Accurate Data Analysis

Tango was used to highlight 60° tilt boundaries about the [0001] crystallographic axis in red, as these correspond to crystallographic twins in the $R\bar{3}m$ system. To obtain accurate twin boundary percentages, isolated mis-indexed pixels and unindexed pixels were filled using the Tango software package. As discussed in Section 4.2.2.2, to clean the EBSD maps effectively, one must be careful to clean unindexed pixels in areas where the sample truly exists while minimizing the number of artificially filled pixels (indexing pixels in areas where voids exist). To achieve this

goal in this experiment, only unindexed pixels that had at least 5 of their 8 nearest neighbors defined were filled in.

4.3. Microstructural Evolution in Porous $Bi_{0.5}Sb_{1.5}Te_{3+x}$

4.3.1. Identification of Tellurium in As-Pressed and Annealed $Bi_{0.5}Sb_{1.5}Te_{3+x}$

Considering that the equilibrium synthesis process does not involve expelling excess Te, one of the first questions that must be address is the location and phase identity of excess Te. Characterizing the distribution of Te is difficult in BST samples where it is present in slight excess. Common large field of view and bulk scale detection techniques may not be able to detect phase segregation above the background of the 60 at.% BST matrix. The most prominent diffraction peak in Te occurs very near that of BST. If the Te is finely distributed at grain boundaries or heavily strained, the signal from Te may not be able to be resolved. Additionally, in SEM-EDS the interaction volume of the electron beam with the sample is on the order of microns, which is roughly the size of the grains in these samples. This means that the sampling volume of the electron beam may be too large to identify small areas of Te enrichment without also obtaining signal from the surrounding stoichiometric BST compound ($Bi_{0.5}Sb_{1.5}Te_3$). Due to the limitations in the spatial resolution of SEM-EDS, STEM-EDS was performed which reduces the interaction volume to approximately the size of the electron probe (which in this case was about 1 nm). Long exposure times generated maps with millions of counts that revealed the presence of specific grains that are Te-rich and deficient in Bi and Sb. It should be considered that the amount of Sb in these Te-rich grains could be misleading because of the proximity of Sb and Te characteristic X-ray peaks in EDS.

To determine the phase of the Te, the crystal structure must be known in addition to the composition. EDS maps were used to locate Te-rich grains (such as that shown in **Figure 4.6**) and Selected Area Electron Diffraction (SAED) was performed on the Te-rich grain in Figure 4.6 to obtain crystallographic information of this area of the sample. The electron diffraction pattern that was obtained reveals that the crystal structure is that of elemental Te (space group 152) rather than that of BST (space group 166). The electron diffraction in combination with the EDS data confirm that the Te-rich phase is elemental Te with potentially trace amounts of Sb and/or Bi impurities. The presence of Te grains accounts for a majority of the excess Te that remains in the system after pressing, however it should be noted that STEM-EDS was still not able to rule out slight grain boundary Te segregation.

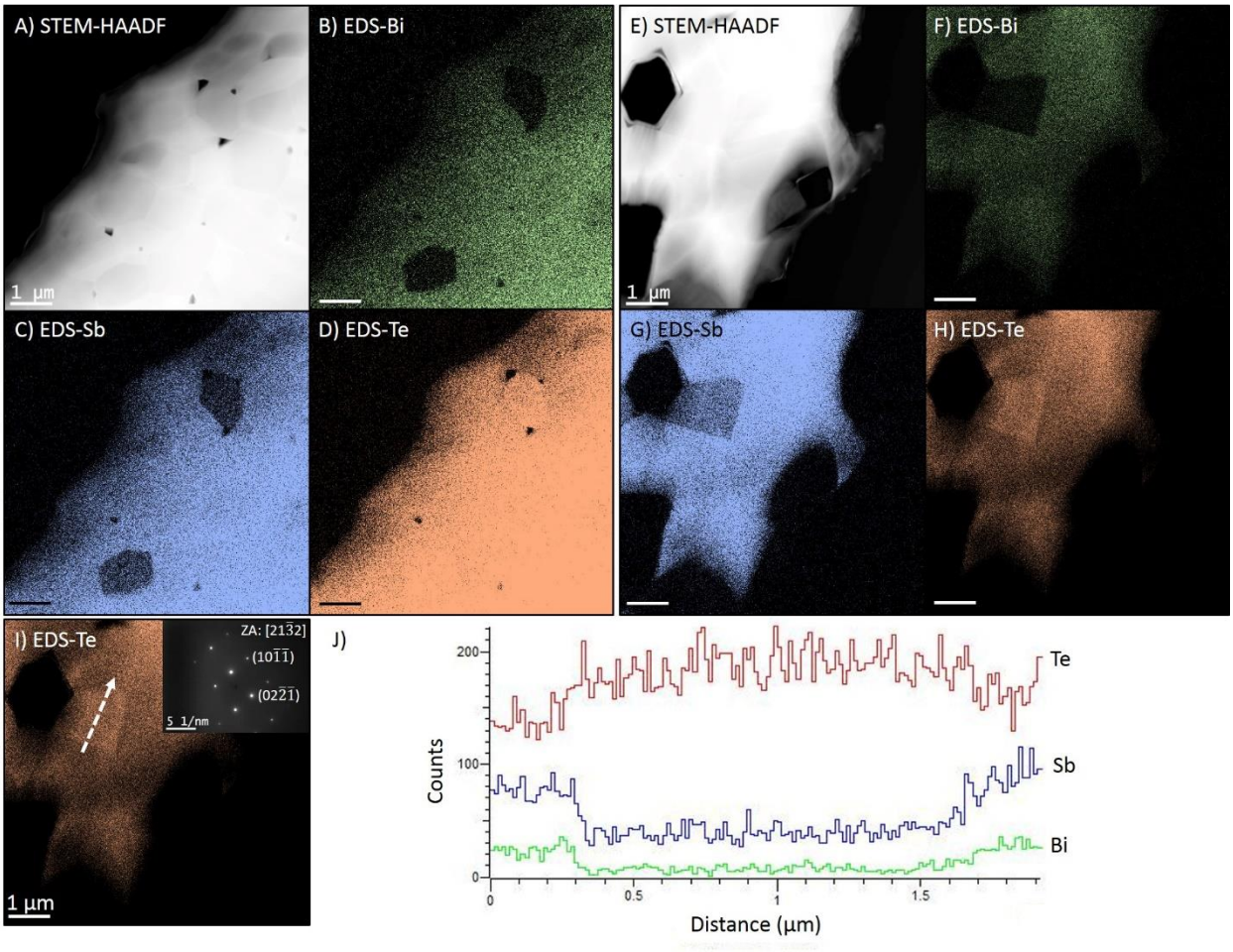

Figure 4.6. Image A) is a High Angle Annular Dark Field (HAADF) STEM image of an as-pressed, excess-Te BST sample with accompanying EDS maps of B) Bi, C) Sb, and D) Te. Likewise, E-H) are a STEM-HAADF image and its accompanying EDS maps for Bi, Sb, and Te (respectively) of an annealed, excess-Te BST sample. Image J) is the line-scan data extracted from the line-scan shown in image I), and the inset of image I) is an electron diffraction pattern from the Te-rich region, revealing a crystal structure consistent with that of elemental Te.

4.3.2. In-Grain and Grain Boundary Dislocations

As discussed earlier, dislocations have been theorized to be the cause of the very low lattice thermal conductivities observed in liquid phase sintered BST due to phonon scattering from their

strain fields.[26,46] However, the annealing process performed in this report should act to reduce the dislocation density of the final annealed material. BF-TEM analysis, as show in **Figure 4.7B**, shows intragranular dislocations (including a dislocation array in the vicinity of a grain boundary) in the as-pressed material. Such dislocations occur at a much lower density in the annealed samples. This makes sense, as extended anneals with very low deformation rates at elevated temperatures should mobilize dislocations allowing them to annihilate with each other, at boundaries, or at surfaces. Evidence of slip and dislocation annihilation at a surface is evidenced by the stepped features on the surfaces of pores as visible in Figure 4.7D. Beyond the effects of annealing, the presence of excess Te should inhibit the formation of immobile dislocation loops that have been observed in these materials.[166,167] A special type of dislocation should be noted, however. In this system, during the annealing process, some twin boundaries (such as those seen in Figure 4.7C) appear slightly modified by small steps. These steps are present to some degree in the as-pressed sample, but are observed more frequently in TEM in the annealed samples. Other studies have reported similar features in Bi_2Te_3 (which has the same crystal structure as BST).[168] There, the steps were found to be comprised of $\frac{1}{3}\langle 01\bar{1}0\rangle$ dislocations. This suggests that the twin boundaries, specifically, may be modified by dislocations during the annealing process.

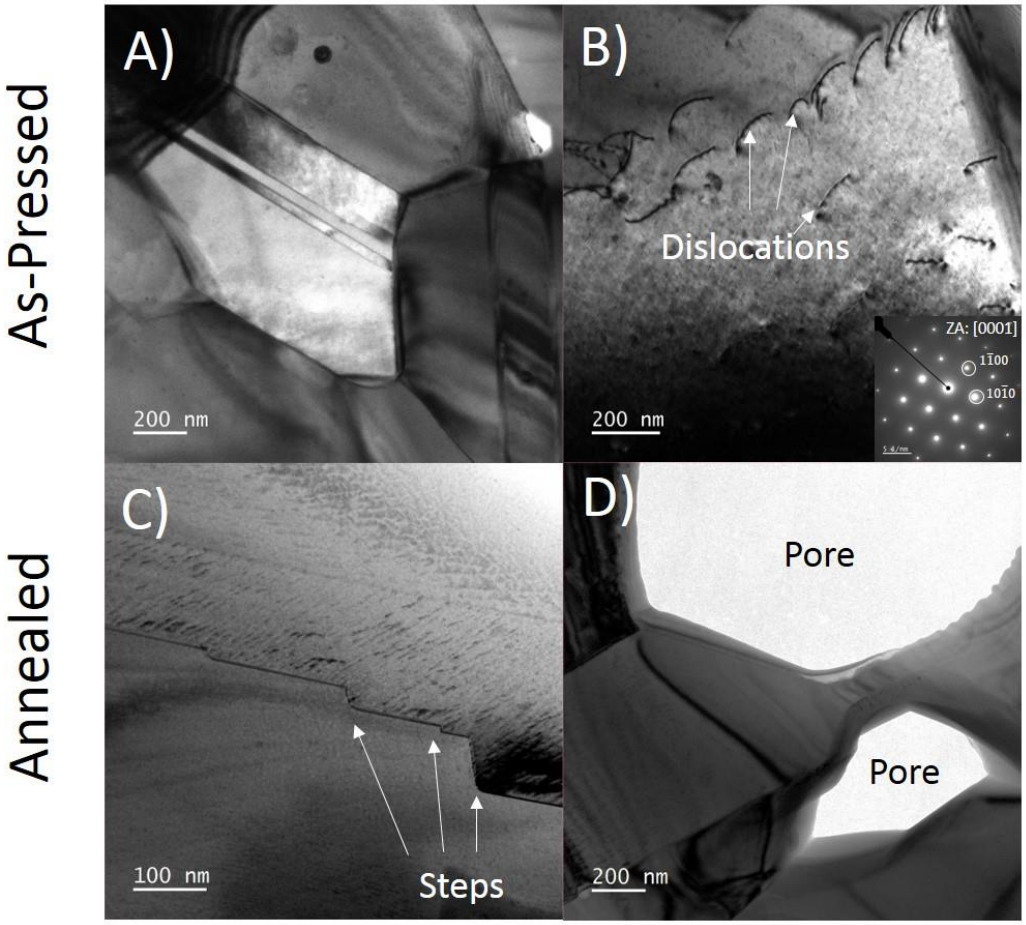

Figure 4.7. Bright Field TEM images from as-pressed (A, B) and annealed samples (C, D) shows differences in defect type and distributions. Both samples show a high density of twins, visible as perfectly straight boundaries often near other parallel twin boundaries. The twins in the as-pressed sample are straight and clean (A), while steps can be found in the twins of the annealed sample (C). In-grain dislocations can be imaged within some grains of the as-pressed sample (B) but are observed much less frequently in the annealed samples. Near pores (D), stepped surfaces can be seen indicating where slip has occurred during swelling.

4.3.3. Uniform Texturing Revealed by EBSD

Figure 4.8 shows EBSD maps and pole figures from an as-pressed sample and a porous sample that had been annealed at 350°C for 48 hours. The pole figures extracted from the EBSD data reveal preferential orientation of the [0001] axis of the grains along the pressing axis. Some degree of *c*-axis texturing is typical of pressed Bi_2Te_3-based materials, because of their anisotropic crystal structure, and is why it is necessary to specify the direction being characterized.[118] A common method of enhancing the performance of polycrystalline Bi_2Te_3 materials is texturing, or in other words, increasing the alignment of different grains along a desired crystallographic direction.[169–171] By increasing texture, performance enhancement in anisotropic materials will occur in one sample direction, while performance would decrease in other sample directions that coincide with crystallographic directions with less preferable properties. This behavior is not observed in the experimental BST materials, as fairly uniform properties perpendicular to the pressing direction are observed while performance is enhanced parallel to the pressing direction. This suggests that the *zT* improvement with swelling is not due to an increase of texturing. Furthermore, the EBSD data shows that the amount of texturing is comparable before and after annealing, as evidenced by the similar multiples of uniform density (MUD) values in our pole figures. The preferential orientation is important, however, as it may explain the anisotropy in swelling. On average, the strain during swelling was 67% larger in the direction parallel to pressing than normal. Texturing would create a nonrandom distribution in grain boundary misorientations.[171] This implies a preferential fracture during swelling at grain boundaries where one or both grains have their [0001] axis normal to the boundary plane.

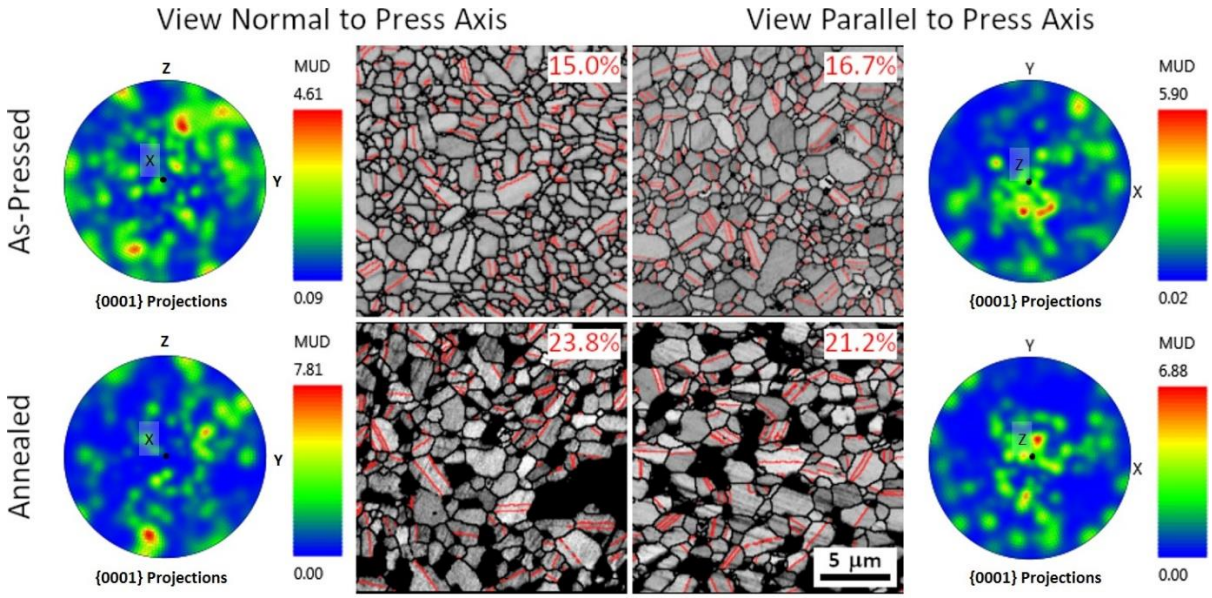

Figure 4.8. Band Contrast EBSD maps of as pressed and porous annealed samples reveals intergranular pores and grains of comparable size. The boundaries highlighted in red are twins formed by a 60° rotation about the [0001] axis (other boundaries in black), and the percentages in each image indicate the fraction of all grain boundaries in the map which are twins. The fraction of twin boundaries increases during the swelling process. Pole figures for the {0001} axis indicate preferential orientation of this crystallographic direction parallel to the pressing axis. (MUD = "multiples of uniform density").

4.3.4. Evolution of Twin Boundary Ratio Revealed using EBSD

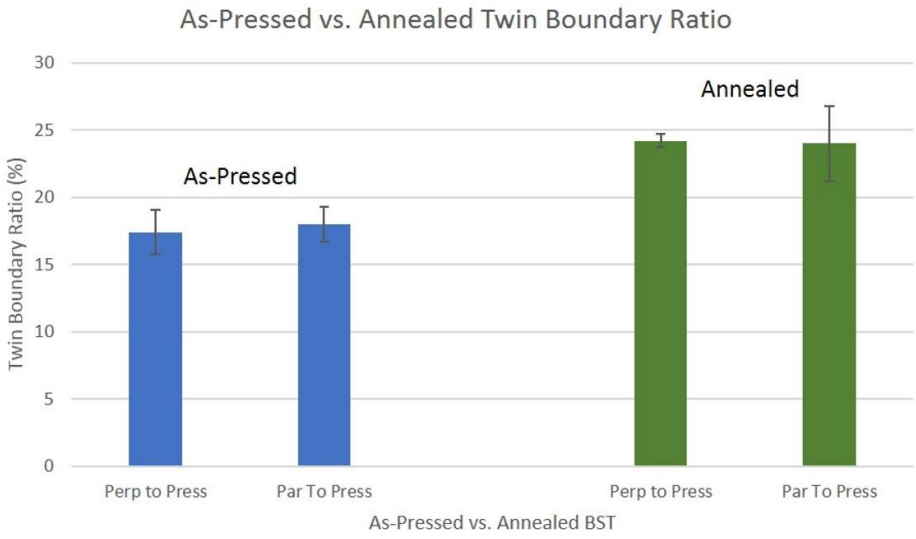

Figure 4.9. This graph shows the change in the ratio of twin boundary length to total boundary length (Twin Boundary Ratio) across all EBSD scans collected during this investigation. EBSD scans for annealed samples had roughly 400 grains per scan, while as-pressed samples had closer to 700 grains per scan, due to the fact that annealed samples also had larger grain sizes and porosity, but the map area remained 200x200 μm^2 for all scans. Multiple scans were collected for each of the 4 columns above, and approximately 4000 grains were analyzed in total for the collection of this dataset.

Investigation of nanoscale defects using BF-TEM reveals that twin boundaries can be modified during the annealing process; it is now of interest to understand the prevalence of twin boundaries in the BST system through the study of larger length scales. EBSD can provide both visual and quantitative tools to study the density of twin boundaries. In Figure 4.8, EBSD band contrast maps are color coded so that all boundaries lying between grains that are misoriented by 60° about the [0001] axis are highlighted in red. This is the grain misorientation required for

twinning in the 166-space group. This visual tool is aided by the fact that post-processing EBSD data allows the calculation of the percentage of grain boundaries that are twins. The results of these calculations are located in the upper right of each map. After processing multiple scans, encompassing thousands of grains, it was found that the twin boundary ratio rose during the annealing process an average of 6.4% across both the parallel and perpendicular directions. This is a 36% improvement over the initial twin boundary ratio in the as-pressed samples (**Figure 4.9**). This increase is not necessarily due to the nucleation of new twins, but instead can be attributed in part to the elimination of other boundaries during the swelling process. During annealing, the overall population of grain boundaries is expected to shift towards lower energy boundaries.[172,173] Twins have high site coincidence giving them particularly low boundary energy.[174,175] **Figure 4.10** illustrates that, as the material swells, higher energy grain boundaries are eliminated by pore growth (high angle boundaries become pore edges), while twins remain intact. This means that even if the number of twin boundaries does not change, the overall ratio of twins to total boundary length increases as pores grow. Total boundary length also decreases in part due to grain growth. Larger grains have less total grain boundary area and we calculate an increase in average grain size from the maps below: a change from 0.843 μm^2 to 1.03 μm^2.

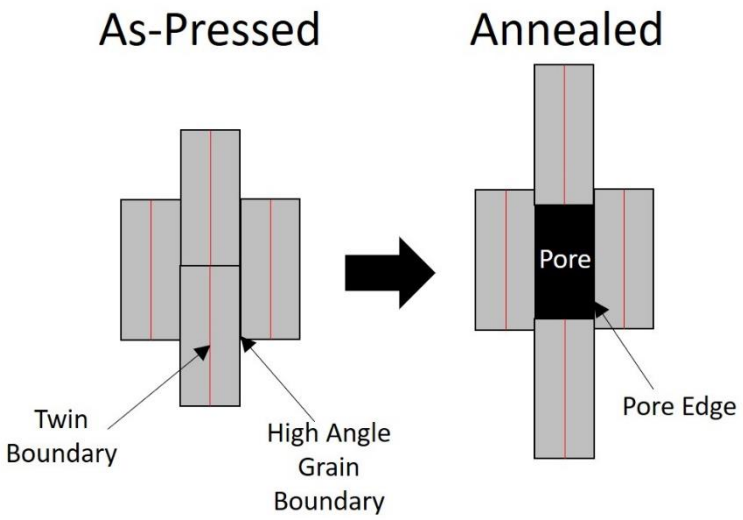

Figure 4.10. A schematic showing how the pore formation seen in Figure 4.8 decreases the length of high-angle grain boundaries in BST. As a result of the elimination of high energy high-angle grain boundaries (while low energy twin boundaries remain intact), the ratio of twin boundaries to total boundary length will increase.

4.4. Explaining Pore Formation and Property Enhancement

4.4.1. Introducing Trapped Gas Theory

In most materials, high temperature annealing of a polycrystalline material will result in densification, because eliminating the pore surfaces results in an overall decrease in energy.[176] Densification has been observed in BST when annealing cold pressed powder compacts.[177,178] Swelling, sometimes referred to as “foaming” or “bloating”, occurs when a material is heated enough such that the increased pressure of an entrapped gas is sufficient to plastically deform and expand the material. The pressurized gas could be introduced during processing, such as the argon environment used during hot pressing, or originate from the material itself generated either by

reaction or vapor pressure.[176,179–181] Swelling has been previously reported in bismuth telluride alloys [164,182–184] as well as other thermoelectrics such as PbTe alloys[185,186] and skutterudites.[181,187] It has also been implemented as a method to produce metal foams.[179,180,188]

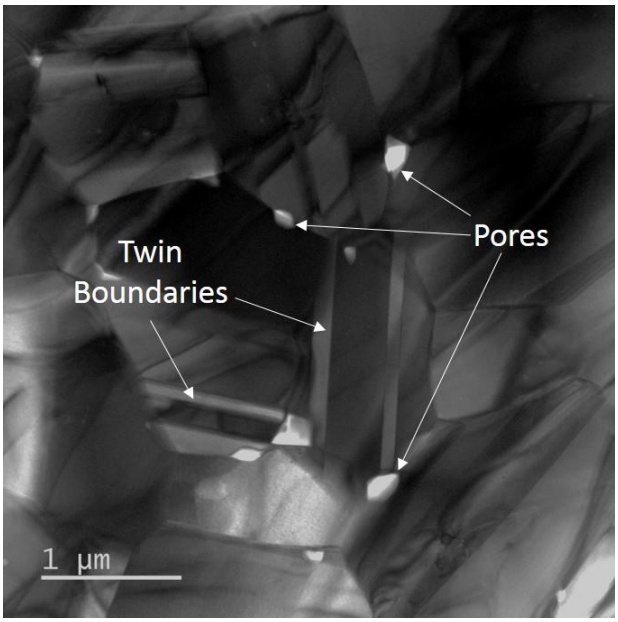

Figure 4.11. This Bright Field TEM image reveals that small intergranular pores are present in the as-pressed samples. Gas entrapped within these pores expands during annealing causing the material to swell and decrease in density.

During pressing, closed pores shrink until the pressure of the entrapped gas equals the applied pressure. As shown in **Figure 4.11**, residual intergranular pores are present within the as-pressed BST pellets. Upon heating, the gas within these pores can exert significant enough pressure to cause the material to swell. To produce porous BST samples, as-pressed pellets were annealed at temperatures between 250°C and 400°C, or 59-76% of the melting temperature of BST.[189] In addition, it was observed that two key processing conditions were required for significant swelling: the precursor powder must have been ball milled, and the material must contain more than

nominally 60 at.% Te. When annealed for 24 hours at 300°C, pellets produced from ball milled powders having nominal Te concentrations of 58.5% and 60% decreased in density from 6.85 to 6.79 g cm^{-3} and from 6.81 to 6.76 g cm^{-3}, respectively. In contrast, a nominally 61.5% Te pellet produced and annealed by the same methods decreased from 6.81 to 6.30 g cm^{-3}. When 61.5% Te-rich powder was instead produced by hand grinding the starting ingot using an agate mortar and pestle in an argon atmosphere, the resulting pellet only decreased from 6.82 to 6.81 g cm^{-3}. The observed density decrease was almost entirely due to volume expansion and not any loss of material. Mass losses were less than 0.2% of the total across all samples and mostly attributable to sample chipping rather than sublimation. As the excess Te only accounts for ~4% of the total initial volume, complete evaporation could not result in porosities as large as those observed (up to ~25%).

The identity of the entrapped gas in the material is unknown. Previous reports on foaming in bismuth telluride and its alloys have suggested that Te evaporation is responsible.[164,177,182,183] Solid phase nominally $Bi_{0.5}Sb_{1.5}Te_3$ has been found to evaporate incongruently with the vapor phase having up to three times the ratio of Te to Bi/Sb as the solid.[190] However, the vapor pressure of pure Te at 400°C (the highest annealing temperature in this study) is less than 10 Pa and not sufficient alone to induce the observed deformation.[191,192] Other potential candidates such as tellurium oxides[193] or other tellurium compounds with bismuth or antimony have even smaller vapor pressures.[190] Further, if the vapor pressure of Te is driving swelling, the pressure should remain constant until all Te has been evaporated, but the dramatic reduction in swelling rate over time (shown in **Figure 4.12b**) points towards a limited and decreasing driving force, consistent with pressure reduction during gas expansion. Instead of driving the expansion by vapor pressure,

the excess Te could instead play a secondary role. Tellurium-rich conditions can change point defect concentrations and may influence diffusion or grain growth.[194] If the excess Te was present at grain boundaries, it could serve as a lubricant to allow grain sliding. The presence of a second phase could also facilitate swelling through its own deformation.[176] This could reduce the amount of deformation required in the BST grains for translation and rotation.

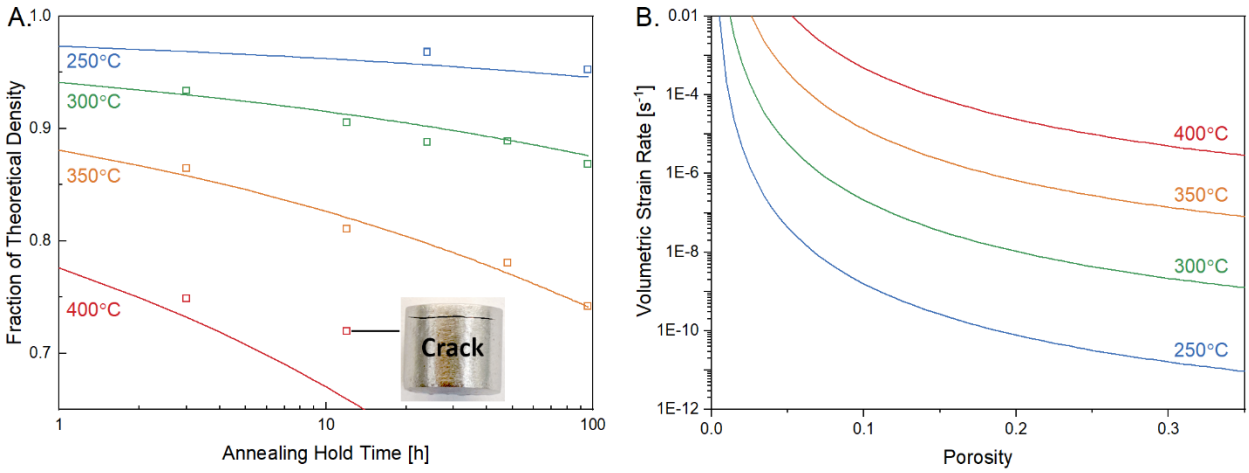

Figure 4.12. The swelling of Te-rich BST is dependent upon the annealing time and temperature, but also the density itself. (A) Each data point represents an individual pellet annealed. The curves are the result of fitting the creep model of Wilkinson and Ashby.[199] The model fits well for densities above 70% where pores have coalesced and reached the external surface of the pellet (inset image – horizontal crack). Panel (B) shows the calculated volumetric strain rates predicted by the Wilkinson and Ashby model. The rate decreases dramatically with increasing porosity presumably due to the inverse relationship of pore volume and pressure of entrapped gas.

It is not immediately clear what the mechanism is that requires ball milling to induce swelling. One possibility for the connection could be argon becoming trapped within the powder particles during the milling process. Hand grinding the powder within an argon atmosphere may

not be violent enough to result in similar porous agglomerations of fine particles. Grain size differences could also play a role in the strength of the BST. BST becomes very soft above 250°C due to the strongly temperature dependent activation of dislocation glide, but this occurs at temperatures as low as 170°C in material with submicron grain size.[166,195–198] If ball milling the precursor powder resulted in a finer grained pellet, the material may be easier to plastically deform. Further, differences in grain size would lead to differences in pore size distribution for a given porosity and the effect of this is unknown.

4.4.2. Creep-Enabled Pore Growth

Presuming the gas species causing swelling can be treated as an inert, ideal gas, it is possible to predict its effect when samples are produced in a controlled, repeatable manner. The rate of density change during annealing can be well fit using the power law creep sintering model of Wilkinson and Ashby[188,199]:

$$\dot{\rho} = -\frac{C}{T}\frac{\rho(1-\rho)}{\left[1-(1-\rho)^{1/n}\right]^n}\left\{\frac{3T}{2n}\frac{1-\rho_0}{\rho_0}\frac{\rho}{1-\rho}\right\}^n e^{-Q/k_BT} \tag{4.12}$$

Where ρ is the fractional density, ρ_0 is the initial density, T is the absolute temperature, n is the creep exponent for power law creep, Q is the creep activation energy, and C is a constant containing terms such as the Burgers vector and temperature independent portion of the shear modulus and diffusion coefficient. If the rate of change of the density is known, the volumetric strain rate can also be calculated:

$$\frac{d}{dt}\frac{\Delta V}{V_0} = -\frac{\rho_0}{\rho^2}\dot{\rho} \tag{4.13}$$

Where ΔV is the difference between the current volume and the initial volume, V_0. Figure 4.12a shows this model describes the porous samples when fit with squared error minimization determined values C = 1.4*10^{10} K$^{-8.7}$, n = 7.7, and Q = 214 kJ mol^{-1}. In large grain (> 100 μm) cast Bi_2Te_3, a creep exponent between 3-6 was observed between 400°C and 500°C making this value slightly higher.[200] This difference may be attributable to differences in composition and grain size. The presence of a second Te-rich phase may also play a role as samples were annealed between 72-93% of the melting point of Te (450 °C). The creep activation energy reported for large grained Bi_2Te_3 was 145 kJ mol^{-1}, while the activation energy for swelling in nanograined Te-rich Bi_2Te_3 has been reported as 270 kJ mol^{-1}.[183,200] The experimentally determined value for the creep activation energy of 214 kJ mol^{-1} in Te-rich BST seems reasonable as it falls in between these two reported values. It should also be noted that the sample annealed at 400°C for 12 hours is denser than the creep model would predict. This is likely attributable to the release of trapped gas as pores coalescence and connect to the outer surface of the pellet as evidenced by significant cracks visible to the naked eye (inset of Figure 4.12a). This release of the internal gas pressure ultimately sets the upper limit on porosity.[179,180] It should be noted that the material becomes increasingly fragile with porosity. Careful preparation and handling was require for samples with near 30% porosity. Porous samples may not be ideal for the production of thermoelectric modules, but as will be discussed, the other defects enhanced during the swelling process could be desirable.

This swelling phenomenon has significant implications for BST samples produced by Te-rich synthesis methods, e.g. liquid phase sintering, as it can occur at relatively low temperatures. For example, if the pellet is not under pressure during cooling (after pressing), it could swell and become porous and may explain the reported porosity in some liquid phase sintered BST

studies.[140,148,182] In this study, the density of an as-pressed, Te-rich sample was found to decrease from 6.78 g cm^{-3} (99.4% dense) to 6.62 g cm^{-3} (97.1% dense) during the course of measuring the thermal diffusivity up to 250°C, while heating and cooling at a rate of 3°C min^{-1}. This density change resulted in a decrease in thermal diffusivity at 50°C of 2%, and a 4% overall decrease in thermal conductivity between the heating and cooling values. This density loss also likely resulted in a decrease of electrical conductivity; however, this was not measured prior to the thermal diffusivity. Samples should be measured during both heating and cooling to check for stability and the density monitored with every thermal treatment. If the sample is not thermally stable, errors in estimation of performance could arise depending on the order of characterization. Note that such density changes during measurement were not detectable in the annealed porous samples as presumably the internal pressure of the entrapped gas phase had decreased, and the swelling rate slowed. Further swelling may still occur if the material were held at elevated temperatures over time scales like the expected service life of thermoelectric modules.

4.5. Relationship Between Microstructural Evolution and Thermoelectric Transport

Transport of both electronic charge carriers as well as phonons can be affected by a multitude of different microstructures. In this material system it was found that in order to begin to understand the importance of certain defects at the nanoscale that the micro-and mesoscale must also be well-documented. The larger mesoscale is of importance because, even if the defects are unable to scatter phonons or charge carriers directly, these features may give insight into the formation mechanisms present in a material, as well as allude to the prevalence of defects that form at the nanoscale.

4.5.1. The Role of Excess Te in Transport

Low magnification STEM and electron diffraction were able to identify micron sized grains of elemental Te. Discovering the location and morphology of the excess Te in this sample allowed the majority matrix phase in EMT calculations to be treated as stoichiometric BST (which has well-documented properties), rather than an arbitrary off stoichiometric compound. More importantly elemental Te could be excluded from the EMT calculations because it was determined that elemental Te was present in minimal amounts and was present to the same degree in both the as-pressed and annealed samples. Ultimately, identifying the size, density, and phase of Te in both as-pressed and annealed BST led to the conclusion that while excess Te likely plays a role in swelling, the Te grains are not directly responsible for the enhancement in *B*.

4.5.2. The Role of Pores in Transport

The second defect that needed to be understood in order to compare experimental samples to the ideal EMT model was the micron sized pores in the annealed samples. These pores are large relative to the expected mean free path of phonons (tens of nm).[151,201] This means that the decrease in thermal and electronic conductivities with increasing porosity is primarily due to the increase in solid path length and not due to an enhancement in scattering by the pores. Yet there is still a comparatively large decrease in lattice thermal conductivity in the annealed samples compared to the ideal EMT case. This hints at a need for a further explanation for what causes the additional decrease in lattice thermal conductivity. Additionally, the fact that elemental Te and pores have been ruled out as sources of property enhancement suggests that the lattice thermal conductivity decrease is likely due to changes in the defect structure within the BST phase.

4.5.3. Grain Boundary Dislocation Formation

TEM studies of the BST phase confirm that there is some evidence of dislocations within grains and in the vicinity of high angle grain boundaries. Yet, there did not appear to be any significant increase in the density of these dislocations during swelling. Furthermore, due to increased atomic diffusion, one would expect increased dislocation annihilation during annealing, yielding a lower density of in-grain dislocations. However, stepping of twin boundaries in annealed samples, which requires the presence of twin boundary dislocations, was documented. Stepping of twin boundaries can be indicative of both twin boundary growth through annealing as well as deformation.[168] EBSD provides evidence to support both mechanisms of twin stepping as both grain growth, as well as grain shearing in the final annealed BST samples were observed. Because the annealing process involves both heat and pressure, it may require further investigation outside the scope of this work to deconvolute which of these two sources are responsible for twin boundary step formation. Although twin boundary stepping has been identified as a mechanism to induce dislocations into BST during the annealing process, it is difficult to quantify the enhancement that these defects will have on overall material performance without an idea of the density of twin boundaries.

4.5.4. Twin Boundary Ratio Increases during Annealing

Through mesoscale EBSD analysis of BST, it was found that not only do twins make up approximately $1/6^{th}$ of total boundary length in the as-pressed samples, but that annealing causes a statistically significant shift in boundary distribution which favors lower energy twin boundaries. This results in a twin boundary ratio in annealed samples as high as ~24%. Although the pores themselves do not affect thermoelectric properties directly, as they grow, boundaries fracture

and/or slide allowing the material to swell. Higher energy, high angle boundaries will be eliminated preferentially compared to more stable twins, resulting in a porous material that has a larger fraction of electrical and thermal transport paths traveling through low energy boundaries. These boundaries are favorable defects for thermoelectric performance due to their high site coincidence. This means that twin boundaries do not scatter charge carriers as strongly as random high angle boundaries and thus do not significantly impact electrical conduction. [170,202,203] Bismuth telluride and its alloys are also layered compounds and anisotropic in mechanical properties. This means that the elastic properties differ across a twin boundary, meaning impinging phonons can be scattered and the thermal conductivity reduced.[203] Twins have been shown to have reduced thermal conductivity compared to the bulk in Bi, YBCO, and Si, however to our knowledge the thermal resistance has not been measured in BST.[204–206] The presence of twins has been previously reported to improve the thermoelectric performance of BST bulk and nanowires.[207–209] Two points should be noted here. First, although the twin boundary ratio increased, the magnitude of twins per sample volume did not significantly increase (if at all), meaning no true thermoelectric enhancement should be expected. Second, according to literature twin boundaries are favorable because they scatter electronic carriers less than random high angle boundaries while scattering phonons to the same degree. If this is true, and if twins alone were responsible for the increase in thermoelectric performance, it should be expected to see the EMT underestimate weighted mobility and correctly estimate lattice thermal conductivity (instead of correctly predicting weighted mobility and overestimating lattice thermal conductivity as seen in Figure 4.2a and 4.2b). These two points further emphasize why a second mechanism, such as modification of the twin

boundaries via stepping, may be necessary to fully explain thermoelectric enhancement after annealing.

4.5.5. Texture and Anisotropic Properties

The last mesoscale feature of note is the material texture. By analyzing sample texture, via pole projections generated from EBSD data, it can be seen that there is preferential alignment of the crystallographic c-axis of grains with the pressing direction. As stated previously, this means that there is a non-random preference of cracking and pore formation developing between (0001) interfaces in the pressing direction, which is consistent with the observation of both larger expansion of the pellets and larger enhancement of thermoelectric performance parallel to the pressing direction.

4.6. Summary and Conclusions

This chapter reports an equilibrium processing method in which porosity and property enhancement are achieved in Te-rich BST. It was reported that the quality factor (*B*) increases with increasing porosity, particularly parallel to the pressing direction, displaying improvements in *B* as high as 45% parallel to the pressing direction for samples having ~20% porosity. The large decrease in lattice thermal conductivity, which was responsible for this property enhancement, could not be explained by an increase in porosity alone (as described by EMT). Therefore, like in the case of kinetically processed melt-centrifuged BST, it was proposed that the mechanisms responsible for porosity may also be contributing to the addition of phonon scattering structural defects in the BST matrix. The deformation mechanism was determined by fitting the swelling of BST samples with annealing time and temperature. Fitting experimental data with the Wilkinson

and Ashby creep model it was concluded that the samples were expanding and deforming due to creep.

The defects that were introduced into the sample during creep were studied using a combination of traditional nano- and microscale Scanning/Transmission Electron Microscopy techniques with the incorporation of mesoscale Electron Backscattered Diffraction. The traditional microscopy techniques were able to identify dislocations, twin boundary stepping, and the location of the excess Te, while the post-processing of mesoscale data enabled the measurement of the population of twin boundaries, average grain size, and texturing. It was concluded that the decrease in lattice thermal conductivity was primarily due to a combination of twin boundary stepping (caused by creep), and a simultaneous increase in the twin boundary ratio, which forces phonons and charge carriers to pass through more of these modified special boundaries. In conclusion, this investigation highlights 1) the importance of mesoscale characterization techniques for developing a complete picture of the distribution of defects in a material, 2) reinforces the need for further detailed exploration of the benefits of twin boundaries, and 3) emphasizes the potential benefits of controlling formation mechanisms such as creep that can modify thermoelectric material microstructure.

Chapter 5. The Implications of Extrinsic Doping on Sintering, Microstructure, and Thermoelectric Performance

Previous chapters have explored the influence of structural defects such as point defects, dislocations and grain boundaries on thermoelectric efficiency, as well as investigated how processing methods such as melt centrifugation, induction hot pressing, and thermal annealing modify the microstructure of chalcogenide-based thermoelectrics. Whereas previous chapters attempted to address how processing affects microstructure and thermoelectric efficiency, this chapter attempts to address how composition (via extrinsic doping) affects high temperature thermal stability. Specifically, this chapter describes the influence of p-type dopants (Na, K, and Ag) on the types of point defects present in PbSe. It is shown here that the types of point defects can limit the doping efficiency and lead to changes in grain size and low angle grain boundary (LAGB) distribution, which, in turn, influence both thermoelectric efficiency as well as sublimation at high temperatures. Performing mesoscale analysis with Scanning Electron Microscopy on thermally treated samples reveals that the greatest differences in microstructure and high temperature mass loss exist between Na and Ag-doped PbSe, while K-doped samples display intermediate microstructure and thermal stability. Ultimately, it is shown that Na and K cations are predominantly substitutional point defects, while Ag sits at interstitial sites and exhibits lower solubility. These differences in combination with cation size change the dopants' ability to alter carrier concentration, while also affecting the mechanical properties of PbSe during processing. Although the change in mechanical properties alters the final microstructure, this chapter shows that an improved fundamental understanding of the dopant-microstructure relationship can be used to intentionally modify processing techniques (such as powder processing

and Spark Plasma Sintering) to achieve the desired microstructure required to optimize thermoelectric efficiency and thermal stability. This study was a collaboration between the lab groups of Professors Vinayak P. Dravid, Mercouri G. Kanatzidis, and Christopher Wolverton. My direct collaborators were Dr. Tyler Slade who performed PbSe synthesis, annealing, and mass loss measurements and Dr. Shiqiang Hao who performed the DFT calculations. At the time of submission, the work covered in this chapter of the dissertation has been submitted but not formally accepted for publication in any peer-reviewed academic journals.

5.1. Introduction to Extrinsic Doping

5.1.1. Efficiency and Longevity of Thermoelectric Materials and Devices

As has been discussed previously, thermoelectric devices are an attractive technology for a variety of applications such as waste-heat energy conversion, space flight, and electronic cooling because of their ability to directly convert heat into electricity (and vice versa). Another attractive feature of thermoelectrics is their lack of moving parts, which allows them to function for decades without degradation from mechanical wear and tear.[3,5,18,210] An incredible display of longevity is the fact that the Radioisotope Thermoelectric Generators (RTGs) used to power Voyager 1 have been functioning since the deep space probe was launched by NASA in the late 1970's.[18,211] Although thermoelectric devices have proven to be successful in space, for most terrestrial applications these materials need to be more efficient to become economically feasible.[210]

5.1.2. Extrinsic Doping and Semiconducting Thermoelectric Materials

Semiconductors are of particular interest in thermoelectricity because they have intrinsically high Seebeck coefficients compared to metals. With the addition of small amounts of

impurity elements (dopants) to increase the carrier concentration, the electrical conductivity and subsequently the power factor of degenerately doped semiconductors becomes highly favorable for thermoelectric applications.[4] In addition to enhancing the power factor, point defects created by doping lead to additional scattering mechanisms for phonons that decrease thermal conductivity.[212] Owing to the ability to tune the Fermi level (carrier concentration) while simultaneously enhancing phonon scattering, extrinsic doping is often used to optimize the performance of semiconducting thermoelectric materials. Although increasing the carrier concentration and adding point defects are vitally important to increasing the efficiency of thermoelectrics, energy conversion efficiency is not the only metric that determines the potential effectiveness of a thermoelectric device. The use of thermoelectrics in RTGs makes it clear that the longevity of thermoelectric materials is also an essential quality, so for practical application, optimal performance for thermoelectrics should take into consideration both a material's efficiency as well as its durability (or resistance to degradation over time). For example, when specifically considering doping, some dopants such as Ag may provide better high temperature stability to lead chalcogenides than either Na or K because of the high diffusion rate of alkali metals.[213] However to date, the broader impacts of doping outside of its contributions to transport properties have been sparsely considered and not thoroughly investigated.

To address these concerns, PbSe was selected as a model system because it is already a commonly studied material. PbSe is a promising analogue to PbTe (one of the best performing intermediate temperature thermoelectrics) because of its similar crystal and electronic band structure, and because of the relative Earth abundance of Se compared to Te.[20,214,215] PbSe has a combination of light and heavy valence bands which make it favorable for p-type doping, and

therefore this study focuses on the direct comparison of different p-type dopants.[54,213,214,216] Specifically, this report investigates PbSe doped with Na, K, and Ag and uses defect energy calculations to reveal the nature of the underlying point defects and the relationships to doping efficiency, microstructure, and thermal stability of PbSe. Furthermore, this chapter illustrates how developing a keen understanding of the relationship between dopant selection and microstructure can help inform synthesis processes, leading to the manufacture of thermoelectrics optimized for efficiency as well as reduced material degradation.

5.2. Experimental Methods

5.2.1. Sample Fabrication

5.2.1.1. Synthesis

The starting materials were Pb wire (99.99%, American Elements), Se shot (99.99%, American Elements), Na cubes (99.95%, Sigma Aldrich), Ag pieces (99.999%, Sigma Aldrich), and K cubes (99.95%, Sigma Aldrich). Polycrystalline ingots of doped PbSe were first synthesized as follows. According to the desired nominal compositions, $A_xPb_{1-x}Se$ (A = Na, Ag, K) stoichiometric quantities of each element were weighed into 13 mm diameter carbon coated fused silica tubes and then flame sealed at ~$2x10^{-3}$ Torr. Typical samples used 10 grams of total starting material. The tubes were heated in a box furnace to 500°C over the course of 12 hrs, held for 2 hrs, then heated to 1150°C in 7 hrs where they dwelled at temperature for 5 hrs. The tubes were next brought to room temperature over 12 hrs.

5.2.1.2 Post-Synthetic Processing

The as-cast ingots were removed from the tubes and subject to different preparatory procedures. All samples were hand ground into powder with an agate mortar and pestle, and the sample powders were then passed through a sieve using either a 53, 70, or 150 μm mesh. The use of different mesh sizes allows for control over the grain size in the final samples. The sieved powder was loaded into a 12.7 mm graphite and sintered into dense pellets by Spark Plasma Sintering (SPS-211LX, Fuji Electronic Industrial Co. Ltd). The sintering process was conducted under dynamic vacuum at 550°C, and the samples were held at temperature for 10 min under 40 MPa of uniaxial pressure before being cooled to room temperature. The resulting pellets were cut into square prisms with approximate dimensions of 4x4x2 mm^3 for sample analysis.

5.2.2. Sample Preparation for Electron Microscopy

Surface scratches and deformation are detrimental to Electron Backscattered Diffraction (EBSD) because this technique uses a Scanning Electron Microscope (SEM) to collect diffraction patterns to obtain crystallographic information from the surface of a sample. Because of this technique's reliance on diffraction, any deviations from the ideal structure in the surface results in a distorted signal.[217] As a result, careful polishing was required to eliminate surface deformation as much as possible so that surface micro-strain did not obscure the true crystal structure of the sample.

The cut samples were cold mounted into quick dry epoxy, with the large face exposed. The sample was then ground using 600, 800, and 1200 grit SiC grinding paper on a rotary grinding wheel, using ethanol as a water-free lubricant. Next samples were polished for 30 min and 45 min

with 1 μm and 0.1 μm glycol-based diamond slurry, respectively. Upon finishing this step, samples were placed into a vibratory polisher for 3 hours at 62.7 Hz in a bath of 0.1 μm glycol-based diamond slurry. The samples were then removed from the cold mount using acetone, flipped over, and this process was repeated so that both large faces, had the same polish and surface roughness.

5.2.3. Scanning Electron Microscopy

After polishing, samples were mounted to SEM stubs using paraffin wax and then copper tape was applied as a contact between the sample and the SEM stub to ensure that there was an electrically conductive connection. Any sample charging in the SEM during EBSD can result in sample drift and other charging effects that interfere with image and data collection. Therefore, chamber pressure was maintained at 0.1 Torr to further reduce charging effects.[52] For both imaging and EBSD, accelerating voltage was set to 30 kV with a working distance of approximately 10 mm and was carried out using a FEI Quanta 650 ESEM. EBSD patterns were collected over an area of 200 μm x 200 μm with a 0.8 μm step size using an Oxford Instrument's Nordlys II detector and post processing was performed using Oxford Instruments CHANNEL 5 software suite. After thermal treatment, samples did not need to be re-polished. In fact, due to annealing, the surface deformations that remained after polishing were reduced yielding sharper EBSPs. Consequently, thermally treated samples were immediately characterized under the same SEM conditions described above without any additional grinding or polishing.

5.2.4. Thermal Treatment and Mass Loss Measurements

After preliminary SEM imaging and EBSD had been performed, samples were weighed and then flame sealed in 9 mm diameter tubes at ~$2x10^{-3}$ Torr. The tubes were then placed in

furnaces pre-heated to 650 °C and annealed for 48 hr. After dwelling the samples were quenched in air. The samples were removed from the tubes and weighed again to determine their mass loss during annealing. It should be noted that high temperature mass loss experiments resulted in large error due to differences in surface quality around edges, cracking of samples while annealing, and potential chipping of brittle samples throughout the annealing and measurement process. Because of the possibility for large amounts of error, 3 to 5 trials were performed for each sample to obtain average mass loss measurements at elevated temperatures. Yet even with these precautions, doped samples had standard deviations as high as 3% mass loss, while the standard deviation of pure PbSe remained at around 1%.

5.2.5. Density Functional Theory Calculations

To provide additional insight on how dopants interact with the PbSe crystal structure, Density Functional Theory (DFT) was used to calculate the thermodynamically stable point defects in each doped PbSe sample. The calculations were based on density functional theory (DFT) within the generalized-gradient approximation (GGA).[218] The projector augmented wave pseudopotential was applied as implemented in the VASP package.[219] Calculations for bulk PbSe with different defects were performed using a 3x3x3 for 54 atom cell with very dense k-point mesh corresponding to 4000 k-points per reciprocal atom. The plane-wave basis-set cutoff energy was set to 500 eV and the convergence criterion with respect to self-consistent iterations was assumed the residual forces were less than 0.01 eV/A. In the defect calculations, the lattice parameters were fixed to the calculated bulk values, but all the internal coordinates were fully relaxed.

The formation energy of a defect X in charge state q was defined as

$$E^f(X^q) = E_{tot}(X^q) - E_{tot}^{bulk} - \Delta n_i \mu_i + q(E_V + \Delta_V + \varepsilon_F)$$

in such a way that the negative values suggest favorable formation and the positive values unfavorable.[220] In the equation, $E_{tot}(X^q)$ and E_{tot}^{bulk} are respectively the total energies of a supercell containing the defect X and of a supercell of the perfect bulk material; μ_i is the atomic chemical potential of species i (and is referenced to the standard state), and Δn_i denotes the number of atoms of species i that have been added ($\Delta n_i > 0$) or removed ($\Delta n_i < 0$) to form the defect. ε_F is the Fermi level referenced to the valence-band maximum in the bulk (E_V). The potential alignment term Δ_V is the shift in the band positions due to the presence of the charged defect and the neutralizing background, obtained by aligning the average electrostatic potential in regions far away from the defect to the bulk value. Note that we denote defect X in charge state q as X^q. The chemical potential selection in the above defect formation energy calculations is based on the phase diagrams of A-Pb-Se (A = Na, K, Ag) from the open quantum materials database.[221,222] In each phase diagram, the convex hulls have been constructed from a set of possible phases using grand canonical linear program methods. The chemical potentials corresponding to each set of the three-phase equilibrium are solved relative to the composition of each element.

5.3. The Effects of Extrinsic Doping on PbSe

5.3.1. Microstructure

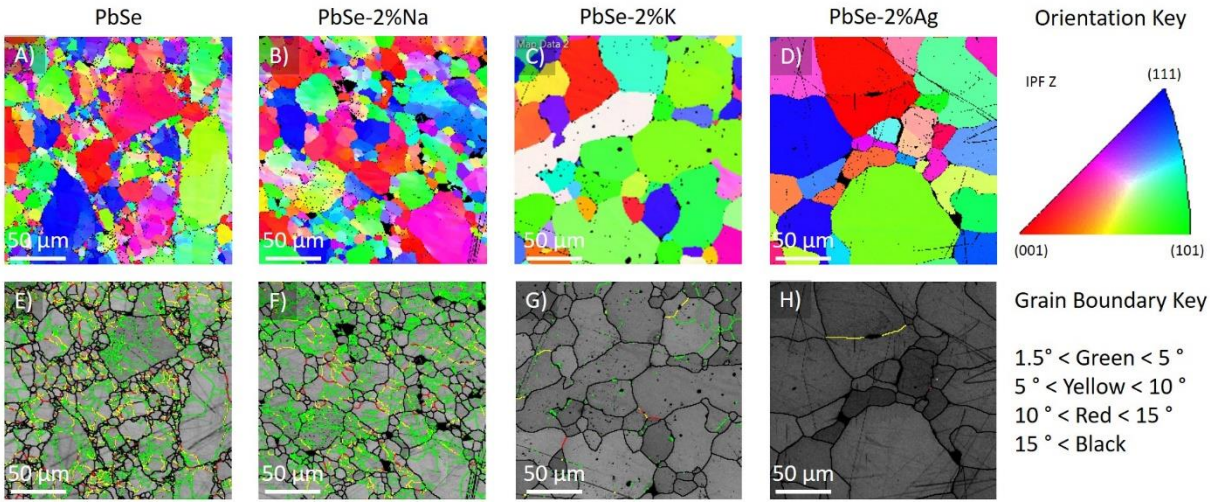

Figure 5.1. Unannealed, single sieved PbSe with varying dopant species. EBSD (A-D) Inverse Pole Figure orientation maps highlighting the grain size and (E-H) Band Contrast maps with color coded LAGBs.

The initial doped and undoped samples in this investigation underwent the same synthesis and post synthetic processes, yet upon investigation of the microstructure, there were stark differences in both the grain size and the population of low-angle grain boundaries (LAGBs). The only difference between the samples is the identity of the p-type dopant: pure PbSe (no dopant), PbSe-2%Na, PbSe-2%K, and PbSe-2%Ag. **Figure 5.1** reveals both the grain structure and grain boundary angle distribution in the PbSe samples prior to annealing. It should be noted that after annealing there appears to be some amount of grain growth in some samples (see **Figure 5.2**), however the difference in grain size between samples remains large throughout the thermal treatment. To compare the thermal stability of different samples, grain size needs to be consistent

during exposure to high temperature so that microstructural variation would not convolute the subsequent mass loss results.

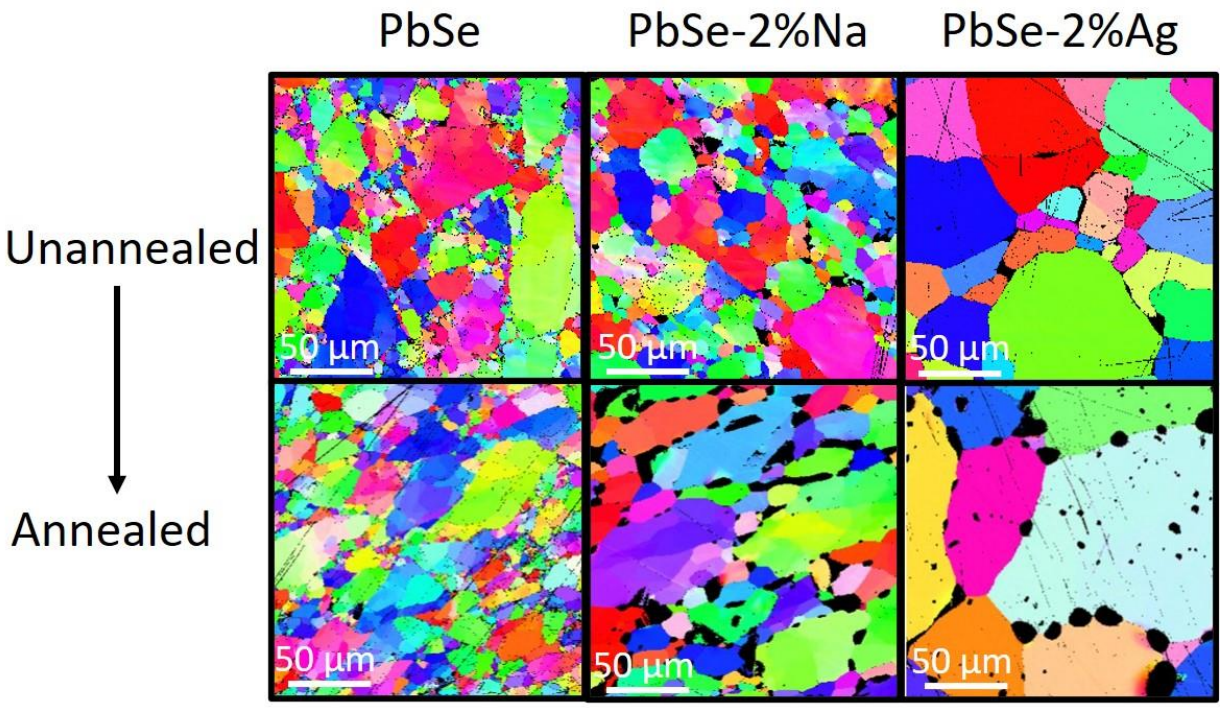

Figure 5.2. Electron Backscattered Diffraction illustrating the change in grain size before and after annealing. Ultimately, the difference in grain size remained large during this experiment, so it was still necessary to find ways to alter the grain size during processing. This set of images also shows the development of pores in the doped samples forms to a higher degree than in the undoped PbSe sample.

To reduce the variation in grain size, a processing step referred to as “double sieving” was introduced into the standard post-synthetic sample preparation process. The idea behind sieving is to mechanically sort powder particles so that the powder particles are the size of the desired grains. This powder is then solidified, which in our case is done through Spark Plasma Sintering (SPS), and the resulting grain size will be roughly equal to the size of the powder particles. It is important

to note that this process assumes that the powder particles do not have multiple grains. In other words, it is assumed that the size of the final powder particles is much smaller than the grains of the as-cast ingot materials that are being crushed to produce the powder. Previous studies show that the size of grains in similarly processed lead chalcogenide ingots is on the order of millimeters, while the powder size is targeted to be 10s of micrometers, so this is a safe assumption.[28,30] In typical sieving, crushed powder is passed through a mesh. All particles smaller than the mesh size will be filtered through the mesh, and it is the filtered powder that is sintered to make the final thermoelectric sample. It is important to know that the mesh only determines maximum powder size, not the minimum powder size. In the case of PbSe-2%Na, even though the mesh size was 70 μm the sample has many grains on the order of 10-20 μm. To both ensure a tighter distribution and to fix a minimum grain size, a second sieving step was introduced. In the new process, powders are sieved through a 150 μm mesh and then the resultant powder is sieved through a 53 μm mesh. The intermediate sized powder (that was sifted through the first mesh but that did not get filtered through the second mesh) is SPSed to create new, large grain thermoelectric samples. By utilizing the "double sieving" method, both the minimum and maximum powder size (even in materials which tend to have smaller grains due to the dopant being used) can be controlled.

EBSD of the large grained PbSe-2%Na sample reveals that grains were enlarged by using the modified synthesis method. However, the microstructure of the large grain Na-doped material still differs from that of the Ag-doped PbSe. The main difference is the large amount of low angle grain boundaries (LAGBs) that are present in Na-doped PbSe. This network of LAGBs is displayed in the EBSD band contrast map in **Figure 5.3d,** which highlights LAGBs in green, yellow, and

red, while those with misorientation angles above 15°, also known as high angle grain boundaries (HAGBs), are highlighted in black.[223]

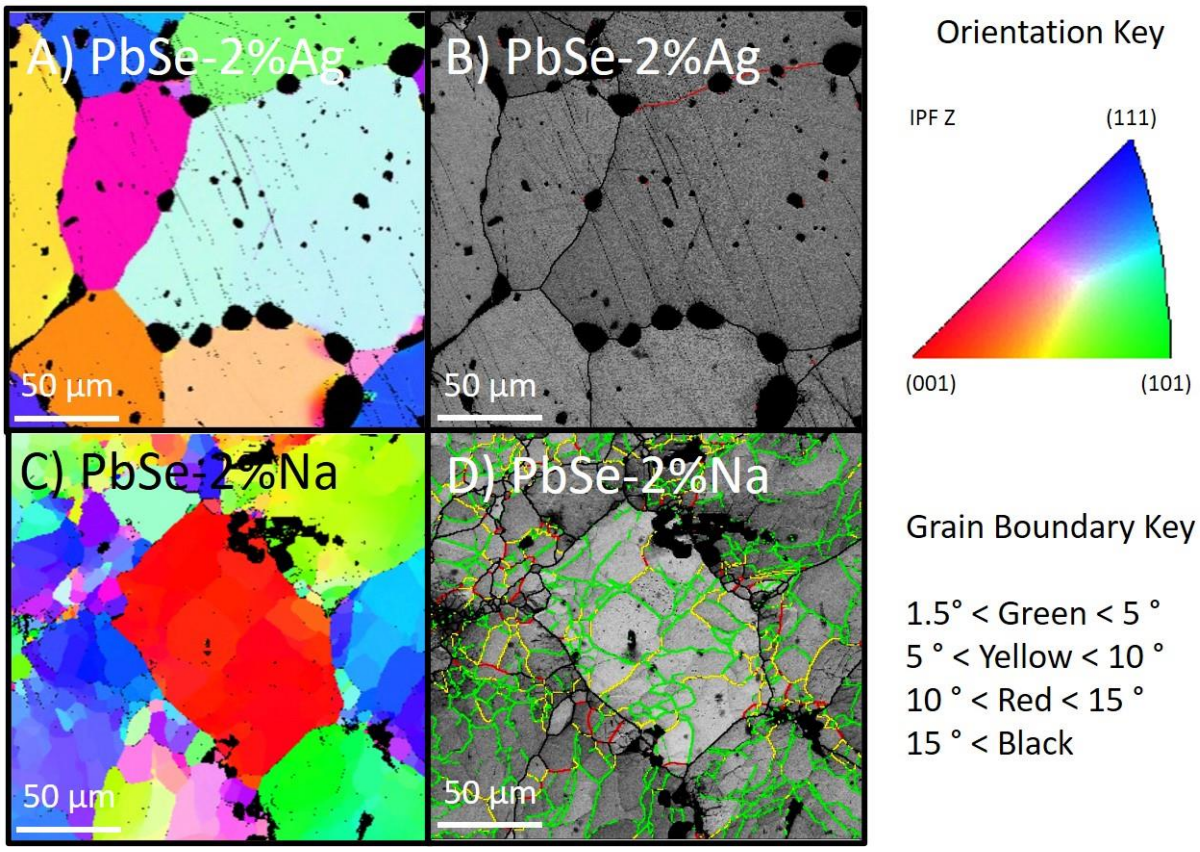

Figure 5.3. A-B) Annealed PbSe-2%Ag with pores forming at grain boundaries. C-D) Annealed large grained PbSe-2%Na (processed using the "double sieve" method) with pores predominantly forming at HAGBs.

5.3.2. High Temperature Mass Loss

To document the thermal stability of doped PbSe, highly polished Na-doped PbSe samples were exposed to temperatures of 600-650 °C for 48 hours. SEM was then used to record the quality of the surfaces after annealing to gain a qualitative understanding of the extent of mass loss. **Figure 5.4** shows a combination of surface pores, rough surface grains, and plateau/tree-like structures.

These features formed because of material removal from the surface of the sample, which had originally been smooth and polished for EBSD using the steps described in the methods section. From this figure, it can be seen that these new pores are located at what appear to be grain boundaries, which agrees with the fact that grain boundaries sublimate at a higher rate than the defect free material.[224–226] Figure 5.3a further illustrates the strong relationship between grain boundaries and mass loss by using EBSD to highlight pores preferentially forming at HAGBs. Simultaneous EDS-EBSD scans of unannealed samples (see **Figure 5.5**) reveals homogenous samples and suggests that the increased mass loss at grain boundaries was not due to the presence of a second phase, but rather is a function of the elevated defect energy of grain boundaries due to their structural imperfections. Although SEM imaging and EBSD could not directly compare the difference in mass loss between different samples, these techniques were vital in confirming the influence of microstructure on thermal stability.

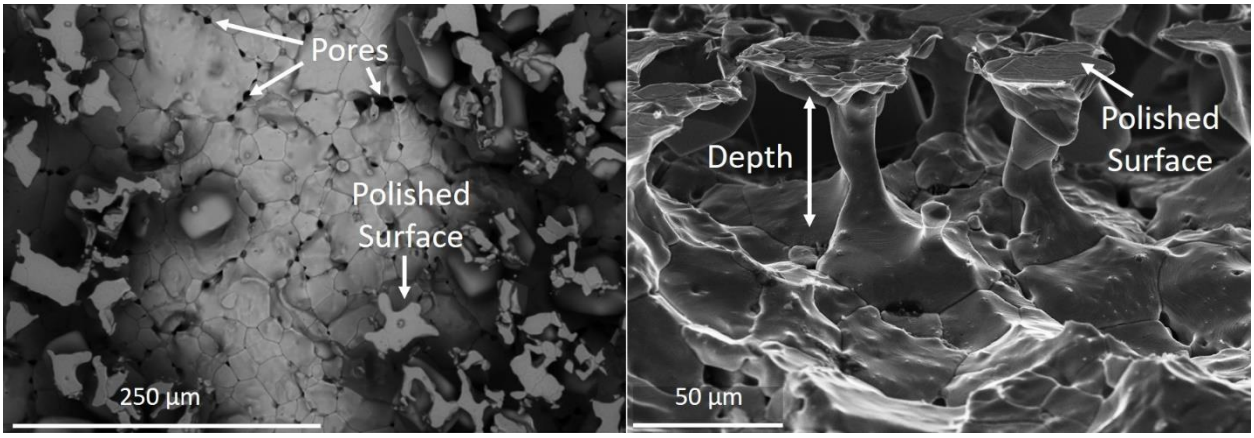

Figure 5.4. Secondary electron images of (Left) the top and (Right) angled side view of the surface features of Na-doped PbSe samples that had been annealed between 600 °C and 650 °C for 48 hours. Annealing resulted in the sublimation of the surface of the material and subsequent degradation of material below the initial surface as well. The flat features are the remnants of the original sample surface that had been polished for EBSD prior to annealing, while the rough textured surfaces and pores are portions of the sample that have been exposed due to the removal of the original surface material.

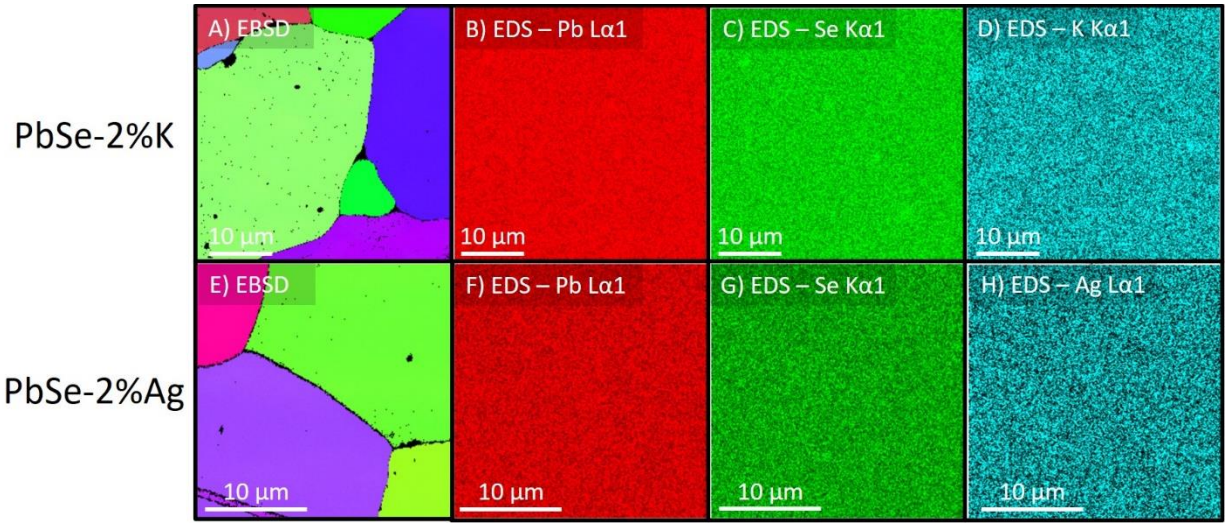

Figure 5.5. Simultaneous EDS-EBSD scans were performed to observe the grain boundaries of samples prior to annealing. As can be seen in both K and Ag-doped samples, no significant segregation was detected at the grain boundaries. This proves that any sublimation attack at grain boundaries is more likely due to the high energy of these defects rather than the sublimation of a second phase.

To obtain more quantitative results, the mass of PbSe samples was measured before and after annealing. The first set of mass loss experiments were performed on the same set of samples seen in Figure 5.1 (pure PbSe and PbSe doped with 2% Na, K, and Ag), which were all synthesized using a single sieve powder separation method. The results of the first mass loss experiment can be seen in **Figure 5.6a**. Because grain sizes change drastically between PbSe samples doped with different elements, and because grain boundaries increase pore formation (and presumably mass loss), further experiments were performed to better understand the effects of mass loss without the influence of microstructure. Additionally, because pure PbSe exhibited the lowest mass loss in the first set of experiments, a test of the effects of dopant concentration on thermal stability was also of interest. For this reason, a second set of quantitative mass loss experiments was performed on

large grain PbSe-2%Na and large grain PbSe-0.4%Na. Data displayed in Figure 5.6b shows that reducing the dopant concentration from 2% to 0.4% in Na-doped samples reduces mass loss from an average of 5% to 2%. Furthermore, with standardization of grain size, the mass loss of PbSe-0.4%Na becomes comparable to the mass lost from PbSe-2%Ag.

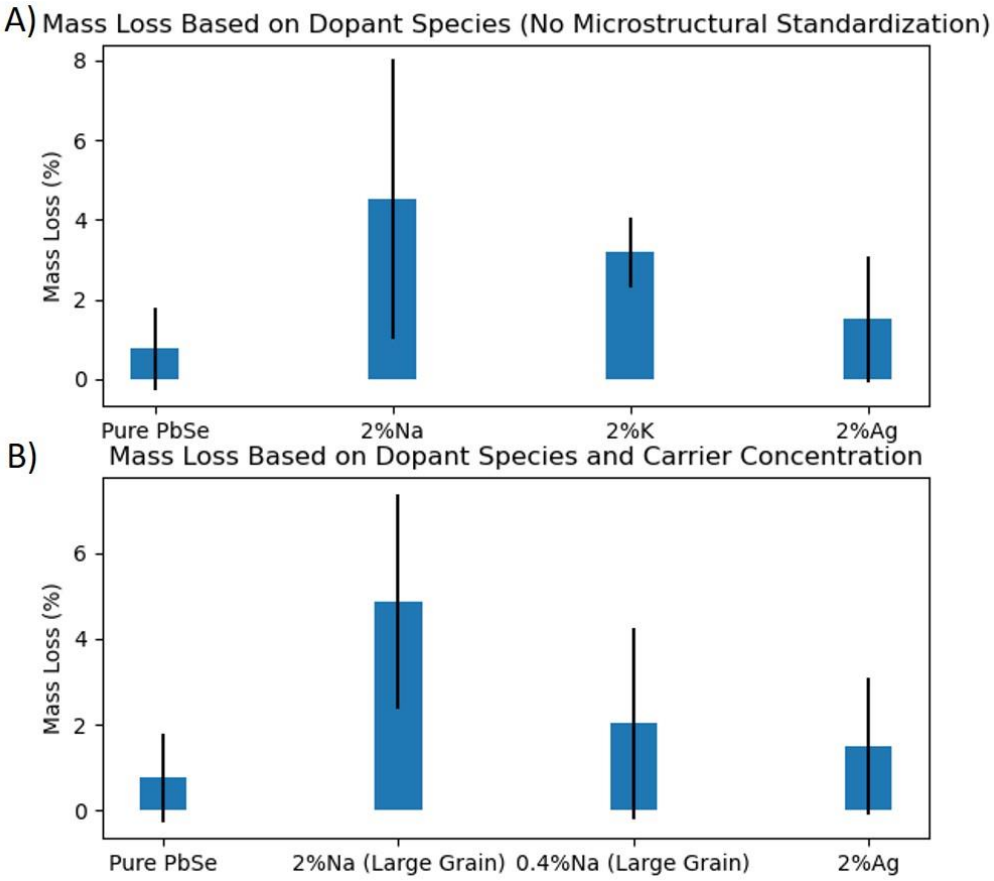

Figure 5.6. Mass Loss due to annealing PbSe at 650 °C for 48 hours. A) Initial mass loss experiments comparing mass loss of PbSe with equal amounts of different dopant species prior to microstructural standardization. B) Na-doped samples were synthesized using "double sieving" and with reduced carrier concentration to measure the effects of dopant concentration and dopant species on samples with comparable grain sizes.

5.3.3. DFT Defect Energy Calculations

DFT was used to calculate defect energies to help provide insight into the underlying point defects present in extrinsically doped PbSe samples. **Figure 5.7** plots the defect energies in the three doped PbSe samples as a function of Fermi level (E_F), where E_F=0 eV corresponds to the valence band maximum, and a decrease in E_F indicates an increase in p-type doping. The nominal composition of doped PbSe in this investigation is $A_xPb_{1-x}Se$, where A = Na, K, Ag, and can alternatively be written as xASe—(1-x)PbSe. Therefore, the chemical potentials used in the DFT calculations plotted in Fig. 5 were obtained from the equilibrium three-phase regions in the A-Pb-Se phase diagram which either encompassed or included the ASe—PbSe tie-line. These regions were PbSe-NaSe-Na_2Se, PbSe-KSe-K_2Se, and PbSe-Se-Ag_2Se for Na-doped, K-doped, and Ag-doped defect energy calculations, respectively. In these plots the defects were defined using Kröger-Vink notation with effective charge defined by

$$q_e = z_d - z_s$$

where q_e is the effective charge, z_d is the charge of the defect, and z_s is the charge of the original site.[227] Using this notation, a cation substitution that results in p-type doping would be written as X'_{Pb} , where X is the dopant species. In this case, Pb^{2+} is the original cation and gives z_s a value of 2, while the dopants (Na^+, K^+, or Ag^+) give z_d a value of 1. According to Equation (2), the effective charge of the defect is -1, and the Kröger-Vink notation for the cation substitutional defect is X'_{Pb}.

In all three doped materials, cation substitutions are the lowest energy defect at the onset of doping, and therefore are the dominant defect species, until E_F becomes sufficiently negative and a cross over between defect energies occurs. In Na and K-doped PbSe this crossover is due to

the presence of Se vacancies ($V_{Se}^{2\bullet}$), while in Ag-doped PbSe the crossover is due to the presence of Ag^{+} interstitials ($Ag_i^{\bullet}$). Additionally, the crossover in Ag-doped PbSe occurs at a higher Fermi level than in the Na and K-doped materials, which indicates that cation substitutions will stop being the dominant defect at lower levels of doping when using Ag as a p-type dopant compared to either Na or K.

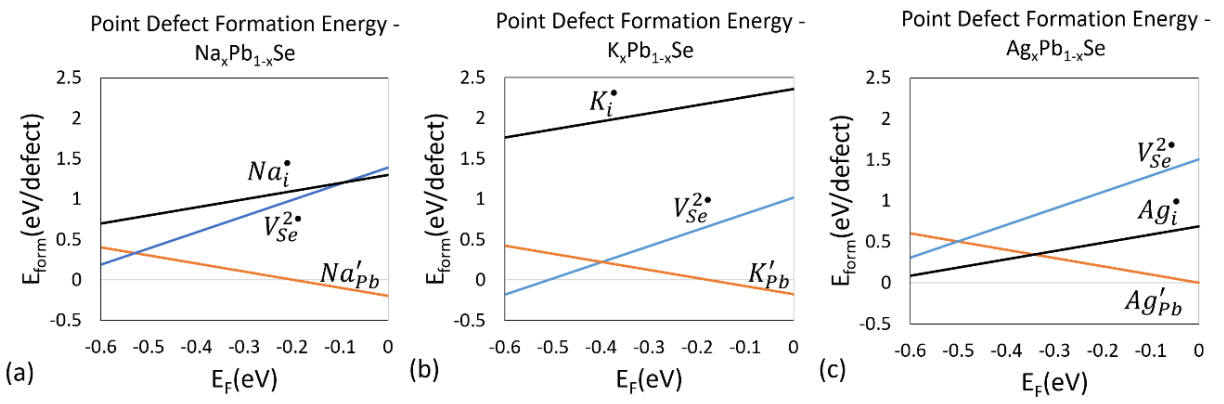

Figure 5.7. DFT calculations of defect energies in PbSe doped using different dopants. A Fermi level (E_F) of 0 eV corresponds to the top of the valence band, and as p-type doping increases, E_F becomes more negative. The primary point defect in the system is that which has the lowest defect energy at a given E_F. The crossover point shows the level of doping at which compensating defects begin to dominate. Ag interstitial cations (denoted by $Ag_i^{\bullet}$) are the primary compensating defect in Ag-doped PbSe and their crossover point occurs at a higher Fermi level than the Se vacancy ($V_{Se}^{2\bullet}$) crossover points in any of the three material systems calculated.

5.4. Extrinsic Dopants: Processing, Microstructure, and Performance

5.4.1. Point Defects and Doping Efficiency

DFT reveals that changing the dopant species in PbSe can alter the types of point defects that are present in the material. These results are further confirmed by the fact that the types of defects that were predicted by our DFT study align well with the documented behavior of doping efficiency in PbSe. Doping efficiency is the relationship between the quantity of dopant added and the resulting number of charge carriers, which is critical to increasing carrier concentration to its optimal level. There is not a perfect relationship between the quantity of dopant that is added and the resulting number of carriers. This is because, in addition to the desired substitutional point defects caused by doping, additional defects of opposite charge (compensating defects) also form. In Na and K-doped PbSe, these compensating defects manifest as Se vacancies while in Ag-doped PbSe these defects manifest as cations sitting at interstitial sites, both of which contribute electrons to the system rather than holes. Ultimately compensating defects will limit the maximum carrier concentration by pinning the Fermi level at the energy crossover, because the compensating defects become the dominant defect and p-type dopants cannot be added without the creation of defects that add electrons to the system.[228–230]

The DFT results show that the energy crossover in Ag-doped PbSe occurs at a higher E_F than in Na and K-doped PbSe, indicating that compensating defects should occur at lower levels of doping, lowering the p-type doping efficiency. As illustrated in **Figure 5.8**, the p-type doping efficiencies predicted by our calculations are consistent with prior reports of carrier concentrations in doped PbSe, where Ag-doped PbSe shows a strong deviation from perfect doping efficiency

(and a low maximum p-type carrier concentration) compared to its Na and K-doped counterparts.[213,214,216] Ag's amphoteric behavior, which results in its donation of both holes and electrons to lead chalcogenides, has previously been linked to a combination of interstitial point defects and precipitates in PbTe.[31,32] In PbSe, specifically, precipitates have been predicted to form when the concentration of Ag is between 0.5% and 1%.[213] Although our DFT calculations only investigate the energies of point defects, the finding that Ag does not occupy cation sites, supports the narrative that Ag forms interstitials which may lead to its low solubility. Furthermore, the large deviation from ideal doping efficiency of Ag-doped lead chalcogenides is supported by the idea that Ag interstitials form at lower levels of doping which results in the addition of electrons rather than holes to the system. In summary, DFT predicts that the type of dopant used in a material can alter the underlying point defects. Using PbSe as a model system, we were able to prove the validity of this premise by showing that the specific types of point defects predicted to be present in doped PbSe are also those that are necessary to produce the known changes in doping efficiency.

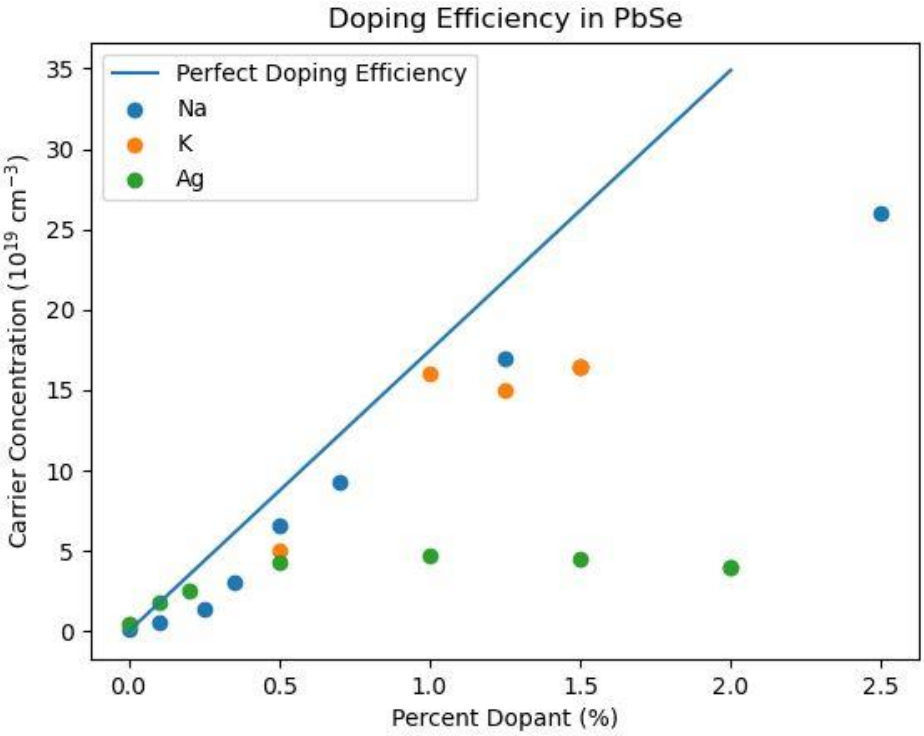

Figure 5.8. A plot of data collected from literature illustrating the difference in doping efficiency of Ag-doping[213], Na-doping[214], and K-doping[216] in the PbSe thermoelectric system.

5.4.2. Low Angle Grain Boundaries

LAGBs are potentially of interest because they are formed by arrays of dislocations, which are thought to be ideal for scattering intermediate wavelength phonons. This has made dislocations the focus of multiple studies aiming to decrease lattice thermal conductivity in thermoelectric materials.[46,100,148] However, the formation mechanism of LAGBs is important. Recrystallization (the formation of new strain free grains) is driven by the reduction of stored energy in a material.[231] If LAGBs and subgrains form as a result of recrystallization, then this may reduce phonon scattering in thermoelectric materials. In terms of thermal stability, LAGBs generally exhibit lower defect energies than HAGBs, making them less susceptible to high temperature mass loss via sublimation.[232] The fact that LAGBs and subgrain formation can influence material volatility as

well thermal transport makes controlling these defects important to thermoelectric performance. This investigation reveals a definitive change in the prevalence of LAGBs that is dependent on the type of dopant being used. In this section, several mechanisms are discussed that may contribute to the specific trend in decreasing LAGB density as dopants change from Na to K to Ag in PbSe.

For dislocation stacking (and therefore LAGB formation) to occur, dislocations need to be mobile. In ceramics this happens at high homologous temperatures and pressures when dislocation creep occurs, meaning that stress exponents exceed 3.[233–236] Past studies have shown how creep affects chalcogenide-based thermoelectrics during high temperature operation, but extreme conditions can be present during processing as well.[200,237,238] During the synthetic and post-synthetic processing performed in this investigation, the only step that exposes materials simultaneously to high temperatures and pressures is SPS. Specifically, samples are exposed to pressures of 40 MPa and temperatures as high as 550 °C (0.61T_m of PbSe). These conditions are presumably adequate to create dislocation motion in PbSe, as they are in excess of the conditions that produce a stress exponent of n=4.4 in its structural analogue, PbTe, at 400 °C (0.56T_m of PbTe) with pressures ranging from 7-35 MPa.[238]

Because PbSe is exposed to creep conditions during SPS, it will either act as a Class I material (with stress exponent close to n=5), in which subgrain form easily and dislocation climb is the dominant mechanism, or a Class II material (with stress exponent closer to n=3) in which dislocation glide dominates, and subgrains form with more difficulty.[233–236] Generally speaking, non-metals with $r_{anion}/r_{cation} < 2$ exhibit Class I behavior, and so one would expect PbSe (much like PbTe) would have a stress exponent closer to n=5.[239] Additionally, it has been shown in a

variety of ionic rocksalt compounds, that pure ceramics (such as NaCl, KCl, KBr, and CoO) achieved subgrain formation at lower temperatures and pressures than their alloyed counterparts (such as KCl-KBr, KCl-NaCl, and impure CoO).[234–236,240] Specifically in the case of CoO, the stress exponent decreased from n=4.6 to n=3.25 with the addition of just 0.5% impurities.[240] These studies indicate that although some pure ceramics have high stress exponents and display Class I behavior, that it is possible for impurities to reduce the stress exponents to a regime in which materials display Class II behavior.[234–236,240]

Specifically, Figure 5.1 illustrates that the addition of 2% aliovalent cation impurities alters the prevalence of subgrains and LAGBs in the final sintered material. The exact mechanism or combination of mechanisms is unknown, but several mechanisms could contribute to this phenomenon. One possible explanation for the change in LAGB density is that adding impurities reduces the dislocation mobility during SPS, and in some cases, to the point where dislocations cannot coalesce to form LAGBs. When dislocation glide is the dominant mechanism, dislocation mobility is impeded by the dragging of solute ion atmospheres, and the resultant steady state creep rate is inversely proportional to the square of the mismatch in cation size ($\dot{\epsilon} \propto 1/e^2$).[233] In other words, a large cation mismatch (e, which is related to strain) will result in a decrease in the dislocation creep rate ($\dot{\epsilon}$) and an increase in the time needed to form LAGBs. Assuming the reduction in creep rate is based solely on the cation size deviation from Pb^{2+}, it would be expected that increasing creep resistance follows the trend: $Ag^+ < Na^+ < K^+$. This is because the cation radius of Pb^{2+} is 119 pm, while the radii for the Ag^+, Na^+, and K^+ cations are 115 pm, 102 pm, and 138 pm (resulting in radial deviations of -4 pm, -17 pm, and 19 pm, respectively). Furthermore, although the difference in cation radii of Na^+ and K^+ from Pb^{2+} are -17 pm and 19 pm, respectively,

the change in volume of a crystal due to the substitution of a smaller cation is less than the change in volume produced by substituting larger cation with the same deviation in size from the original cation.[241] This difference in lattice strain can help explain the difference in LAGB density between Na and K-doped PbSe despite similar size deviations of these substitutional cations from Pb^{2+}.

The behavior of Ag-doped PbSe, however, does not follow the above trend based on cation size difference alone. One consideration not accounted for was that the DFT study shows that Ag^{+} is most likely an interstitial defect, while Na^{+} and K^{+} sit on cation sites. Because Ag^{+} is large for an interstitial cation, it will result in much more strain in the lattice than if it was a on a cation site. Therefore, when accounting for the point defects present in the system, one should observe an increasing lattice strain from each dopant in the order Na^{+}, followed by K^{+}, followed by Ag^{+}. Additionally, in Ag-doped PbSe specifically, the role of precipitates on dislocation mobility cannot be ignored. Because this compound is suspected to have precipitates at concentrations above 1%, it must be assumed that these impede dislocation mobility as well.[213] As a result, it remains to be determined which mechanism (interstitials or precipitates) inhibits dislocation mobility to a larger degree, but either way it can be hypothesized that the presence of Ag results in atomic and nanoscale structures and defects that impede the mobility of dislocations and prevent LAGBs from forming.

Another explanation for the variation in LAGB density is that stress relaxation mechanisms such as recovery through polygonization and recrystallization that can occur concurrently with deformation during high temperature creep.[231,242] During hot plastic deformation, strain softening can occur in parallel with deformation and results in the reduction and redistribution of dislocation

density, as well as the potential nucleation and growth of stress free grains through the migration of HAGBs in what is known as dynamic recrystallization. It has also been documented that in addition to processing parameters such as temperature, degree of deformation, and deformation rate, the recrystallization process can be influenced by material properties such as stacking fault energy, second phase particles, and the presence of foreign atoms.[231] Because of the dependence of recrystallization on atomic and nanoscale structures, it is feasible that the variation in dopants (and the defects that they engender) may have an influence over the recrystallization rate in doped PbSe. As a result, some materials may fully undergo dynamic recrystallization or polygonization during SPS while others do not, which would result in varying degrees of subgrain formation, like those observed.

In summary, it was confirmed that creep occurs in PbSe during SPS, and that the addition of dopants to PbSe influences the subgrain structure in the final material. Furthermore, it is hypothesized that both dynamic recrystallization and changes in dislocation mobility contribute to the final microstructure of PbSe but acknowledge that the exact relationship between these two mechanisms is not perfectly understood. To fully understand the relationship between dopants, point defects, and post-processed material microstructure, more in-depth creep studies need to be performed on doped semiconducting materials. With improved knowledge of these mechanisms, informed modification of sintering conditions (such as time, temperature, and pressure) based on dopant species and material composition could lead to better control over final material microstructure, which is vital to optimizing thermoelectric performance.

5.4.3. Grain Size

Designing a thermoelectric material with a tailored grain size is important for a variety of reasons. First, minimizing grain size is beneficial for reducing lattice thermal conductivity because the increase in the number of grain boundaries assists in the scattering of large wavelength phonons.[16,121,243] However, as shown in Chapter 2, in more ionic material systems with low dielectric constants, including some heavily alloyed forms of PbSe, grain boundaries are capable of creating a charge carrier screening effect that is detrimental to low temperature electrical conductivity.[30] Therefore, when optimizing grain structure in materials that are known to be more ionic, larger grains may actually result in an improvement in efficiency in low temperature regimes. One such recent example is Mg_3Sb_2, in which it was recently found that larger grains resulted in higher overall thermoelectric efficiency.[83] These works emphasize the importance of considering the impact of microstructure on both phonon scattering and charge carrier mobility when engineering thermoelectric materials.

In addition to optimizing transport properties, grain size may also affect a material's mass loss rate at elevated operating temperatures, due to the presence of grain boundaries at the surface of a material. Grain boundaries are known to be sources of elemental segregation, dislocations, and changes in surface topology, all of which may increase sublimation mass loss.[224–226] With these considerations in mind, it is clear that thermoelectric materials should be designed with specific grain sizes selected to achieve both optimal efficiency and reduced material degradation. Understanding the inherent tendency of a material to develop certain grain sizes based on dopant species is important so that processing can be adjusted to optimize performance. In this study we not only revealed the changes in post-synthetic grain size due to doping species, but we also

introduced the “double sieving” method which allowed us to synthesize materials with the desired microstructure.

The solution hardening rate in ionic compounds can be increased by an order of magnitude by introducing aliovalent cations into a material rather than isovalent cations, and it is widely accepted that this is caused by the compensating point defects that form in conjunction with the aliovalent cations.[244] As shown earlier, different dopants result in different combinations of point defects and compensating defects, and as a result, it is not surprising that PbSe samples doped with different elements had observably different mechanical properties when undergoing hand grinding to obtain powder for SPS solidification. To eliminate the possibility that differences in mechanical properties resulted in different sized powders and powder size distributions, double sieving was used to control the maximum and minimum powder size prior to SPS, which helped with the control of final PbSe grain size (not including the LAGBs that formed during SPS due to creep). In this experiment large grain Na-doped PbSe samples were produced with comparable grain sizes to PbSe-2%Ag (see Figure 5.3). Obtaining large grains in PbSe is significant because large grains will reduce low temperature suppression of electrical conductivity.[30] Therefore the ability to synthesize PbSe with a high carrier concentration, provided by a high efficiency dopant like Na, while also obtaining the desired grain size is important for optimizing efficiency. This manipulation of grain size illustrates that although a change in dopant species can alter grain size, if these changes are understood from the outset of material synthesis, intentional modifications to processing can be made to account for these changes.

5.4.4. Sublimation and Microstructure

Sublimation is a major source of degradation in thermoelectric devices which can cause cross-sectional reduction of the thermoelements and can eventually lead to mechanical failure of device components.[211] Because thermoelectric modules should ideally operate for years at elevated temperatures the materials must be robust to sublimation over extended periods of time. Despite the risk that sublimation poses, it is often overlooked as it is not easily identifiable in during transport measurements. This is because when obtaining transport data, thermal cycling lasts for a relatively short period of time, resulting in only minor sublimation. The amount of material that is lost is often not enough to manifest itself as an artifact in the transport data. In addition, if sublimation does take place, the surface pores and pock marks that form are on the order of microns, which is too small to be observed with the naked eye, and too large to be very noticeable when performing TEM or other high-resolution with limited fields of view. In PbSe specifically, PbSe(g) is the dominant gaseous species, leading to the hypothesis that high temperature mass loss is due to sublimation of the parent phase, and not necessarily due to the sublimation of the dopant or a second phase.[245]

By utilizing the versatility of the SEM, combination of imaging and EBSD were used to confirm the importance of microstructure in facilitating mass loss. Imaging and EBSD both reveal that pores form at grain boundaries upon exposure to temperatures above 500 K. The inclusion of SEM-EDS (as seen in Figure 5.5) helps confirm these boundaries have similar composition to the grains and reinforces that any preferential sublimation at the boundaries is due to structural imperfections of the boundaries rather than presence of a second phase. Additionally, EBSD in Figure 5.3 shows pores form in the presence of both LAGBs and HAGBs, and further reveals that

HAGBs were often the nucleation sites for pore formation, but the pores then have a tendency to grow along LAGBs and HAGBs as sublimation continues.

Pure PbSe has on average the least mass loss compared to PbSe samples with p-type dopants added (Figure 5.6a). This occurs despite pure PbSe having the smallest average grain size (as seen in Figure 5.1), and therefore the least favorable microstructure for preventing sublimation. So, despite having the highest energy defects at its surface, pure PbSe still loses less mass on average during annealing than all the doped samples. Unlike pure PbSe, the doped samples experience decreasing average mass loss as dopants change from Na, to K, to Ag. This trend in mass loss also corresponds to increasing grain size in the doped samples, and therefore the mass loss of these samples cannot be directly compared without ruling out the influence of microstructure.

Although samples were doped with the same nominal amount of dopant, it is known that the carrier concentration of these samples can vary by as much as an order of magnitude (as seen in Figure 5.8).[213,214,216] The variation in doping efficiency brings into question whether the absolute amount of dopant incorporated into a material's lattice structure affects the sublimation. In other words, it is interesting to consider whether it is more beneficial to dope a material using a small amount of an efficient dopant rather than using a large amount of a less efficient dopant. To deconvolute both the effect of grain size and test the effect of dopant species and concentration on sublimation, large grained PbSe-2%Na and large grained PbSe-0.4%Na were synthesized using the "double sieving" method. The lower concentration of Na was selected to be 0.4% to provide approximately the same carrier concentration as 2%Ag in PbSe based on the respective doping

efficiencies. Sublimation mass loss in Figure 5.6b shows there is a sizeable reduction in mass loss when the amount of Na doping is reduced from 2% to 0.4%, indicating that adding less total dopant to a material is beneficial for reducing mass loss. This is consistent with the fact that pure PbSe appears to be more stable than any of the doped compounds. Despite this reduction, the mass loss in large grained PbSe-0.4%Na samples is still comparable to PbSe-2%Ag.

It should be noted that no conclusions can be made concerning the relative sublimation rates of different dopants due to several factors. The first is that even when adjusting powder synthesis to increase grain size, there is still a variation in LAGBs population, and this can contribute to sublimation differences. Although, it appears that LAGBs are not nearly as volatile as HAGBs (which can be seen in Figure 5.3b), it is still a concerning difference in microstructure that must be accounted for. Secondly, because of the error in mass measurements discussed earlier, the average sublimation rates of large grained PbSe-0.4%Na and PbSe-2%Ag are too similar to each other to derive any meaningful conclusions concerning the difference in sublimation rate due to dopant species. Despite these limitations, the sublimation experiments still suggest that the sublimation of PbSe increases due to the presence p-type dopants, and that the concentration of dopant added affects the thermal stability of doped PbSe compounds. This study also provides further evidence of the influence of microstructure on sublimation and shows why understanding how dopants affect microstructure is necessary for producing more robust thermoelectric materials.

5.5. Summary and Conclusions

In this study the PbSe system is used to emphasize the care that should be taken when selecting dopant species to extrinsically dope thermoelectric materials. Conventional practice suggests that dopants are mostly utilized for the improvement of carrier concentration, while providing the additional benefit of thermal conductivity reduction through point defect scattering. This chapter illustrates how the introduction of different dopant species can change the underlying point defects, which affects doping efficiency as well as mesoscale microstructural features. These large-scale changes in microstructure, such as changes in average grain size and LAGB distribution, subsequently influence thermoelectric material efficiency as well as material degradation due to sublimation. Furthermore, it is shown how implementing intentional processing techniques (like “double sieving” or changing processing conditions during SPS) can result in a desired microstructure that enables a material to achieve an optimal combination of thermoelectric efficiency and thermal stability. In conclusion, the idea is put forth that in order to achieve true material optimization, it is essential to understand the broader implications of selecting particular dopants for a thermoelectric material system, because dopants can alter material microstructure and subsequently overall thermoelectric performance.

Chapter 6. Summary, Conclusions, and Future Work

6.1. Summary and Conclusions

The purpose of this dissertation was to investigate the relationship between processing, microstructure, and the performance of thermoelectric materials, while emphasizing the importance of understanding the often-overlooked mesoscale. With the additional information provided by the documentation of this length scale, using techniques such as EBSD, mechanisms governing bulk thermoelectric processing were explored and thermoelectric design principles were revealed.

6.1.1. Bulk Thermoelectric Processing

6.1.1.1. Spark Plasma Sintering

Spark Plasma Sintering is a bulk processing sintering technique used for mechanical strengthening that was previously thought to cause no changes in thermoelectric performance (beyond potentially lowering lattice thermal conductivity due to the increased presence of grain boundaries). Through the investigation of $NaPb_mSbTe_{m+2}$ (SALT) compounds it was found that SPS did in fact change the electronic behavior these samples, yielding nearly intrinsic n-type behavior in samples that were degenerately p-type doped prior to SPS. Mesoscale chemical and structural analysis preformed in conjunction with synchrotron x-ray diffraction revealed that the non-SPSed samples were two-phase materials with separate Pb-rich and Sb-rich phases. Through mesoscale analysis it was found that during SPS, Sb diffuses into the main phase, making the compound a more homogenous solid solution. Because Sb diffuses into the main lattice, Sb^{3+} cations replace Pb^{2+} on Pb-sites, resulting in an increase in negative charge carriers. This

investigation ultimately helped produce optimized SALT compounds with large zT_{avg}, but more importantly, provided evidence that SPS is a more complex process than previously thought. These results suggest that not only is chemical diffusion possible during SPS, but that it must be accounted for in order to synthesize fully optimized thermoelectrics.

6.1.1.2. Melt-Centrifugation and Induction Hot Pressing

Both Melt-Centrifugation and Induction Hot Pressing (followed by thermal annealing) of Te-rich BST compounds resulted in porous samples that were more efficient than their fully dense counterparts. Melt-Centrifugation proved useful in introducing a variety of defects into the BST matrix, and S/TEM characterization in combination with thermal modeling confirmed the benefits that these defects had on energy conversion efficiency. However, Melt-Centrifugation is extremely kinetic, and it is difficult to modify the microstructure of BST in a controlled way using this synthetic process. Annealing Te-rich Induction Hot Pressed BST proved to be a highly controllable process that can create a specific porosity based on the time and temperature of the anneal. By combining deformation modeling with a study of nano and mesoscale structures, it was discovered that creep during expansion and pore formation is responsible for the stepping of twin boundaries, and as a result, the increase in grain boundary dislocations in BST. In conclusion, this study identified creep as a key mechanism responsible for both the porosity and defect formation, the latter of which causes a decrease in lattice thermal conductivity.

6.1.1.3. Doping and Processing Considerations

Extrinsic dopants have typically been treated as a method to increase carrier concentration, with little consideration given to their additional effects on thermal electric materials (beyond a

decrease in lattice thermal conductivity due to point defect scattering). By using PbSe as a model system, it was shown that this premise is false, and that extrinsic dopants cause the generation of point defects (substitutional, interstitial, and sometimes compensating anion vacancies), which in turn cause drastic changes in grain size and the prevalence of low-angle grain boundaries. DFT reveals that different dopant species will generate different point defects, which can alter the mechanical properties of PbSe. Due to these altered mechanical properties, using identical powder processing and SPS conditions for samples with different dopants will result in different distributions of defects that can be observed in EBSD. By developing an understanding of dopant-microstructure relationships, material processing conditions can be altered to yield optimized microstructures. These results are significant to the field of thermoelectricity because the concept of dopant-microstructure interaction can be generalized and adopted in the study of any semiconducting thermoelectric material that utilizes extrinsic dopants.

6.1.2. The Mesoscale and Thermoelectric Design Principles

6.1.2.1. Grain Boundary Screening

Conventional wisdom suggests that materials with smaller grains are always more effective thermoelectrics than their larger grained counterparts because small grain materials have more grain boundaries which are known to scatter phonons, thereby lowering lattice thermal conductivity. However, it was shown in Chapter 2 that some small grain materials have lower electrical conductivities (at low temperatures), lowering their zT_{avg}. Prior to this investigation the culprit of this conductivity suppression was thought to be ionized impurity scattering. Ionized impurity scattering should occur uniformly throughout a material, yet EBSD analysis helped prove

that this anomalous conductivity effect is dependent on grain size, thereby ruling out ionized impurity scattering as the mechanism causing electrical conductivity suppression, and suggesting that this effect is related to grain boundaries. Further nanoscale analysis established that grain boundaries are chemically identical to their surrounding grains (within the detection limit of STEM-EDS) in both Te and Se based compounds. The microstructural analysis of these compounds helped support the theory that this conductivity suppression is due to an intrinsic property of the pure material, rather than due to chemical segregation at the grain boundaries. Materials with higher dielectric constants (high m, less ionic materials) often did not experience any suppression, while $NaPb_mSbQ_{m+2}$ compounds with lower dielectric constants lower (low m, more ionic materials) displayed electrical conductivity curves with a clear grain size dependance. In summary, it was proven that in more ionic materials, small grain sizes suppress electrical conductivity, which runs counter to conventional wisdom that small grain sizes are always preferable in thermoelectric materials. As a result, a new design principle was established which suggests that grain sizes need to be optimized to account for both electrical conductivity suppression due to material ionicity in addition to thermal conductivity reduction due to phonon scattering.

6.1.2.2. Dependence of Sublimation on Doping and Microstructure

Thermal stability is crucial to thermoelectric performance because thermoelectric materials often need to operate for long periods of time in extreme environmental conditions. However, most research on thermoelectric materials usually focuses on energy conversion efficiency alone, which can lead to a lack of understanding of how materials will truly perform during operation. Therefore, in addition to microstructure analysis, Chapter 5 also investigated the effects of doping on

sublimation. Qualitative evidence of the dependence of sublimation on microstructure was provided by EBSD of annealed large grain Ag-doped and Na-doped PbSe samples. These samples revealed that pores formed via sublimation of PbSe at high-angle grain boundaries rather than within grains. Quantitatively, annealing experiments revealed that doped samples lost more mass than undoped PbSe, which was further supported by the fact that there is a decrease in sublimation when Na content is decreased from 2% to 0.4% in doped PbSe. In conclusion, although energy conversion efficiency is vital for thermoelectric performance, this work established that when designing thermoelectric materials holistically, the relationship between doping, microstructure, and sublimation should be considered in order to produce materials that are thermally stable as well as efficient.

6.2. Future Work

This dissertation illustrated the importance of analyzing microstructural defects across a variety of length scales to identify mechanisms and design principles that are critical for designing thermoelectric materials with both high thermoelectric efficiency and high thermal stability. As a result, this work also motivates continuing research in two major areas that are related to maintaining the stability of microstructural defects during processing and operation.

6.2.1. Study of Creep Deformation

As established in both Chapters 4 and 5, creep is a deformation mechanism that has the potential to benefit thermoelectric performance, if understood and utilized correctly. Chapter 5 describes how creep is induced in chalcogenides during powder sintering by exposing materials to simultaneous high temperature and pressure regimes. Furthermore, it was shown how variations

in the composition of PbSe due to extrinsic doping can change the density of low-angle grain boundaries present in the final samples. Unfortunately, the exact mechanisms that are induced during creep are not understood, and therefore a more in depth investigation involving the control of pressure, time, and temperature could enable the investigating the fundamental mechanisms behind low-angle grain boundary formation that was introduced in Chapter 5. By subjecting PbSe, BST, or other ceramic thermoelectric materials to controlled deformation in different creep regimes (e.g. diffusional creep vs. power-law creep), useful information regarding time, temperature, and pressure profiles required to obtain specific amounts of low-angle grain boundaries formation, twin boundary formation and stepping could be obtained. Furthermore, by performing these creep studies in conjunction with speed of sound and other conventional bulk thermoelectric property measurements, it could be determined whether these microstructures form as a result of strain relaxation mechanisms, or if these microstructures ultimately assist in the overall decrease in lattice thermal conductivity. This would inform future scientists on whether creep, or specifically what creep regimes, are beneficial for the overall performance of thermoelectric materials.

6.2.2. Study of Defect Composition

During the study of extrinsic doping in PbSe, it was found that different intrinsic dopants formed different types of point defects, and that these point defects likely result in varying levels of lattice strain. Furthermore, point defects have a tendency to segregate to edge dislocations, due to the strain relaxation that these defects provide.[246] As a result, one might expect different dopants to segregate more strongly to defect sites. In fact, a recent study by Yu, *et al.* used Atom Probe Tomography (APT) to document the increased concentration of Ag in the vicinity of dislocations

in PbTe. Furthermore, this same study incorporated Debye-Callaway thermal modeling with experimental thermoelectric transport data to show how the composition of dislocations contributes to reducing lattice thermal conductivity.[247] To continue the work started in Chapter 5, atomic scale resolution imaging and analytical techniques will be critical to developing a stronger understanding of the relationship between dopant species and dislocation composition and their effects on both dislocation mobility (during creep) and thermoelectric transport. This could be achieved by combining aberration corrected STEM imaging (with sub angstrom resolution) and analytical electron microscopy techniques, with APT (which can detect single atoms compared to EDS which has a detectability limit of ~1000 parts per million).

The use of high sensitivity and high spatial resolution analytical techniques can benefit more than just the study of dislocations. Grain boundaries and interfaces are also known to possess higher concentrations of impurities than the bulk sample.[16] Knowing the true composition of grain boundaries is useful for understanding sublimation and thermoelectric transport. As seen in this dissertation, grain boundaries sublimate more easily than the defect free material and therefore when if grain boundaries have a different composition than the bulk, that may indicate that certain elements are sublimating at a disproportionate rate. This is especially critical to know in the case of extrinsic dopants where small variations in composition can vastly change the carrier concentration, and subsequently the thermoelectric properties of a material. Increased chemical sensitivity provided by APT may even enable scientists to differentiate between the amount of segregation at different types of grain boundaries such as high-angle, low-angle, and special (e.g. twin) grain boundaries. Although APT cannot identify grain orientation, by combining the techniques of Focused Ion Beam (FIB) and EBSD in SEM, all 5 macroscopic degrees of freedom

of grain boundaries can be determined using image reconstruction in what is known as 3D EBSD. Now that mesoscale analysis has established the severity of sublimation in certain chalcogenide thermoelectrics, higher resolution imaging, analytical, and diffraction techniques will become invaluable in determining the extent to which sublimation alters performance and the level to which this can be controlled by careful microstructural design.

References

1. Kong, L. B. *et al. Waste Energy Harvesting*. **24**, (2014).

2. Velmre, E. Thomas Johann Seebeck (1770-1831). *Proc. Est. Acad. Sci. Eng.* **13**, 276–282 (2007).

3. Riffat, S. B. & Ma, X. Thermoelectrics: A review of present and potential applications. *Appl. Therm. Eng.* **23**, 913–935 (2003).

4. Alam, H. & Ramakrishna, S. A review on the enhancement of figure of merit from bulk to nano-thermoelectric materials. *Nano Energy* **2**, 190–212 (2013).

5. Snyder, G. J. & Toberer, E. S. Complex thermoelectric materials. *Nat. Mater.* **7**, 105–114 (2008).

6. Yee, S. K., LeBlanc, S., Goodson, K. E. & Dames, C. $ per W metrics for thermoelectric power generation: beyond ZT. *Energy Environ. Sci.* **6**, 2561–2571 (2013).

7. Zhang, H. & Talapin, D. V. Thermoelectric tin selenide: The beauty of simplicity. *Angew. Chemie - Int. Ed.* **53**, 9126–9127 (2014).

8. Snyder, G. J. & Snyder, A. H. Figure of merit ZT of a thermoelectric device defined from materials properties. *Energy Environ. Sci.* **10**, 2280–2283 (2017).

9. Sales, B. C. Electron Crystals and Phon lLasses: A new Path to Improved Thermoelectric Materials. *MRS Bull.* **23**, 15–21 (1998).

10. Daniels, L. M. *et al.* Phonon-glass electron-crystal behaviour by A site disorder in n-type

thermoelectric oxides. *Energy Environ. Sci.* **10**, 1917–1922 (2017).

11. Bulusu, A. & Walker, D. G. Review of electronic transport models for thermoelectric materials. *Superlattices Microstruct.* **44**, 1–36 (2008).

12. v. Muench, W. & Statz, H. Solid-to-solid diffusion in the gallium arsenide device technology. *Solid. State. Electron.* **9**, 939–942 (1966).

13. Wang, X. & Editors, Z. M. W. *Nanoscale Thermoelectrics*. **16**, (2014).

14. Kittel, C. *Introduction to Solid State Physics*. **25**, (John Wiley & Sons, Inc., 2005).

15. Girard, S. N. *et al.* High performance Na-doped PbTe-PbS thermoelectric materials: Electronic density of states modification and shape-controlled nanostructures. *J. Am. Chem. Soc.* **133**, 16588–16597 (2011).

16. Biswas, K. *et al.* High-performance bulk thermoelectrics with all-scale hierarchical architectures. *Nature* **489**, 414–418 (2012).

17. Zhao, L.-D., Dravid, V. P. & Kanatzidis, M. G. The panoscopic approach to high performance thermoelectrics. *Energy Environ. Sci.* **7**, 251–268 (2014).

18. He, J., Kanatzidis, M. G. & Dravid, V. P. High performance bulk thermoelectrics via a panoscopic approach. *Mater. Today* **16**, 166–176 (2013).

19. Vineis, C. J., Shakouri, A., Majumdar, A. & Kanatzidis, M. G. Nanostructured thermoelectrics: Big efficiency gains from small features. *Adv. Mater.* **22**, 3970–3980 (2010).

20. Pei, Y., Wang, H. & Snyder, G. J. Band engineering of thermoelectric materials. *Adv. Mater.* **24**, 6125–6135 (2012).

21. Zeier, W. G. *et al.* Thinking Like a Chemist: Intuition in Thermoelectric Materials. *Angew. Chemie - Int. Ed.* **55**, 6826–6841 (2016).

22. Yang, J., Yip, H.-L. & Jen, A. K.-Y. Rational Design of Advanced Thermoelectric Materials. *Adv. Energy Mater.* **3**, 549–565 (2013).

23. Biswas, K. *et al.* Strained endotaxial nanostructures with high thermoelectric figure of merit. *Nat. Chem.* **3**, 160–166 (2011).

24. Qiu, B. *et al.* First - Principles Simulation of Electron Mean - Free - Path Spectra and Thermoelectric Properties in Silicon. *Europhys. Lett.* **109**, 1–9 (2015).

25. Toberer, E. S., Zevalkink, A. & Snyder, G. J. Phonon engineering through crystal chemistry. *J. Mater. Chem.* **21**, 15843 (2011).

26. Kim, H.-S., Kang, S. D., Tang, Y., Hanus, R. & Jeffrey Snyder, G. Dislocation strain as the mechanism of phonon scattering at grain boundaries. *Mater. Horiz.* **3**, 234–240 (2016).

27. LeBlanc, S. Thermoelectric generators: Linking material properties and systems engineering for waste heat recovery applications. *Sustain. Mater. Technol.* **1**–**2**, 26–35 (2014).

28. Slade, T. J. *et al.* Absence of Nanostructuring in NaPbmSbTem+2: Solid Solutions with High Thermoelectric Performance in the Intermediate Temperature Regime. *J. Am. Chem. Soc.* **140**, 7021–7031 (2018).

29. Slade, T. J. *et al.* High Thermoelectric Performance in PbSe – NaSbSe 2 Alloys from Valence Band Convergence and Low Thermal Conductivity. *Adv. Energy Mater.* **1901377**, 1–12 (2019).

30. Slade, T. J. *et al.* Understanding the thermally activated charge transport in NaPb m SbQ m+2 (Q = S, Se, Te) thermoelectrics: weak dielectric screening leads to grain boundary dominated charge carrier scattering. *Energy Environ. Sci.* **13**, 1509–1518 (2020).

31. Witting, I. T., Grovogui, J. A., Dravid, V. P. & Snyder, G. J. Thermoelectric transport enhancement of Te-rich bismuth antimony telluride (Bi0.5Sb1.5Te3+x) through controlled porosity. *J. Mater.* **6**, 532–544 (2020).

32. Yamini, S. A. *et al.* Rational design of p-type thermoelectric PbTe: Temperature dependent sodium solubility. *J. Mater. Chem. A* **1**, 8725–8730 (2013).

33. Volykhov, A. A., Yashina, L. V. & Shtanov, V. I. Phase relations in pseudobinary systems of germanium, tin, and lead chalcogenides. *Inorg. Mater.* **42**, 596–604 (2006).

34. Minnich, A. J., Dresselhaus, M. S., Ren, Z. F. & Chen, G. Bulk nanostructured thermoelectric materials: current research and future prospects. *Energy Environ. Sci.* **2**, 466 (2009).

35. Lalonde, A. D., Ikeda, T. & Snyder, G. J. Rapid consolidation of powdered materials by induction hot pressing. *Rev. Sci. Instrum.* **82**, 025104 (2011).

36. Bernard-Granger, G. *et al.* Spark plasma sintering of a commercially available granulated zirconia powder: Comparison with hot-pressing. *Acta Mater.* **58**, 3390–3399 (2010).

37. Williams, D. B. & Carter, C. B. *Transmission Electron Microscopy Part 1: Basics*. (Springer Science+Buisness Media, LLC., 2009).

38. Williams, D. B. & Carter, C. B. *Transmission Electron Microscopy Part 2: Diffraction*. (Springer Science+Buisness Media, LLC., 2009).

39. Williams, D. B. & Carter, C. B. *Transmission Electron Microscopy Part 3: Imaging*. (Springer Science+Buisness Media, LLC., 2009).

40. von Alfthan, S. *et al.* The Structure of Grain Boundaries in Strontium Titanate: Theory, Simulation, and Electron Microscopy. *Annu. Rev. Mater. Res.* **40**, 557–599 (2010).

41. Nellist, P. D. Scanning Transmission Electron Microscopy. in *Springer Handbook of Microscopy* (eds. Hawkes, P. W. & Spence, J. C. H.) 49–99 (Springer International Publishing, 2019). doi:10.1007/978-3-030-00069-1_2

42. Pennycook, S. J. The impact of STEM aberration correction on materials science. *Ultramicroscopy* **180**, 22–33 (2017).

43. Neikov, O. D. & Yefimov, N. A. Chapter 1 - Powder Characterization and Testing. in *Handbook of Non-Ferrous Metal Powders: Technologies and Applications* (eds. Neikov, O. D., Naboychenko, S. S. & Yefimov, N. A. B. T.-H. of N.-F. M. P. (Second E.) 3–62 (Elsevier, 2019). doi:https://doi.org/10.1016/B978-0-08-100543-9.00001-4

44. Lejcek, P. Grain Boundaries : Description , Structure. *Grain Bound. Segreg. Met.* 239 (2010). doi:10.1007/978-3-642-12505-8

45. Ratanaphan, S., Yoon, Y. & Rohrer, G. S. The five parameter grain boundary character

distribution of polycrystalline silicon. *J. Mater. Sci.* **49**, 4938–4945 (2014).

46. Kim, S. I. *et al.* Dense dislocation arrays embedded in grain boundaries for high-performance bulk thermoelectrics. *Science (80-.).* **348**, 109–114 (2015).

47. Kowoll, T. *et al.* Contrast of backscattered electron SEM images of nanoparticles on substrates with complex structure. *Scanning* **2017**, 4907457 (2017).

48. Deal, A., Tao, X. & Eades, A. EBSD geometry in the SEM: Simulation and representation. *Surf. Interface Anal.* **37**, 1017–1020 (2005).

49. Wilkinson, A. J. & Britton, T. Ben. Strains, planes, and EBSD in materials science. *Mater. Today* **15**, 366–376 (2012).

50. Steinmetz, D. R. & Zaefferer, S. Towards ultrahigh resolution EBSD by low accelerating voltage. *Mater. Sci. Technol.* **26**, 640–645 (2010).

51. Childs, K. D. *et al.* Comparison of submicron particle analysis by Auger electron spectroscopy , time-of-flight secondary ion mass spectrometry , and secondary electron microscopy with energy dispersive x-ray spectroscopy. **14**, 2392–2404 (1996).

52. Mohan, A., Khanna, N., Hwu, J. & Joy, D. C. Secondary Contrast in the Variable Pressure Scanning Electron Microscope. *Scanning* **19**, 221–222 (1997).

53. Moore, M. A. & Douthwaite, R. M. Plastic Deformation Below Worn Surfaces. *Metall. Trans. A* **7A**, 1833–1839 (1976).

54. Yu, Y., Cagnoni, M., Cojocaru-Mirédin, O. & Wuttig, M. Chalcogenide Thermoelectrics

Empowered by an Unconventional Bonding Mechanism. *Adv. Funct. Mater.* **30**, (2020).

55. Zhang, Q. *et al.* Heavy doping and band engineering by potassium to improve the thermoelectric figure of merit in p-type PbTe, PbSe, and PbTe 1- ySe y. *J. Am. Chem. Soc.* **134**, 10031–10038 (2012).

56. Qiu, B., Bao, H., Zhang, G., Wu, Y. & Ruan, X. Molecular dynamics simulations of lattice thermalconductivityandspectral phononmean freepath of PbTe: bulk and nanostructures. *Comput. Mater. Sci.* **53**, 278–285 (2012).

57. Huang, X., Wang, X. & Cook, B. Coherent nanointerfaces in thermoelectric materials. *J. Phys. Chem. C* **114**, 21003–21012 (2010).

58. Lo, S. H., He, J., Biswas, K., Kanatzidis, M. G. & Dravid, V. P. Phonon scattering and thermal conductivity in p-type nanostructured PbTe-BaTe bulk thermoelectric materials. *Adv. Funct. Mater.* **22**, 5175–5184 (2012).

59. Chen, Z. G., Hana, G., Yanga, L., Cheng, L. & Zou, J. Nanostructured thermoelectric materials: Current research and future challenge. *Prog. Nat. Sci. Mater. Int.* **22**, 535–549 (2012).

60. Minnich, A. J., Dresselhaus, M. S., Ren, Z. F. & Chen, G. Bulk nanostructured thermoelectric materials: Current research and future prospects. *Energy Environ. Sci.* **2**, 466–479 (2009).

61. Wang, H. *et al.* High-performance Ag0.8Pb18+xSbTe20 thermoelectric bulk materials fabricated by mechanical alloying and spark plasma sintering. *Appl. Phys. Lett.* **88**, 1–4

(2006).

62. Zhou, M., Li, J. F. & Kita, T. Nanostructured AgPbmSbTem+2 system bulk materials with enhanced thermoelectric performance. *J. Am. Chem. Soc.* **130**, 4527–4532 (2008).

63. Quarez, E. *et al.* Nanostructuring, compositional fluctuations, and atomic ordering in the thermoelectric materials AgPbmSbTe2+m. The myth of solid solutions. *J. Am. Chem. Soc.* **127**, 9177–9190 (2005).

64. Androulakis, J. *et al.* Nanostructuring and high thermoelectric efficiency in p-type Ag(Pb 1-ySny)mSbTe2+m. *Adv. Mater.* **18**, 1170–1173 (2006).

65. Tan, G. *et al.* Non-equilibrium processing leads to recod high thermoelectric figure of merit in PbTe-SrTe. *Nat. Commun.* **7**, (2016).

66. Zhang, X. *et al.* Ion beam induced artifacts in lead-based chalcogenides. *Microsc. Microanal.* **25**, 831–839 (2019).

67. Huang, Z. Combining Ar ion milling with FIB lift-out techniques to prepare high quality site-specific TEM samples. *J. Microsc.* **215**, 219–223 (2004).

68. Bonifacio, C. S. *et al.* Removal of Ga Implantation on FIB-prepared Atom Probe Specimens Using Small Beam and Low Energy Ar+ Milling. *Microsc. Microanal.* **24**, 1118–1119 (2018).

69. Poudeu, P. F. P. *et al.* High Thermoelectric Figure of Merit and Nanostructuring in Bulk p-type Na1−x Pbm Sby Tem +2. *Angew. Chemie - Int. Ed.* **45**, 3835–3839 (2006).

70. Tan, G. *et al.* High Thermoelectric Performance in SnTe–AgSbTe2 Alloys from Lattice Softening, Giant Phonon–Vacancy Scattering, and Valence Band Convergence. *ACS Energy Lett.* **3**, 705–712 (2018).

71. Wu, D. *et al.* Superior thermoelectric performance in PbTe–PbS pseudo-binary: extremely low thermal conductivity and modulated carrier concentration. *Energy Environ. Sci.* **8**, 2056–2068 (2015).

72. Nielsen, M. D., Ozolins, V. & Heremans, J. P. Lone pair electrons minimize lattice thermal conductivity. *Energy Environ. Sci.* **6**, 570–578 (2013).

73. Lioutas, C. B., Frangis, N., Todorov, I., Chung, D. Y. & Kanatzidis, M. G. Understanding Nanostructures in Thermoelectric Materials: An Electron Microscopy Study of AgPb18SbSe20 Crystals. *Chem. Mater.* **22**, 5630–5635 (2010).

74. Hoang, K., Desai, K. & Mahanti, S. D. Charge ordering and self-assembled nanostructures in a fcc Coulomb lattice gas. *Phys. Rev. B - Condens. Matter Mater. Phys.* **72**, 064102 (2005).

75. Barabash, S. V., Ozolins, V. & Wolverton, C. First-Principles Theory of Competing Order Types, Phase Separation, and Phonon Spectra in Thermoelectric AgPbmSbTem+2 Alloys. *Phys. Rev. Lett.* **101**, 155705 (2008).

76. Zunger, A., Wei, S. H., Ferreira, L. G. & Bernard, J. E. Special Quasirandom Structures. *Phys. Rev. Lett.* **65**, 353–356 (1990).

77. El-Sharkawy, A. A., El-Azm, A. M. A., Kenawy, M. I., Hillal, A. S. & Abu-Basha, H. M.

Thermophysical properties of polycrystalline PbS, PbSe, and PbTe in the temperature range 300–700 K. *Int. J. Thermophys.* **4**, 261 (1983).

78. Ravich, Y. I., Efimova, B. A. & Smirnov, I. A. *Semiconducting Lead Chalcogenides*. (Springer, 1970).

79. Lee, Y. *et al.* Contrasting role of antimony and bismuth dopants on the thermoelectric performance of lead selenide. *Nat. Commun.* **5**, 3640 (2014).

80. He, J. *et al.* Role of Sodium Doping in Lead Chalcogenide Thermoelectrics. *J. Am. Chem. Soc.* **135**, 4624–4627 (2013).

81. Mao, J. *et al.* Manipulation of ionized impurity scattering for achieving high thermoelectric performance in n-type Mg3Sb2-based materials. *Proc. Natl. Acadamies Sci. USA* **114**, 10548 (2017).

82. Zhang, J. *et al.* Discovery of high-performance low-cost n-type Mg3Sb2-based thermoelectric materials with multi-valley conduction bands. *Nat. Commun.* **8**, 13901 (2017).

83. Kuo, J. J. *et al.* Grain boundary dominated charge transport in Mg3Sb2-based compounds. *Energy Environ. Sci.* **11**, 429–434 (2018).

84. Pan, L. *et al.* The Role of Ionized Impurity Scattering on the Thermoelectric Performances of Rock Salt AgPbmSnSe2+m. *Adv. Funct. Mater.* **26**, 5149–5157 (2016).

85. Wang, S. *et al.* Grain boundary scattering effects on mobilities in p-type polycrystalline SnSe. *J. Mater. Chem.* **5**, 10191–10200 (2017).

86. Lee, Y. K., Luo, Z., Cho, S. P., Kanatzidis, M. G. & Chung, I. Surface Oxide Removal for Polycrystalline SnSe Reveals Near-Single-Crystal Thermoelectric Performance. *Joule* **3**, 719–731 (2019).

87. He, J. *et al.* Morphology Control of Nanostructures: Na-Doped PbTe–PbS System. *Nano Lett.* **12**, 5979–5984 (2012).

88. Blum, I. D. *et al.* Dopant Distributions in PbTe-Based Thermoelectric Materials. *J. Electron. Mater.* **41**, 1583–1588 (2012).

89. Kim, Y.-J., Zhao, L.-D., Kanatzidis, M. G. & Seidman, D. N. Analysis of Nanoprecipitates in a Na-Doped PbTe–SrTe Thermoelectric Material with a High Figure of Merit. *ACS Appl. Mater. Interfaces* **9**, 21791–21797 (2017).

90. Lipskis, K., Sakalas, A. & Viscakas, J. Hall effect in thin CdSe films. *Phys. Status Solidi, A.* **5**, 793–801 (1971).

91. Orton, J. W. Interpretation of Hall mobility in polycrystalline thin films. *Thin Film Solids* **86**, 351–357 (1981).

92. Grovenor, C. R. M. Grain boundaries in semiconductors (Thesis). *J. Phys. C Solid State Phys.* **18**, 4079–4119 (1985).

93. Seto, J. Y. W. The electrical properties of polycrystalline silicon films. *J. Appl. Phys.* **46**, 5247–5254 (1975).

94. *Non-Tetrahedrally Bonded Elements and Binary Compounds I.* (Springer Berlin Heidelberg, 1998). doi:10.1007/10681727_719

95. *Non-Tetrahedrally Bonded Elements and Binary Compounds I*. (Springer Berlin Heidelberg, 1998). doi:10.1007/10681727_895

96. *Non-Tetrahedrally Bonded Elements and Binary Compounds I*. (Springer Berlin Heidelberg, 1998). doi:10.1007/ 10681727_881

97. Goldsmid, H. J. & Douglas, R. W. The use of semiconductors in thermoelectric refrigeration. *Br. J. Appl. Phys.* **5**, 386–390 (1954).

98. Poudel, B. *et al.* High-Thermoelectric Performance of Nanostructured Bismuth Antimony Telluride Bulk Alloys. *Science (80-.).* **320**, 634–638 (2008).

99. Zhao, H. *et al.* Engineering the Thermoelectric Transport in Half-Heusler Materials through a Bottom-Up Nanostructure Synthesis. *Adv. Energy Mater.* **7**, 1700466 (2017).

100. Chen, Z. *et al.* Vacancy-induced dislocations within grains for high-performance PbSe thermoelectrics. *Nat. Commun.* **8**, 1–8 (2017).

101. Zhang, Y. *et al.* A Mesoporous Anisotropic n-Type Bi2Te3 Monolith with Low Thermal Conductivity as an Efficient Thermoelectric Material. *Adv. Mater.* **24**, 5065 (2012).

102. Khan, A. U. *et al.* Nano-micro-porous skutterudites with 100% enhancement in ZT for high performance thermoelectricity. *Nano Energy* **31**, 152–159 (2017).

103. Rowe, D. M. *CRC Handbook of Thermoelectrics*. (CRC Press, 2012).

104. Liu, W. *et al.* New Insight into the Material Parameter B to Understand the Enhanced Thermoelectric Performance of Mg2Sn1−x−yGexSby. *Energy Environ. Sci.* **9**, 530–539

(2016).

105. Kang, S. D. *et al.* Enhanced stability and thermoelectric figure-of-merit in copper selenide by lithium doping. *Mater. Today Phys.* **1**, 7–13 (2017).

106. Wang, H., Lalonde, A. D., Pei, Y. & Snyder, G. J. The Criteria for Beneficial Disorder in Thermoelectric Solid Solutions. *Adv. Funct. Mater.* **23**, 1586 (2013).

107. Chasmar, R. P. & Stratton, R. The Thermoelectric Figure of Merit and its Relation to Thermoelectric Generators. *J. Electron. Control* **7**, 52–72 (1959).

108. Mahan, G. D. Figure of merit for thermoelectrics. *J. Appl. Phys.* **65**, 1578–1583 (1989).

109. Day, T. W., Zeier, W. G., Brown, D. R., Melot, B. C. & Snyder, G. J. Determining conductivity and mobility values of individual components in multiphase composite Cu1.97Ag0.03Se. *Appl. Phys. Lett.* **105**, 172103 (2014).

110. Bruggeman, D. A. G. Berechnung verschiedener physikalischer Konstanten von heterogenen Substanzen. I. Dielektrizitätskonstanten und Leitfähigkeiten der Mischkörper aus isotropen Substanzen. *Ann. Phys.* **416**, 636 (1935).

111. Landauer, R. Electrical conductivity in inhomogeneous media. *AIP Conf. Proc.* **40**, (1978).

112. Stroud, D. Generalized effective-medium approach to the conductivity of an inhomogeneous material. *Phys. Rev. B* **12**, 3368 (1975).

113. Cohen, M. H. & Jortner, J. Effective Medium Theory for the Hall Effect in Disordered

Materials. *Phys. Rev. Lett.* **30**, 696 (1973).

114. Juretschke, H. J., Landauer, R. & Swanson, J. A. Hall Effect and Conductivity in Porous Media. *J. Appl. Phys.* **27**, 838–839 (1956).

115. Bergman, D. J. & Levy, O. Thermoelectric Properties of a Composite Medium. *J. Appl. Phys.* **70**, 6821–6833 (1991).

116. Tritt, T. M. *Thermal Conductivity: Theory, Properties, and Applications*. (Springer Science & Buisness Media, LLC., 2004).

117. Zheng, Y. *et al.* Mechanically Robust BiSbTe Alloys with Superior Thermoelectric Performance: A Case Study of Stable Hierarchical Nanostructured Thermoelectric Materials. *Adv. Energy Mater.* **5**, 1401391 (2014).

118. Goldsmid, H. J. *Introduction to Thermoelectricity*. (Springer Berlin Heidelberg, 2016).

119. Goldsmid, H. J. Recent Studies of Bismuth Telluride and Its Alloys. *J. Appl. Phys.* **32**, 2198 (1961).

120. Casimir, H. B. G. Note on the conduction of heat in crystals. *Physica* **5**, 495–500 (1938).

121. Wang, Z., Alaniz, J. E., Jang, W., Garay, J. E. & Dames, C. Thermal conductivity of nanocrystalline silicon: Importance of grain size and frequency-dependent mean free paths. *Nano Lett.* **11**, 2206–2213 (2011).

122. Murdoch and Christopher A Schuh, H. A. "Estimation of grain boundary segregation enthalpy and its role in stable nanocrystlline alloy design. *J. Mater. Res.* **28**, 2154–2163

(2013).

123. Kirchheim, R. Reducing grain boundary, dislocation line and vacancy formation energies by solute segregation. I. Theoretical background. *Acta Mater.* **55**, 5129–5138 (2007).

124. Klemens, P. G. The thermal conductivity of dielectric solids at low temperatures (theoretical). *Proc. R. Soc. Lond. A. Math. Phys. Sci.* **208**, 108–133 (1951).

125. Kim, K., Lee, J., Kim, H. & Lee, Z. Quantitative Evaluation of Dislocation Density in Epitaxial GaAs Layer on Si Using Transmission Electron Microscopy. *Appl. Microsc.* **44**, 74–78 (2014).

126. Borup, K. A. *et al.* Measurement of the Electrical Resistivity and Hall Coefficient at High Temperatures. *Rev. Sci. Instrum.* **83**, 123902 (2012).

127. Iwanaga, S., Toberer, E. S., LaLonde, A. & Snyder, G. J. A High Temperature Apparatus for the Measurement of the Seebeck Coefficient. *Rev. Sci. Instrum.* **82**, 063905 (2011).

128. Kang, S. D. & Snyder, G. J. Transport property analysis method for thermoelectric materials: material quality factor and the effective mass model. *arXiv:1710.06896v1 [cond-mat.mtrl-sci]* (2017).

129. Cahill, David, G., Watson, S. K. & Pohl, R. O. Lower limit to the thermal conductivity of disordered crystals. *Phys. Rev. B* **46**, 6131 (1992).

130. Hu, L.-P. *et al.* Shifting up the optimum figure of merit of p-type bismuth telluride-based thermoelectric materials for power generation by suppressing intrinsic conduction. *NPG Asia Mater.* **6**, e88 (2014).

131. Hu, L., Zhu, T., Liu, X. & Zhao, X. Point Defect Engineering of High-Performance Bismuth-Telluride-Based Thermoelectric Materials. *Adv. Funct. Mater.* **24**, 5211 (2014).

132. Hao, F. *et al.* High Efficiency Bi2Te3-Based Materials and Devices for Thermoelectric Power Generation Between 100 and 300 °C. *Energy Environ. Sci.* **9**, 3120–3127 (2016).

133. Kim, H.-S. *et al.* High Thermoelectric Performance in (Bi0.25Sb0.75)2Te3 Due to Band Convergence Improved by Carrier Concentration Control. *Mater. Today* **20**, 452–459 (2017).

134. Mion, C., Muth, J. F., Preble, E. A. & Hanser, D. Thermal conductivity, dislocation density and GaN device design. *Superlattices Microstruct.* **40**, 338–342 (2006).

135. Klemens, P. G. The Scattering of Low-Frequency Lattice Waves by Static Imperfections. *Proc. Phys. Soc. Sect. A* **68**, 1113 (1955).

136. Carruthers, P. Scattering of Phonons by Elastic Strain Fields and the Thermal Resistance of Dislocations. *Phys. Rev.* **114**, 995 (1959).

137. Medlin, D. L., Erickson, K. J., Limmer, S. J., Yelton, W. G. & Siegal, M. P. Dissociated 1/3〈01¯11〉dislocations in Bi2Te3 and their relationship to seven-layer Bi3Te4 defects. *J. Mater. Sci.* **49**, 3970–3979 (2014).

138. Yang, F., Ikeda, T., Snyder, G. J. & Dames, C. Effective thermal conductivity of polycrystalline materials with randomly oriented superlattice grains. *J. Appl. Phys.* **108**, 034310 (2010).

139. Snyder, G. J. Application of the compatibility factor to the design of segmented and cascaded thermoelectric generators. *Appl. Phys. Lett.* **84**, 2436 (2004).

140. Zhang, C. *et al.* Enhanced Thermoelectric Performance of Solution-Derived Bismuth Telluride based Nanocomposites via Liquid Phase Sintering. *Nano Energy* **30**, 630–638 (2016).

141. Deng, R. *et al.* Thermal Conductivity in Bi0.5Sb1.5Te3+x and the Role of Dense Dislocation Arrays at Grain Boundaries. *Sci. Adv.* **4**, eaar5606 (2018).

142. Kim, Y. M. *et al.* Enhancement of Thermoelectric Properties in Liquid-Phase Sintered Te-Excess Bismuth Antimony Telluride Prepared by Hot-Press Sintering. *Acta Mater.* **135**, 297–303 (2017).

143. Rice, R. W. *Porosity of Ceramics*. (Marcel Dekker, 1998).

144. Lee, H. *et al.* Effects of Nanoscale Porosity on Thermoelectric Properties of SiGe. *J. Appl. Phys.* **107**, 094308 (2010).

145. Kashiwagi, M. *et al.* Enhanced Figure of Merit of a Porous Thin Film of Bismuth Antimony Telluride. *Appl. Phys. Lett.* **98**, 023114 (2011).

146. Heremans, J. P., Jaworski, C. M., Jovovic, V. & Harris, F. Thermoelectric Materials Having Porosity. (2012).

147. Qiao, J. *et al.* Tailoring Nanoporous Structures in Bi2Te3 Thin Films for Improved Thermoelectric Performance. *ACS Appl. Mater. Interfaces* **11**, 38075–38083 (2019).

148. Pan, Y. *et al.* Melt-Centrifuged (Bi,Sb)2Te3: Engineering Microstructure toward High Thermoelectric Efficiency. *Adv. Mater.* **30**, 1802016 (2018).

149. Xu, B. *et al.* Highly Porous Thermoelectric Nanocomposites with Low Thermal Conductivity and High Figure of Merit from Large-Scale Solution-Synthesized Bi2Te2.5Se0.5Hollow Nanostructures. *Angew. Chemie - Int. Ed.* **56**, 3546–3551 (2017).

150. Takashiri, M., Tanaka, S., Hagino, H. & Miyazaki, K. Combined Effect of Nanoscale Grain Size and porosity on Lattive Thermal Conductivity of Bismuth-Telluride-Based Bulk Alloys. *J. Appl. Phys.* **112**, 084315 (2012).

151. Hellman, O. & Broido, D. A. Phonon Thermal Transport in Bi2Te3 from First Principles. *Phys. Rev. B* **90**, 134309 (2014).

152. Sharp, J. W., Poon, S. J. & Goldsmid, H. J. Boundary Scattering and Thermoelectric Figure of Merit. *Phys. Status Solidi, A.* **187**, 507–516 (2001).

153. German, R. M., Suri, P. & Park, S. J. Review: Liquid Phase Sintering. *J. Mater. Sci.* **44**, 1–39 (2009).

154. Shtern, Y. I., Malkova, A. S., Pashinkin, A. S. & Fedorov, V. A. Heat Capacity of the n-Bi2Te2.88Se0.12 and p-Bi0.52Sb1.48Te3 Solid Solutions. *Inorg. Mater.* **44**, 1057–1059 (2008).

155. Scherrer, S. & Scherrer, H. Bismuth Telluride, Antimony Telluride, and Their Solid Solutions. in *CRC Handbook of Thermoelectrics* (CRC Press, 1995).

156. May, A. & Snyder, G. Introduction to Modeling Thermoelectric Transport at High

Temperatures. in *Thermoelectrics and Its Energy Harvesting: Materials, Preparation, and Characterization in Thermoelectrics* (CRC Press, 2012).

157. Ha, H. P., Cho, Y. W., Byun, J. Y. & Shim, J. D. The Effect of Excess Tellurium on the Thermo Electric Properties of Bi2Te3-Sb2Te3 Solid Solutions. *J. Phys. Chem. Solids* **55**, 1233–1238 (1994).

158. Horak, J., Drasar, C., Novotny, R., Karamazov, S. & Lost'ak, P. Non-Stoichiometry of the Crystal Lattice of Antimony Telluride. *Phys. Status Solidi* **149**, 549–556 (1995).

159. Miller, G. R. & Li, C.-Y. Evidence for the Existence of Antistructure Defects in Bismuth Telluride by Density Measurements. *J. Phys. Chem. Solids* **26**, 173–177 (1965).

160. Hashibon, A. & Elsasser, C. Density-Functional Theory Study of Point Defects in Bis2Te3. in *Thermoelectric Bi2Te3 Nanomaterials* (eds. Eibl, O., Nielsch, K., Peranio, N. & Volklein, F.) 165–186 (Wiley-VCH Verlag GmbH & Co. KGaA, 2015).

161. Stary, Z., Horak, J., Stordeur, M. & Stolzer, M. Antisite Defects in Sb2-xBixTe3 Mixed Crsytals. *J. Phys. Chem. Solids* **49**, 29–34 (1988).

162. Champness, C. H., Chiang, P. T., Grabowski, K. & Muir, W. B. Influence of Growth Conditions and Tellurium Phase on the Thermoelectric Properties of Bismuth Telluride-Type Materials. *J. Appl. Phys.* **39**, 4177 (1968).

163. Garnett, J. C. M. Colours in Metal Glasses and in Metallic Films. *Phil. Trans. R. Soc. Lond. A.* **203**, 385–402 (1904).

164. Zhou, L. D., Zhang, B.-P., Liu, W. S., Zhang, H. L. & Li, J.-F. Effects of Annealing on

Electrical Properties of n-type Bi2Te3 Fabricated by Mechanical Alloying and Spark Plasma Sintering. *J. Alloys Compd.* **467**, 91–97 (2009).

165. Goldsmid, H. J. Application of the Transverse Thermoelectric Effects. *J. Electron. Mater.* **40**, 1254–1259 (2011).

166. Fu, X. *et al.* Improving Deformability of Sb2Te3 Layered Material By Dislocation Climb at Anti-Phase Boundary. *Scr. Mater.* **135**, 10–14 (2017).

167. Delavignette, P. & Amelinckx, S. Large Dislocation Loops in Antimony Telluride. *Philos. Mag.* **6**, 601–608 (1961).

168. Medlin, D. L. & Yang, N. Y. C. Interfacial Step Structure at a (0001) Basal Twin in Bi2Te3. *J. Electron. Mater.* **41**, 1456–1464 (2012).

169. Hu, L. *et al.* Enhancement in Thermoelectric Performance of Bismuth Telluride Based Alloys by Multi-Scale Microstructural Effects. *J. Mater. Chem.* **22**, 16484 (2012).

170. Kims, S. S., Yamamoto, S. & Aizawa, T. Thermoelectric Properties of Anisotropy-Controlled p-Type Bi-Te-Sb System via Bulk Mechanical Alloying and Shear Extrusion. *J. Alloys Compd.* **275**, 107–113 (2004).

171. Medlin, D. L. & Snyder, G. J. Interfaces in Bulk Thermoelectric Materials: A Review for Current Opinion in Colloud and Interface Science. *Curr. Opin. Colloid Interface Sci.* **14**, 226–235 (2009).

172. Saylor, D. M., El Dasher, B. S., Rollett, A. D. & Rohrer, G. S. Distribution of Grain Boundaries in Aluminum as a Function of Five Macroscopic Parameters. *Acta Mater.* **52**,

3649–3655 (2004).

173. Saylor, D. M., Morawiec, A. & Rohrer, G. S. Distribution of Grain Boundaries in Magnesia as a Function of Five Macroscopic Parameters. *Acta Mater.* **51**, 3663–3674 (2003).

174. Hsieh, I.-T. & Huang, M.-J. An Investigation into the Thermal Boundary Resistance Associated with the Twin Boundary in Bismuth Telluride. *Nanoscale Microscale Thermophys. Eng.* **23**, 36–47 (2019).

175. Medlin, D. L., Ramasse, Q. M., Spataru, C. D. & Yang, N. Y. C. Structure of the (0001) Basal Twin Boundary in Bi2Te3. *J. Appl. Phys.* **108**, 043517 (2010).

176. German, R. M. Coarsening in Sintering: Grain Shape Distribution, Grain Size Distribution, and Grain Growth Kinetics in Solid-Pore Systems. *Crit. Rev. Solid State Mater. Sci.* **35**, 263 (2010).

177. Kim-Hak, O. *et al.* Microwave Sintering and thermoelectric Properties of p-type (Bi0.2Sb0.8)2Te3 Powder. *Powder Technol.* **226**, 231–234 (2012).

178. Mehta, R. J. *et al.* A New Class of Doped Nanobulk High-Figure-of-Merit Thermoelectrics by Scalable Bottom-Up Assembly. *Nat. Mater.* **11**, 233–240 (2012).

179. Oppenheimer, S. & Dunand, D. C. Porous NiTi by Creep Expansion of Argon-Filled Pores. *Mater. Sci. Eng. A* **523**, 70–76 (2009).

180. Oppenheimer, S. & Dunand, D. C. Solid-State Foaming of Ti-6Al-4V by Creep or Superplastic Expansion of Argon-Filled Pores. *Acta Mater.* **58**, 4387–4397 (2010).

181. Zhao, D., Tian, C., Liu, Y., Zhan, C. & Chen, L. High temperature sublimation behavior of antimony in CoSb3 thermoelectric material during thermal duration test. *J. Alloys Compd.* **509**, 3166–3171 (2011).

182. Hamachiyo, T., Ashida, M. & Hasezaki, K. Thermal Conductivity of Bi0.5Sb1.5Te3 Affected by Grain Size and Pores. *J. Electron. Mater.* **38**, 1048–1051 (2009).

183. Humphry-Baker, S. A. & Schuh, C. A. Spontaneous Solid-State Foaming of Nanocrystalline Thermoelectric Compounds at Elevated Temperatures. *Nano Energy* **36**, 223–232 (2017).

184. Zheng, Y. *et al.* Thermal Stability of p-Type BiSbTe Alloys Prepared by Melt Spinning and Rapid Sintering. *Mater.* **10**, 617–627 (2017).

185. Ni, J. E. *et al.* The Thermal Expansion Coefficient as a Key Design Parameter for Thermoelectric Materials and Its Relationship to Processing-Dependent Bloating. *J. Mater. Sci.* **48**, 6233–6244 (2013).

186. Ni, J. E. *et al.* Bloating in (Pb0.95Sn0.05Te)0.92(PbS)0.08-0.055% PbI2 Thermoelectric Specimens as a Result of Processing Conditions. *J. Electron. Mater.* **41**, 1153 (2012).

187. Schmidt, R. D. *et al.* The Temperature Dependence of Thermal Expansion for p-Type Ce0.9Fe3.5Co0.5Sb12 and n-Type Co0.95Pd0.05Te0.05Sb3 Skutterudite Thermoelectric Materials. *Philos. Mag.* **92**, 1261 (2012).

188. Murray, N. G. D. & Dunand, D. C. Effect of Thermal History on the Superplastic Expansion of Argon-Filled Pores in Titanitum: Part II Modeling of Kinetics. *Acta Mater.*

52, 2279–2291 (2004).

189. Caillat, T., Carle, M., Perrin, D., Scherrer, H. & Scherrer, S. Study of the Bi-Sb-Te ternary phase diagram. *J. Phys. Chem. Solids* **53**, 227–232 (1991).

190. Borkowski, K. & Przyluski, J. Investigation of Vacuum Deposition of Bi2Te3-Based Thermoelectric Materials. *Mater. Res. Bull.* **22**, 381–387 (1987).

191. Brooks, L. S. The Vapor Pressures of Tellurium and Selenium. *J. Am. Chem. Soc.* **74**, 227–229 (1952).

192. Ubelis, A. P. Temperature Dependence of the Saturated Vapor Pressure of Tellurium. *J. Eng. Phys.* **42**, 309–315 (1982).

193. Malinauskas, A. P. *Vapor Pressure of Tellurium Oxide*. (1968).

194. West, D., Sun, Y. Y., Wang, H., Bang, J. & Zhang, S. B. Native Defects in Second-Generation Topological Insulators: Effect of Spin-Orbit Interaction on Bi2Se3. *Phys. Rev. B* **86**, 121201(R) (2012).

195. Shen, J. J. *et al.* Thermoelectric and Thermomechanical Properties of the Hot Presses Polycrystalline Bi0.5Sb1.5Te3 Alloys. *J. Alloys Compd.* **509**, 161–164 (2011).

196. Eyidi, D., Maier, D., Eibl, O. & Westphal, M. Chemical Composition and Crystal Lattice Defects of Bi2Te3 Peltier Device Structures. *Phys. Status Solidi* **187**, 585–600 (2001).

197. Peranio, N. & Eibl, O. Gliding dislocations in Bi2Te3 materials. *Phys. Status Solidi* **206**, 42–49 (2009).

198. Lavrentev, M. G. *et al.* Improved Mechanical Properties of Thermoelectric (Bi0.2Sb0.8)2Te3 by Nanostructuring. *APL Mater.* **4**, 104807 (2016).

199. Wilkinson, D. S. & Ashby, M. F. Pressure Sintering by Power Law Creep. *Acta Mater.* **23**, 1277–1285 (1975).

200. Guan, Z. P. & Dunand, D. C. Compressive creep behavior of cast Bi2Te3. *Mater. Sci. Eng. A* **565**, 321–325 (2013).

201. Wang, Y., Qiu, B., McGaughey, J. H., Ruan, X. & Xu, X. Mode-Wise Thermal Conductivity of Bismuth Telluride. *J. Heat Transfer* **135**, 091102 (2013).

202. Lu, L., Shen, Y., Chen, X., Qian, L. & Lu, K. Ultrahigh Strength and High Electrical Conductivity in Copper. *Science (80-.).* **304**, 422–426 (2004).

203. Cook, B. A., Kramer, M. J., Wei, X., Harringa, J. L. & Levin, E. M. Nature of the Cubic to Rhombohedral Structural Transformation in (AgSbTe2)15(GeTe)85(AgSbTe2)15(GeTe)85 Thermoelectric Material. *J. Appl. Phys.* **101**, 053715 (2007).

204. Matsuo, T. & Suzuki, H. Phonon Scattering by Lattice Defects in Deformed Bismuth Crystals. *J. Phys. Soc. Japan* **43**, 1974–1981 (1977).

205. Fishman, I. M., Kino, G. S. & Wu, X. D. Density of Normal Carriers Below Tc and Thermal Resistance of Twin Boundaries in YBa2Cu3O7-x Single Crystals. *Phys. Rev. B* **50**, 7192 (1994).

206. Maiti, A., Mahan, G. D. & Pantelides, S. T. Dynamical Simulations of Nonequilibrium

Processes — Heat Flow and the Kapitza Resistance Across Grain Boundaries. *Solid State Commun.* **102**, 517–521 (1997).

207. Yu, Y. *et al.* Simultaneous Optimization of Electrical and Thermal Transport Properties of bi0.2Sb1.5Te3 Thermoelectric Alloy by Twin Boundary Engineering. *Nano Energy* **37**, 203–213 (2017).

208. Shin, H. S. *et al.* Twin-Driven Thermoelectric Figure-of-Merit Enhancement of Bi2Te3 Nanowires. *Nanoscale* **6**, 6158 (2014).

209. Bessas, D. *et al.* Phonon Spectroscopy in a Bi2Te3 nanowire Array. *Nanoscale* **5**, 10629 (2013).

210. Hamid Elsheikh, M. *et al.* A review on thermoelectric renewable energy: Principle parameters that affect their performance. *Renew. Sustain. Energy Rev.* **30**, 337–355 (2014).

211. Yang, J. & Caillat, T. Thermoelectric Materials for Space. *MRS Bull.* **31**, 224–229 (2006).

212. An, D. *et al.* Low Thermal Conductivity and Optimized Thermoelectric Properties of p-Type Te-Sb2Se3: Synergistic Effect of Doping and Defect Engineering. *ACS Appl. Mater. Interfaces* **11**, 27788–27797 (2019).

213. Wang, S. *et al.* Exploring the doping effects of Ag in p-type PbSe compounds with enhanced thermoelectric performance. *J. Phys. D. Appl. Phys.* **44**, (2011).

214. Wang, H., Pei, Y., Lalonde, A. D. & Snyder, G. J. Heavily doped p-type PbSe with high thermoelectric performance: An alternative for PbTe. *Adv. Mater.* **23**, 1366–1370 (2011).

215. Zhang, Q. *et al.* Enhancement of thermoelectric figure-of-merit by resonant states of aluminium doping in lead selenide. *Energy Environ. Sci.* **5**, 5246–5251 (2012).

216. Zhang, Q. *et al.* Heavy doping and band engineering by potassium to improve the thermoelectric figure of merit in p-type PbTe, PbSe, and PbTe 1- ySe y. *J. Am. Chem. Soc.* **134**, 10031–10038 (2012).

217. Wynick, G. L. & Boehlert, C. J. Use of electropolishing for enhanced metallic specimen preparation for electron backscatter diffraction analysis. *Mater. Charact.* **55**, 190–202 (2005).

218. Perdew, J. P., Burke, K. & Ernzerhof, M. Generalized gradient approximation made simple. *Phys. Rev. Lett.* **77**, 3865–3868 (1996).

219. Kresse, G. & Furthmüller, J. Efficient iterative schemes for ab initio total-energy calculations using a plane-wave basis set. *Phys. Rev. B - Condens. Matter Mater. Phys.* **54**, 11169–11186 (1996).

220. Janotti, A. & Van De Walle, C. G. Native point defects in ZnO. *Phys. Rev. B - Condens. Matter Mater. Phys.* **76**, 1–22 (2007).

221. Doak, J. W., Michel, K. J. & Wolverton, C. Determining dilute-limit solvus boundaries in multi-component systems using defect energetics: Na in PbTe and PbS. *J. Mater. Chem. C* **3**, 10630–10649 (2015).

222. Saal, J. E., Kirklin, S., Aykol, M., Meredig, B. & Wolverton, C. Materials Design and Discovery with High-Throughput Density Functional Theory: The Open Quantum

Materials Database (OQMD). *JOM* **65**, 1501–1509 (2013).

223. Winning, M. & Rollett, A. D. Transition between low and high angle grain boundaries. *Acta Mater.* **53**, 2901–2907 (2005).

224. Zhao, D., Tian, C., Tang, S., Liu, Y. & Chen, L. High temperature oxidation behavior of cobalt triantimonide thermoelectric material. *J. Alloys Compd.* **504**, 552–558 (2010).

225. Munir, Z. A. & Hirth, J. P. Surface morphology of sublimated crystals of cadmium and zinc sulfides. *J. Appl. Phys.* **41**, 2697–2704 (1970).

226. Mullins, W. W. Theory of Thermal Grooving. *J. Appl. Phys.* **28**, 333–339 (1957).

227. Tilley, R. J. D. *Defects in Solids*. *Encyclopedia of Inorganic Chemistry* (John Wiley & Sons, Inc., 2008). doi:10.1002/0470862106.ia062

228. Male, J. *et al.* The importance of phase equilibrium for doping efficiency: Iodine doped PbTe. *Mater. Horizons* **6**, 1444–1453 (2019).

229. Walsh, A. & Zunger, A. Instilling defect tolerance in new compounds. *Nat. Mater.* **16**, 964–967 (2017).

230. Walukiewicz, W. Intrinsic limitations to the doping of wide-gap semiconductors. *Phys. B Condens. Matter* **302**–**303**, 123–134 (2001).

231. Alaneme, K. K. & Okotete, E. A. Recrystallization mechanisms and microstructure development in emerging metallic materials: A review. *J. Sci. Adv. Mater. Devices* **4**, 19–33 (2019).

232. Rohrer, G. S. Grain boundary energy anisotropy: A review. *J. Mater. Sci.* **46**, 5881–5895 (2011).

233. Cannon, W. R. & Langdon, T. G. Creep of ceramics - Part 2 An examination of flow mechanisms. *J. Mater. Sci.* **23**, 1–20 (1988).

234. Duong, H., Beeman, M. & Wolfenstine, J. High temperature creep behavior and substructure in KCl-KBr solid solution alloys. *Acta Metall. Mater.* **42**, 1001–1012 (1994).

235. Mohamed, F. A. & Langdon, T. G. Creep Behavior of Ceramic Solid-Solution Alloys. *J. Am. Ceram. Soc.* **58**, 533–534 (1975).

236. Cannon, W. R. & Sherby, O. D. High-Temperature Creep of NaCl-KCl Solid-Solution Alloys. *J. Am. Ceram. Soc.* **53**, 346–349 (1970).

237. Chang, M. C., Agne, M. T., Michi, R. A., Dunand, D. C. & Snyder, G. J. Compressive creep behavior of hot-pressed GeTe based TAGS-85 and effect of creep on thermoelectric properties. *Acta Mater.* **158**, 239–246 (2018).

238. Li, C. C., Snyder, G. J. & Dunand, D. C. Compressive creep behaviour of hot-pressed PbTe. *Scr. Mater.* **134**, 71–74 (2017).

239. CANNON, W. R. & SHERBY, O. D. Third-Power Stress Dependence in Creep of Polycrystalline Nonmetals. *J. Am. Ceram. Soc.* **56**, 157–160 (1973).

240. Krishnamachari, V. & Jones, J. T. Compressive Creep of CoO Single Crystals. *J. Am. Ceram. Soc.* **57**, 506 (1974).

241. Murphy, S. T., Lu, H. & Grimes, R. W. General relationships for isovalent cation substitution into oxides with the rocksalt structure. *J. Phys. Chem. Solids* **71**, 735–738 (2010).

242. Nes, E. Recovery Revisited. *Acta Metall. Mater.* **43**, 2189–2207 (1995).

243. Klemens, P. G. Phonon scattering and thermal resistance due to grain boundaries. *Int. J. Thermophys.* **15**, 1345–1351 (1994).

244. Mitchell, T. E. & Heuer, A. H. Solution Hardening by Aliovalent Cations in Ionic Crystals. *Mater. Sci. Eng.* **28**, 81–97 (1977).

245. HANSEN, E. E., MUNIR, Z. A. & MITCHELL, M. J. Sublimation Pressure and Sublimation Coefficient of Single-Crystal Lead Selenide. *J. Am. Ceram. Soc.* **52**, 610–612 (1969).

246. Cottrell, A. H. & Jaswon, M. A. Distribution of solute atoms round a slow dislocation. *Proc. R. Soc. London A* **199**, 104–114 (1949).

247. Yu, Y. *et al.* Ag-Segregation to Dislocations in PbTe-Based Thermoelectric Materials. *ACS Appl. Mater. Interfaces* **10**, 3609–3615 (2018).